Universidade de Aveiro Departamento de Engenharia Mecânica
2013

**Tatiana
Vladimirovna
Zhiltsova**

Otimização do processo de moldação para obtenção de peças microestruturadas

Injection moulding process optimization for microstructured parts production

Tese apresentada à Universidade de Aveiro para cumprimento dos requisitos necessários à obtenção do grau de Doutor em Engenharia Mecânica, realizada sob a orientação científica da Doutora Mónica Sandra Abrantes de Oliveira Correia, Professora Auxiliar do Departamento de Engenharia Mecânica da Universidade de Aveiro e do Doutor Jorge Augusto Fernandes Ferreira, Professor Auxiliar do Departamento de Engenharia Mecânica da Universidade de Aveiro.

Apoio financeiro da FCT e do FSE no âmbito do III Quadro Comunitário de Apoio SFRH/BD/45585/2008.

“Strive not to be a success, but rather to be of value”.
Albert Einstein

Dedico este trabalho à memória da minha mãe.

o júri

Prof. Doutor Vasile Staicu
Professor Catedrático do Departamento de Matemática da Universidade de Aveiro

Prof. Doutor Manuel José Cabral dos Santos Reis
Professor Associado com Agregação da escola de Ciências e Tecnologia
da Universidade de Tràs-os-Montes e Alto Douro

Prof. Doutor Vítor António Ferreira da Costa
Professor Associado com Agregação do Departamento de Engenharia Mecânica
da Universidade de Aveiro

Prof. Doutor Joel Oliveira Correia Vasco
Professor Adjunto do Instituto Politécnico de Leiria

Prof.ª Doutora Mónica Sandra Abrantes de Oliveira Correia
Professora Auxiliar do Departamento de Engenharia Mecânica
da Universidade de Aveiro. (Orientadora)

agradecimentos

A autora agradece de forma reconhecida:

- Aos seus orientadores, a Prof.ª Doutora Mónica Oliveira e o Prof. Doutor Jorge Augusto Fernandes Ferreira;
- À Fundação para a Ciência e Tecnologia pelo financiamento da sua bolsa de doutoramento SFRH/BD/45585/2008;
- Ao Prof. Doutor António Sérgio Duarte Pouzada do Departamento de Polímeros da Universidade de Minho que permitiu a utilização de recursos fundamentais para o desenrolar deste doutoramento;
- Ao Prof. Doutor António José Vilela Pontes do Departamento de Polímeros da Universidade de Minho que permitiu a utilização de recursos fundamentais para o desenrolar deste doutoramento;
- Ao Prof. Doutor Joel Oliveira Correia Vasco pela ajuda na adaptação e operação do micromolde;
- Ao Doutor Victor Fernando Santos Neto pelo apoio na maquinação dos protótipos;
- Aos mestres Andressa Pereira, Cátia Ribeiro e Luis Filipe Martins do Departamento de Polímeros da Universidade de Minho pelo apoio na operação da máquina de injeção de termoplásticos à escala micro;
- Ao Eng.º João Teles, do Departamento de Engenharia Mecânica da Universidade de Aveiro, pelo apoio na operação da máquina de injeção de termoplásticos;
- Ao Prof. Doutor Sushil Kumar Mendiratta do Departamento de Física da Universidade de Aveiro que permitiu a utilização do microscópio de luz polarizada;
- Ao Eng.º Jorge Humberto da Silva Monteiro do Departamento de Física da Universidade de Aveiro pelo apoio na microscopia de luz polarizada;
- Ao Eng.º António Festas, do Departamento de Engenharia Mecânica da Universidade de Aveiro, pela maquinação dos sistemas auxiliares do molde;
- Ao Eng.º Maurício José Aires Malheiro do Departamento de Polímeros da Universidade de Minho pelo apoio na microscopia de luz polarizada e Análise Mecânica Dinâmica (DMA);
- Ao mestre Bruno Silva pelo apoio na preparação das amostras;
- Ao André Válega pelo apoio na aquisição das propriedades mecânicas.

palavras-chave

micromoldação por injecção, modelos reológicos, modelação constituitiva, fluência, viscoelasticidade, relaxamento de tensões, simulação numérica

resumo

Ao longo das últimas décadas, a micromoldação (µ-moldação) por injeção de termoplásticos ganhou um lugar de destaque no mercado de equipamentos eletrónicos e de uma ampla gama de componentes mecânicos. No entanto, quando o tamanho do componente diminui, os pressupostos geralmente aceites na moldação por injeção convencional deixam de ser válidos para descrever o comportamento reológico e termomecânico do polímero na microimpressão. Por isso, a compreensão do comportamento dinâmico do polímero à escala micro bem como da sua caraterização, análise e previsão das propriedades mecânicas exige uma investigação mais alargada. O objetivo principal deste programa doutoral passa por uma melhor compreensão do fenómeno físico intrínseco ao processo da µ-moldação por injeção. Para cumprir com o objetivo estabelecido, foi efetuado um estudo paramétrico do processo de µ-moldação por injeção, cujos resultados foram comparados com os resultados obtidos por simulação numérica. A caracterização dinâmica mecânica das µ-peças foi efetuada com o objetivo de recolher os dados necessários para a previsão do desempenho mecânico das mesmas, a longo prazo. Finalmente, depois da calibração do modelo matemático do polímero, foram realizadas análises estruturais com o intuito de prever o desempenho mecânico das µ-peças no longo prazo. Verificou-se que o desempenho mecânico das µ-peças pode ser significativamente afetado pelas tensões residuais de origem mecânica e térmica. Estas últimas, resultantes do processo de fabrico e das condições de processamento, por isso, devem ser consideradas na previsão do desempenho mecânico e do tempo de serviço das µ-moldações.

keywords

microinjection moulding, rheological models, constitutive modelling, creep, viscoelasticity, stress relaxation, numerical simulation.

abstract

Over the last decades, microinjection moulding (µIM) of thermoplastics has gained a pertinent place on the market of electronic equipment and a broad range of the mechanical aids. However, when size of components drop to the micro level, the assumptions of the conventional injection moulding cease to describe the complex rheological and thermo-mechanical behavior of the polymer in the microimpression. Therefore, understanding of the polymer flow dynamics at the micro scale as well as characterization, assessment and prediction of the final mechanical properties require a great deal of additional research. The prime objective of this doctoral thesis is to get an insight into the physical phenomena inherent to µIM process. In order to comply with the established objective, a number of parametrical studies of the µIM process were carried on an instrumented micromould and then their results were compared with the obtained numerical simulation results gathered from process modeling phenomena. Dynamical mechanical characterization of µ-moulded parts was performed in order to collect the data required for prediction of their long-term mechanical performance. Finally, after calibration of polymer material model, a long-term transient structural analysis was carried out. It was found out that the structural performance of microparts was significantly affected by the thermo-mechanical (residual) stresses. The latter is an inherent feature of the injection moulding processing, and therefore has to be accounted for the prediction of the µ-moulded parts' service life.

Table of Contents

List of Figures

List of tables

List of equations

List of symbols

Abbreviations

3D	Three-dimensional
AC	Accuracy Criterion
AFM	Atomic Force Microscopy
AMDL®	Autodesk Moldflow Design Link
AMI®	Autodesk® Moldflow® Insight
CTE	Coefficient of Thermal Expansion
DLC	Diamond Like Carbon
DMA	Dynamical Mechanical Analysis
DMTA	Dynamical Mechanical Thermal Analysis
DOE	Design of Experiments
IDDM	Interpolated Domain Decomposition Method
IB	Ion Beam
IM	Injection Moulding
FFD	Flow Front Delay
HTRS	Hybrid Thermo-rheological Structural analysis
HTC	Heat Transfer Coefficient
LIGA	Lithographie Galvanoformung Abformung
MPI®	Moldflow Plastics Insight
μIM	Micro Injection Moulding
MIS	Micro Injection Simulation
μEDM	Micro Electric Discharge Machining
OFAT	One Factor At Time
OM	Optical Microscopy
PLM	Polarized Light
PSD	Principal Stress Difference
RTR	Rapid Thermal Response
SFM	Scanning Force Microscopy
SN	Signal-to-Noise Ratio
SPH	Smooth Particle Hydrodynamic
TTSP	Time–Temperature Superposition Priciple
UV	Ultra Violet
WEDG	Wire Electro Discharge Grinding
WLF	Williams-Landel-Ferry

Thermoplastic materials

ABS	Acrylonitrile Butadiene Styrene
COC	Cyclic Olefin Copolymer

HDPE	High Density Polyethylene
PBT	Polybutylene Terephthalate
PC	Polycarbonate
PEEK	Polyether Ether Ketone
PEI	Polyetherimide
PMMA	Poly(methyl methacrylate)
POM	Polyoxymethilene
PPE	Polyphenyl-ethers
PP	Polypropylene
PS	Polystyrene
z-n LLDPE	Ziegler-Natta Linear Low Density Polyethylene

Greek symbols

α	Linear thermal expansion coefficient
α_T	Horizontal shift factor
γ	Shear strain
$\dot{\gamma}$	Shear rate
$\underline{\dot{\gamma}}$	Rate of deformation tensor
δ	Loss angle
η	Viscosity
η_0	Zero shear rate viscosity
λ	Wavelength of light
μ	Micro
$\mu(t)$	Shear Relaxation Function
ρ	Density
σ	Stress
$\underline{\sigma}$	Stress tensor
ε	Tensile strain
ε_i	Linear shrinkage
τ	Relaxation Time
ω	Angular frequency

Latin symbols

b_T	Vertical shift factor
c_p	Specific heat
$D(t)$	Tensile creep compliance
E_a	Activation Energy
E_i	Spectral Strength
E_r	Reduced modulus
$E(t)$	Tensile modulus

$\vec{g}$	Gravitational force vector
G(t)	Stress relaxation modulus
G´	Storage modulus
G´´	Loss modulus
G*	Complex modulus
H	Hardness
H(τ)	Spectrum of relaxation time
J(t)	Creep compliance in shear
k	Thermal conductivity
K(t)	Bulk function
L(τ)	Spectrum of retardation times
Δn	Birefringence
N_D	Deborah Number
P_i	Injection pressure
P_h	Holding pressure
p	Pressure
R	Gas constant
S_p	Screw/ram position
T	Temperature
T_m	Mould temperature
T_{melt}	Melt temperature
t	Time
t_c	Cooling time
t_h	Holding time
$\vec{v}$	Velocity vector
V_i	Injection speed
V_t	Total volume
ωg*	non-dimensional shear relaxation function

Mathematical symbols

∇	Del - vector differential operator
:	Double dot tensor product
·	Vector scalar product or vector tensor product

Chapter 1 Introduction

1.1 Microinjection moulding of thermoplastics (µIM): process and materials

Microinjection moulding of thermoplastics is a manufacturing technique by which tiny components can be produced quickly and at low cost, taking an advantage of its cyclic nature and an ability to produce the microcomponents in a highly automated fashion. Markets for micromoulded thermoplastic components are expanding continuously over the last decades. Micromoulded components have gained a place in a variety of new applications such as automotive micro switches, computer connectors, printer ink heads, fiber optics connectors, electronic micro parts, medical implants, micromechanics, watch industry, optics lenses among others [1]. Definitions for micromoulded components widely vary and may be divided into three main categories [2-4]:

- Microstructured parts – the conventional injection moulded parts with features within the micrometre range (Figure 1a);
- Microparts with all the dimensions in micro scale and mass within a few milligrams (Figure 1b);
- Parts with precision of dimensional tolerances in µm.

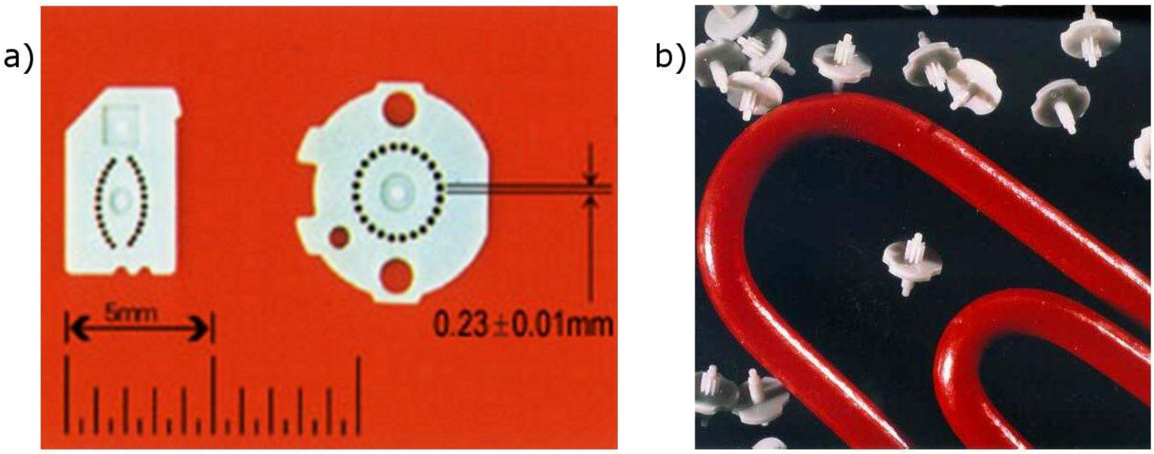

Figure 1 - a) Miniature holes in a dot matrix printer head (PBT); b) micro gear for watch industry (POM) (adapted from[1])

The workflow of the µIM process is quite similar to the conventional one (Figure 2). It starts by pushing melted polymer into a mould cavity, followed by the packing stage to compensate polymer shrinkage during solidification. Thereafter when the polymer entrance solidifies no more material can be added and the component keeps cooling until it reaches a temperature that guarantees free damage ejection from the mould [5]. However, the reduced cavity dimensions of a microcomponent alter drastically the polymer behaviour and may lead to two opposite flow pattern scenarios, namely: premature solidification of the polymer (incomplete filling) or polymer damage due to excessive shear heating.

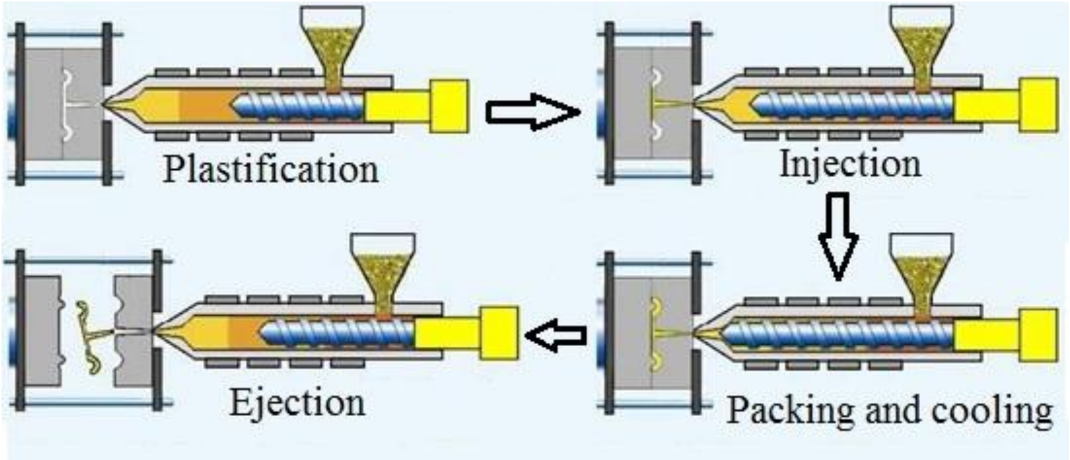

Figure 2 - Processing cycle of conventional injection moulding process(adapted from [6])

Polymers are materials composed from the long chains of repeating molecules (monomers). They are typically obtained through the chemical reactions of monomers, ratio of reactants, special additives, temperature and pressure, separation and recovery. Each family of polymers represents a wide range of properties, differing in molecular weight, distribution, degree of crystallinity, and type of additives. Polymer properties are greatly affected by the geometry of the molecular chains architecture. Three major configurations are presented in Figure 3, namely: linear chain, a branched chain and a cross-linked chain. The two first configurations represent thermoplastic polymers, which can be easily moulded and remoulded to any configuration. While with the latter configuration, by increasing the degree of cross-linking, the molecular chain loses its mobility and a polymer becomes thermoset, impossible to reshape under the application of heat and pressure [7].

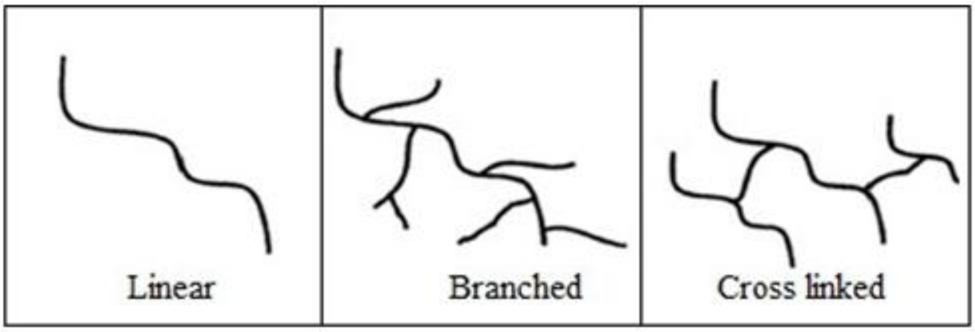

Figure 3 - Structure of polymer chains (adapted from [7])

1.2 Challenges of the µIM process

Despite the seeming simplicity, µIM does not resume to mere miniaturization of the conventional injection moulding. A great deal of phenomena occurs inside the microcavity making a simple rescale unlikely to occur. A number of issues have to be addressed in order to solve the problems imposed by the miniaturization. The main difficulty encountered in the moulding of micro parts is related to the instant increase in polymer viscosity at the vicinity of the relatively cold mould wall. The latter could lead to the premature solidification of the polymer and hence incomplete filling of the cavity. In recent years, significant progress has been made in micromoulding technology in both industry and scientific research. In a number of studies, several issues are referred to be responsible for the complex thermo-rheological behaviour of the polymer flow in a micro cavity/channel i.e.: elongation flow, heat transfer in varying thicknesses, wall slip and micro rheology [4, 8, 9]. Such drastic alteration of the rheological behaviour may eventually influence the final thermal and mechanical properties of the processed polymers. For this reason the existent macro rheological models should be used with precautions when numerical prediction of the polymer flow at the micro scale is in concern. So far, the majority of the studies to evaluate the influence of the injection moulding process variation (i.e. rheological behaviour) on the quality of the microcomponent are mainly in terms of dimensional stability and visual appearance [10-18]. However, the complex thermo-rheological behaviour of the polymer flow confined to a micro-cavity can create drastic alterations of the mechanical properties of the final product and consequently could be critical for its short and long-term performance. To the author´s knowledge, only a couple of studies have investigated the connections between the micro-rheological behaviour of polymer and the mechanical performance of the micropart, where such criterion as weld line strength was adapted as a quality output [19, 20]. Plenty of questions related to the assessment of polymer flow dynamics in the microimpression and evaluation of the mechanical properties of the micromoulded components still remain. The prime objective of this doctoral thesis is to discover cause-effect relations between size, geometry characteristics of the micro tool, injection moulding processing conditions and final mechanical properties of the micromoulded parts, aiming toward improvement and optimization of their performance during each duty cycle.

1.3 Thesis outline

This thesis contains six chapters which are organized as follows.

First chapter presents a brief description of the µIM process and highlights its challenges.

In Chapter 2, several significant aspects of the µIM process are discussed in depth. In addition, such topics as viscoelastic nature of polymers, development and assessment of the residual stresses in IM parts are presented. This chapter is concluded by outlining the motivation and the objectives for this thesis.

Chapter 3 contains a detailed description of the experimental equipment, techniques, materials and methodologies used for obtaining microparts and their characterization.

Chapter 4 explains the numerical simulation routine applied for prediction of polymer’s behavior at µ-scale and was divided in two general steps. First, Autodesk Moldflow Insight 2012 (AMI®) simulation code has been employed for parametrical study of polymer flow in the microimpression. At the second stage, the previously obtained results of AMI numerical simulations were converted into the ABAQUS compatible file for assessment of the residual stresses in µIM parts with and without external deformation.

Chapter 5 provides a holistic approach for assessment of polymer dynamics in the microimpression and structural performance of µ-parts, which embraces both experimental data and their numerical prediction. First, the parametrical study highlights the influence of the µIM processing conditions on the behavior of Acrylonitrile Butadiene Styrene (ABS), Polypropylene (PP) and Polyoxymethylene (POM) polymers in the microimpression. Multiple quality criteria were chosen as experiment outputs and are listed as follows: polymer dynamics at µ-scale, µIM process variability, maximum cavity temperature, and weld line position and width. AMI numerical simulation of the polymer flow in the microimpression may be divided in two stages. First, a study on the finite element mesh refinement towards improvement of the prediction accuracy was carried out. Then, a set of numerical simulations were conducted for comparison of the experimental and predicted polymer dynamics and weld line locations and shapes. Thereafter, numerically predicted process induced residual stresses were compared for ABS, PP and POM polymers in ABAQUS numerical simulation program.

Mechanical testing of ABS µ-parts was carried out with the mechanical dynamical thermal analysis, which data were subsequently used for calibration of the material model in ABAQUS structural analysis. The latter allowed clarifying the influence of the thermorheological history of ABS µ-parts on their long-term performance.

Finally, the major conclusions from this research work and some topics that required further investigation are provided in Chapter 6.

Chapter 2 Literature review

This chapter is divided in eleven sections, and embraces several significant aspects of the µIM as well as of nature of polymer materials.

In the first section, a brief discussion of the strategies applied for adaptation of the conventional injection moulding equipment to micro scale will be introduced.

The second section is dedicated to the process/tool/polymer interaction and its influence on the quality signatures of micromoulded parts. In the third section, monitoring and control of the µIM is discussed.

The following two sections overview the rheological models of the polymer flow at micro-cavities and the numerical simulation of the µIM.

Quality evaluation of the micromoulded parts require considering both polymer morphology assessment and final mechanical properties. At the µ-scale, the acquisition of the latter is unlikely by means of conventional mechanical testing, therefore in the sixth section; a brief summary of the mechanical testing for micro polymeric parts will be presented.

Development and assessment of residual stresses in IM parts are known to be of utmost importance for their life-time performance and therefore will be a topic of discussion in the seventh section.

Viscoelastic nature of polymers behaviour will be presented in the section number eight and will be followed by a brief description of polymer’s temperature dependence in the section 9.

A mechanism underlying the phenomena of the time temperature superposition principle (TTSP) will be discussed in the section ten.

The penultimate section discusses a combined thermo-rheological and structural analysis of the thermoplastic part, intended to link processing history and mechanical solicitations of the part to its short and long-term performance.

Based on an analysis provided by the literature review, this chapter will be concluded by formulating of the research objectives intended to be accomplished in the scope of the presented doctoral thesis.

2.1 Systems and tools for micromoulding of thermoplastics

2.1.1 Injection moulding machines

In order to accomplish accurate and defect free moulding of microcomponents, every functional system of the macro moulding machine has to undergo a series of profound modifications. There is a variety of motives why the conventional injection moulding machines fail to satisfy the requirements of the microinjection moulding process. One of the main reasons so far concerns the minimum metering size of a typical macro moulding machine which is apparently too big in comparison to the tiny quantity of material required to produce a microcomponent. The latter turns precise metering very complicated along with a considerable increase of the time of melt residence in the barrel and eventually may lead to material degradation. In addition, clamping force also has to be reduced in order to guaranty free damage release of the micropart [2, 21]. Until now, several commercially available and home-made machines are used for production of the micromoulded components and may be divided in two main groups:

- where modifications are accomplished by simple rescale/miniaturization of the metering and injection units of the conventional injection moulding machine (reciprocating-screw type) towards precise dosage of polymer melt in every shot [2, 22];
- where, as shown in Figure 4, the alteration implies the separation of the plasticization from the injection unit, being therefore performed in the extrusion screw or hot cylinder, mounted at the angle to the inject axis. The latter is followed by the polymer melt entering the injection unit, where the mini plunger pushes the prepared shot to fill the mould cavity [23-27].

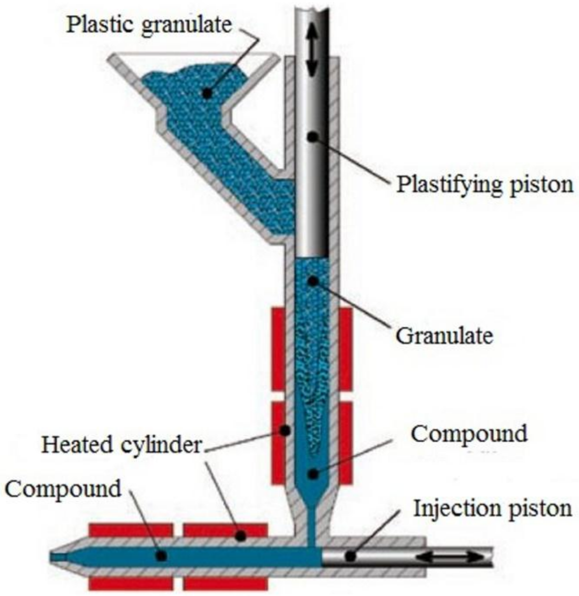

Figure 4 - Plasticization and injection unit of formicaPlact® microinjection molding machine (adapted from [28])

2.1.2 Demoulding

Along with metering and injection problems demoulding of the microparts has become a critical issue as failure frequently occurs during part removal from the mould. The interactions of polymer shrinkage and the coefficient of friction between the polymer and the core may have detrimental effects on the component failure during ejection [29, 30]. Moreover, the micro features with high aspect ratios have a larger contact surface between the mould and the polymer which results in higher frictional resistance during ejection.

Several studies have emphasized that smooth cavity surface finishing is essential for friction decrease at the polymer/insert interface [21, 31, 32]. Similarly to macro injection moulding, coatings are frequently used to improve the roughness properties of micro cavities and consequently achieve superior surface quality of microparts. Griffiths *et al.* [33] reported that for a cavity coated with DLC, considerably fewer forces were required for ejection of the polycarbonate (PC) and ABS microparts. Navabpour and co-workers [34] discovered that, in order to avoid polymer breaking at ejection, adhesive bond between polymer and stainless steel should not exceed the tensile strength of the polymer. In addition to the experimental techniques, the magnitude of the stress on the polymer/metal interface could be assessed with the aid of finite elements stress analysis [35]. Considering fragility of the microparts, conventional ejection with pins becomes unlikely and may eventually lead to irreversible damage. In order to overcome those weaknesses, alternative solutions have to be considered. For example, if geometry of microparts allows for a positive draft angle, the latter could assist the proper demoulding of the microparts [35-37]. Alteration of the mould design was adopted by Wu *et al.*, [37] where the micro ejection block was used as striper plate to thrust the microparts. For moulding high aspect ratio micro structures within the rough surface μ-impression, Michaeli *et al.* [38] proposed vacuum assisted demoulding. In case of microinjection moulding, the choice of a demoulding system will eventually depend on the cavity geometry, surface finishing and the material to be moulded. In addition, a special attention should be given to correct calculation of the ejection forces and proper design of the ejection system, as both factors can be detrimental for the micropart quality.

2.1.3 Mould insert fabrication

In the conventional injection moulding process, the cavity is machined directly in the mould plate, an altogether different concept is adopted when moulding of the microparts is concerned. It turns to be more practical, in terms of energy saving and versatility of the mould tool, to machine the impression in the interchangeable mould insert. This way all necessary mould tool transformations can be applied locally and the microparts of different configuration could be produced using the same injection mould. The choice of the technique for the insert fabrication generally depends on three main factors: insert material used, surface finishing (roughness) and aspect ratio demanded by the application. Techniques used for micro fabrication may be divided into two groups: direct structuring and an indirect structuring. The former category includes: laser ablation, micro electrical discharge machining (μEDM) and mechanical micromachining (diamond turning, micro milling). Lithographie Galvanoformung Abformung (LIGA) process and silicon etching fall into a latter group, where several operation steps are required to obtain a microimpression [39, 40]. The following diagram (Figure 5) summarizes the fabrication technologies used, so far, for microimpression fabrication.

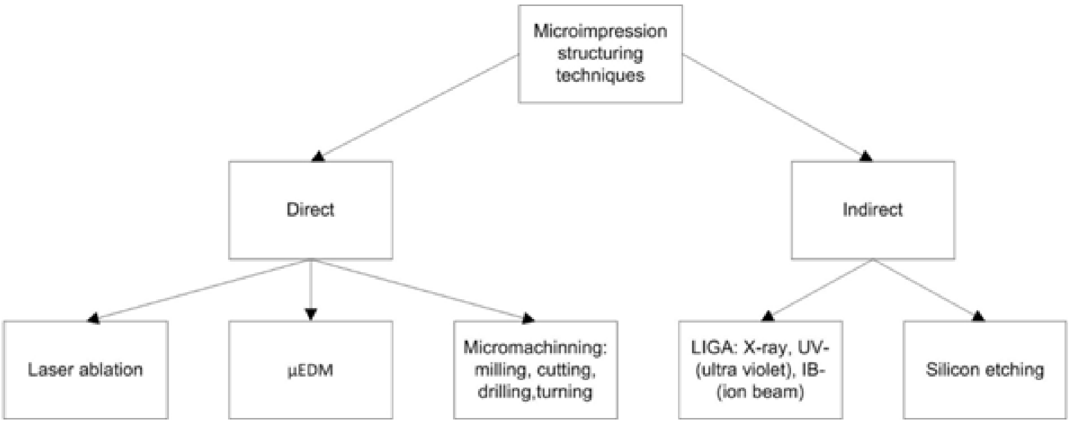

Figure 5 - System view of the structuring techniques for microimpression fabrication

LIGA process is a technology developed in the Forschungszentrum Karlsruhe in Germany in 1980s. Since the start of the micro technology development, it has been referred as a suitable technique for fabrication of the high aspect ratio microstructures with surface roughness down to 30 nm and such a low lateral resolution as 200 nm [41-43]. Being a multi stage process, LIGA may be divided in three main steps: lithography, electroforming and plastic moulding (Figure 6). The quality of the patterns obtained by deep X-ray LIGA is highly dependent on correlation of radiation intensity, mask composition and substrate type. Novel approaches for improvement of X-ray LIGA process for micro insert fabrication is in permanent research in academy [44-46].

With deep X-ray LIGA it is possible to obtain very accurate patterns of micro features with high aspect ratios up to 100 and micro structures with size less than 250nm. Nevertheless, in spite of all the above mentioned benefits, it is still not a widespread commercial technique for micro replication, being time consuming and costly [42, 44, 47]. Ultra violet (UV) LIGA and ion beam (IB) LIGA technologies are less complex when compared to the X-ray LIGA process. In UV LIGA, the ultraviolet source, instead of the X-ray, is used to expose the resists making the process less expensive. The size of micro structures obtained by this technique is less than 100nm, yet the electrons are very light and may cause the loss of resolution and poor surface finishing [43, 48-50]. In case of low volume production, silicon microstructured inserts may be a suitable alternative to the expensive LIGA process.

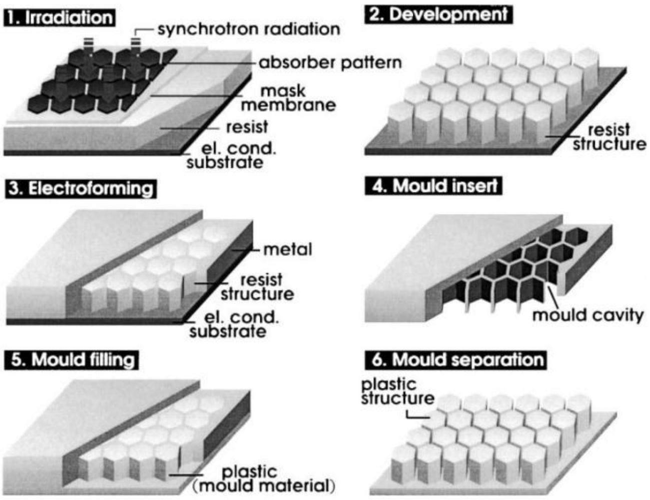

Figure 6 - Principle process steps for the fabrication of microstructures by the LIGA technique (adapted from [41])

The impressions in silicon are usually obtained by wet etching and in spite of the inherent fragility of the material, low roughness of surface finish makes this technique quite satisfactory for moulding of microparts in limited quantities [51-53].

The direct structuring techniques are far more economically attractive and can be easily applied for the micro insert fabrication of hard metals and alloys. When the complex geometries of the micro features are concerned, a variety of micro cutting techniques are currently available and may be enumerated as follows: micro milling (for microgrooves and micro 3D shapes), micro turning (for micro pins), and micro drilling (for micro holes) [54, 55]. Micromachining is accomplished by the diamond and cemented carbide cutting miniaturized tools whereas any particular application depends on the required surface finishing and material processed.

Applicability of diamond cutting tools is limited to soft non-ferrous metals as brass, aluminium, copper and nickel. It was reported that very fine surface finishing with roughness of 48nm can be accomplished [54, 56, 57]. More resilient materials like steel are processed with the cemented carbide tool of diameters down to 50µm, however, the surface resolution was lower (0.1–0.3µm) in comparison to the one obtained by the diamond cutting tools [58]. Although maximum aspect ratios, achieved by micro cutting, are considerably smaller in comparison to the other micro fabrication techniques, high level of automation, continuous improvement in precision of the tools along with the ability to work with hard metals, makes it an appropriate technique for microstructured insert fabrication. Another popular direct structuring technique for hard metals and alloys is the micro electrical discharge machining (μEDM). The heat is applied through the thin metal wire (usually brass) in the form of pulsed discharges, which cut metal by melting and evaporation [54]. The different types of μEDM may be classified by the type of electrode and/or by electrode-work peace movement. Proper choice of the size and shape of the electrodes, to a great extent, determines replication quality and aspect ratios up to 100 may be realized with optimum conditions [54]. Fine electrodes of 20μm, used in wire electro discharge grinding (WEDG), permit to machine patterns of complex shapes with resolution of 5μm and roughness of 0.1μm. Nonetheless, a maximum aspect ratio of the micro structures scarcely reaches 17 times the wire diameter [54, 56]. Surface resolution obtained by laser ablation is similar to that of micro cutting techniques making this method very popular for machining of a wide range of engineering materials [58]. Ultra short pulsed lasers with optimized pulse energy and focus size are able to produce microstructures with a size from 10μm, aspect ratio of 10 and roughness of 0.16μm [40, 59]. It is worth mentioning, however, that in terms of surface quality and minimum achievable dimensions, the output from the micro laser ablation is inferior to the LIGA and μEDM.

2.1.4 Rapid heating/cooling process

In conventional injection moulding process, mould temperature is far below the temperature of the injected polymer. At such conditions, the frozen layer forms near the cavity wall while the core is significantly hotter and continues cooling down to ejection temperature at the end of the moulding cycle. When the polymer melt is injected to the micrometric cavity, high surface-to-volume ratio and the reduced dimensions of microparts promote the instantaneous drop of melt temperature and consequently lead to incomplete filling [60]. In order to achieve complete filling of the microcavity, a temperature gradient between mould and molten polymer should be minimized during injection stage. The latter may be accomplished by heating the mould up to the glass transition temperature (T_g) for amorphous thermoplastics and to the melt temperature (T_{melt}) for the crystalline. Thereafter, mould temperature should decrease below the ejection temperature of polymer for successful demoulding. Such temperature variation may be accomplished with a special heating/cooling (variotherm) system shown in Figure 7 [3, 61].

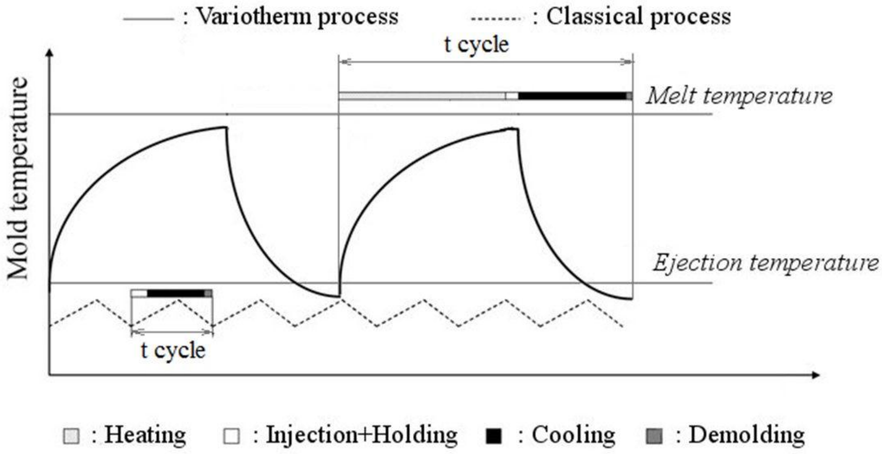

Figure 7 - Comparison of the mould temperature profile in the classical and variotherm processes (adapted from [62])

When mould temperature is close to processing temperature, even microstructures of the high aspect ratios may be eventually filled. Moreover, isothermal filling tends to induce less residual stresses and surface defects in the microparts [61, 63-65]. However, temperature amplitude during the variotherm process is significantly higher than that of the convenient process, which may lead to longer cycle times compromising the economic feasibility of the micromoulding process [62]. In order to successfully implement the variotherm process, two main issues have to be addressed. The first is related to the choice of the heating technique capable of rising promptly the mould temperature above T_g/T_{melt}. The second issue has to be focused on the efficient heat removal for the fastest possible cycle times. So far, there are two main approaches to transport the required power to the mould: external type (infrared radiation and induction heating) and internal/built-in (joule/resistive, high-frequency proximity, water and oil heating). The main limitation to use water as a heating media is that the maximum heating temperature does not exceed 95°C, which is less than the glass transition/melt temperature of the majority of polymers. As a result, water is generally used for cooling in the variotherm process [60, 63, 65-67]. Heat retention properties of oil and its ability to be heated up to 140°C make it a more adequate candidate as heating medium. However, the lower heat transfer coefficient (comparing to water) leads to longer cycle times [4, 62, 68, 69]. Perhaps other heat transfer fluids could be considered, namely the so called water based nanofluids, with considerable higher thermo-physical properties and promising heat extraction rates without the usual sedimentation problems of other double-phase fluids [70].

Application of joule/resistive heating in the variotherm process has been extensively investigated by many researchers [60, 64, 66, 67, 71]. Eventually, nano features with aspect ratios up to 300 could be realized if moulded above the glass transition/melt temperature of the polymer. Unfortunately, the cycle times may increase up to several minutes due to the thermal inertia of the mould material [66]. Adequate isolation of the heating elements from the mould base will favour the cycle time reduction and increase economic efficiency of the microinjection moulding process [62]. Yao *et al.* [72] have implemented a local heating of the mould insert by high-frequency current. Unlike the conventional resistive techniques, mould surface heating rate can reach 40°C/s with an apparent heating power of $93 W/cm^2$, while only the local electrical insulation of the mould insert is necessary. The main advantage of the external heating over the internally built systems is an ability to heat up locally the insert surface allowing for faster cycle times. In a number of studies, infrared heating has been applied for precise localized heating of the microcavity surface [73-75]. Although an increase in the local temperature with an aid of halogen lamps requires considerably less time in comparison to that necessary with resistive heaters, uneven distribution of the infrared heating sources may result in variation of the mould surface temperature [62, 63, 75]. In addition, residual oil or resin particles, exposed to localized heating, may burn and contaminate the microcavity surface causing surface defects in the micromoulded parts. This problem could be eventually solved with periodical cleaning of the mould cavity [63]. Direct infrared radiation heating of polymer inside the cavity has been proposed by Saito *et al.* [74]. It has been found out that, during injection, the temperature gradient between polymer and mould was significantly reduced by applying CO_2 laser, directed to the mould wall through the transparent window. With this technique, the molecular orientation in the surface region of the micropart has been decreased, which resulted in significant improvement of the surface replication. It was widely reported that induction heating is able to promptly increase the cavity temperature [23, 64, 65, 71]. According to Michaeli *et al.* [23], the heating could be accomplished in several seconds and consequent cooling is also very fast because of the minimum amount of heat generated in the mould. However, high-temperature cycling may lead to the thermal fatigue and eventual shortage of the mould service time [69].

2.1.5 Mould evacuation

Negative effect of the air presence in the mould cavity is a well-known phenomenon in the conventional injection moulding. The latter is responsible for burn marks on mouldings and long-term formation of corrosive residue in the mould which may lead to its permanent damage [5]. In order to remove air from the cavity moulds of conventional size are supplied with special venting channels, however, this solution cannot be easily adapted for the micromoulding where the part dimensions are frequently comparable in size to the venting grooves. Moreover, high injection speed and complex geometry of micro features may aggravate air entrapment and lead to incomplete filling, being especially critical in case of the blind hole features with high aspect ratios [51]. In a number of studies, evacuation of air from the cavity prior to injection is referred to as an efficient method for improvement of the microparts replication [17, 24, 42, 51, 76]. A typical layout of the mould evacuation system is shown on Figure 8. However, in the research conducted by Sha *et al.* [76], it was not observed any influence of cavity evacuation on the part filling.

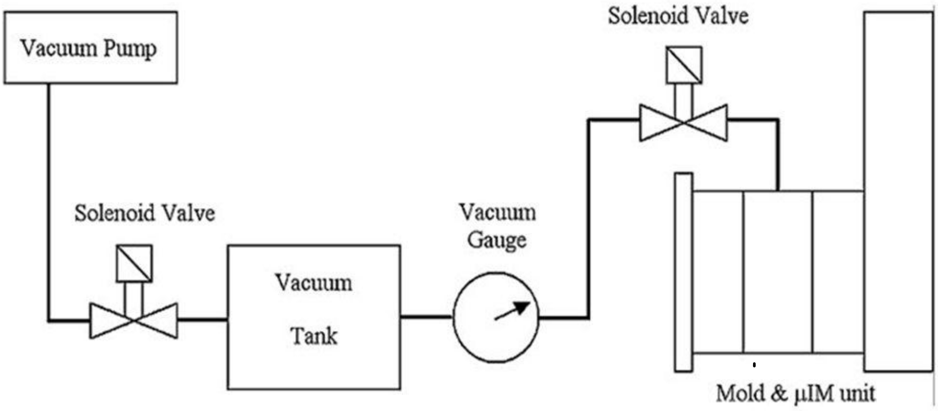

Figure 8 - Layout of the vacuum mould unit (adapted from [24])

A possible explanation of this phenomenon may be attributed to the fact that the micro feature's geometries were aligned with the parting line of the mould where air eventually can escape through the partition. In order to assist more efficient air evacuation, the mould platens must be properly adjusted for hermetic sealing of the cavity [42]. Nevertheless, air suction may exert negative influence on the moulding of thermally sensitive polymers, such as POM, by decreasing the cavity temperature [76]. Considering the pros and cons of the vacuum assisted cavity evacuation, its implementation has to be carefully considered in every case of the microinjection moulding taking into account polymer type, geometry and cavity surface finishing.

2.1.6 Process monitoring and control

Microinjection moulding is inherently a black box process, where the extreme processing conditions and rapid process variations do not lead to the linear correlation of the inputs and outputs. Monitoring of the micro moulding process parameters is critical to assess the rheological state of polymer throughout all moulding cycle. The sensors currently available at the market are too big to install in the micro cavity. To overcome these limitations, an indirect monitoring could be applied to gather information about the mould temperature, heat flux, injection pressure, injection speed and displacements [4, 77, 78]. The pressure sensor embedded into the plunger of the microinjection moulding machine was implemented to monitor the metering size and pressure evolution. It does not however represent the polymer behaviour inside the cavity [77]. Cavity pressure monitoring is considered to be the best approach to verify the process variation. For example, a single axis force sensor, embedded into the mould-core extrusion mechanism was used to monitor the pressure in the cavity [78]. According to Whiteside *et al.* piezoelectric force transducer located behind the cavity ejector pin could indicate the progress of filling and the part's solidification time [4, 68]. The importance of the mould temperature has already been referred earlier. With the aid of J type thermocouples embedded at depths of several millimetres in the cavity wall, it was not only possible to measure temperature but also monitor resin solidification inside the cavity [4, 68, 77]. When the direct monitoring of the micro moulding is concerned, only a few sensors have been referred to be appropriate for the micro applications. The majority of the above mentioned sensors hardly satisfy the micro criteria with the contact area diameter varying from 1 to 4 millimetres [79-81]. However, those sensors were reported to provide reliable data about the temperature and pressure evolution in the cavity and, if properly located, could be used to control the micromoulding process. Further miniaturization of the sensors is the one of the key factors to provide an insight to rheology of the polymer flow in micro cavity. The obtained data could be further applied for the better process control as well as for the improvement of the rheology models used for numerical simulation of the micro moulding process. So far, the market offer for the micro pressure and temperature sensors is quite limited. For example, a combined sensor for measuring of the mould cavity pressure and contact temperature in the cavity with front diameter of 1mm, was launched by KISTLER® [82]. Whereas PRIAMOS presented the only up–to-date micro scaled sensor of 0.6mm of diameter to measure melt temperature at contact with the cavity wall [83]. The real time monitoring of the micro moulding process is highly dependent on the sensors, capable of reliably screen the instant process variations. The latter is the key-factor for efficient process control and high quality micromoulded product. With further sensors miniaturization and increase of precision, it would be possible to achieve the higher level of automation and superior economical viability of the micro moulding process.

2.2 Effect of the process/tool/polymer interaction on the quality of micromoulded components

Quality of the micromoulded parts is, to a great extent, determined by the complex interactions of the process parameters, polymer and mould tool properties. Considering variability of the microparts geometry, its quality may be evaluated in terms of filling length, dimensional stability, surface finishing and structural performance [21]. There are two systematic approaches for correlation of the process/polymer/tool factors with the quality output namely; the one factor at time experiment (OFAT) and the design of experiment approach (DOE). While the former method highlights the leading trends, the latter is addressed to the optimization of the process by identifying the factors interactions. Both methods are extensively explored in recent research [11-15, 17-20, 31, 84-87]. As mentioned earlier, preheating of the mould tool above the glass transition temperature of polymer has been reported to avoid the incomplete filling and improve the overall part quality [17, 18, 20]. According to Xie *et al.* variotherm mould cycling and high injection temperature could significantly improve the weld line strength of the micro tensile test samples [20]. Furthermore, at higher mould temperature viscosity of the polymer melt decreases significantly and, therefore, injection pressure and speed may be reduced [18, 42]. The same tendency was verified for conventional mould temperatures, where its higher values promoted better cavity filling for a wide range of the polymers tested [11, 14-16, 20, 31, 84-86]. In the study conducted by Michaeli *et al.*, an increase of bonding strength of the overmoulded micro needles was achieved by a combination of the high holding pressure, high mould and low melt temperatures [84]. An empirical correlation of the part quality and process parameters, proposed by Tofteberg *et al*. highlights the positive effect of high mould and melt temperatures on replication of the micro features of cyclic olefin copolymer (COC) and poly(methyl methacrylate) (PMMA) [86]. Moreover, with the increase of microparts complexity, the mould temperature factor prevails over the other process parameters [15]. Premature solidification of polymer may be reduced, to some extent, by injection at high injection speed. The latter was reported to assist the micro pins filling, having on the other hand, an adverse effect on the surface finishing [11]. According to Theilade *et al.*, high injection speed and its interaction with the injection temperature were decisive for high-quality replication of the PP micro walls [18]. Frequently, volume of the feeding system (cold runners) is more than one order of magnitude of the micropart volume. Such discrepancies make precise metering difficult, increasing the probability of incomplete filling [13, 14]. However, there is no explicit mention of the metering precision on the microparts quality [12, 19, 84, 85, 87]. Several authors reported that some difficulties related to the metering precision and process fluctuations may be attenuated by applying higher holding pressure [12, 15, 17]. Liou *et al*. have observed the improvement of filling the micro and sub-micron structures with the holding pressure increase. However, it seems difficult to differentiate single holding pressure influence from its interaction with the mould temperature effect [17]. Polymer choice has a dominant effect on the quality of micromoulded parts. Several studies highlight the discrepancies in rheological behaviour of the different grades of plastics under the same process conditions. The easy flow grades should be preferred to guaranty the proper filling and acceptable surface quality [13-15, 42, 84, 86]. In addition, correct choice of polymer may be an additional guaranty for successful moulding of microparts, making the overall process more economically efficient, even without variotherm cycling of the mould [18]. Adhesion properties may vary significantly for different polymer grades and should account for free damage demoulding of the microparts. Fine surface finishing of the mould cavity, positive draft angles and release agents were reported to promote successful microparts demoulding [35-37]. The variety of factors, involved into the transformation of the polymer melt within the microcavity, makes the interpretation of the cause-effect relationship a complex task and, therefore, an insight into the rheological properties of polymer through the overall moulding cycle is definitely required and will be performed in the next section.

2.3 Rheology of the polymer flow in micro channel/cavity

Rheology properties dictate the polymer behaviour at a molten state, being strongly affected by the material structure and the interfacial characteristics [88, 89]. During the macro scale mould filling, polymer flow is assumed to be laminar, when the injection speed is constant and without thickness variation [52]. The whole picture turns altogether different in case of the microinjection moulding, where polymer is frequently under ultra-high speed due to the reduced dimensions of the impression. The latter is one of the principal causes of the polymer slip at the mould wall, which could be attributed to the excessive shear rate and disentanglement of polymer molecules at the melt/wall interface. Moreover, when polymer flow is confined to microcavity, surface tension, roughness of the tool and heat transfer phenomena could influence significantly polymer viscosity [52, 90, 91]. Accuracy of the micro-injection moulding simulation is, to a great extent, dependent on the reliability of rheological data. A number of studies indicate that the existent numerical simulation codes are unable to predict some aspects of the polymer flow behaviour at micro scale. This fact may eventually be addressed to the macro scale rheological data used during the simulations [60, 92-94]. Capillary and slit viscosimeters are frequently used to investigate melt viscosity dependence on shear rate and temperature. During the test, the molten polymer is forced to flow through the capillary at a given pressure and thereafter the collected data is mathematically processed to calculate the melt viscosity at a specified shear rate [90]. In the study conducted by Mnekbi *et al.* it was determined that with a decrease of the die diameter shear rate of a high-density polyethylene reached $10^5 s^{-1}$. At such shear rate, polymer flow becomes very irregular showing significant spurt, which could be attributed to the wall slip phenomena [95]. In the mathematical model proposed by Rosenbaum *et al.* slip-velocity calculations include the correction for the effect of viscous heating. Comparing to the custom methods of slip velocity estimation, this approach was verified to provide more accurate results [96]. Ultra-fast injection speed, applied to the polymer under microinjection moulding conditions, alters the transient behaviour of the polymer melt and may be in disagreement with the rheological data obtained close to the equilibrium state [52, 91].

For further approximation to the real injection moulding conditions, on-line measurement of polymer viscosity could be performed with a small mould installed on the injection moulding machine either of micro or conventional type [52, 90, 91, 97]. In the study of Chen *et al.*, POM polymer was rheologically tested on the injection moulding machine where viscosity was found out to be lower than that obtained with a traditional capillary rheometer for the same channel sizes. In addition, molten polymer turns more inviscid with a decrease of the channel size. This trend was confirmed by Vasco *et al.*, [97] where the critical values of the shear rate for the wall slip initiation in POM were established for a range of micro-channels configurations (Figure 9).

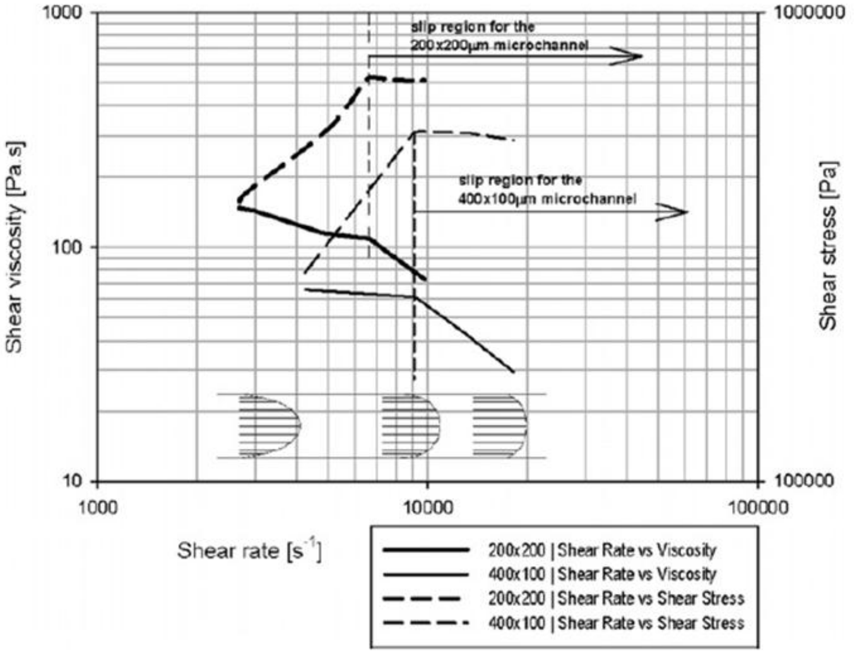

Figure 9 - Flow curves from rheometry calculations based on the 200 × 200μm and 400 × 100μm microchannel pressure data (adapted from [97])

Similar results were reported for ABS, where the polymer viscosity reduction becomes more representative with further miniaturization of the channel [90]. According to the study of Chien *et al.* wall slip occurs more easily with the decrease of the micro-channel's size and an increase of the melt temperature [52].

2.4 Numerical simulation of thermoplastic microinjection moulding

Numerical simulation of the microinjection moulding is not a trivial task where both rheological model and discretization of physical domain could influence reliability of the predicted results. Model discretization can be done in three different manners: 1) mid-plane mesh, 2) surface mesh and 3) solid mesh. The first is a 2D-model, where the planar mid-plane with a defined thickness is used to represent the 3D-geometry of the part. The second represents the 2.5D-part with double skin or shell mesh elements on the surfaces of the solid model, giving an acceptable representation of the thin-walled parts with uniform thickness. Those two models adopt the Hele–Shaw approximation [98]. However, when a model includes the combination of the macro and micro features, severe dimensional variations could not be framed to the traditional thin-wall design and it is just the case when a full 3D-model is definitely required [94, 99]. In addition, mesh refinement and precision are other issues to be properly considered towards the reliability of the numerical simulation results [94, 100]. It was reported that fine three-dimensional discretization of the variable thickness micropart allows for quite accurate prediction of the flow pattern and also weld line shape and position [100]. Importance of the mesh refinement was also confirmed by Yang *et al.* [101]. In their study, filling lengths of the micro features were predicted with reasonable accuracy with three dimensional mesh of 5μm size and 9 layers of elements through the thickness. In order to improve consistency of the numerical simulation results, a set of the additional parameters may be incorporated into rheology models for more reliable simulation of the polymer flow at micro-scale. Up-to-date only a few studies reported improved rheological models for microinjection moulding simulation. Kim *et al.* [102] incorporated the surface tension effect into the Hele-Shaw approximation for non-Newtonian isothermal filling flow. The adapted model was able to predict flow blockage at the entrance in the narrow width channel which was attributed to the negative effect of surface tension on pressure driven flow. Yao *et al.* [9] developed a model accounting for size-dependent viscosity, wall slip, surface tension, and based on the same Hele-Shaw approximation. Simulation results for polystyrene indicated an increase of predicted pressure by 20–30% comparing to the standard simulation approach. It was established that for the cavity thickness less than 100µm viscous heating effect was ignored and, during injection, polymer melt was assumed to be under the isothermal conditions. Micro Injection Simulation (MIS) code based on Smoothed Particle Hydrodynamics (SPH) mesh free method was developed by Fan *et al.* [103]. Their rheology model includes mould wall friction effect as a substitute for the traditional non-slip assumption. The pressure difference, predicted from the capillary rheometer tests, was found out to match the experimental data quite well. On the contrary, assuming the non-slip condition, the pressure difference was over predicted by 30%. In a number of studies, commercial simulation codes have been used for simulation of the polymer behaviour within the µ-cavity where viscosity obeyed the Cross-Williams-Landel-Ferry (WLF) model [36, 60, 93, 94, 99, 101, 104-106]. A hybrid Interpolated Domain Decomposition Method (IDDM) analysis based on the Hele-Shaw approximation enables differential mesh refinement of the microstructured model. The prediction of the premature solidification inside the micro features was predicted with 3D numerical simulation and corroborated with experimental results [94]. Several studies emphasize that variable local melt/wall interface heat transfer coefficient is more efficient than one averaged default value for prediction of the filling length of micro features [93, 104, 106]. It has also been reported that heat transfer coefficient varies along with the local pressure in the cavity increasing with a decrease of the cavity thickness and injection speed [106]. Other authors agree that if no correction is incorporated in the rheological models and/or in the boundary conditions commercial simulation codes are not accurate enough for quantitative prediction of polymer behaviour at micro scale, restricting their application to the qualitative prediction [36, 60, 105].

2.5 Morphological characterization of polymer at micro scale

Polymer morphology comprises the overall form of molecular structure, including crystallinity, branching and any kind of molecular arrangement [107]. Injection moulded components of conventional size typically exhibit “skin-core” structure where distribution of the spherulites through the part thickness is influenced by two factors: processing conditions during injection moulding and intrinsic polymer properties [108-110]. A detailed description has been provided by Giboz *et al.* [27]. Four distinct zones through the thickness of the macro injection moulded component have been delimited in Figure 10 as follows: skin layer (A), shear layer (B), fine-grained layer (C) and core (D).

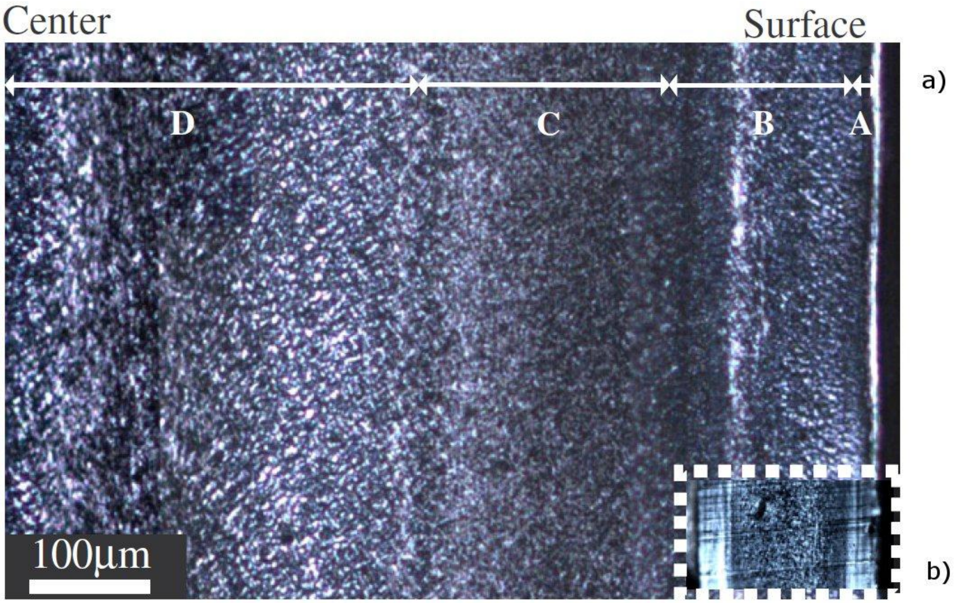

Figure 10 - Optical micrograph under the polarized light a)-half of the cross-section of the macro part; b) optical micrograph of the complete cross-section of the µ-part (adapted from [27])

A skin layer consists of non spherulite crystalline microstructures formed by elongated polymer chains, which appears as a thin transparent region under polarized light. The layer is relatively homogeneous with an average thickness of 50µm. With an increase of the solidified polymer layer, the cross-sectional area of the cavity decreases. This restriction results in high injection pressure and high shear stress, which favours the formation of highly oriented lamellar structures (shear layer B). After the end of filling, polymer continues to cool under low speed and high packing pressure. These conditions trigger growth of spherulites, although small, which comprise the fine-grained layer. In the centre of the cavity, polymer cools slower promoting growth of the biggest spherulite structures. Thickness of the core depends on the thickness of the cavity, and it generally tends to be the thickest zone of the macro injection part. When scale drops to micrometric level, rheological behaviour of the polymer melt undergoes significant changes [52, 91, 95-97]. Therefore, it is reasonable to expect that morphology of a micromoulded semicrystalline component may deviate from that of the macro scale, being affected at the various steps of crystallization, nucleation and growth of crystalline lamellae [27, 68, 111]. In the work of Whiteside *et al.* [68], the skin-core morphology was observed in 0.25mm high density polyethylene (HDPE) plaque, where the largest spherulite crystals grow in the centre and then gradually decrease in size, eventually disappearing towards the mould wall. In addition, nanoindentation tests were performed to assess mechanical properties. It was verified that material with higher crystallinity content at the centre of the micropart had a greater modulus than the less crystalline material near the cavity wall. It was also concluded that the size of spherulites is likely to be restricted by instantaneous cooling.

Slightly different morphology was verified for 150 µm micropart moulded from HDPE. In the two layers “skin-core” arrangement (Figure 10a), the skin layer corresponds to 40% of the total micropart thickness. Core layer, contrary to the previous study, contains little spherulites of the same size evenly distributed through the core. This arrangement differs significantly from the morphology detected in the macro part (Figure 10b) [27]. Similar results have been reported for PP microstructures of cylindrical shape where the ratio of skin to core layer tended to decrease with an increase of the mould temperature and injection pressure [111]. Quite different results were reported by Li *et al.* [112] for cylindrically shaped microstructures, which show three zones morphology: skin, shear region and spherulite core. The thickness of the skin region is about 5µm and thicker shear zone reflects high shear rates inherent to the microinjection moulding. Spherulite size decreases from the centre to surface, nucleating first at the colder zone, while the spherulites at the centre have more time to grow at quiescent conditions. With a decrease of the micro column size, spherulite size decreases as a result of a smaller temperature gradient through the thickness and hence less time for crystallization. In addition, nanoindentation results revealed anisotropy of the mechanical properties through the thickness of the microstructures, where the hardness and modulus increase from core zone towards shear zone and skin layer.

2.6 Mechanical testing of micro-scaled polymeric components

Molecular arrangement of polymers makes its deformation behaviour quite different from that of the elastic materials like metals. Polymeric materials exhibit stress–strain behaviour which falls between perfectly elastic (Hookean) material and perfectly viscous (Newtonian) liquid and frequently designated as viscoelastic. The response to loading of viscoelastic materials is strongly dependent on temperature, speed and duration of the test [113-115]. There are two types of mechanical testing currently in use for thermoplastic polymers short-term and long-term. The former is primarily intended for quality evaluation, by assessment properties such as Young's modulus, ultimate tensile stress and yield strength, while the latter is addressed to the estimation of the long term mechanical properties. When polymer is subjected to constant stress, it permanently deforms (creep) over time, which eventually will lead to excessive permanent plastic deformation and failure. The inverse to creep is stress relaxation, which occurs when polymer undergoes constant strain. Both creep and stress relaxation phenomena are objects of long-time testing of polymers [115]. Conventional methods of the mechanical testing are not adequate, when the scale of the polymeric component drops to µ-level. Significant challenges, related to handling of microparts, application of the controlled amounts of force for its deformation and the precise measurement of stress and strain, must be overcome to obtain reliable mechanical properties of a small amount of material [116]. Here, it is intended to provide a description of the various testing techniques addressed to the assessment of the wide range of mechanical properties responsible for the short and long-term performance of polymeric microparts. Nanoindentation is frequently used for testing of a small amount of material. It is simply an indentation test where the length scale of penetration is in nanometers range [116]. The indentation procedure developed by Oliver and Pharr has been widely used for hard materials such as metals and ceramics [117]. A significant advantage of using the nanoindentation approach is that it makes possible to retrieve not just short-term properties as hardness and modulus but also contact viscoelastic creep for a micro-scaled specimen [118-124]. However, the obtained results depend on the specific analysis model and can be very sensitive to the analysis particulars. For example, distribution of stresses may be influenced by type and size of the indenter tips, making difficult to isolate the interference of testing tool from the material response [119, 121, 122]. Both quasi-static (time dependent) [119, 121, 122, 125, 126] and dynamic (frequency dependent) techniques [120, 127] are currently in use. A quasi-static nanoindentation test is performed by applying a load to a sample with a geometrically well-defined probe, which is sequentially removed in a controlled manner [128]. It produces a typical force versus displacement curve (Figure 11). The unloading segment of the curve provides information regarding to reduced modulus (E_r) and hardness (H). In addition, this technique allows to investigate the local surface linear viscoelastic properties [122]. Several methods based on the linear viscoelasticity assumptions (small stress and strain less than 1%), have been proposed for quasi-static measurement of the Young's modulus, hardness and steady-state creep (short-term creep).

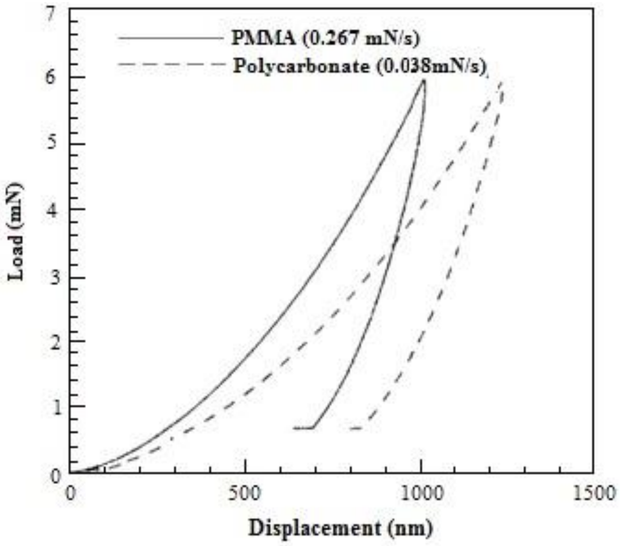

Figure 11 - Load and depth curves for PMMA and PC materials from nanoindentation tests (adapted from [122])

Steady-state nanoindentation creep can be designated as short-term creep because the duration of the nanoindentation test is normally about decades of seconds. A variety of studies have been conducted on direct measurement of the material creep function, assuming an instantaneous step-loading condition [119, 122, 125]. In case of the ramp loading history, a hereditary integral operator should be applied in order to solve this moving boundary problem and find the time-dependent stresses and deformations, based on the associated solution for a linearly elastic material [119, 122, 129, 130]. There were a number of attempts to fit the viscoelastic creep data to the constitutive material models. Huang *et al*. calculated the appropriate parameters for the bulk K(t) and shear relaxation μ(t) functions represented by the generalized Maxwell model [121]. In another study, steady-state creep data was fitted with a logarithmic equation. Prediction of the structural performance was more successful at higher creep loads and less accurate with an increase of polymer anisotropy [119]. In contrast to the quasi-static nanoindentation, dynamic testing enables quantitative studies of dynamic mechanical properties in terms of loss and storage-moduli. During the tests, indenter displacement and phase shift of the measured signal are recorded with respect to the excitatory signal [128]. Dynamic nanoindentation allows for quick assessment of the long-term viscoelastic properties of polymers through measurements over a range of frequencies rather than extended time [127]. So far, application of the dynamical nanoindentation for polymer testing has been limited to several studies [120, 127]. In the study conducted by Odegard *et al*. [127], a set of eight engineering polymers were tested with the different harmonic frequencies and amplitudes. It was concluded that variation of harmonic frequency did not have any significant effect on the measured dynamic storage and loss moduli of the tested polymers. Harmonic amplitude variation, however, alter both storage and loss moduli in a very distinct manner for each polymer tested. Huang *et al*. [120] applied step and ramp load modes for harmonic indentation in order to calculate the complex compliance of PP and PMMA. Both these studies reported that the nanoindentation experimental results were in good agreement with the data obtained by Dynamical Mechanical Analysis (DMA).

Atomic force microscope (AFM) has been frequently referred as a useful tool for evaluating polymeric materials on a sub-micrometer scale. In this technique, a compressive load is applied to a specimen by AFM tips with a nanometre's contact area [131]. The resultant force displacement curve can be analysed for extraction of the mechanical response. AFM nanoindentation has been used for assessment of hardness and Young's modulus of polymers in several studies [124, 131, 132]. In addition, when the thickness of polymeric film drops to the nanometre dimensions, Scanning Force Microscopy (SFM) may be used for investigation of the temperature dependent micro mechanical properties [133].

2.7 Residual stresses in IM parts

2.7.1 Development of residual stresses

Moulded part shrinkage is a well-known material property inherent to the molecular structure of polymers. At high temperatures, van der Waals forces between the polymer chains become weaker allowing for increased molecular vibrations. It also explains high thermal expansion coefficients of majority of polymers [134]. Warpage or distortion of the moulded part without presence of the external forces is caused by differential shrinkage. The latter may occur at the different places of the moulded part and also may vary in flow and transversal flow directions. Shrinkage and warpage lead to development of the internal residual stresses. It starts during the injection of molten polymer into a cavity and follows during the packing stage when plastic starts to shrink from the mould wall. Residual stress is a process-induced stress, frozen in a moulded part. It can be either flow-induced, generated by viscoelastic deformation of the polymer during processing, and thermally-induced, formed during cooling and solidification of the polymer [135]. In the former case, it leads to generation of the shear normal and extensional stresses during the injection phase, which cannot fully relax and become frozen due to increase in relaxation times during packing and cooling [136]. In the layers of material closest to the mould wall, molecules tend to orient in the direction of the flow as the polymer is sheared and elongated. After solidifying, this molecular orientation become frozen as it can be depicted from Figure 12 [137]. This anisotropy in morphological structure through the thickness has been reported to affect the performance of IM parts [138]. In order to avoid the confusion of terminology in the following text, it has to be mentioned that in literature the terms flow-induced residual stress and flow-induced molecular orientation are often used interchangeably.

Typically, in macro IM process, the magnitude of the flow-induced residual stress was found to be an order lower than that of the thermally-induced [139, 140]. Thermally-induced stresses are caused by the asymmetric temperature distribution through the thickness of the mould cavity. Hotter material inside is allowed to cool for longer periods thus polymer chains has more time to recover the deformation undergone during the IM process, shrinking at higher rate and producing thermally-induced stresses. In addition, when polymer melt solidifies under the packing pressure, it results in frozen-in compressive stresses referred as pressure induced stresses [136, 141, 142].

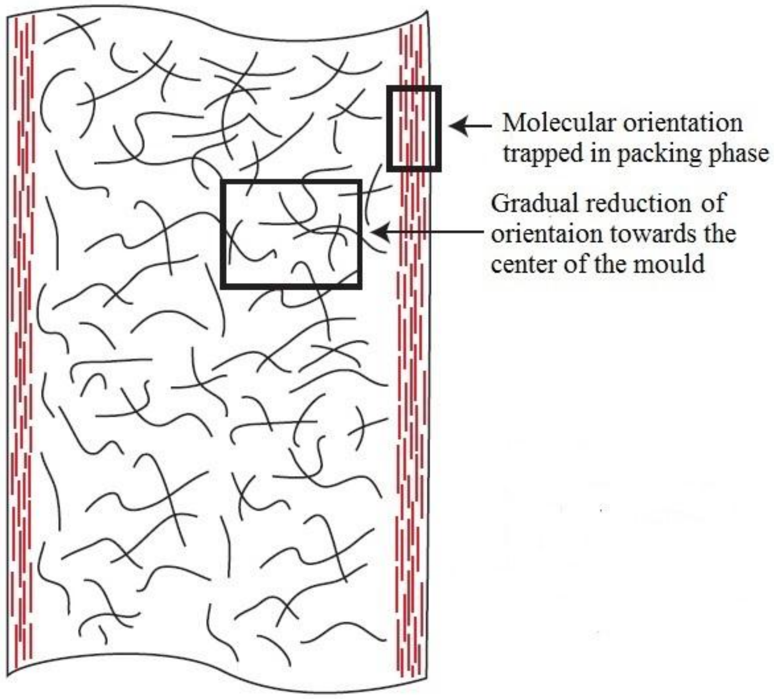

Figure 12 - Molecular orientation through the thickness of the part (adapted from [137]

Knowledge about the state of residual stresses in the plastic part may give a valuable insight into its performance through the variety of conditions during service time. For plastically deformable materials as thermoplastics, the residual and applied stresses are cumulative and therefore the former must be considered for onset of plastic deformation [143].

2.7.2 Assessment of residual stresses

There are several methods currently employed in assessment of the residual stress and molecular orientation in IM parts. The majority of the techniques are of the destructive nature. Solvent stress analysis is generally used for qualitative rather than quantitative assessment of the internal residual stresses. When moulded part is immersed and maintained in the solvent, calibrated to a specific solubility factor, appearance of cracks and crazes indicates the part’s locations above the critical stress. Extensive description of this method is presented elsewhere [144, 145]. Another relatively simple approach for evaluating the degree of the process induced residual stresses is a heat reversion technique. First, the moulding is heated above the glass transition temperature then it is allowed to cool down to ambient temperature. Relaxation of residual stresses originates change in part's dimensions, where larger shrinkage and/or distortion represent higher level of the frozen-in internal stresses [146].

Hole drilling and layer removal techniques are widely applied for assessment of the residual stress in polymers, through measuring the relaxed strains on the sample surface after removing layers of material [138]. Layer removal method may be designated as the one of the most used technique for assessment of the residual stress distribution in flat moulded parts. During the procedure, a thin layer of material is removed from moulding for subsequent measurement of the unrestrained moulding curvature. Thereafter, the curvature plot versus removed thickness is transformed to the residual stress versus thickness through the equation elaborated by Treuting and Readt [147]. In the hole drilling technique, local stress relaxation is measured when a small hole is drilled in the part. It leads to a local change in surface strain which can be measured with the strain gauges located around the hole and thereafter transformed for recreation of the original stress in the removed material. This method is considered to be semi destructive as generally hole is small and, if not located in critical place, the part may be still functional [138, 148]. Both, layer removal and hole drilling techniques have been referred in literature as valuable tools for correlation of the internal residual stresses with the processing history of the IM part [140, 149-152].

An extensive research has been carried out by Siegmann *et al*. [149] in order to find out a connection between the processing conditions and residual stress development in Poly(p-phenylene oxide) (PPO) polymer parts. They found out that, for all tested processing conditions, the residual stresses in surface layers tended to decrease further from the gate. At higher melt and mould temperatures, the maximum residual stress was found out to decrease drastically, especially at the surface of the moulding, while at the mid-plane the residual stresses were affected very slightly. It was attributed to the lower thermal gradient, which means more time given to restore original molecular conformations. The injection rate had also a significant impact on the residual stress, although its interpretation was not straightforward as in the case of the mould and melt temperatures. At low injection rates, the residual stresses at surface are tensile and become compressive as the injection rate reached the critical values, changing with the distance from the gate. The maximum residual stresses were observed for the injection rate between 20 and 60g/s. Increase in the injection and packing pressures mostly affected the residual stresses at the surface layers, reaching their maximum in the middle of the tested pressure range and then steadily decreasing.

Investigation of Hastenberg *et al.* [150] emphasised the positive effect of high mould temperature and annealing on the reduction of the residual stress. As depicted in Figure 13, the normalized (z1/b) half thickness residual stress profile of polystyrene (PS) part can be roughly divided into three regions: surface region and core region with tensile (+) stresses, and an intermediate region with compressive (-) stresses. Both compressive and tensile stresses were found out to decrease when the mould temperature rises from 25 up to 55°C.

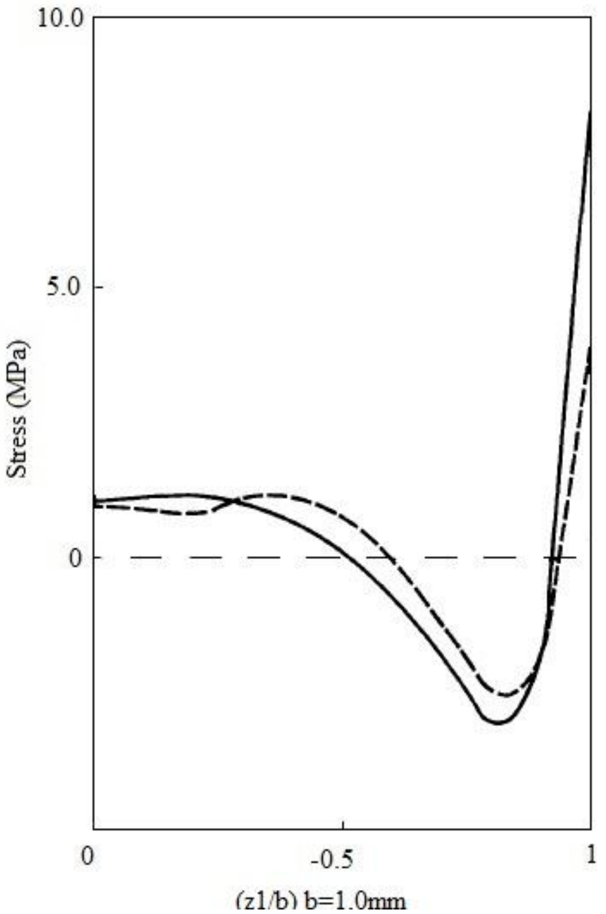

Figure 13 - Stress distribution for polystyrene: Tm 25°C – solid line, Tm 55°C –dashed line (adapted from [150])

The similar effect was observed for parts moulded from polycarbonate and a polyphenylene ether/high-impact polystyrene blend (Noryl). In addition, the surface residual stress at the end of the flow path was slightly lower for that at the gate region, while in the intermediate region local maxima of compressive stress was higher for PS and Noryl and lower for PC. The above mentioned difference in residual stress distribution was referred to have a strong correlation with the cavity pressure profiles recorded at the same locations. In the research conducted by Pham *et al.* [151], 10°C increase in the mould temperature did not show any significant change in the residual stress patterns in the near the gate section of polycarbonate bars, yielding to a compressive stress the centre of the sample and tension stress at the surface. While in these regions far from the gate, the residual stresses patterns were reported to change their polarities, being compressive at the surface and tensile at the centre of the samples. Moreover, at the gate vicinity, increase in injection rate originated change in residual stress sign at the part surface: from compressive stress for slow injection velocity to tensile stress for high injection velocity. At the end of the flow path, however, only tensile core and compressive surface can be distinguished over all injection velocity variation. Residual stress at surface appeared to be more sensitive to faster injection velocity which is in accordance with the results of Siegmann *et al.* [149]. Similarly to the previous investigations, Wimberger-Fried *et al.* [152] reported that magnitude and curvature of its distribution of the residual stress in polycarbonate was found out to decrease with an increase of the mould temperature. Aspect of the asymmetrical cooling was considered by Zoetelief *et al.* [140]. Although the temperature difference between the mould halves did not exceeded 4ºK and originated only slight imbalance in the symmetry of the ABS stress profile, it led to a noticeable warpage in the moulding.

Kim and Youn [153] compared the residual stress patterns in polystyrene obtained by both: layer removal and hole drilling techniques. More balanced residual stress distribution was obtained by the layer removal method, while the hole drilling technique was proven to be less precise and liable to the measurements errors. Annealing at the temperature close to the glass transition decreased the residual tensile stress, especially at surface, while annealing and subsequent quenching led to the inverse in the residual stress distribution becoming compressive at surface and tensile at core. Numerical simulation of the residual stresses in Moldflow has shown the same trend as the measurements results.

The state of the residual stresses can also be evaluated through the assessment of anisotropy of molecular structure and orientation in plastic parts. Photoelasticity is a method based on the birefringence (Δn) or double refraction of light phenomenon, which is an optical property of anisotropic transparent materials. It measured as retardation of polarized light crossing the sample [154, 155]. For semicrystalline polymers, in addition to the amorphous molecular orientation, arrangement of the molecules within the crystallites also results in birefringence. That is reason why this technique is generally applied for morphology assessment such as the size and distribution of spherulites and local orientations [156].

Specimen's preparation for the birefringence analysis may be both destructive and non-destructive. The former approach implies the cutting of the sample through the thickness in order to assess the three-directional birefringence distribution. However, considerable forces generated during the cutting may introduce an additional stress in the specimen and thus alter the internal residual stress state, leading sometimes to crazing and cracking of the sample [136, 157]. To surpass these difficulties, a method for samples preparation and subsequent birefringence analysis has been proposed by Hemsly and Robinson [158]. Two triangular orthogonal wedges, cut from the moulded part, were mounted on the optically isotropic glass block and immersed in layer of liquid with the refractive index intermediate between the glass and the polymer in order to reduce refraction and scattering. When the wedge in the 45° position was exposed between the crossed polarisers, the dark fringes position then was correlated with the thickness and the angle of the wedge in the same exact point, enabling the birefringence calculation through the thickens by the following equation:

$$\Delta n = \frac{\lambda}{l \times tan\theta} \qquad \text{Equation 1}$$

Where λ is wavelength of light, l is a distance between two consecutive fringes and θ is an angle of the wedge. A number of researchers used this technique due to simplicity of the sample preparation and semi-destructive nature [157, 159, 160]. Kamal *et al.* [157] employed the photoelastic approach to study the development of the frozen stresses in injection moulded polystyrene. The birefringence values in the flow direction were found out to be higher comparing to those in the cross flow. It was also found that birefringence steadily decreases through the length of the IM part. Shear stress at wall, calculated with the monitored cavity pressure data, was used for estimation of the frozen-in orientation. They claimed that predictions were quite accurate. Yu *et al*. [159] described the birefringence patterns observed in polyphenyl-ethers (PPE) and polyetherimide (PEI) polymers as parabolic in shape with the local maxima at the mould wall. The applied mathematical modelling of the birefringence, however, failed to predicts its distribution through the thickness, matching close to the mould wall and diverging in the centre of the sample due to underestimation the unrelieved thermal stresses. Neves *et al.* [160] used the birefringence data to predict the mechanical performance of PC injection moulded plates. Stiffness was calculated through the correlation of the Herman’s orientation factor and birefringence. Based on this approach, numerically estimated flexural stiffness was over predicted comparing with the experimental data, supposedly due neglecting the residual stress component of the total birefringence along with its variation through the flow path. They also reported that birefringence may be minimized with an increase of flow rate and mould and melt temperatures. Wimberger-Fried *et al.* [152] investigated the contribution of the residual stresses to the total birefringence. They were able to differentiate the contribution of the residual stress from that of molecular orientation by subtracting the birefringence values between the original and reduced cross-section of the PC plate. The birefringence from thermally-induced orientation was found out to be of the same order of magnitude as the flow-induced orientation and was mainly determined by a constant tensile orientation. Flow birefringence, which is an optical characteristic exhibited by flowing molten polymer, was addressed by Lee and Mackley [161]. Principal stress difference (PSD) of the Ziegler-Natta based linear low density polyethylene (z-nLLDPE) was calculated from the birefringence patterns assessed through the quartz optical window while molten polymer was forced through the multi-pass rheometer. The PSD reached the maximum values at the entrance, and the exit from the capillary slit due to restriction imposed by its geometry, tending to increase with higher mass flow rate.

Rapid Thermal Response (RTR) moulding technique was applied by Chen *et al*. [162] for minimization of the flow-induced birefringence and the thermally induced stresses.

Comparison of the gap-wise birefringence distribution, with and without preheating of the mould surface above the glass transition temperature, indicated that the local, maximum of the birefringence was reduced by 75% in RTR moulded parts.

Weng *et al.* [99] compared the experimentally assessed residual stresses in microlens arrays with the data numerically predicted using the optical properties of PC. Parametrical study indicated that the residual stress, estimated with the birefringence analysis, is sensitive to processing conditions, decreasing with the higher melt temperature, mould temperature, packing pressure and cooling time. Inverse relation was observed for the flow rate, while no systematic relationship was detected for the packing time. The numerical estimation, however, did not appear to match the experimental results, which was attributed to the limitation of the used commercial code. In order to improve the numerical prediction, the same authors used ANSYS programmed code to carry out the residual stress analysis. They reported that divergence with the experimentally obtained residual stress was minimized. The still remained discrepancies were attributed to viscoelastic stress relaxation after ejection, which was not accounted in the numerical simulation model [163].

It seems reasonable to conclude that development of residual stresses is affected in both magnitude and distribution by processing history of IM parts as well as by its post-processing treatment. In what concerns µIM process, application of the majority of the previously discussed techniques does not seem feasible primarily due to difficulties imposed by preparation and handling of micro specimens and due to inadequacy the existent experimental equipment. To the author’s knowledge, no experimental results related to the residual stresses’ measurement in µIM parts have been reported so far.

2.8 Viscoelastic behaviour of polymers

In section 2.6, the viscoelastic nature of polymers has already been briefly mentioned. Here, the viscoelasticity principle will be presented in detail in order to get a better insight into long-term behaviour of polymers. Viscoelastic materials respond to external stresses in a way which lays in between the behaviour of an elastic solid and a viscous fluid.

Manifestation of the material’s elastic or viscous responses depends on time scale of the experiment and decision about whether the material solid or liquid may be expressed by the Deborah number, N_D, defined as:

$$N_D = \frac{\tau}{\tau_{exp}} \qquad \text{Equation 2}$$

where τ is the time required to reach complete relaxation and τ_{exp} is the time scale of the experiment. For viscoelastic material, Deborah number is on the order of unity, while for Newtonian liquids N_D is close to zero and for elastic solids tends to infinity [164]. Comparing with metals, successfully treated within the limits of linear elasticity, mechanical properties of plastics show more complex load, time and temperature dependence [165]. Currently, two basic methods exist for treatment of the viscoelasticity: continuum mechanics or phenomenological approach and molecular approach. The former approach does not consider molecular structure of polymer and apply analytical solution to derive viscoelastic properties, whilst the latter provides an insight into the molecular origin of viscoelastic behaviour [165, 166]. Polymer response to a mechanical perturbation is sensitive to the material’s chemistry and microstructure and typically involves several types of molecular motion due to rearrangement of polymer chains. Firstly, the lengths and angles of the chemical bonds connecting the atoms may distort, moving the atoms to new positions of greater internal energy. Second way of molecular motion involves further disentanglement of the chains and longer relaxation time shows a strong correlation with the molecular weight and branching of the system [164].

Molecular theory of viscoelasticity will not be discussed here; instead, a concise description of phenomenological approach for investigation of the long-term deformation of polymers in the linear region will be presented. Linear viscoelastic behaviour implies that both strain and rate of strain are infinitesimal, often typically considered to be less than 1% [155]. In this case, the time-dependent stress-strain relations can be described by linear differential equations with constant coefficients, implying that the ratio of stress to strain is not a function of stress magnitude but solely of time or frequency [166].

2.8.1 Transient experiments

Generally, three kinds of experiments are used to study the long-term properties of polymers: dynamic (sinusoidal) loading, stress relaxation and creep experiments [167].

The creep test consists of measuring the time dependent strain under steady stress. Resulting strain is measured as a function of time and the experimental setup can be performed in both shear and tensile modes. Polymer does not maintain a constant deformation under steady stress but continues to deform over time or creeps. In tensile mode, the corresponding creep compliance may be defined as follows [165]:

$$D(t) = \frac{\varepsilon(t)}{\sigma_{E,0}} \qquad \text{Equation 3}$$

where $\varepsilon(t)$ states for observed tensile strain and $\sigma_{E,0}$ is the constant tensile stress.

In other transients experiment, a specimen is maintained at constant deformation and the stress is measured as a function of time. Under these conditions, the stress required to hold the deformation undergo gradual decrease or relaxes. Designating $\sigma_E(t)$ as recorded tensile stress and ε_0 as constant deformation, the resultant tensile relaxation modulus $E(t)$ is expressed as:

$$E(t) = \frac{\sigma_E(t)}{\varepsilon_0} \qquad \text{Equation 4}$$

Third kind of transient testing is a dynamical mechanical analysis, where polymer is subjected to the sinusoidally varied stress or strain. Dynamic modulus values measured through such perturbations are functions of angular frequency (ω) rather than time. For perfectly elastic materials, the stress response is instantaneous and phase angle is equal to 0, while for viscous fluid it will be 90º out of phase. Viscoelastic nature of polymers manifests itself as the strain response lag before the stress by the loss angle (δ) which value may vary between 0 and 90º. The resultant complex modulus (G^*) then consists of two components: elastic which is in-phase (G' storage modulus) and viscous which is out of phase (G'' loss modulus). The ratio of these moduli ($\tan\delta$) represents the energy loss due to viscous flow.

For dynamic experiment in shear mode the storage, loss moduli and $tan\ \delta$ may be defined as follows:

$$G' = \left(\frac{\sigma_0}{\gamma_0}\right) cos\,\delta \qquad \text{Equation 5}$$

$$G'' = \left(\frac{\sigma_0}{\gamma_0}\right) sin\,\delta \qquad \text{Equation 6}$$

$$G^* = G' + iG'' \qquad \text{Equation 7}$$

$$tan\,\delta = \frac{G''}{G'} \qquad \text{Equation 8}$$

where σ_0 and γ_0 are the amplitudes of the shear stress and strain respectively [165].

2.8.2 Mathematical models for linear viscoelastic behaviour

In order to calculate the time dependent viscoelastic response of polymers it is necessary to introduce an equation which in a certain degree reflects the molecular motions under applied deformations. It has traditionally been modelled with the combination of elastic and viscous components such as springs and dashpots. Maxwell and Kelvin-Voigt models are based on this principle [164-166].

In the Maxwell model, the instantaneous tensile modulus E states for response of the spring and η_E represents the viscosity of the liquid in the dashpot (Figure 14), while these two elements are connected in series. These two quantities are related through the relaxation time (τ) as $\eta_E = \tau \cdot E$. Equation of motion for the Maxwell model shows a linear combination of the deformation rates of the perfectly elastic behaviour (time derivative of Hooke's law) and perfectly viscous behaviour according to the Newton's law:

$$\frac{d\varepsilon}{dt} = \frac{1}{E}\frac{d\sigma_E}{dt} + \frac{\sigma_E}{\eta_E} \qquad \text{Equation 9}$$

where σ_E stands for the tensile stress.

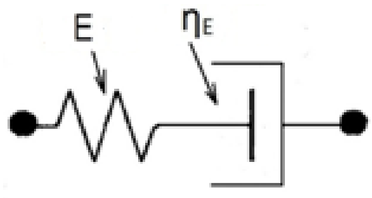

Figure 14 - Representation of the Maxwell model (adapted from [165])

During the creep experiment, the model is subjected to an instantaneous tensile stress which is maintained constant thereafter. Integrating the Equation 9 from t = 0 to some arbitrary time *t* and then dividing all by σ_E leads to a form:

$$\frac{\varepsilon(t)}{\sigma_{E,0}} = \frac{\varepsilon_0}{\sigma_{E,0}} + \frac{t}{\eta_E}$$ Equation 10

Where $\varepsilon_0/\sigma_{E,0}$ is the reciprocal of E or the tensile compliance of the spring - D and the left side of the equation is the tensile creep compliance *D(t)*. After rewriting the Equation 10 in terms of the creep compliance, the response of the Maxwell model in creep is:

$$D(t) = D + \frac{t}{\eta_E}$$ Equation 11

Equation 11 indicates that the creep compliance of the Maxwell model increases linearly (Figure 15a) without a limit, showing the behaviour of a viscoelastic fluid and therefore failing to predict the behaviour of polymers, where the strain rate is known to decrease with time [166].

In a stress relaxation experiment, a sample is instantly deformed and the strain is fixed in order to study a change in stress *E(t)* required to sustain the constant strain. This instantaneous strain is assumed to be purely elastic (spring element), then the dashpot will gradually relax thus the stress will decreases as a function of time.

After integration of the Equation 9 from $\sigma_{E,0}$ at time t = 0 to $\sigma_{(t)}$ at some arbitrary time t, and some mathematical manipulations, extensively presented in [165], it leads to the following representation of the stress relaxation:

$$E(t) = Ee^{\frac{-t}{\tau}} \quad \text{Equation 12}$$

where E is the modulus of the spring and $E(t)$ is the tensile relaxation modulus. The Maxwell model therefore suggests the exponential decay of the stress (Figure 15b), meaning that at times considerably shorter than the relaxation time of the spring/dashpot arrangement, the element behaviour is governed exclusively by spring. Moreover, if times are long compared to the relaxation time of the dashpot, the stress decays to zero, thus considering only a dashpot. At times comparable to the relaxation time, the response reflects the influence of both spring and dashpot. This behaviour approximates more closely to the observed in polymers.

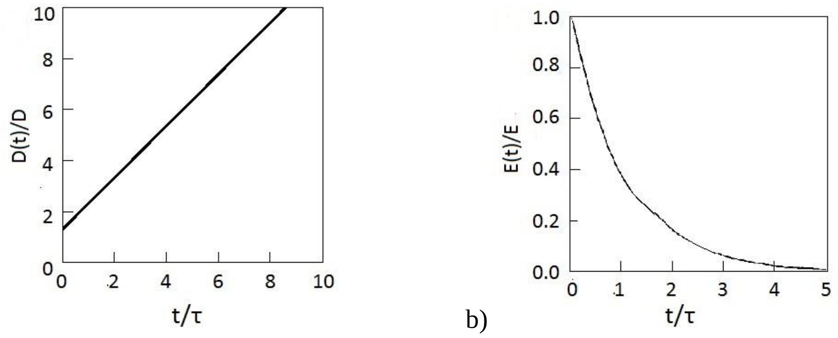

a) b)

Figure 15 - Maxwell body deformation: a) creep; b) stress relaxation (adapted from [165])

In the Kelvin–Voigt model, the same spring and dashpot elements are connected in parallel instead of in series as depicted in Figure 16.

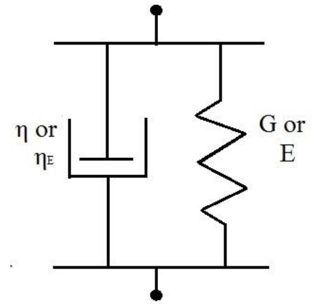

Figure 16 - Kelvin–Voigt model (adapted from [165]

This particular arrangement of the spring and the dashpot implies that the strain must be equal for both elements and consequently the total stress will be the sum of their stresses. Equation of motion for Kelvin-Voigt element in shear mode goes as follows:

$$\sigma_{(t)} = \gamma(t)G + \eta\frac{\partial\gamma(t)}{\partial t} \qquad \text{Equation 13}$$

where G is shear modulus and $\gamma(t)$ is shear strain.

When the model is under the constant stress (creep experiment), the Equation 13 becomes:

$$\frac{\sigma_0}{\eta} = \frac{\partial\gamma(t)}{\partial t} + \frac{\gamma(t)}{\tau} \qquad \text{Equation 14}$$

After integrating within the limits $\gamma = 0$ and $\gamma = \gamma(t)$ and some simplifications, the creep compliance is given by:

$$\frac{\gamma(t)}{\sigma_0} = J(t) = J(1 - e^{\frac{-t}{\tau}}) \qquad \text{Equation 15}$$

where $J(t)$ is the creep compliance in shear and $J = 1/G$ with G representing a response of a spring in the model. It is evident from the Equation 15 that creep cannot be properly predicted with the Kelvin-Voigt model, lacking an elastic component of the initial deformation. Moreover, when this model operates in the stress relaxation regime, the constant strain introduced into the Equation 13 makes the stress relaxation impossible as $G(t)$ is constant i.e. does not change with time. Thus, the equation of motion of the Voigt element reduces the latter to Hooke's law: $G(t)=G$ [165].

As it has been shown, the Maxwell and Kelvin-Voigt models are not accurate enough to provide good quantitative representations of the viscoelastic nature of polymers. Their response to a mechanical perturbation accounts only for a single relaxation time whilst experimental evidence suggests a distribution of relaxation or retardation times [164, 166].

Closer approximation of the experimentally observed data may be achieved by a combination of the enough springs and dashpots to achieve a good approximation to the polymer real behaviour. The Maxwell and Kelvin-Voigt models can be generalized by an arrangement of certain number of Maxwell elements in series or Kelvin-Voigt elements in parallel as is respectively depicted in Figure 17a and Figure 17b. In order to account for the instantaneous elastic response, an elastic element (E_∞) has been added to Maxwell generalized model and to the Kelvin-Voigt analogue (E_0).

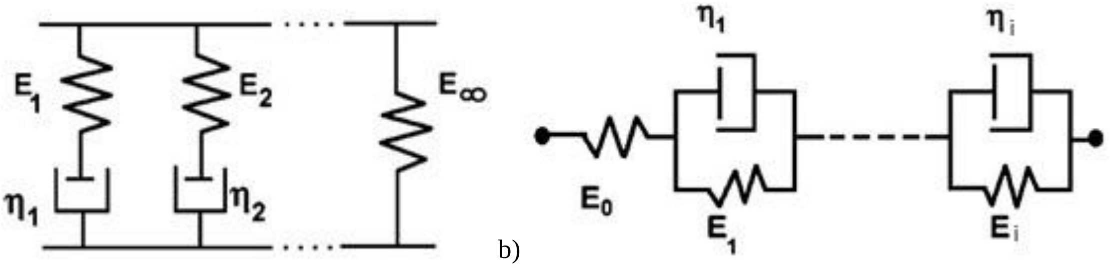

a) b)

Figure 17 - a) Maxwell's elements in parallel, b) Kelvin-Voigt elements in series (adapted from [168])

The relaxation function for the generalized Maxwell model in the case of a discrete distribution of relaxation times is given by:

$$E(t) = E_\infty + \sum_{i=1}^{n} E_i \, e^{-t/\tau_i} \qquad \text{Equation 16}$$

The specific creep function for the generalized Kelvin-Voigt model goes as follows:

$$D(t) = \frac{1}{E_0} + \sum_{i=1}^{n} \frac{1}{E_i} (1 - e^{-t/\tau_i}) \qquad \text{Equation 17}$$

These generalized models can represent the relaxation and creep data with any desired degree of precision if large enough number of Maxwell elements is considered. However, if the latter increases drastically aiming to include a wide discreet spectrum of relaxation and retardation times, it turns more practical to replace the summation in the equation by integration i.e. by introducing the continuous spectra [165]. A group of parallel Maxwell elements represents a discrete spectrum of relaxation times, being associated with a spectral strength E_i.

By transforming the Equation 16, relaxation modulus is given as:

$$E(t) = \int_0^\infty E_D(\tau) e^{-t/\tau} d\tau \qquad \text{Equation 18}$$

Where, $E_D(\tau)$ is the probability density of relaxation times. $E(\tau)dt$ is each infinitesimal contribution to system rigidity with relaxation times between τ and $\tau + d\tau$. Continuous relaxation spectrum can also be represented as $H(\tau) = \tau \cdot E(\tau)$. Then, in terms of $H(\tau)$ the Equation 18 becomes:

$$E(t) = \int_{-\infty}^{\infty} \frac{H(\tau)}{\tau} e^{-t/\tau} d\tau = \int_{-\infty}^{\infty} H(\tau)\, e^{-t/\tau} d\, ln\, \tau \qquad \text{Equation 19}$$

A similar method is used to consider compliance functions for the Voigt-Kelvin model. Here, the model will represent a continuous spectrum of retardation times $L(\tau)$ defined as:

$$J(t) = \int_{ln\,\tau = -\infty}^{ln\,\tau = \infty} L(\tau) e^{-t/\tau} d\, ln\, \tau \qquad \text{Equation 20}$$

2.8.3 Boltzmann superposition principle

When viscoelastic system undergoes force perturbation and then its removal, the response of the system does not disappear. It occurs due to the fact that the deformation depends not only on the actual stress but also on the mechanical history undergone by the material earlier. Acting within the limits of the linear behaviour, the responses to different perturbations superpose. Therefore, the stress may be described as a function of rate of strain history and may be represented as function of the history of rate of change of stress [164-166].

If in a shear creep experiment, the stress σ_1 applied instantaneously not at $t = 0$ but at any arbitrary time s_l, then for $t \geq s_l$ the stress and strain are related as follows:

$$\gamma(t) = \sigma_1 J(t - s_1) \qquad \text{Equation 21}$$

where, J states for the creep compliance in shear mode.

In case of the application of two stress increments σ_0 and σ_1, at the times t = 0 and $t = s_l$ respectively, the Boltzmann superposition principle states that the two stresses act independently and the resultant strains add linearly, as depicted in Figure 18, leading to the following expression:

$$\gamma(t) = \sigma_0 J(t) + \sigma_1 J(t - s_1)$$

Equation 22

Expanding this equation to more generic representation i.e. for multiple stress increments: $\sigma_1, \sigma_2 ......\sigma_n$, applied at times t = $s_l, s_2 ....s_n$ gives:

$$\gamma(t) = \sum_{i=1}^{n} \sigma_i \, J(t - s_i)$$

Equation 23

Replacing the summation by an integration results in the following expression:

$$\gamma(t) = \int_{-\infty}^{t} \frac{\partial \sigma(s)}{\partial s} J(t - s) \partial s$$

Equation 24

Where, in order to account for the complete stress history to the observed strain, lower limit of integration is taken as -∞ and the upper limit is *t*, because the stresses applied after *t* have no influence on the observed strain.

Similarly, an equation representing the stress $\sigma(t)$ in a sample that has experienced some continuous strain history goes as follows:

$$\sigma(t) = \int_{-\infty}^{t} \frac{\partial \gamma(s)}{\partial s} G(t - s) \partial s$$

Equation 25

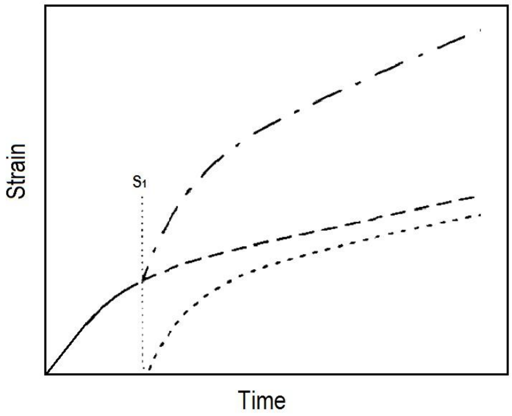

Figure 18 - Linear addition of strains resulting from sequentially applied stresses (adapted from [165])

2.9 Temperature dependence of viscoelastic polymer behaviour

As it has been referred earlier, polymers undergo drastic change in mechanical properties during the long-term transient tests (creep and stress relaxation) so emphasizing the effect of time on their viscoelastic behaviour. Temperature has been widely referred to exert great influence on polymer properties [134, 169]. These alterations in the mechanical properties may be explained by change in the molecular conformational freedom as the temperature is raised [165].

In linear and cross-linked amorphous polymers, four regions of viscoelastic behaviour through increase in temperature may be identified: glassy, transition, rubbery and flow (Figure 19). At low temperature, plastics are hard and glassy and although may undergo several secondary so-called γ and β-transitions, their molecular motions induce rather insignificant changes in modulus. With an increase in temperature, thermal energy gradually rises and eventually surpasses the potential energy barriers to rotation and translation of the molecular segments. At this threshold temperature, principal α-transition from glassy to rubbery state occurs and initiates long-range molecular movement in the plastic [165]. This phenomenon can also be explained with the free volume theory, where free volume means the difference between the volume of the liquid phase and the extrapolated value at absolute zero temperature. At a glassy state, only a small fraction of polymer mass is not occupied with polymer molecules, i.e. there is not enough space for movement of polymer chains. After reaching the glass transition temperature, free volume increases drastically and viscosity decreases as it can be seen in Figure 20 [170, 171]. The glass transition is not a thermo dynamical transition but rather the manifestation of viscoelasticity, thus the glass transition temperature is not a single value but a range of temperatures delimitating the transition region. In linear amorphous polymers, glass transition temperature is also positively correlated with the molecular weight [165, 167]. It is evident that for most amorphous plastics the service temperature should not exceed the glass-transition temperature in order to prevent permanent deformation [167].

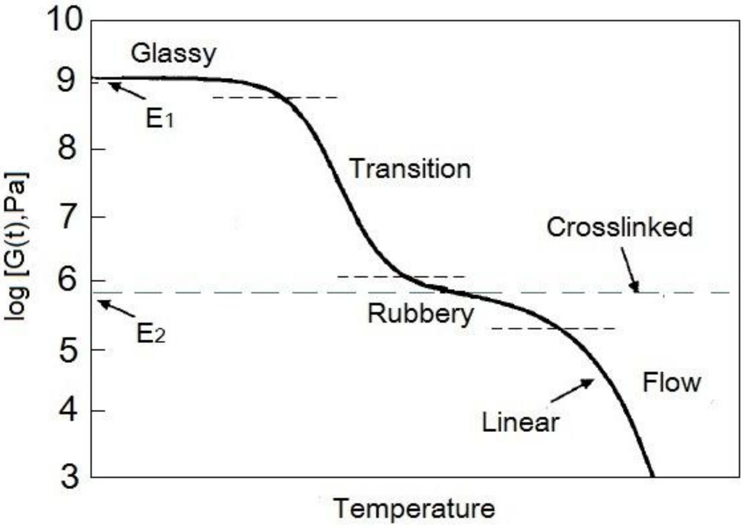

Figure 19 - Regions of viscoelastic behaviour (adapted from [165])

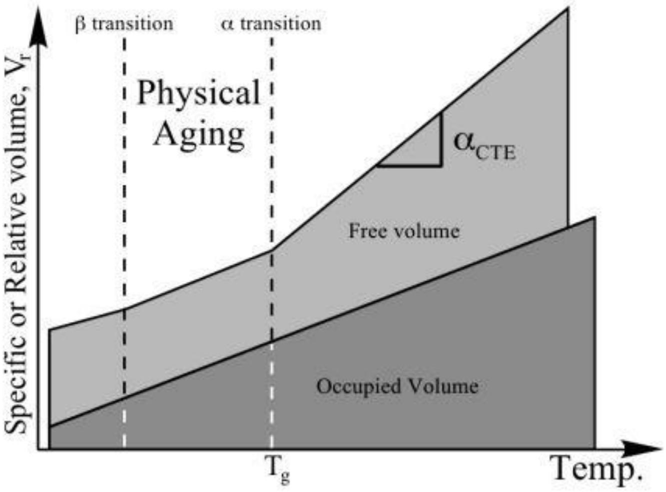

Figure 20 - Specific volume vs. temperature for amorphous polymer (adapted from [171]

With the further temperature increase, the relatively sharp gradient of the modulus in the transition region becomes less steep stabilizing into the rubbery plateau. This relative stability may be attributed to the fact that the local interactions between the polymer chains are still strong preventing their diffusion. This applies to both, linear and cross-linked polymers though through the different interaction mechanisms: entanglements for the former and primary chemical bonds for the latter. As temperature rises, the modulus of cross-linked polymers will be maintained at this approximate level due to cross-links (primary chemical bonds) up to the temperature sufficiently high to cause unrecoverable deformation due to chemical degradation of material.

No such restrictions exist for linear polymers, where molecules experience both large scale translations and rotations leading to transformation of the malleable plastic to a liquid state. This relatively free movement of molecules results in very low modulus as it can be seen in Figure 19.

Contrary to amorphous polymers, semicrystalline ones have two principal transitions: glass transition and melting point. Their dimensional stability is not generally affected at temperatures above the glass transition. However, contrary may be observed for some polymers with an excessive crystalline fraction which become brittle at temperatures below the T_g. As temperature increases above T_g, their crystalline structure maintains intact while rotation and translation of the molecular segments in amorphous regions render them to a rubber-like state. This combination of the rubbery amorphous regions and the stiff, crystalline regions contributes for polymer’s ductility and may extend its usage up to the crystalline melting point [167]. The latter is the temperature at which the last crystallites melt. After reaching the melt temperature, the modulus rapidly decays and as melting continues all the crystallites are dissolved turning a polymer to a fluid state [165].

2.10 Time temperature superposition principle (TTSP)

Time and temperature dependence of polymer’s mechanical properties require an extensive experimental testing in order to predict its performance over the service life, which in some cases can be extended over the decades. It is evident that the amount of experimental testing involved would be unrealistic. To circumvent this problem, a method of reduced variables or time temperature superposition principle (TTSP) has been introduced allowing for estimation of the long-term behaviour of a material through the short-term tests which may be applied for prediction a number of variables including stress, strain, humidity, degree of cure and etc. [172].

Time temperature superposition principle works on principle that a range of relaxation times belonging to a given relaxation process has the same temperature dependence [173]. Therefore the testing time may be significantly reduced by conducting several short tests to measure desired property at higher temperatures. Thereafter, the relaxation modulus, creep compliance or other viscoelastic property curves may be superimposed on a logarithmic time scale by shifting over the isotherm of reference to obtain a single property-time master curve that encompasses a wider time range. Generally, this reference temperature is chosen arbitrarily, being frequently a temperature of service for a polymer under consideration. The same principle is also applied for temperature frequency dependence [171, 172, 174].

Predictions based on TTSP require a formula to account for the temperature dependence and materials that obey these rules are considered to be thermorheologically simple. It implies that all contributing relaxation and retardation mechanisms have the same temperature dependence and therefore the relaxation modulus or creep compliance curves may be superimposed horizontally by a time shift factor log α_T and vertically by a stress shift factor b_T [175]. An example of horizontal shifting is shown in Figure 21, where the reference temperature (T_1) was fixed in place whilst the other isotherms were shifted to right.

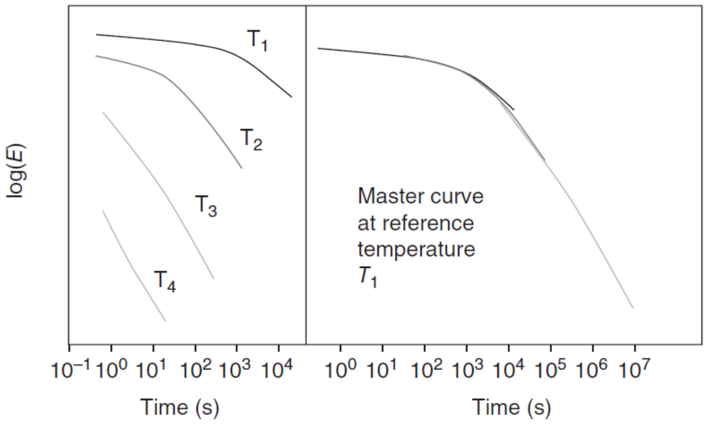

Figure 21 - Formation of a master curve by shifting several sets of simulated modulus data (adapted from [176]

2.10.1 TTSP shift factors

There are two empirical equations currently used for calculation of the horizontal shift factor $\alpha_T(T)$ namely Arrhenius equation and Williams, Landel, Ferry (WLF) equation. The latter equation is based on the assumptions of the Doolittle's concept of free volume, briefly mentioned in the previous section. Its theoretical basis and derivation is extensively described in literature [166, 177, 178] and therefore will be omitted here, presenting the equation's final form:

$$log\,\alpha_T = log\frac{\eta}{\eta_0} = \frac{-C_1(T - T_0)}{C_2 + T - T_0} \qquad \text{Equation 26}$$

where C_1 and C_2 are constants; T is any arbitrary temperature, T_0 is the reference temperature; η and η_0 are viscosities. It is known to be valid for majority of amorphous polymers in the glass transition region i.e. between the glass transition temperature T_g and T_g + 50 K. Ferry [166] advocated that these constants vary insignificantly for a large number of amorphous polymers, if T_g is used as a reference for the superposition, and their values may be given as 17.44 and 51.6 for C_1 and C_2 respectively.

Validity of the WLF equation within the glass transition region of amorphous polymers may be explained with the kinetic theory of polymers [166, 171]. However, its extrapolation for the temperatures below the glass transition becomes questionable as, according to the free volume theory, the slope of the specific volume curve (Figure 20) suffers a discontinuity at glass transition temperature [171].

Below T_g conformational changes in molecular motions almost cease to exists, instead, the viscoelastic responses are attributed to the local backbone and side chain motions, characteristic for the β-relaxation zone [178]. Moreover, amorphous materials are not in thermodynamic equilibrium at temperatures below their glass transition which leads to a phenomena so-called physical aging. The latter may be seen as gradual slow approach to equilibrium and change in material properties, especially those affected by T_g. Aged material becomes stiffer and more brittle, its damping decreases and so do its creep and stress relaxation [179].

A shift factor below the T_g can be calculated with the energy equation which represents the relaxation time in terms of activation energy:

$$\tau(T) = Ae^{E_a/RT} \qquad \text{Equation 27}$$

where τ is the relaxation time, E_a is the activation energy, R is the gas constant and T is the absolute temperature. After, rewriting in logarithmic form and taking the ratio at an arbitrary temperature (T) and the reference temperature (T_0), the equation transforms in:

$$log\alpha_T = log\frac{\tau(T)}{\tau(T_0)} = \frac{E_a}{2.303R}\left(\frac{1}{T} - \frac{1}{T_0}\right) \qquad \text{Equation 28}$$

The previously mentioned vertical stress shift factor b_T may be considered as measure of entropy in the system. It is estimated on the basis of the proportionality of the stress magnitude to the product of the temperature and density and presented as follows [175, 180]:

$$b_T = \frac{T_0\rho_0}{T\rho} \qquad \text{Equation 29}$$

In many cases, application of the vertical shift tends to be neglected due to little variation of the density with temperature. However, some authors stress that in the glassy state where the time and frequency dependences are small; the vertical shift is a more important than in the glass transition zone where the horizontal shift associated with the time scale prevail [166, 181].

When construction of a master curve is not possible, a material is considered to be thermorheologically complex. Beside a single transition whose shape and width are temperature dependent, this scenario also include several overlapping transitions with different temperature dependences [182]. Urzhimtsev [180] found out that, for such typical representative of thermorheologically complex materials as glass-reinforced polyester, α_T was not exclusively a function of the single argument T but also depended on the deformation time. Thermorheological complexity may be detected by construction of a Cole–Cole plot, i.e. plotting the loss modulus G´´ versus storage modulus G´ at various temperatures. Vertical shift may be omitted if the behaviour of the Cole-Cole plot is temperature independent, confirming the thermorheological simplicity [183]. If the Cole-Cole plot is temperature dependent, both vertical and horizontal shift factors are required to perform superposition. The analysis of van Gurp and Palmen introduce another way to evaluate the thermorheological complexity, where the loss angle tan δ is have to be plotted versus the absolute value of the complex modulus G*. Beside sorting out thermorheological state of material, with this method, exact amount of the vertical shift required for superposition may be calculated [173].

2.10.2 TTSP validity

Although the TTSP principle has been proven to hold in many cases, extensive experimental observations summarized by Ferry [166] helps to establish some limits to its applicability. First, the TTSP is considered to hold if no mismatch is detected in the superposition of the adjacent curves with the same values of $\alpha_{T,}$ implying temperature independence of all viscoelastic functions. Second, the temperature dependence i.e. the method to obtain the shift factors must have a form of WLF or Arrhenius theoretical basis. In addition, in dynamic measurements, experimentally obtained results usually do not extend over more than three decades of frequency presented in a logarithmic format. Hence, another limitation arises from the cumulative errors in calculation of the shift factors which generally occurs due to expanding the span of frequencies or times over many decades from the much more limited range of experimental measurements [166].

Moreover, over long periods, water absorption and chemical changes may introduce deviation in the mechanical response which is not accounted in the method of reduced variables [173].

Applicability of the TTSP has known to be of limited validity for semicrystalline polymers. Generalization of their viscoelastic response with TTSP fails due to different relaxation mechanisms inherent to the crystalline and amorphous structures. Moreover, crystallites inserted between the amorphous regions may decrease their segmental mobility thus changing the viscoelastic response when compared with purely amorphous materials [174]. In some cases, superposition becomes possible but only for limited ranges of temperature over which the molecular structure is only changed slightly and thus the relaxation times have the same temperature dependence [172, 184-186]. Sometimes, the superposition is achieved with addition of the vertical shift factor b_T to compensate change in density with temperature [187].

Another category of materials which display a different temperature-dependent rheology is polymer blends. It, by definition, implies the TTSP failure due to different relaxation time of the blend’s components. Moreover, inspection of the superposition failure may supply valuable information about specific interactions occurring in the homogeneous system i.e. to be some kind of probe of the molecular interactions. Single-phase structure of homogeneous (miscible) blends presumes averaged glass transition temperature due to their intimate mixing and therefore it is reasonable to expect good TTSP. It, however, was not observed for PEO/PMMA blends being attributed to very small scale heterogeneities of components where each one retains their own temperature sensitivity [173, 188]. In heterogeneous (immiscible) polymer blends, TTSP is more likely to fail due to different temperature dependencies of both constituents. This, however, may not be the case if their activation energies are not very different and therefore the experimental data may be superposed. Extensive investigation of the TTSP validity for polymer blends were summarised in the review of Van Gurp and Palmen [173].

2.11 Hybrid thermo-rheological and structural analysis

The main objective of any analysis and/or simulation is the closest match of the predicted performance to the real conditions and accurate assessment of the final product properties. As it has been discussed earlier, a great deal of uncertainty still exists about the rheological phenomena occurring in the microcavity, and it definitely should be taken into account for reliable prediction of the final mechanical properties and lifetime service. In a number of studies, some sort of conjunction of thermo-rheological and structural analysis has been applied to account for the residual stresses and material properties generated during the filling and its impact on the final product performance. The results quoted so far are based on coupling of Autodesk® Moldflow® Insight (AMI) plastic injection moulding simulation software [189] with ABAQUS ® for structural analysis [190]. This hybrid thermo-rheological and structural (HTRS) analysis has been adopted in a number of studies over the recent years [64, 191-194]. In the study of Yoo *et al.*, distribution and magnitude of residual stresses in polyether ether ketone (PEEK) cage implant have been used to optimize the injection moulding process conditions. Residual stress calculation was based on linear elastic properties of solid PEEK at the ambient temperature [191]. Other applications of HTRS analysis have been dedicated to assessment of the complex thermo-mechanical properties and creep induced distortion of fibre reinforced polymers, where the field of the moulding residual stresses were accounted in the power-law creep model [192]. Research of Kröner *et al.* has been dedicated to a nonlinear orthotropic behaviour of reinforced polybutylene terephthalate (PBT) where the generalized Hooke's law was applied for simulation of uniaxial tension [194]. In what concerns micro applications, to the author's knowledge, just one study involving HTRS analysis has so far been reported. Here the Moldflow simulation has been combined with linear constitutive viscoelastic model for prediction of the stress relaxation and deformation in overmoulded polymeric films [193]. However, no experimental validation has been presented.

2.12 Research Objectives

The results so far presented show that μIM of thermoplastics is a well-established technique. However, it is consensual that the research areas dedicated to the understanding of the polymer flow dynamics at the micro scale as well as the characterization, assessment and prediction of the final mechanical properties require a great deal of additional investigation.

In order to comply with the established objective of this doctoral thesis, an integral approach for optimization of the thermoplastic microparts production will be implemented. It is expected to be accomplished by discovering cause-effect relationship between size, geometry characteristics of the micro tool, injection moulding processing conditions and final mechanical properties of the micromoulded parts.

The specific objectives are outlined below:

- Polymer dynamics in the microcavity of semicrystalline and amorphous polymers will be assessed by monitoring cavity temperature and pressure as relevant process parameters. Optimization of the microimpression filling will be accomplished through the design of experiment (DOE), where the quality targets were established to determine a set of the optimum injection moulding processing conditions.
- Simulation of the micro injection molding process will be conducted with the commercial Autodesk Moldflow Insight® (AMI) software, duplicating the experimental processing conditions. By comparison of the experimental and numerical results, it is intended to establish the numerical code applicability

limits for µIM process simulation and, with the appropriate premises, to extract the numerical data required for the following hybrid thermo-rheological and structural analysis.

- Mechanical properties of the micromouldings will be assessed by Dynamical Mechanical Analysis. The method of reduced variables will be applied to extend a time span of experiment.
- Prediction of the long-term mechanical properties of microparts will be accomplished with ABAQUS® numerical simulation software. Linear viscoelastic model for structural analysis will be calibrated with the DMA experimental data. Long-term structural performance of the microparts is expected to be influenced by the thermo-mechanical (residual) stresses, induced during processing and therefore have to be accounted for the prediction of life time performance of the thermoplastic microparts.

Therefore, this research aims at contributing to the worldwide scientific knowledge answering to the following questions:

1. What is the influence of the processing conditions, cavity geometry factor and polymer type on the dynamics of the polymer flow in the µ-impression?
2. To what extents commercial numerical simulation codes are applicable for prediction of the polymer behaviour in the µ-impression? What can be done to improve its prediction accuracy?
3. How the thermo mechanical history of µ-moulded parts may affect its structural performance?

Chapter 3 Experimental techniques

The current chapter is dedicated to the detailed description of the experimental equipment, techniques, materials and methodologies used for obtaining microparts and their characterization. An overview of the materials, injection moulding equipment and tools will be provided in what concerns equipment specifications, manufacturing techniques as well as instrumentation and data acquisition. Methodologies applied for analysis of polymer dynamics, process variability and the mechanical properties' characterization will also be presented in detail.

3.1 Materials, injection moulding equipment and tools

3.1.1 Materials

Three thermoplastic materials were selected for the present study: amorphous terpolymer, acrylonitrile butadiene styrene (ABS) CYCOLAC GPM5500S, with MFR of 24g/10 min (220°C, 10 kg) supplied by SABIC Innovative Plastics Europe; and two semicrystalline: homopolymer isotactic polypropylene (PP) Moplen HP500N, by Lyondell Basell Industries with MFR of 12g/10min (230°C, 10kg), and Polyoxymethylene copolymer (POM) C 9021 with MFR of 9.2g/10min (190°C, 2.16 kg), by TICONA GmbH.

ABS $(C_8H_8 \cdot C_4H_6 \cdot C_3H_3N)n$ is a terpolymer, obtained by polymerizing styrene and acrylonitrile in the presence of polybutadiene. The former monomers add a strength and rigidity to a blend, while an addition of polybutadiene rubber aimed at increasing the toughness [170]. The general chemical structure of ABS is shown in Figure 22.

The material is widely used for quality equipment housings and in automotive industry. It offers high impact resistance, good stiffness, high dimensional stability at elevated temperatures and superior processing [170, 189]. Due to the remarkable processing and mechanical properties ABS has been successfully applied in µIM [11, 31, 195]. Prior processing, raw material should be dried in order to avoid defects caused by high water absorption of ABS.

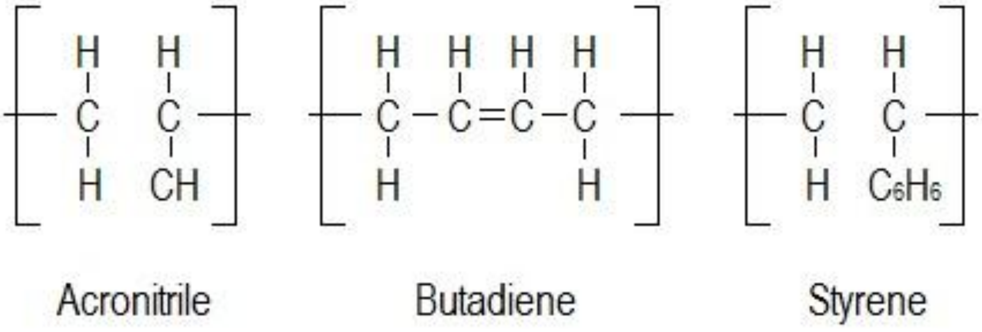

Figure 22 - General chemical structure of acronitrile butadiene styrene (adapted from[196])

Polypropylene (PP) is a translucent semicrystalline thermoplastic polymer with excellent electrical properties, heat resistance, rigidity, toughness, chemical resistance, dimensional stability, low cost and exceptional flex-fatigue resistance. The latter property reflects a capacity of the PP molecular structure to adjust in a way to withstand a lot of additional flexing without failing, which led to the design of “self-hinged” covers. It is worth noting that density of the polypropylene is one the lowest comparing to the other thermoplastics [196]. PP is used for an array of miscellaneous products as automotive dashboards components, microwave food containers, garden furniture, disposable diapers, cleaning wipes among others. It also has been extensively used for moulding of microparts of the variety of configurations [11, 17-20, 31, 85, 195]. Polypropylene molecule (C3H6)n consists of carbon atoms linked to hydrogen atoms, while a pendant methyl group (CH3) is attached to a one half of carbon atom [197]. The way of how the methyl side group is linked to the linear chain determines polypropylene properties. There are three types of special arrangements of the methyl groups: isotactic, sindiotactic and atactic. The PP Moplen HP500N, used in this study, has isotactic arrangement, as it can be depicted from Figure 23, with the methyl groups attached periodically along the same side of the polymer chain. Such linear molecular chain configuration with regularly spaced side groups facilitates crystallization [113].

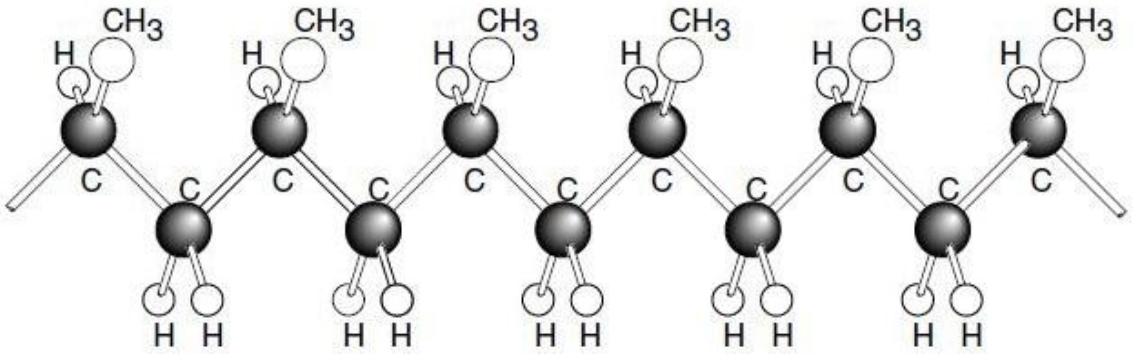

Figure 23 - Chemical structure of isotactic polypropylene (adapted from [113])

Polyacetal or polyoxymethilene is an engineering thermoplastic generally used at macro scale for production of precision parts. Polyacetals are formaldehyde-based thermoplastics. There are two basic types of POM which can be processed by injection moulding: homopolymer and copolymer [7]. Both homopolymer and copolymers are similar in what concerns the majority of properties. It is worth noting, however, that the copolymer has better thermal stability, easier mouldability and better chemical resistance, while the homopolymer possesses slightly higher tensile strength, flexural modulus and greater surface hardness. High degree of crystallinity gives both acetal polymers resilience, good dimensional stability, low friction, high temperature resistance to creep and opaque white appearance [197]. The above referred POM properties can explain the interest demonstrated to its application in µIM [11, 14, 16, 84, 195]. The grade used in this study was Polyoxymethylene Copolymer C 9021. It is typically made through the reaction of monomers of cyclic trimer formaldehyde (C3H6O3) and ethylene oxide (C2H4O) which provides for a higher thermal and chemically stability of copolymer [198]. The chemical structure of the POM copolymer is presented in Figure 24.

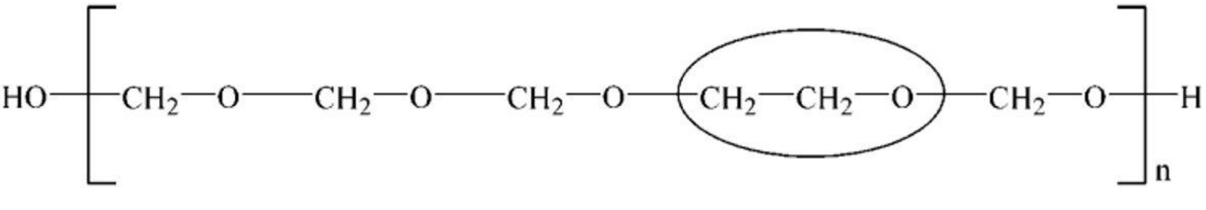

Figure 24 - Chemical structure of acetal copolymer (adapted from [198])

3.1.2 Injection moulding machine

Bearing in mind inadequacy of conventional injection moulding machines for the µIM, a micro injection moulding machine, used in this study, enables precise dosage and homogeneity of the polymer melt along with tight control of the injection speed, pressure and melt temperature [22]. It was a hydraulic reciprocating screw micro injection moulding machine with a two-platen clamping unit, Boy 12 A, developed by Dr Boy® (Neustadt-Fernthal, Germany) and provided by courtesy of the Department of Polymer Engineering at Minho University. This particular brand combines the technical characteristics required for µIM and has been used by a number of researchers [97, 199]. The machine features Ø14 mm injection screw and is able to meter an injection volume of 0.1cm^3 at a high flow rate, up to 15.6cm^3 s^{-1}. The maximum injection pressure and clamping force are limited to 240MPa and 129kN, respectively.

3.1.3 Part geometry

In order to clarify the influence of the part's thickness on the polymer flow dynamics in the microimpression, a model, developed for this study, detains differential thickness along its length (Figure 25). The plate like micropart is 16mm length and 10mm in width with an orifice in the middle and variable thickness of 0.2, 0.3 and 0.4mm (Figure 26). The complete moulding, however, also includes the cold runner system (sprue, trapezoidal runners and gate). The entire systems was modelled using SolidWorks® CAD software [200]. The model geometric details and part dimensions may be depicted from Figure 25-27. From Figure 27, it is clearly visible that the volume of the runner system exceeds considerably that of the micropart which is quantitatively confirmed in Table 1. Moreover, high ratio of the surface area to volume suggests a high cooling rate of polymer in the microimpression [201].

Table 1 - Volume and surface area of the complete moulding

	Volume (mm^3)	Surface area (mm^2)	Ratio of surface area to volume	Volume % of the complete moulding
Sprue+Gate+Runners	1264.53	1110.3	0.88	96.6
Micropart	44.61	268.02	6.01	3.4

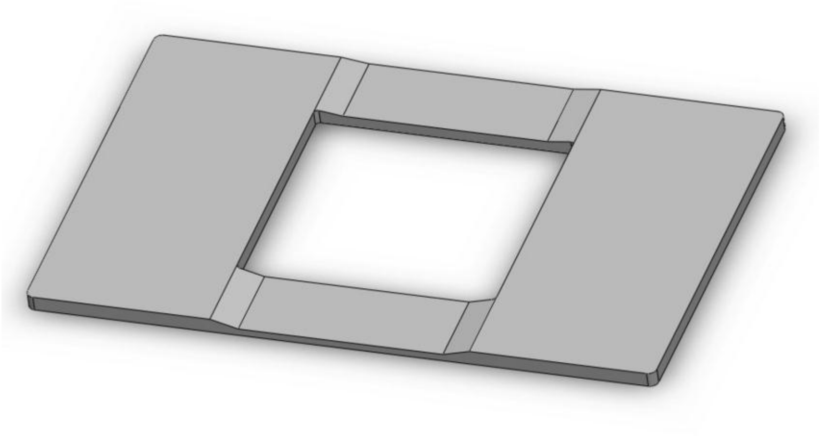

Figure 25 - Three dimensional view of the micropart

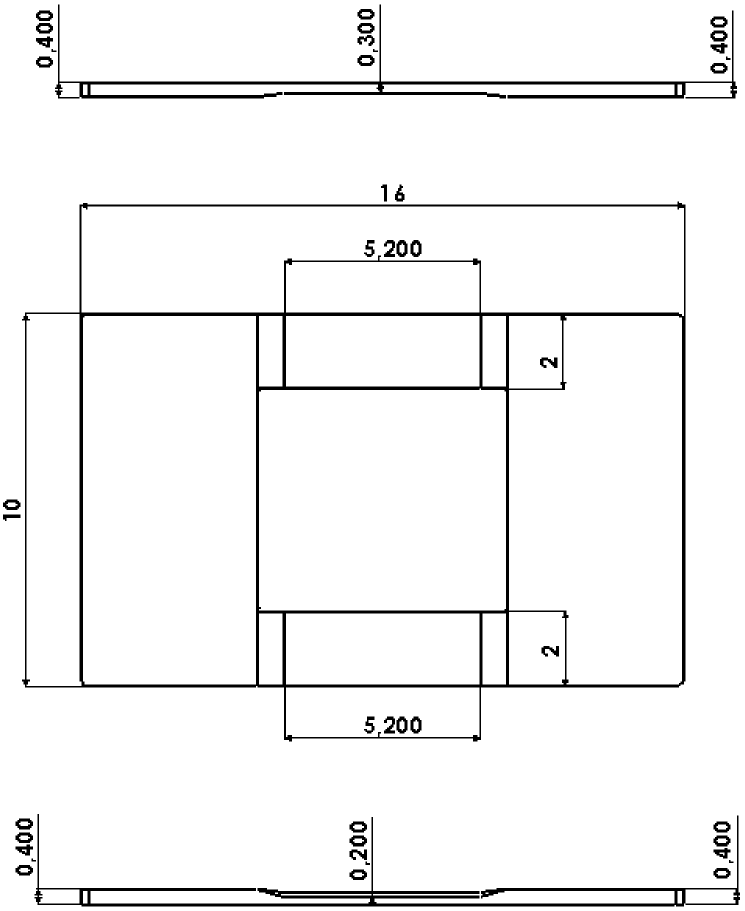

Figure 26 - Dimensions of the micropart

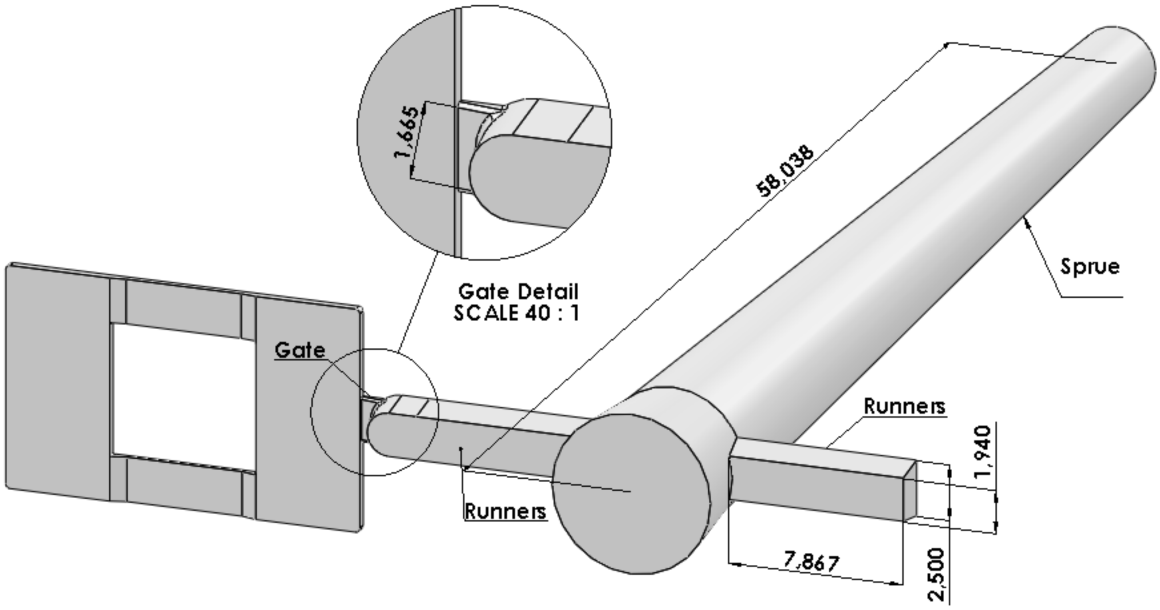

Figure 27 - Three dimensional view of the complete moulding

3.1.4 Micromould

The miniature two plate cold runner mould with the overall dimensions of 155 x 156 x 130mm, used in this study, was specifically designed and developed to fit the microinjection moulding machine Boy 12A requirements. The mould structure is assembled from the standard mould components, enumerated in Figure 28. The detailed description of the mould can be found in the doctoral thesis of Vasco [202]. This micromould was designed to support two interchangeable inserts allowing for a variety of applications. For example, it was previously used for investigating the polymer melt rheology in microchannels [97].

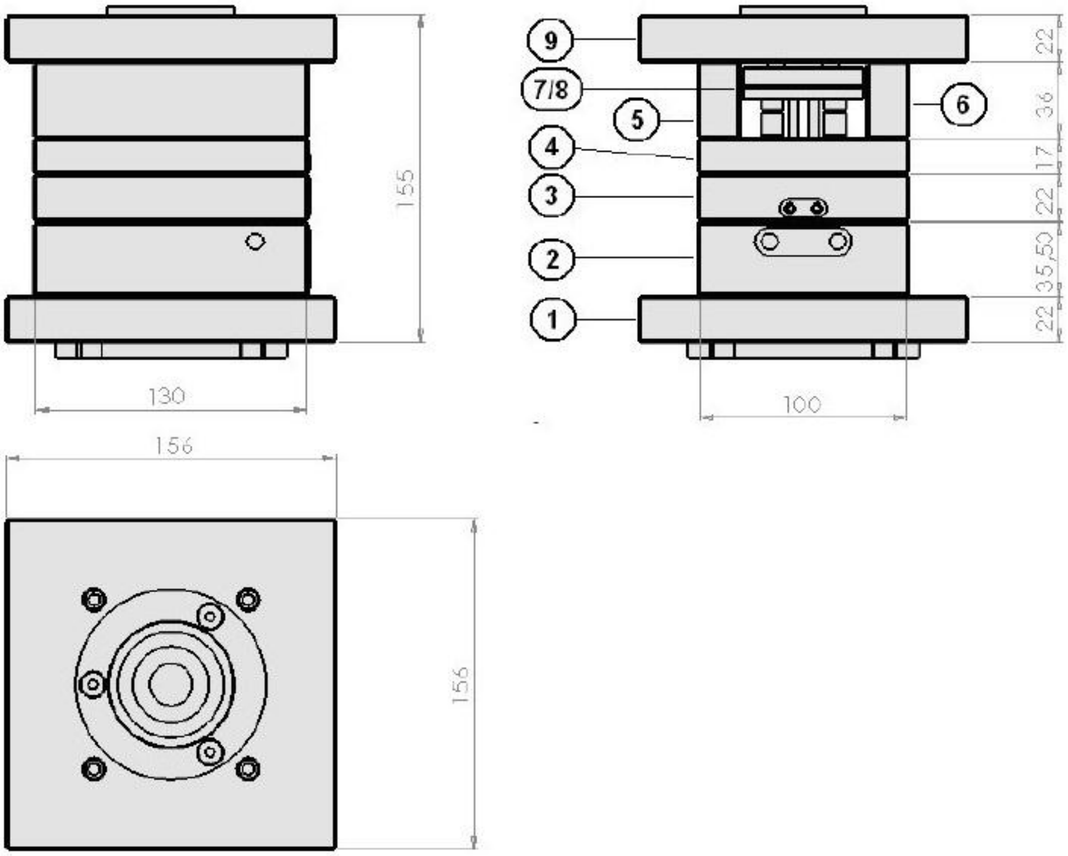

Figure 28 - Mould structure: 1) cavity retainer plate; 2) cavity plate, intended to support the cavity pressure system and the respective wiring; 3) core plate, where the interchangeable moulding blocks are mounted; 4) backing plate, required for removing the moulding blocks; 5, 6) spacers; 7, 8) ejector retainer plate and 9) movable clamping plate (adapted from [202])

A new moulding insert was designed, fabricated and thereafter assembled in the mould structure. Despite the fact that the mould may support two interchangeable mould inserts, only one was effectively used for moulding the microparts. As shown in Figure 29, a spare moulding insert was installed in a fashion to interrupt the polymer flow. Details of the injection moulding insert arrangements are depicted in Figure 29b. A detailed description of the interchangeable mould insert is provided in the following sections.

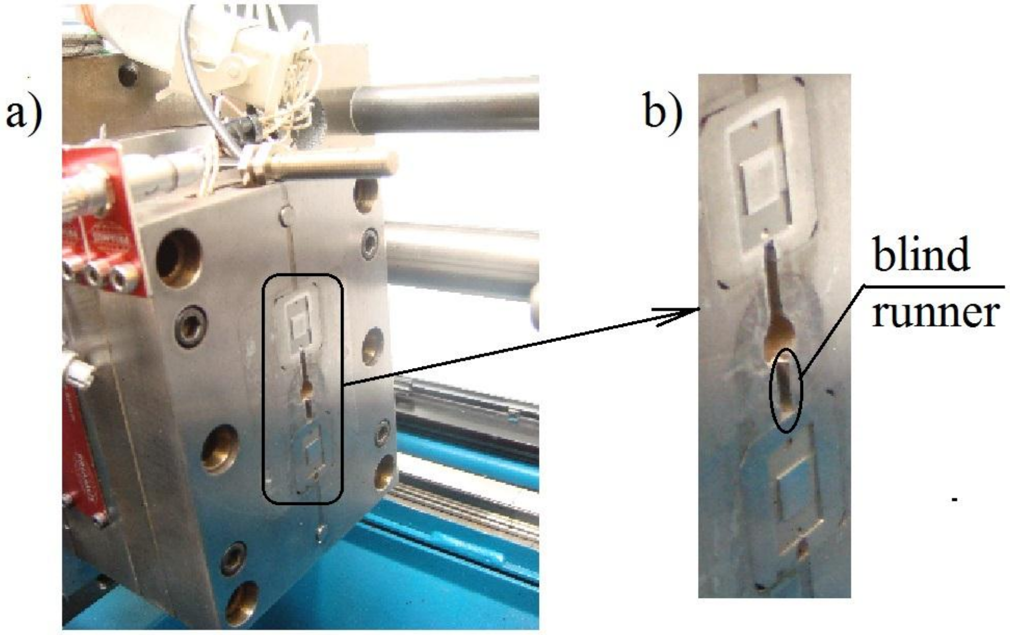

Figure 29 - a) Ejection side of the mould. b)Assembled moulding inserts

Mould temperature control system consists of two separately controlled zones depicted in Figure 30. The portable home-made temperature controller controls the cartridge heaters of diameter of 6.5mm (160W) via feedback from the thermocouples of type J. The thermocouple at the ejection side is fitted directly into the interchangeable mould insert, whilst another one from the injection side is inserted into the mould plate close as possible to the parting line. A cooling system, although existent in this mould, was not actually used. Considering that the mould temperature is to be maintained below the ejection temperature for all polymers and the ratio of surface area to volume of the micropart (Table 1), it seems reasonable to assume that the heat supplied by the polymer is almost instantaneously dissipated by the mould material [201] and therefore the objective of the mould temperature control system is to maintain the temperature of the mould at the pre-set level.

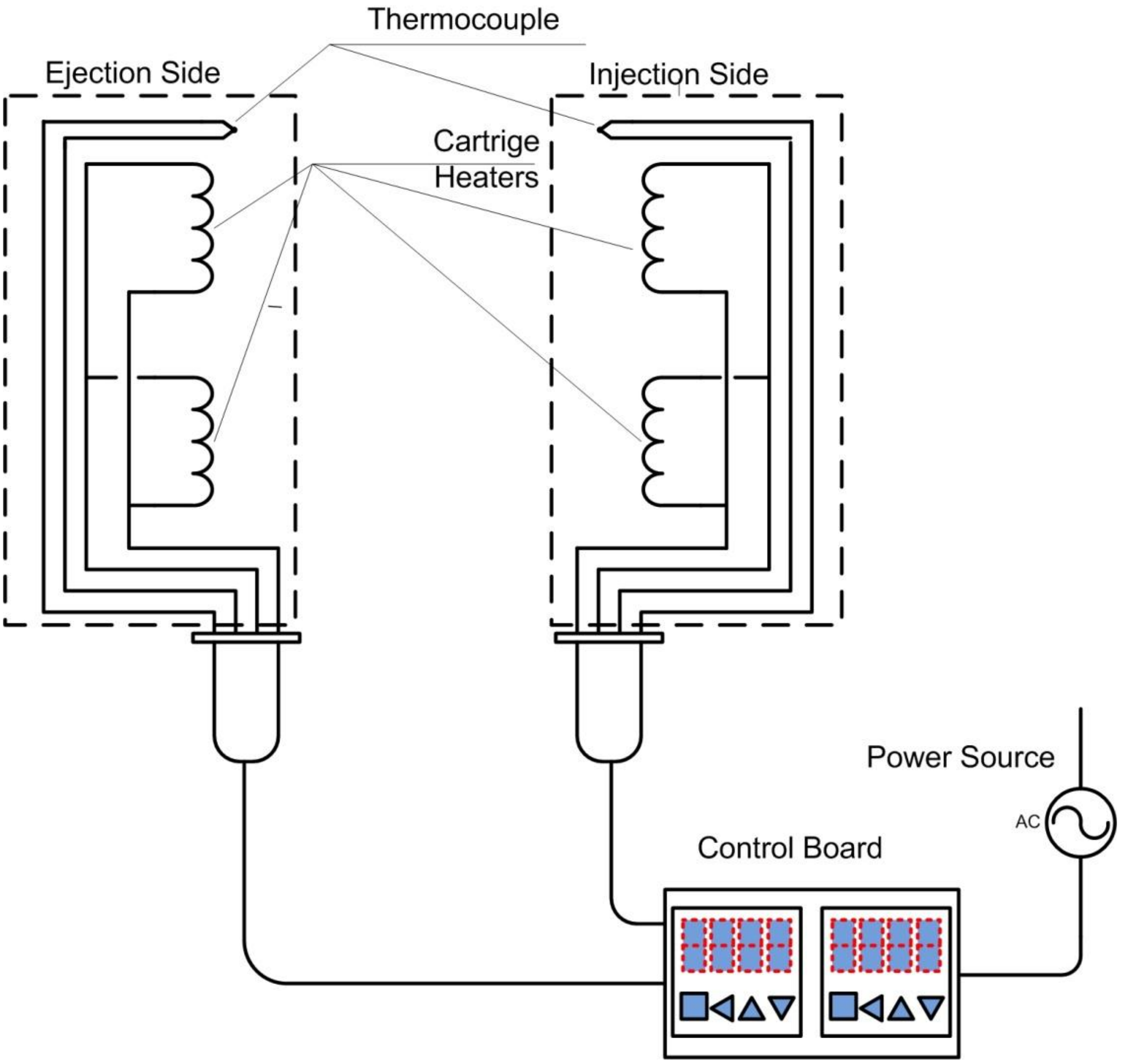

Figure 30 - Schematics of the mould temperature control system

3.1.5 Interchangeable insert fabrication and microimpression machining

The concept of the interchangeable moulding blocks allows for versatility of applications, where one miniature mould can accommodate a number of inserts with different layouts of impression. High injection speed and pressure applied in cyclic mode constitute additional requirements for mould insert materials. Under those extreme conditions, wear resistance of the insert material turns to be the most pertinent property. The steel used for the mould insert fabrication was P20 pre-hardened high tensile nitriding tool steel. In order to increase hardness and reduce wear, the tool steel has been subjected to additional hardening and tempering. It is also worth mentioning that the mould insert dimensions reflect the model size, resembling a cube with sides of 22.5 x 22.5 x 20.5mm (Figure 31a and Figure 31b). As it has already been referred in the section 2.1.3, the choice of the microstructuring technique is closely related to the material properties, model configuration and surface finish requirements. Considering all these factors, the impression of the model, depicted in Figure 25 and Figure 26, was obtained by micromilling. The microcavity, as it can be seen from Figure 31a, also features four holes, where the largest were machined for accommodation of the extractors and the smallest were used for the micro temperature sensors assembles. The mould insert with the installed temperature sensors is shown in Figure 31b. Instrumentation of the mould and insert will be discussed in detail in the following section.

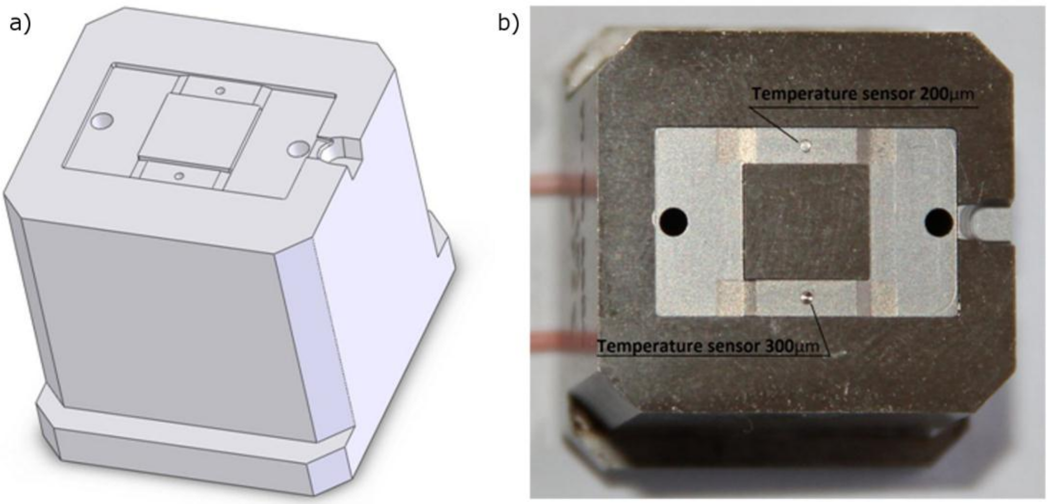

Figure 31 - a) CAD model of the interchangeable mould insert with machined micro impression; b) mould insert with the micro temperature sensors

3.1.6 Mould and insert instrumentation

In order to investigate thermal phenomena of molten polymer in the microcavity, two microcavity temperature sensors PRIAMUS® Type 4012B with the diameter of sensing front of 600µm (PRIAMUS® System Technologies, Schaffenhausen, Switzerland [83]) were flash-mounted at the lateral sides (with thickness of 300 and 200µm) of the microimpression. The monitored temperature difference and amplitude are closely related to the cooling rate of the polymer at a specific location. Pressure in the variable thickness microcavity was monitored via two miniature piezoelectric pressure sensors

PRIAMUS 6006B (PRIAMUS® System Technologies, Schaffenhausen, Switzerland), which were installed at the injection side of the mould. As it can be seen from Figure 32, the sensors are located at pre-defined distances along the polymer flow path allowing for the monitoring of the flow front progress, where P1 is the pressure sensor located near the gate; P2 is the pressure sensor at the end of filling; T1 is the temperature sensor at the section of 300µm; and T2 is the temperature sensor at the section of 200µm. The time elapsed until the flow front gets in touch with each sensor provides the means to determine how each geometrical configuration and processing condition may affect the microimpression filling.

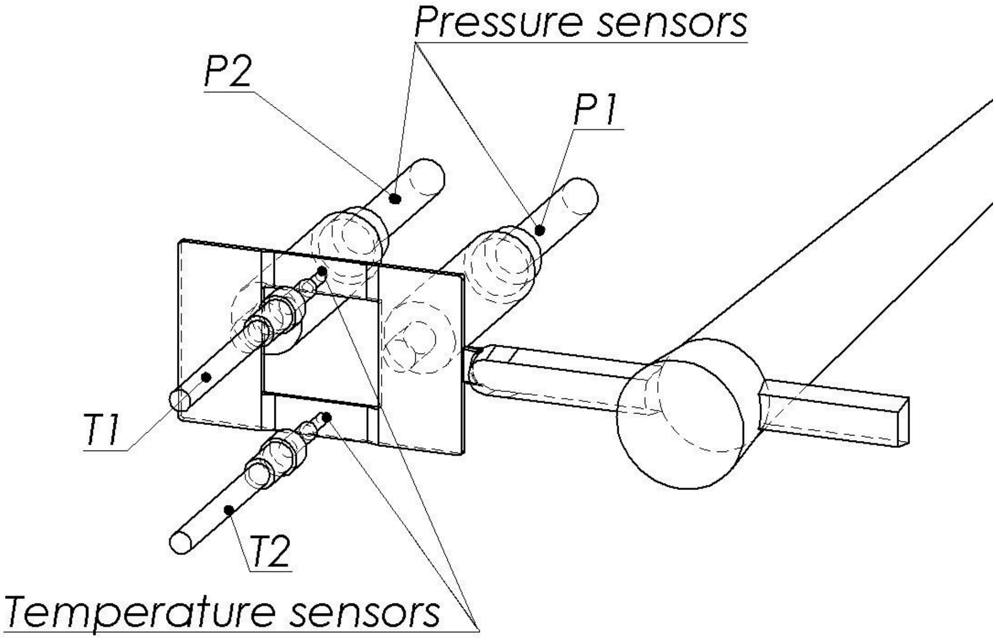

Figure 32 - Complete micromoulding with the pressure and temperature sensor positioning

The data acquisition system also includes an input module Multi DAQ 8101A, which is able to record pressure and temperature data cyclically at sample rates of 1kHz, and the amplifier module, Mobile DAQ 8001B, both from PRIAMUS®. The user interface operates with the PRIAMUS® Moulding Monitor software. The overall arrangement of the injection moulding machine, mould, data acquisition system and temperature regulator, is presented in Figure 33.

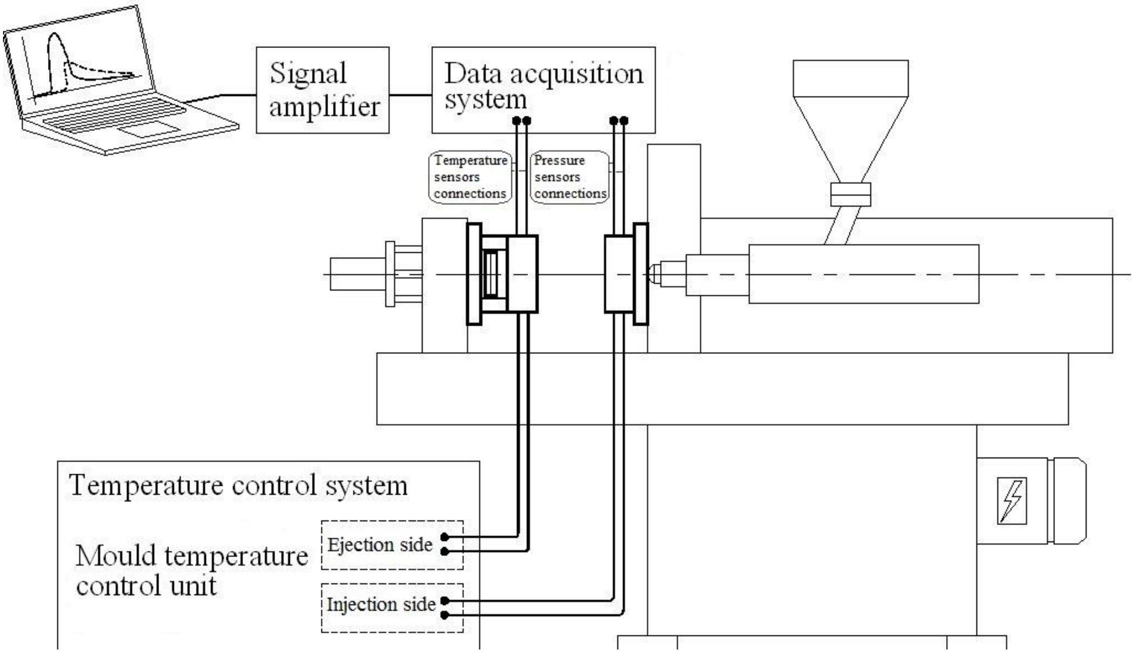

Figure 33 - Layout of the injection moulding machine, mould and auxiliary equipment

3.2 Injection moulding setup

In order to establish the correct dosage of the polymer for the injection moulding experiments, a number of short shot trials were carried for PP polymer. Shot size or total volume (V_t) was determined as the cavity volume plus the volume of the material in the runners (Table 1). Having the screw diameter of the molding machine, the area is easily calculated. Therefore the initial screw/ram position - S_p (mm) can be calculated according the following equation:

$$S_p = \frac{V_t}{\pi r^2}$$

Equation 30

The calculation gives the initial screw position about 8.5mm and also 2mm cushion was added to compensate for polymer shrinkage. During the first trial, the ram position was fixed at 10.5mm. It resulted in incomplete filling (Figure 34a). Therefore, the initial screw position was gradually increased untill the polymer fills the microimpression completely. Final tuning was accomplished, as it can be seen in Figure 34b, with the screw position at 12mm. This value was subsequently used for the injection moulding setup.

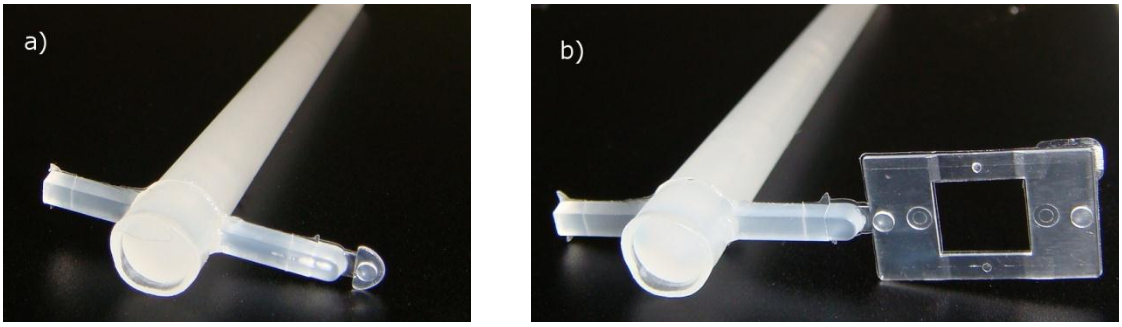

Figure 34 - Filling pattern during screw position set up: a) screw position at 11mm, b) screw position at 12mm

3.3 Parametrical study of the µIM process

In order to characterize the effects of the processing parameters on the replication of the micropart of variable thickness, the injection moulding experiments were carried out by means of the Design of Experiments (DOE) based on the Taguchi method. Three processing parameters were used as input: mould temperature (T_m), melt temperature (T_{melt}) and injection speed (V_i). Their selection has been justified by the data reported in a number of studies [10, 11, 195] as well as by the conclusions withdrawn from previous research conducted by the author and co-workers [203]. The outputs of the experiments were polymer dynamics in the microimpression, peak cavity temperatures and weld line position and width. The two latter quality outputs were further subjected to the analysis of the deviation of their values from the desired ones. Assessment of the polymer dynamics in the microimpressions was accomplished by using the pressure and temperature sensors as flow front markers. The time elapsed until the flow front gets in touch with each sensor, provides the means to evaluate the polymer dynamics in the microimpression. Full factorial design of experiment (DOE) was carried out where the process inputs were varied at two levels: 1- low and 2- high, giving 2^3 runs.

The experiments were carried out in a randomized sequence. The combination of controlled parameters is presented in Table 2. The remaining processing conditions namely: injection pressure (P_i), holding pressure (P_h), holding time (t_h) and cooling time (t_c) were kept constant during the entire study for each polymer tested (Table 3).

In order to minimize process disturbances generated by the change of processing conditions, 10 mouldings were discarded before collecting the microparts and recording the pressure and temperature data.

Table 2 - Combination of the controlled parameters for L8 orthogonal array.

Experiment N°	T_m (°C)			T_{melt} (°C)			V_i (mm/s)
	ABS	PP	POM	ABS	PP	POM	
DOE1	75	50	75	210	220	190	72
DOE2							144
DOE3				250	240	210	72
DOE4							144
DOE5	95	65	115	210	220	190	72
DOE6							144
DOE7				250	240	210	72
DOE8							144

Table 3 - Constant injection moulding conditions

Polymer	Pi (MPa)	P_h (MPa)	t_h (s)	t_c (s)
PP	100	15	2	25
ABS	150	45		
POM				

3.4 Polymer dynamics in the microimpression

Configuration of the pressure and temperature sensors, presented in Figure 32, allows for monitoring the flow front progress within the microimpression. Typical cavity temperature and pressure profiles of ABS (DOE7) polymer within the time interval of 3 seconds are shown in Figure 35. As soon as the polymer melt arrives at the sensor locations, the temperature or pressure profiles start to rise. The time, elapsed until the flow front gets in touch with each sensor, provides the means to determine how each geometrical configuration and processing condition may affect the microimpression filling.

Two time intervals P1-T1 and P1-T2 represent the time required for the polymer flow to travel from the P1 pressure sensor location to the T1 temperature sensor location in the

300µm section (P1-T1), and the time elapsed from the P1 pressure sensor location to T2 temperature sensor location in the 200µm section. The third time interval (T1-P2) represents the amount of time necessary for the polymer to flow from the T1 temperature sensor location to the P2 pressure sensor location. As it has already been mentioned earlier, data for the 25 cycles has been analysed for each polymer tested.

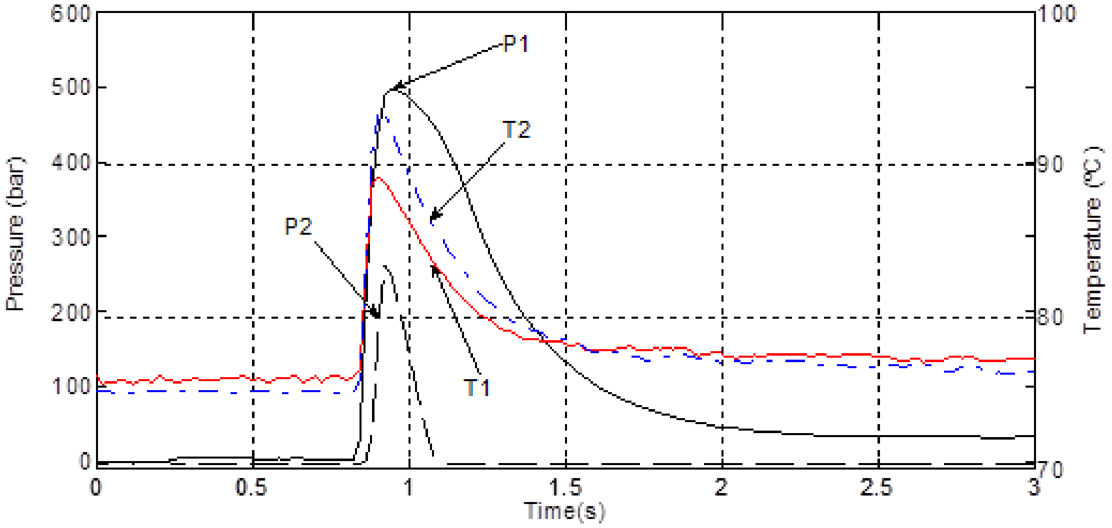

Figure 35 - Typical cavity temperature: T1, T2 and pressure P1, P2 profiles (ABS, experiment number 7)

3.5 Estimation of the µIM process variability

Variability is an inherent characteristic of any process. Therefore, injection moulding is also prone to some natural variability caused mainly by ambient temperature, air humidity, delayed response of the injection moulding machine and variation of barrel temperature [204]. In µIM, the individual effects of these factors and/or their combinations are amplified due to the small dosage of polymer. This may lead to fluctuations in the melt viscosity and result in production of unacceptable defective mouldings.

For each set of injection moulding conditions, 35 moulding cycles were recorded. However in some moulding runs, there were a number of injection cycles resulting in short shots for all three tested polymers. Further observation of the recorded pressure profiles, indicated that the faulty microparts do not have well established pressure patterns. As demonstrated in Figure 36, the peak pressure at the sensor location P2 (ABS, experiment number 7) barely reaches 40bar. However, the peak cavity pressure

(P2) of the completely filled micropart (Figure 35) moulded with the identical processing conditions is about 250bar. Such a small cavity pressure rise suggests that polymer solidifies immediately after touching the sensor and the micropart is shorted.

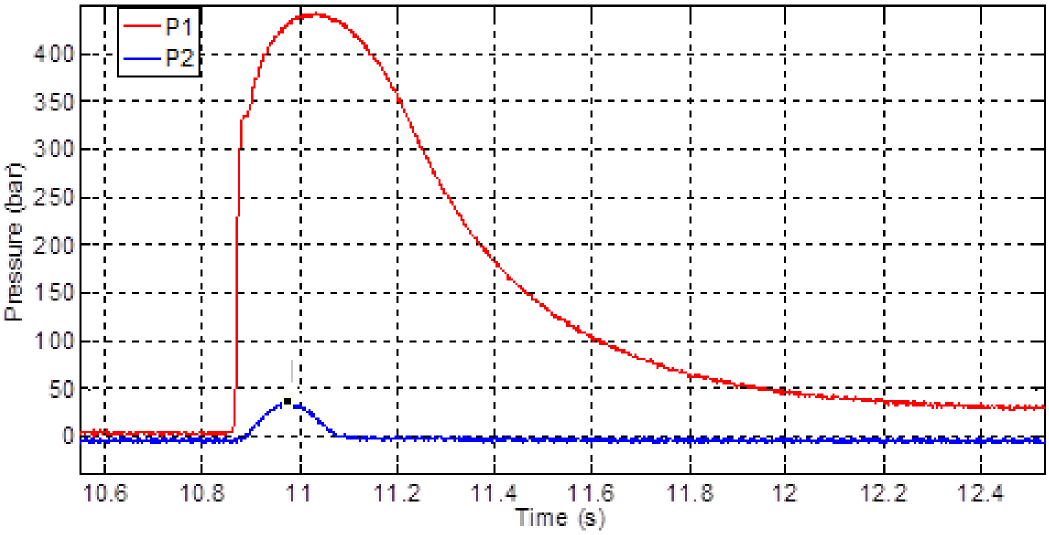

Figure 36 - Cavity pressure P1, P2 profiles for incomplete micropart (ABS, experiment number 7)

To exclude the cycles corresponding to incomplete microparts, all pressure and temperature data were processed with a code specifically developed in MATLAB® platform (MathWorks, Natick, USA). A rejection algorithm, presented in Figure 37 was developed to automatically remove all the cycles where the peak cavity pressure did not reach 100bar. This criterion guarantees that only pressure and temperature data for the complete microparts are considered in the subsequent analysis. Furthermore, the ratio of the recorded cycles to the post-processed ones shows the natural variability (*NV*) of the µIM process and given as:

$$NV = \frac{N_{c.f.}}{N_{c.r.}} \times 100\ (\%) \qquad \text{Equation 31}$$

where *Nc.f.* is the number of filtered cycles and *Nc.r.* is the number of recorded cycles. After processing the pressure and temperature data, 25 cycles for each injection run were randomly selected to assess the influence of the injection moulding conditions on the polymer dynamics in the variable thickness microimpression.

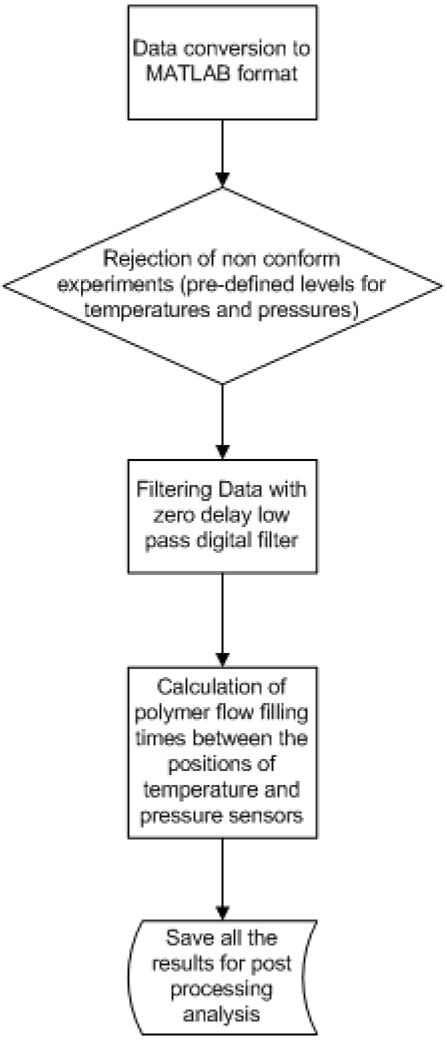

Figure 37 - Data processing flowchart

3.6 Assessment of the cavity temperature

3.6.1 Peak cavity temperature

The measured cavity temperature is much lower than the real melt temperature due to the high cooling rates occurring in the microimpression and slow response of the temperature sensors that were used. Nevertheless, the actual readings provide a trend of the melt temperature dynamic at the mould wall and melt interface. Typical temperature profiles at the sections of 200µm (T2) and 300µm (T1) of ABS at DOE7 processing conditions are shown in Figure 35. The slopes of the temperature curves indicate that in less than 1s the temperature almost reaches the values recorded prior to injection, indicating complete solidification of the micropart at these sections. In order to minimize the measurement error, the averaged values over 25 injection moulding cycles were used for comparison purposes.

3.6.2 Signal-to-Noise ratio

Any experimental results are highly affected by numerous internal and external disturbances, the so-called noise factors. In order to measure the influence of this noise on the outcome of the experiments, a variance index called signal to noise ratio (SN) is used to correlate the sensitivity of the quality characteristics to the noise factors [205]. Higher values of the SN ratio mean that the influence of the input signal is higher than the disturbances of the experiments. In this work, the desired value is the maximum peak cavity temperature. It is well known that higher temperature improves the microimpression filling due to the reduction of the polymer viscosity. Therefore, a ratio for the larger-the-better quality criterion was adopted. The *SN* ratio (larger-the-better) in the i-th experiment can be expressed as:

$$SN_{lb} = -10 \times log\left(\frac{1}{n} \times \sum_{i=1}^{n} \frac{1}{y^2}\right) \qquad \text{Equation 32}$$

where *i* is a number of experiment, *y* is the data and *n* is a number of the trials in each experiment. SN ratio difference between the maximum and minimum levels was calculated to figure out the degree of influence of each controlled factor on the peak cavity temperature. The detailed computational routine for the SN levels is available elsewhere [205].

3.7 Assessment of the weld line position

Weld lines are the visible lines on the surface of moulding where two melt fronts encounter after the obstacles. Conditions of the weld line formation influence, to a great extent, structural integrity and visual appearance of the micromoulded part [37, 206, 207]. When a conventional range of the mould temperature is used, melt temperature in microimpression may decrease significantly at the end of filling, i.e. at the most probable location of the weld line. The weld line formed at such conditions may eventually contribute for premature failure of the micropart if service load is applied at this critical area. Unfortunately, it is impossible to remove weld lines completely. Nevertheless, their appearance may be minimized by relocation of the injection gates or/and by an appropriate set of the injection moulding processing conditions.

In the present work, weld line position was also considered as an additional way for investigation of the polymer flow dynamics at the end of filling, unlikely to be accomplished by other means. Change in the weld line position reflects the alterations in polymer viscosity, induced by the processing conditions and variation of the microimpression's thickness. It was assessed by optical and polarized light microscopy techniques respectively designated as OM and PLM. The noninvasive nature of both OM and PLM, allows for quick weld line evaluation and therefore enabling necessary adjustments towards improvement of microparts' quality. Furthermore, the experimentally assessed weld line positions would be compared with those predicted by the numerical simulation model under the identical set of the injection moulding processing conditions.

3.7.1 Optical microscopy

The optical microscope magnifies an image of small samples by visible light and a system of lenses. The amplified image is directly observable by the eye. The level of magnification depends directly on the objective lenses and can give final magnification from 2 to 2000x [156]. There are a number of illumination techniques aiming to improve the contrast of the optical image: bright field, cross polarized light, dark field and phase contrast. Bright field microscopy is the simplest of all the light microscopy techniques and required minimal sample preparation. The sample is illuminated via transmitted white light from below and observed from above. This method has been reported to reach resolution of less than 1µm for imaging of multiphase polymers. However, it is not possible to observe surface of transparent or translucent polymer with this technique [156].

The bright field optical imaging technique of Nikon Eclipse LV150 microscope was chosen for visualization of the weld line shape and position in opaque POM and ABS microparts. For further processing and analysis, the images were recorded with a high quality digital camera, connected to the computer. The micropart's area probed to localize the probable weld line location was about 4.7 by 4.0mm (dashed line Figure

38a). Under such conditions, a minimum available magnification of 5 gives enough resolution for the weld line observation. Nevertheless, even with this minimum magnification, a field of vision was not enough to acquire a complete image of the weld line. Several snap shots were necessary for proper focusing of this most visible weld line fragment and its complete form was obtained after the stitching. Digitally stored images were calibrated for the assessment and subsequent quantitative comparison of the weld line position. The interior corner of the micropart, closest to the weld line, was chosen as an origin of measurements called thereafter in the text zero point (Figure 38b).

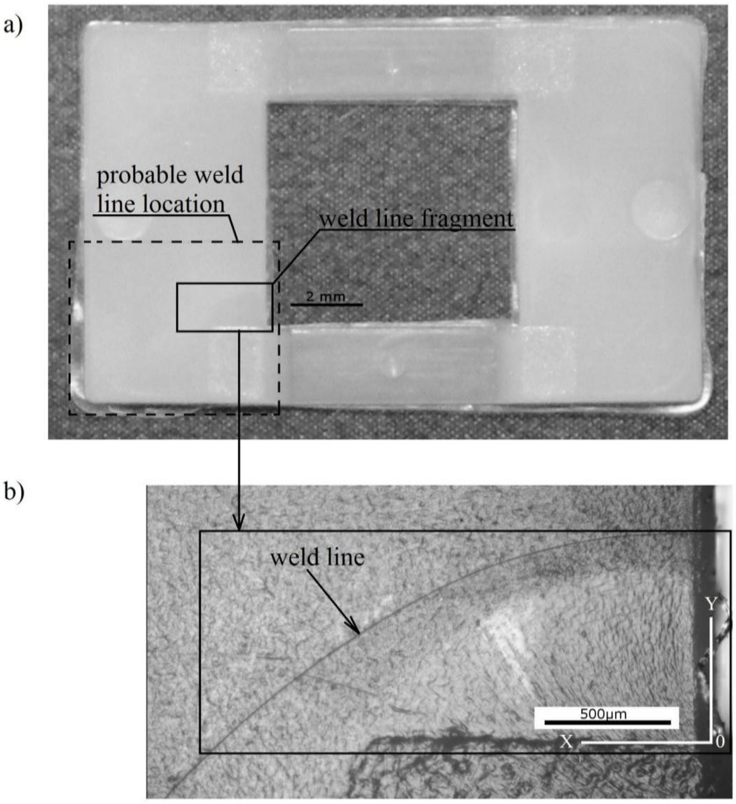

Figure 38 - a) POM micropart (DOE1), b) Micrograph of the weld line fragment

The weld line coordinates used for quantitative assessment and comparison are negative in X direction and positive in Y direction. Statistical significance of the weld line relative position was assured by undertaking measurements for ten randomly selected samples from the eight injection moulding runs (Table 3) for both ABS and POM polymers. A weld line portion used for further analysis is shown in Figure 38b.

3.7.2 Polarized light microscopy

Translucent and transparent polymers show such property as birefringence. Anisotropy is an inherent property of semicrystalline polymers, which are two phase systems and have different refractive angles of crystalline and amorphous regions [208]. Birefringence can be visualized and measured by polarized light microscope. For semicrystalline polymers, this technique is widely applied for morphology assessment such as the size and distribution of spherulites and local orientations [156].

General arrangement of PLM is described in Figure 39. It consists of the analyzer and polarizer which are crossed and oriented at 45º to the main optical axes of the specimen. An introduction of the birefringent compensator between the analyzer and the specimen allows for change of the optical retardation of the two light components in a way that retardation introduced by the specimen is compensated [209]. As mentioned earlier, transparent and translucent polymers are not observable by optical microscopy. As shown in Figure 40a, even in a highly magnified photographical image of the PP micromoulding, the weld line is undetectable. However, when viewed under polarized white light, polymer anisotropy manifests itself as brightly-colored bands or fringes and weld line becomes visible as well (Figure 40b).

The weld line shapes and location in the translucent PP micromouldings were observed with an Olympus ILLC2 microscope under magnification of 7.5. For further processing and analysis, the images were recorded with a high quality digital camera, connected to the computer. For example, the PLM image of the PP micropart, moulded with DOE1 processing conditions (Figure 40b), shows that the weld line is somewhat blurry at the proximity of the inner side of the micropart than gradually getting more visible towards the outer edge.

For future comparison of the weld line shape and position only its fragment with the best visibility (enclosed in solid line rectangle) was considered, as shown in Figure 40b. Similarly to the ABS and POM polymers, the same interior corner of the micropart, was chosen as zero point and therefore both X and Y coordinates, used for the quantitative assessment and comparison of the weld lines, are negative. To minimize measurements error, ten randomly selected samples for each combination of the processing conditions were observed and digital images were recorded.

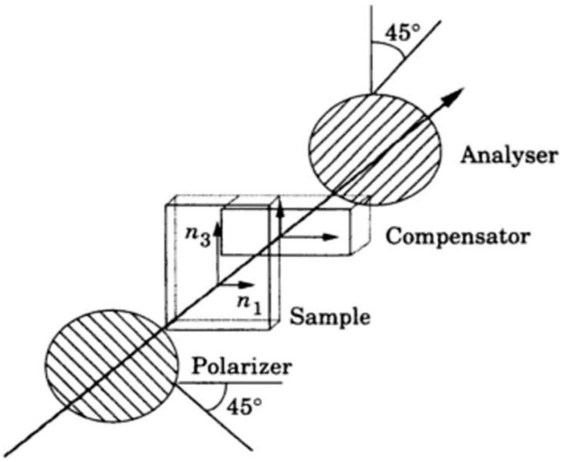

Figure 39 - Optical system for the measurement of orientation in plane [209]

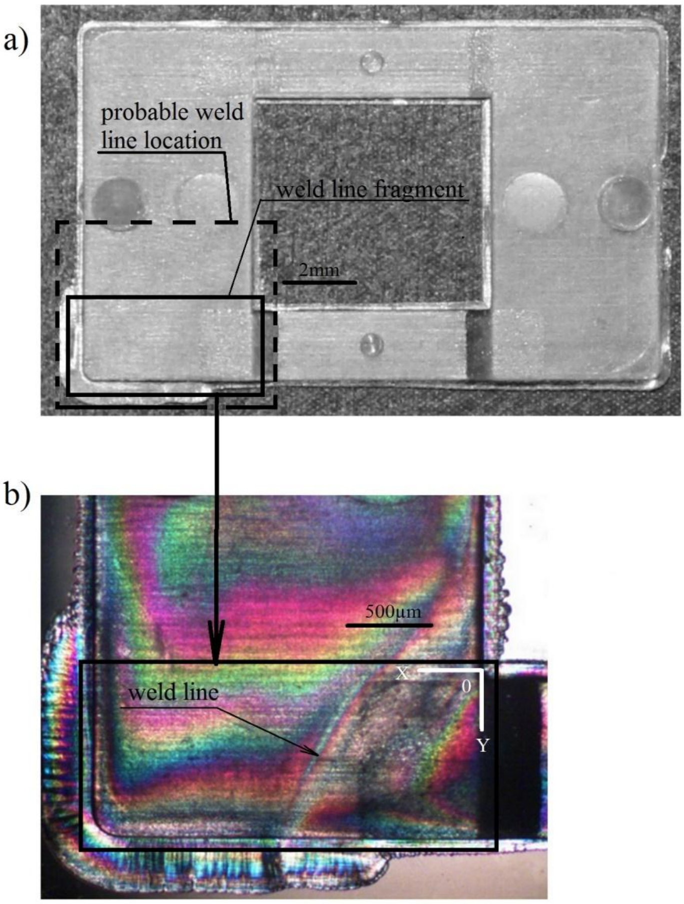

Figure 40 - a) PP micropart (DOE1), b) PLM micrograph of the weld line

3.7.3 Evaluation of weld line severity

So far, several techniques have been reported in the literature for quantitative assessment of the weld line quality of micromoulded parts and may be enumerated as follows: surface scanning, microscopy and mechanical testing [19, 37, 206]. Tosello *et al.* applied an atomic force microscope to ascertain effect of T_m, T_{melt}, V_i and P_h on the weld depth and width. It was found out that the depth of weld lines of PS microparts was reduced up to 50% with an increase of the mould temperature and the injection speed, whilst their width tends to diminish with the mould temperature at high level [206]. The surface width of the weld line and V-notch profile can be also measured by surface profilometers moving its probe perpendicular to the weld line [19, 37]. Wu and Liang [37] reported a good agreement of the weld line width of the PP and HDPE micro tensile specimens measured with this technique when compared with that assessed by means of microscopy. With an increase of the V_i, T_{melt}, and T_m the weld line width was found out to decrease for both polymers. Their findings also indicate that, as the micropart´s cross-section decreases, the tensile strength drops drastically in the weld line vicinity. Beside the geometrical factor, the processing parameters appear to affect the weld line tensile strength in the following order: T_{melt}, V_i, t_h and T_m. In the research of Xie and Ziegmann [19], however, the weld line tensile strength of PP micro tensile specimen was affected mainly by the mould and melt temperatures and in smaller extent by the injection velocity, while the other tested parameters were of less importance. The discrepancies between these two studies may eventually be attributed to the differences in the sample's geometry and also to the fact that in the latter research the variotherm system was employed and T_m was varied in the range above the PP transition temperature.

In the present study, the weld lines width was chosen as a quality signature of ABS and POM polymers and was assessed by optical microscopy. It is, however, understood that 3D assessment is desirable as it reflects to a greater extent the influence of the injection moulding processing conditions on the weld line severity. Nevertheless, in this study, two-dimensional assessment was adopted for the initial evaluation of the weld line quality, while a 3D approach is intended to be applied for the future investigation. The weld line width was always measured at approximately the same distance from the interior board of the µ-part (zero point) for all injection moulding setups. This technique, however, does not allow for evaluation of the weld line width in translucent polymers as PP and therefore only the weld lines severity analysis was undertaken for

POM and ABS microparts. For each injection moulding setup, the average weld line width of the ten samples and the associated standard errors were calculated.

SN (smaller-the-better) ratio was used to correlate the sensitivity of the weld line width to the noise factors present in the µIM process. Narrower weld line width was reported to improve an aesthetic appearance of µIM parts [37]. It seems reasonable to assume that the reduction of the weld line width may be attributed to better interfusion of the polymer fronts and consequently less probability to fail when subjected to mechanical solicitations. The *SN* (smaller-the-better) ratio in the *i*-th experiment can be expressed as:

$$SN_{sb} = -10 \times log\left(\frac{1}{n} \times \sum_{i=1}^{n} y^2\right) \qquad \text{Equation 33}$$

where i is a number of experiment, y is a the data and n is a a number of the trials in each experiment. The detailed computational routine for calculation of the SN levels is explained in literature [205, 210].

3.8 Dynamical Mechanical Thermal Analysis (DMTA)

DMTA tests were carried out in order to assess mechanical properties of ABS polymer. These tests supply valuable information about the complex modulus and its components: storage modulus (stiffness), loss modulus (energy dissipation) and loss angle tan(σ). Using multi-frequency/accelerated temperature measurements and time temperature superposition (TTSP) treatments of the recorded data, stress relaxation in ABS µ-parts was investigated. Applicability of the TTSP for long-term mechanical testing has been previously referred in the literature [173, 211].

3.8.1 Specimen preparation

Two typologies of the specimens have been considered for DMTA testing. In a first case, samples were cut through the micropart's lateral sides (Figure 26), including the 300µm or the 200µm zones, and can be depicted, respectively in Figure 41.

The micrometric thickness of the samples dictated a choice for the most appropriate test mode. According to the D4065-01 ASTM standard, frequency – tensile oscillation was used for conducting the frequency temperature scan.

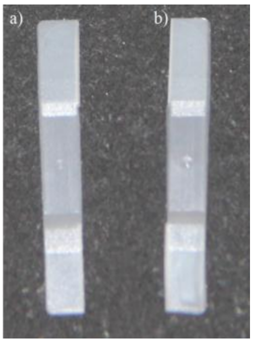

Figure 41 - DMTA samples: a) 300µm section, b) 200µm section

However, in D4065-01 ASTM is explicitly expressed that the plastic specimen might have a uniform cross section, which is obviously not the case of the presented above the samples.

To rule out the possibility of errors induced by the thickness gradient through the sample´s length, another specimen's geometry has been tested. It was a plate with thickness of 600µm, moulded in a conventional type injection moulding machine, under the same set of the processing conditions (DOE8) as for the µ-part of variable thickness. The characteristics of 65ton EURO INJ (Model: D065) injection moulding machine are: 32mm screw diameter and a maximum injection pressure of 1777 bar. Considering the overall dimensions of the plate 45.8 ∗ 45.8 ∗ 0.6mm (Figure 42a), it was cut along the direction of flow in order to comply with the requirements of the DMTA analysis. The final dimensions of the second tested geometry were of 20 ∗ 5 ∗ 0.6mm (Figure 42b).

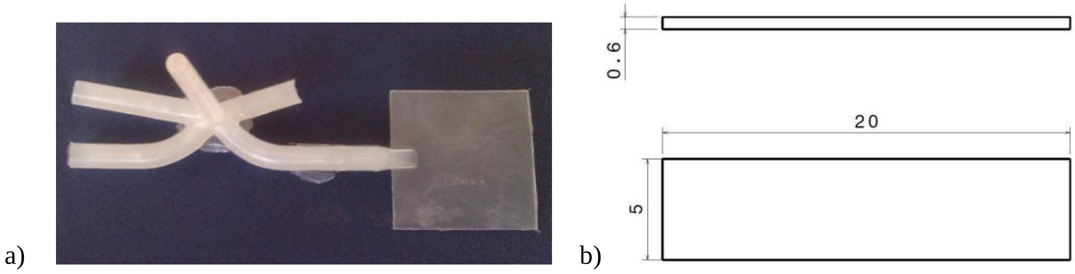

Figure 42 - Second geometry: a) plate with runner system, b) dimensions of cut sample

All tested specimens underwent annealing, which is a heating of a polymeric part below its glass transition temperature in order to relieve the internal stresses introduced into the part during injection molding. Moreover, amorphous polymers can physically age and hence undergo change in mechanical properties even without any deformation applied [146]. In case of ABS, the temperature used was 80ºC, which is the heat deflection temperature of Cycolac GPM5500S. At this temperature, a greatest reduction in the residual stress was reported while not causing any measurable degradation or warping [211].

The overall procedure included the following stages.

- μ-part was placed in an annealing oven.
- It was heated to the annealing temperature at 30ºC/hour.
- It was kept at the annealing temperature for 4 hours.
- Cooling the μ-part to the ambient temperature was performed at 6ºC/hour.

This procedure was necessary in order to comply with the objectives of the investigation. In case of not annealed specimens, a viscoelastic material model based on TTSP will reflect the residual stresses generated by the μIM processing conditions. However, the proposed hybrid thermo-rheological and structural analysis was intended to account for the state of residual stress predicted numerically. Annealing allowed for reduction of the process induced residual stresses and therefore, the material model based on the mechanical properties of annealed parts gave more generalized representation of the viscoelastic material, i.e., the same viscoelastic material model may be used for simulation of the parts moulded under different processing condition.

3.8.2 Dynamical mechanical tester

The DMTA machine used was a Triton Technology TTDMA Dynamical Mechanical Analyser (Figure 43), courtesy of the Department of Polymer Engineering at Minho University. The clamp configuration was set up for the tension tests and the specimens were mounted in a fashion depicted in Figure 44.

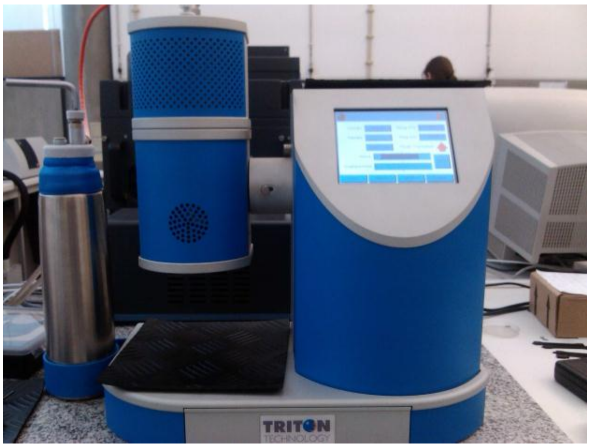

Figure 43 - Triton Technology TTDMA Dynamical Mechanical Analyser

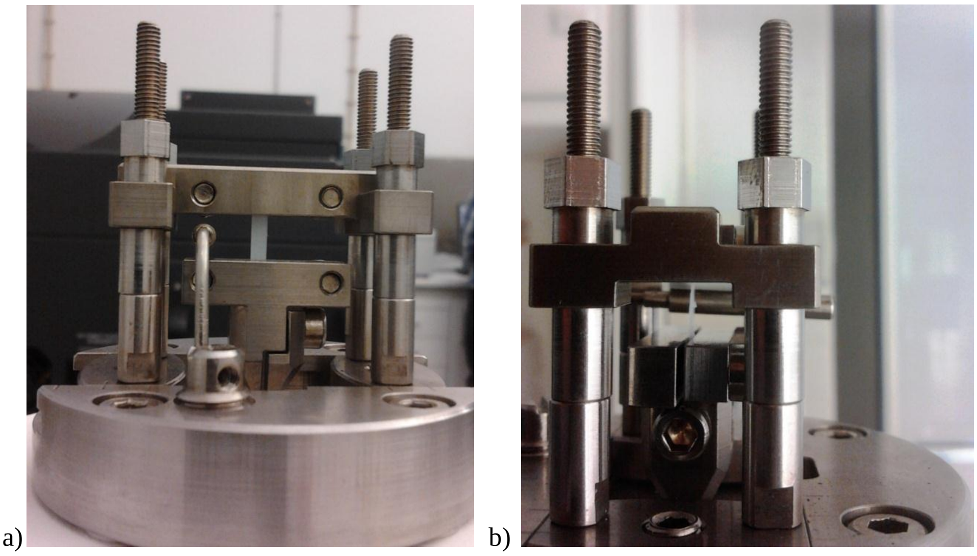

Figure 44 - a) mounted sample - front view, b) mounted sample – side view

3.8.3 DMTA experiment

Dynamical mechanical thermal analysis is the one of the most informative tests for assessment of the mechanical properties of the plastic parts. DMTA tests were carried on each sample at 16 different frequencies, equally spaced from 0.01 to 10Hz over the temperature range of 30 to 75°C at intervals of 5°C. This process was repeated for groups of 3 samples with the same processing conditions. Relaxation tests were carried imposing a displacement of 20µm in order to assure that deformation is maintained within the linear viscoelastic limit. As a result of the experiment, series of curves for storage, loss modulus and tan(σ) were generated for the total of 10 isotherms.

To estimate long-term behaviour of the polymer, a MATLAB® application was run, previously developed by a member of our research team. The latter enables appropriate data selection for the application of the time temperature superposition principle (TTSP) to the recorded data. The application was created to read data from excel files, generated by the interface of the dynamical mechanical thermal analyzer, and to produce the master curves automatically. Furthermore, this automated approach was intended to remove uncertainty inherent to manual shifting processes and therefore always resulting in a meaningful master curve. The developed subroutine for the DMTA data treatment was programmed in the following fashion:

- to retrieve only pertinent analysis data and process it without any further user interaction;
- to ascertain thermo-rheological simplicity of a material, by presenting the recorded DMTA data in a form of two graphics: the Cole-Cole plot and a van Gurp Palmen plot;
- to calculate the best fitting values for the shift factor to superpose the storage and loss modulus data with the calculated shift factors.

.

Chapter 4 Numerical simulation

Two general steps were employed in the numerical simulation routine. First, Autodesk Moldflow Insight 2012 simulation code has been employed for analysis of the polymer flow in the microimpression. Prior to numerical simulations, the most adequate mesh type for simulation of µIM was chosen. It was accomplished through the study of the influence of the mesh discretization on the flow field prediction in the microimpression. Next, the parametrical study was performed replicating the experimental processing conditions presented in Table 2 and 3 (page 70). At the second stage, the results of AMI® numerical simulations, including the finite element model information, material data and residual stresses in the micropart were converted into the ABAQUS® [190] input files for the subsequent structural analysis of µ-parts.

4.1 Modelling and mesh generation

Despite the numerous attempts to figure out the limits of applicability of the existent commercial simulation codes toward µIM, considerable uncertainty still exists regarding to the discretization of the physical domain and the material model used to simulate the process. The former issue was extensively investigated and various finite element models have been applied [94, 102, 104, 106, 212]. Those models could be sequentially characterized as: 1) mid-plane models, 2) surface models and 3) solid models. The first is a 2D-model, where planar mid-plane with a defined thickness is used to represent the 3D-geometry of the part. While the second represents the 3D-part as double skin or shell mesh on the surfaces of the solid model, giving an acceptable representation of the thin-walled parts with uniform thickness. These two models adopt the Hele–Shaw approximation [98].

However, when a model includes the combination of the macro and µ-features, dimensions could vary drastically and do not obey to the criteria of the traditional thin-wall designs. Under such conditions, a full 3D-model is definitely required. This is exactly the case of the micromoulding under investigation, where the runner system exceeds significantly the micropart in size and volume (Table 1, page 60).

It is also worth noting that the quality of the model mesh in both adaption and discretization are of the utmost importance for reliability of the numerical simulation. Theoretically, the mesh size should be infinitely small for the best prediction of the flow advancement. However, an extremely refined uniform mesh could be prohibitive in terms of computational resources, whereas a too coarse mesh may not capture the material behaviour inside the microimpression. To attain the required compromise, dedicated meshing tools such as the Hypermesh module of the Altair® HyperWorks 10 software [213] for generating the differential mesh for the micro component and the runner system, may be considered. Thus, high level of discretization at the micro-component physical domain can be achieved along with the reduction of the number of finite elements otherwise necessary to represent the whole assemble.

Three different scenarios for the micropart and the runner system mesh generation were considered. Two meshes were created in AMI® through the Autodesk® Moldflow® Design Link 2012 (AMDL) translator which automatically determines a suitable global edge length for the mesh: type 1-3D mesh with 6 layers of elements through the thickness and type 2-3D mesh with 8 layers of elements through the thickness. However, as it can be observed from Figure 45a and Figure 45b (mesh type 1 and 2), the algorithm produces a too coarse mesh with maximum aspect ratios at the micropart, and an extremely refined mesh at the runner system. It also should be noted that mesh quality decreases with the increasing number of layers throughout the thickness.

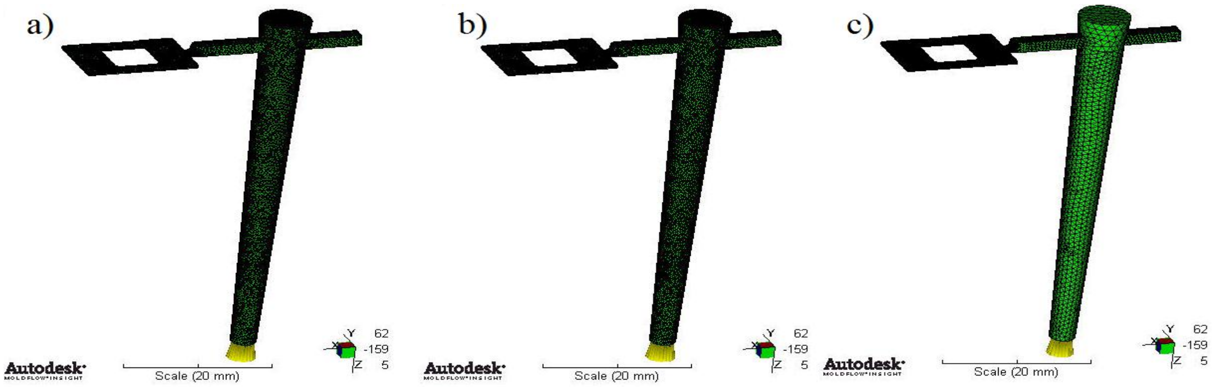

Figure 45 - 3D mesh for complete moulding: a) type 1, b) type2, c) type 3

In order to gain more control over the microcomponent’s discretization, the Hypermesh module of the Altair® HyperWorks 10 was used for mesh generation. After importing the CAD model into the Hypermesh environment, the microcomponent and its runner system were discretized by dual domain surface mesh with differential mesh densities. The microcomponent was discretized with a refined uniform mesh with an average edge length varying from 50 to 100µm, for better representativeness throughout the thickness of the microcomponent, while much coarser mesh was used for the runner system. Thereafter, the dual domain finite element model was imported to the AMI® environment, where 3D-meshing has been performed by applying 6 layers of elements throughout the thickness. The resultant mesh was designated as type 3 (Figure 45c). Differences between these three mesh typologies are presented in Table 4.

Injection locations, marked in yellow in Figure 45, indicate the connection of the runner system to the injection moulding machine. 68 injection points were required for each of the AMDL generated mesh (types 1 and 2), whilst the runner system with coarser mesh (type 3) only needs 28 injection points. The elements located in-between and around the injection locations represents the simulated area of injection, i.e. connection with the injection moulding machine.

Table 4 - Comparison of the finite element meshes

Mesh description		Type 1	Type 2	Type 3
Mesh volume (mm$^{3)}$	Part	44,6x10^{-3}	44,6x10^{-3}	44,6x10^{-3}
	Runner system	1,2615	1,2611	1,247
Tetrahedrons		361513	442662	775959
Injection locations		68	68	28
Computational time (min)		122	140	240
Aspect ratio	Maximum	16,7	22,4	9,2
	Average	4,17	4,5	2,46
	Minimum	1,06	1,06	1,04

To further illustrate the discrepancies between the mesh types 1, 2 and 3, an amplified and more detailed view is presented in Figure 46a, Figure 46b and Figure 46c respectively. Finer discretization of the µ-part's domain (mesh type 3) is clearly visible from Figure 46c when it is compared with the mesh types 1 (Figure 46a) and 2 (Figure

46b). A clearer idea of each finite element mesh quality can be drawn after the observation of the tetrahedron shapes and dimensions for the mesh fragments type 1 (Figure 46d), type 2 (Figure 46e) and type 3 (Figure 46f). Regular shapes and uniform dimensions of the mesh type 3 indicate its superior quality over the other meshes typologies. Moreover, an adaptive discretization of the model applied for the mesh type 3 allows for a very precise and gradual mesh adjustment to the geometry, especially at such critical sections with an abrupt thickness change and steep curvature as the injection moulding gate. The latter statement is clearly illustrated in Figure 47c, where the surface mesh transition from the trapezoidal runner to the injection moulding gate shows the closest match as the model dimensions drastically decrease, whilst the mesh types 1 and 2 fail to achieve such precision (Figure 47a, b). Moreover, in µIM, time discretization should also be adjusted to capture properly the extreme variation in velocities and temperatures during the microimpression filling. It was accomplished by limiting the maximal increase in volumetric filling of the cavity between two successive calculation time steps from the default value of 4% to 0.1%.

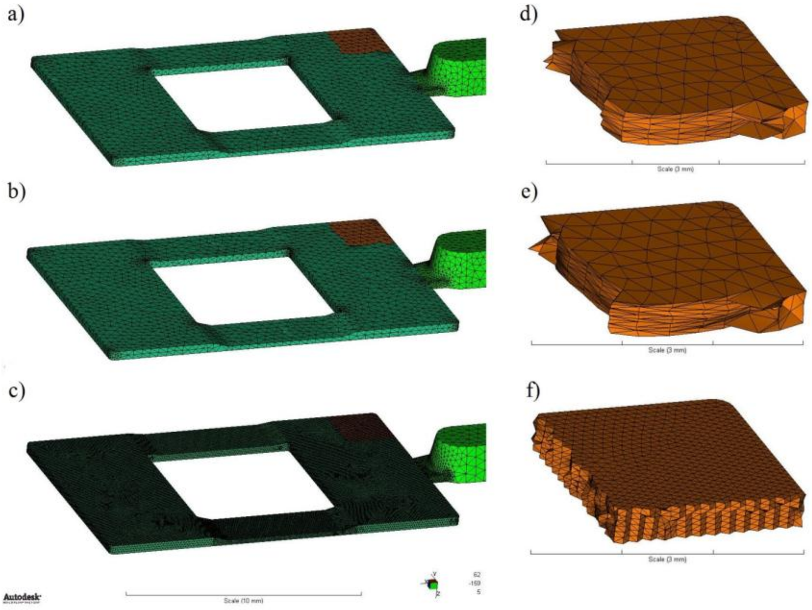

Figure 46 - 3D mesh micropart: a) type 1, b) type2, c) type 3, d) mesh fragment type 1, e) mesh fragment type 2, f) mesh fragment type 3

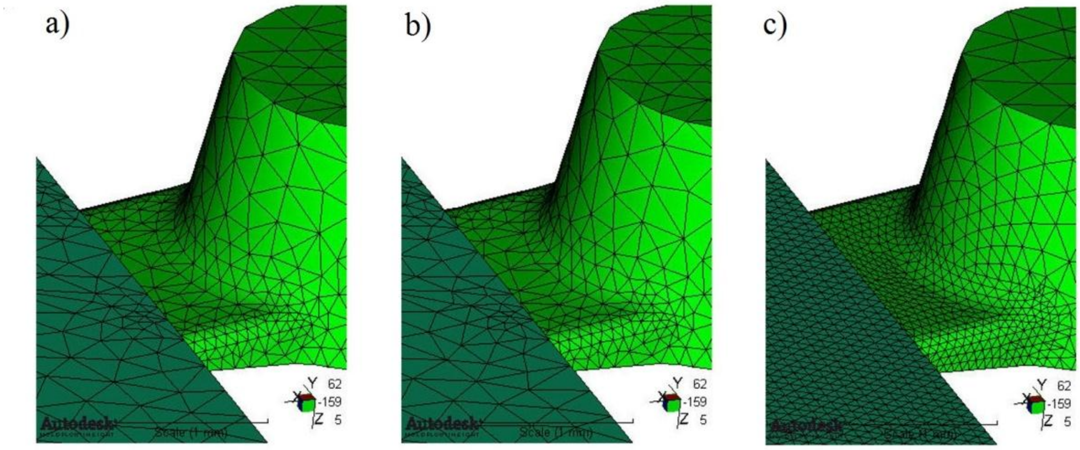

Figure 47 - Fragment of 3D mesh at the injection molding gate: a) type 1, b) type 2, c) type 3

4.2 Governing equations for the 3D Navier-Stokes solver

In AMI® for 3D mesh the following assumptions are applied [137]:

- 3D Navier-Stokes solvers used for non-Newtonian fluid;
- Pressure, temperature and three directional velocities are calculated at each node;
- Heat conduction is considered in all directions;
- Inertia and gravity effects may be included in the calculations;
- Pressure dependency of viscosity effects and extensional viscosity effects, are considered;
- Polymer does not slip over mould wall.

The equations governing the flow of polymer melt comply with the principles of conservation of mass, conservation of momentum, and conservation of energy [214].

The equation of mass, called otherwise continuity equation for a compressible fluid is given by:

$$\frac{\partial \rho}{\partial t} + (\nabla \cdot \rho \vec{v}) = 0$$ Equation 34

where ρ is the fluid density, $\vec{v}$ is the velocity vector and t is time.

The principle of conservation of momentum is given by:

$$\frac{\partial}{\partial t}(\rho\vec{v}) = \rho\vec{g} + \left[\nabla \cdot \underline{\sigma}\right] - \left[\nabla \cdot \rho\vec{v}\vec{v}\right] \qquad \text{Equation 35}$$

where $\vec{g}$ is gravitational force vector and $\underline{\sigma}$ is the stress tensor.

The principle of conservation of energy is given by:

$$\rho c_p\left(\frac{\partial T}{\partial t} + \vec{v} \cdot \nabla T\right) = \beta T\left(\frac{\partial p}{\partial t} + \vec{v} \cdot \nabla p\right) + p\nabla \cdot \vec{v} + \left(\underline{\sigma}:\{\nabla\vec{v}\}\right) + \nabla \cdot (k\nabla T) \qquad \text{Equation 36}$$

where c_p is specific heat, β is the coefficient of volume expansion, p is pressure, k is thermal conductivity and T is temperature.

The equations listed above represent the principles governing the flow of a number of fluids and their solution in general form is quite complex. Considering a particular case of injection moulding, it is advisable to introduce some assumptions aiming to decrease the model complexity, the solution time and material data demands. The premises applied to the polymer properties in AMI® software during the filling phase are enumerated as follows:

- During the filling phase, the polymer density is assumed to be constant, meaning that polymer melt is incompressible
- Polymer melt is assumed to be a Generalized Newtonian Fluid, disregarding the viscoelastic effects.
- Although the thermal conductivity of polymers depends on temperature, it is assumed to be constant during the filling phase.

Considering the assumptions given above, the governing equations 4, 5 and 6 can be rewritten in the following form:

Equation of mass:

$$\nabla \cdot \vec{v} = 0 \qquad \text{Equation 37}$$

Equation of momentum:

$$\rho \frac{\partial \vec{v}}{\partial t} = \rho \vec{g} - \nabla p + \left[\nabla \cdot \eta \underline{\dot{\gamma}}\right] - \rho[\vec{v} \cdot \nabla \vec{v}] \qquad \text{Equation 38}$$

where η is viscosity and $\underline{\dot{\gamma}}$ is rate of deformation.

Energy equation:

$$\rho c_p \left(\frac{\partial T}{\partial t} + \vec{v} \cdot \nabla T\right) = \beta T \left(\frac{\partial p}{\partial t} + \vec{v} \cdot \nabla p\right) + \eta \dot{\gamma}^2 + k \nabla^2 T \qquad \text{Equation 39}$$

where $\dot{\gamma}$ is shear rate.

4.3 Viscosity model.

The Cross-WLF (William-Landel-Ferry) viscosity model was applied for the 3D simulation of the polymer flow, described next by the following equations [204]:

$$\eta(\dot{\gamma}, T, P) = \frac{\eta_0}{1 + \left(\frac{\eta_0 \gamma \cdot}{\tau^*}\right)^{1-n}} \qquad \text{Equation 40}$$

$$\eta_0 = D_1 exp\left[\frac{-A_1(T - T^*)}{A_2 + (T - T^*)}\right] \qquad \text{Equation 41}$$

where η is the viscosity (Pa.s), η_0 is the zero shear rate viscosity (Pa.s), $\dot{\gamma}$ is shear rate (1/s), $\tau*$ is the shear stress at the transition between Newtonian and power law behaviours, T is the temperature (K), T*is the glass transition temperature which obeys the equation $T^*=D_2+PD_3$ (K), where P is the pressure, D_1, D_2, D_3, A_1 and A_2 are the data fitting coefficients.

4.4 AMI® shrinkage prediction for 3D models

During the injection moulding cycle, the part is constrained in the mould. It is assumed that shrinkage of the frozen layer is prevented by two mechanisms: adhesion of the outer layers of material to the mould wall and by the stretching forces of the melt pressure during packing. After ejection from the mould, i.e. when the restriction to shrinkage is removed, polymer chains tend to reach the equilibrium state which results in the residual stress release in the form of shrinkage deformation [215].

In the AMI® shrinkage analysis, two types of shrinkage variations may be distinguished: shrinkage variations through the part’s thickness (differential cooling) and shrinkage difference from through the length. For example, the latter is likely to be caused by the temperature drop through the flow length at the end of filling, where solidification is faster than near the gate. Another reason for length shrinkage to vary may be due to orientation effects (anisotropic shrinkage).

For the sake of simplicity, a solidified part is treated as linear elastic solid and polymer melt is assumed to be purely viscous. The linear shrinkage is calculated as follows:

$$\varepsilon_i = \int_{T_r}^{T_0} \alpha_i(T)dT \qquad \text{Equation 42}$$

where ε_i is the linear shrinkage in *i-th* principal direction; α_i is the linear thermal expansion coefficient (CTE) at temperature T in the *i-th* principal direction; T_0 is the temperature when the local cavity pressure reached the atmospheric condition (value is obtained from the flow simulation); T_r is the room temperature.

4.5 Duplicating of the parametrical study of the µIM process in AMI®

Eight simulation runs of the mould filling, packing and warpage for ABS, PP and POM polymers were carried out duplicating the arrangement performed earlier experimentally in Table 2 and Table 3. Two outputs from the numerical simulations were chosen for comparison with the experimental results, namely: time intervals, used for assessment of the polymer dynamics in the microimpression; and weld line shape and location. The material data for ABS - CYCOLAC GPM5500S, PP - Moplen HP500N and POM - C 9021 are available in the AMI® database. Filling control was chosen as Ram speed (mm) versus Ram position (mm), where the ram speed was identical to the injection speed V_i shown in Table 3.

4.6 Thermo-rheological structural (TRS) analysis

4.6.1 Predicted process-induced residual stresses in µIM parts

The results of the complete simulation (filling + packing + warpage) include calculations of material properties and residual stresses in the plastic part. They are a direct indication of complex thermo-rheological history of the moulded component during processing and therefore might be taken in consideration for assessment of the final mechanical properties of microparts. With the aid of the AMI/ABAQUS interface, the finite element model information was translated from the AMI® into a partial ABAQUS® input file for ABS, PP and POM polymers which gave the total of 24 sets of input data. Moreover, beside the ABAQUS® input file, a number of additional files were generated detaining information about plastic's mechanical properties and state of the residual stresses. ABAQUS® partial input file encloses nodal coordinates, element topology, element properties and boundary conditions sufficient to eliminate the rigid body modes. The residual stress file contains residual stresses description in principal directions associated with that mesh. In order to visualize the magnitude and distribution of the residual stresses, the partial input file must be submitted for analysis through a command line: "Abaqus job = ′file′.inp interactive". It has to be mentioned that at this stage, the partial input file contains only "general static step", which means that only linear elastic properties of the polymer were used for assessment of the internal residual stresses after ejection of the micropart from the mould. This procedure was repeated for evaluation of the processing conditions influence on the residual stresses distribution and magnitude in ABS, POM and PP micromoulded parts.

4.6.2 ABAQUS® structural analysis

After assessment of the internal state of residual stresses in micropart, the next step is to study its long-term performance when subjected to the mechanical solicitation. To do so the translated model must be provided with the correct boundary conditions, loadings, material model data, and solution controls. The schematic representation of this thermo-rheological structural analysis is presented in Figure 48.

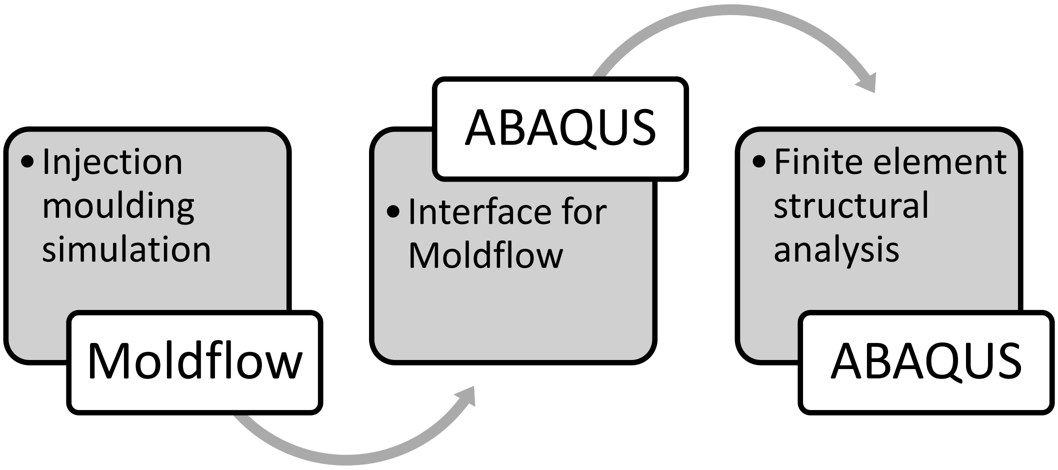

Figure 48 - Workflow of the TRS analysis

To simulate long-term performance of µ-parts, constant deformation was applied and maintained fixed for monitoring stress relaxation. This requires a material model accounting for viscoelastic nature of polymers. Viscoelastic material model must be integrated into the compiled AMI/Abaqus input file.

There are several ways to include the time domain viscoelastic material model data in the ABAQUS® input file such as: creep test data and relaxation test data; direct specification of Prony series parameters $\bar{g}_i^P$, $\bar{k}_i^P, \tau_i$ and frequency-dependent test data [216]. The latter was the chosen option, as DMTA results are frequency dependent. ABAQUS® uses analytical expressions that relate the Prony series relaxation functions to the shear storage and loss moduli. Fourier transforms were applied to convert the expressions for the shear moduli from the time domain to the frequency domain:

$$G_s(\omega) = G_0 - \left(1 - \sum_{i=1}^{N} \bar{g}_i^P\right) + G_o \sum_{i=1}^{N} \frac{\bar{g}_i^P \tau_i^2 \omega^2}{1 + \tau_i^2 \omega^2} \qquad \text{Equation 43}$$

$$G_l(\omega) = G_o \sum_{i=1}^{N} \frac{\bar{g}_i^P \tau_i \omega}{1 + \tau_i^2 \omega^2} \qquad \text{Equation 44}$$

where $G_s(\omega)$ is the storage modulus, $G_l(\omega)$ is the loss modulus, and G_0 is the instantaneous shear modulus, ω is the angular frequency, and N is the number of terms in the Prony series.

The two expressions presented above were used in a nonlinear least-squares fit to determine the Prony series parameters from the storage and loss moduli cyclic test data obtained at *M* frequencies by minimizing the error function:

$$X^2 = \sum_{i=1}^{M} \frac{1}{G_\infty^2} \langle (G_s - \bar{G}_s)_i^2 + (G_l - \bar{G}_l)_i^2 \rangle \qquad \text{Equation 45}$$

where $\overline{G}_s$ and $\overline{G}_l$ are the test data and G_∞ is the long-term shear modulus.

Frequency domain data was introduced in a tabular form, providing as input the real and imaginary parts of ωg∗ (non-dimensional shear relaxation function), where ω is the angular frequency as function of frequency in cycles per time. The real - $\omega\mathfrak{R}(g^*)$ and imaginary - $\omega\mathfrak{I}(g^*)$ parts of ωg∗ are respectively given as follows:

$$\omega\mathfrak{R}(g^*) = \frac{G_l}{G_\infty} \qquad \text{Equation 46}$$

$$\omega\mathfrak{I}(g^*) = 1 - \frac{G_s}{G_\infty} \qquad \text{Equation 47}$$

where: G_l is the loss modulus; G_s is the storage modulus; G_∞ is the long-term modulus. The latter is obtained from the storage modulus when t →∞, which corresponds to G_s at the lowest frequency.

In order to apply correct boundary conditions for the relaxation experiment after the first “general static” step, which simulates ejection from the mould, a second “general static” step was added to the input file. At this step, an instantaneous strain of 20µm was imposed at the one 400µm side of the µ-part, whilst the opposite side was fixed in all directions. Finally, the relaxation process was simulated by applying the third - ”Visco” step, where the viscoelastic properties of polymer were taken into account while the other boundary conditions were maintained unaltered from the previous steps.

Chapter 5 Results and discussion

This chapter provides a holistic approach for assessment of polymer dynamics in the microimpression and structural performance of µ-parts, which embraces both experimental data and their numerical prediction.

5.1 Polymer dynamics in the microimpression

The layout of the pressure and temperature sensors, shown in Figure 32, allows for the monitoring of the flow front progress in the microimpression. As soon as the polymer melt arrives at a sensor location, the local temperature or pressure profile starts to build up. Using the recorded time intervals required for the polymer flow to progress from one sensor to another, the flow pattern and its dynamic may be assessed. Moreover, in the case of symmetrical in-plane but asymmetrical in-thickness mouldings, the flow front advancement may be also evaluated with respect to the moulding thickness. The locations of the sensors P1, P2, T1 and T2 can be depicted from Figure 49a. The time span elapsed between the melt touching each sensor defines three time intervals (P1-T1), (P1-T2) and (T1-P2). These intervals represent the time required for the melt to travel from the P1 pressure sensor location to the T1 temperature sensor location in the 300µm section (P1-T1), the time elapsed from the P1 pressure sensor location to temperature sensor T2 in the 200µm section (P1-T2), and the time necessary for the melt to move from the T1 temperature sensor location to the P2 pressure sensor location (T1-P2). The reason for assuming that the P2 sensor is touched by the flow front arriving from the 300µm section may be explained by the variable thickness of the micromoulded part and the consequent offset of the weld line position with respect to the symmetry axis of the moulding. This statement was found to be valid for all polymers tested through the observation of the short shots of ABS (Figure 49a), PP (Figure 49b) and POM (Figure 49c).

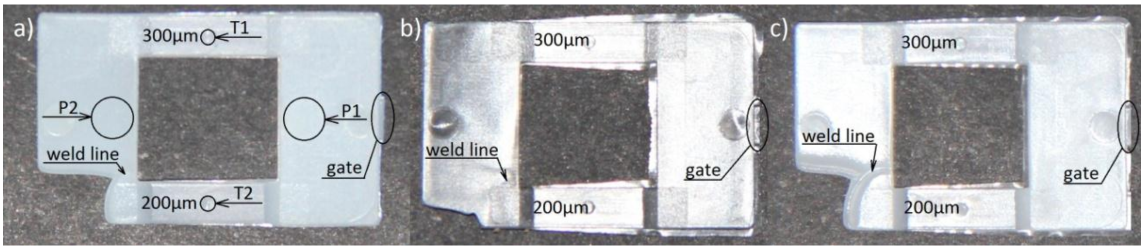

Figure 49 - a) Incomplete ABS micropart; b) incomplete PP micropart; c) incomplete POM micropart

For all 8 moulding runs with ABS, the time intervals (P1-T1), (P1-T2) and (T1-P2) (Figure 50) show that the polymer flow takes longer to reach the sensor T2 located at the 200µm section, which implies a slower velocity in the thinner section. The reduction of the moulding thickness favours the cooling of the melt, hence the consequent increase of viscosity and reduction of melt speed. As expected, the (P1-T1) and (P1-T2) time intervals reflect the change of the injection velocity, increasing and decreasing according to the conditions listed in Table 2. At higher injection velocity, the difference between the time intervals (P1-T1) and (P1-T2) tends to diminish (DOE2, 4, 6 and 8). The latter indicates a reduction of the polymer viscosity and may be attributed to the shear heating effect. The decrease in viscosity was also verified with the increase of the melt temperature at low injection velocity (DOE3 and 7).

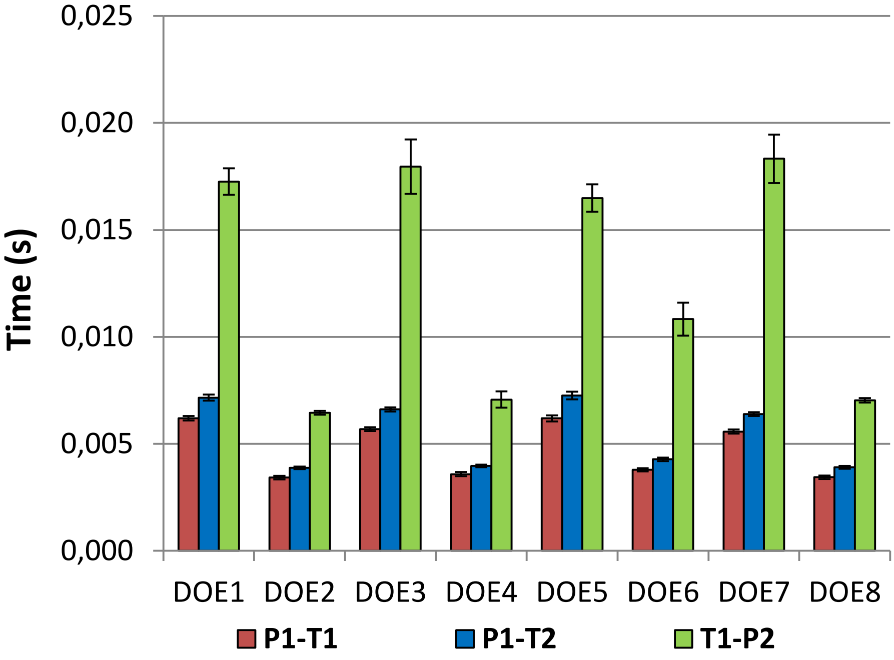

Figure 50 - Time intervals for flow front advancement between (P1-T1) (P1-T2) and (T1-P2) for ABS.

Nevertheless, it is worth mentioning that for the ABS DOE6 injection run, the time intervals are somehow out of the typical variation pattern, being slightly longer than others with identical injection velocity conditions. This occurrence may be eventually attributed to process variability associated with the increased melt viscosity.

Polymer flow of the polyoxymethylene (Figure 51) develops in a fashion quite similar to that observed for ABS. However, the filling times for POM are found out to be somewhat longer for all combination of the processing conditions. At higher injection speed, high mould temperature seems to promote the microimpression filling as the time intervals (T1-P2) of DOE6 and 8 slightly decrease comparing with those of the DOE2 and 4.

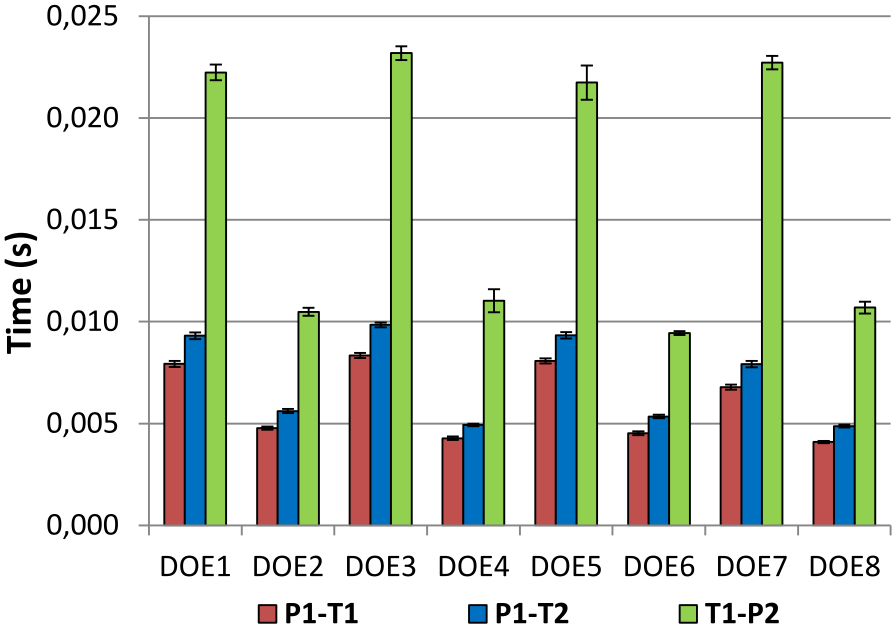

Figure 51 - Time intervals for flow front advancement between (P1-T1) (P1-T2) and (T1-P2) for POM.

Polymer dynamics of PP differ from that of the ABS and POM. At the high injection velocity, microimpression filling is not affected in the same way by the change of the cavity thickness and the difference between the time intervals (P1-T1) and (P1-T2) for DOE2, 4, 6 and 8 becomes quite small (Figure 52). It also has to be noted that the abnormality occurring at the ABS DOE6 injection run was not observed for the homologue set of processing conditions of PP and POM.

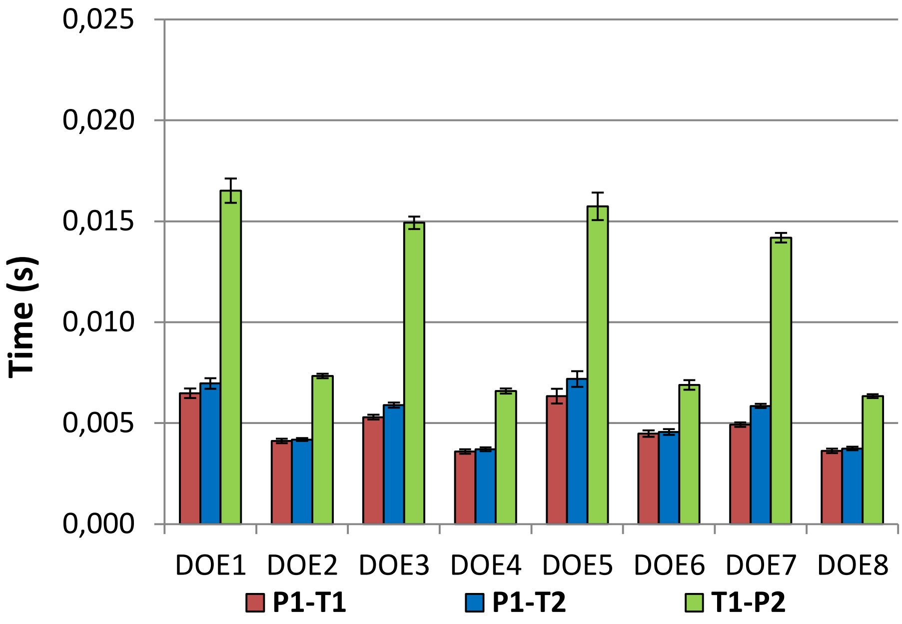

Figure 52 - Time intervals for flow front advancement between (P1-T1), (P1-T2) and (T1-P2) for PP.

As it can be seen in the Figure 32 and Figure 49a, the sensor T1 is equidistantly located, along the length of the microimpression, from the sensors P1 and P2. As the melt flows further from the gate, it keeps cooling and progressively flows more slowly. This was confirmed through comparison of the respective time intervals (P1-T1) and (T1-P2). For all injection runs, the time intervals (T1-P2) are longer than (P1-T1). The flow front delay 1 (FFD_1) is expressed as the ratio of the time intervals (T1-P2) and (P1-T1):

$$\mathrm{FFD}_1 = \frac{\mathrm{T1P2}}{\mathrm{P1T1}} \qquad \text{Equation 48}$$

The observation indicates that all polymers flow slower at the thinner section of the microimpression. In order to underline how the microimpression's thickness alter the polymer dynamics, an equation similar to Equation 48 was used to calculate the flow front delay 2 (FFD_2) and was given as the ratio of the time intervals (P1-T2) and (P1-T1):

$$\mathrm{FFD}_2 = \frac{\mathrm{P1T2}}{\mathrm{P1T1}} \qquad \text{Equation 49}$$

The comparison of FFD_1, shown in Table 5, suggests that regardless of the polymer injected (ABS, POM or PP), it cools drastically as the flow front advancement becomes approximately three times slower at low injection velocity (DOE1, 3, 5 and 7) and about twice slower at high injection velocity (DOE2, 4, 6 and 8). PP, however, appears to flow slightly faster than ABS and POM. Moreover, at low mould temperature, difference in the flow front advancement of the latter polymer is not so pronounced with the variation of the injection velocity.

Apparently, neither the mould nor melt temperatures seem to have any definite effect on the velocity of ABS, PP and POM, as it flows from the middle sections to the end of the micropart (FFD_1). In addition, for ABS at the processing conditions corresponding to DOE6 (Table 3), the interval T1-P2 (Figure 50) does not seem to fall into the pattern previously observed for the other injection runs at higher injection velocity. It was somehow longer indicating a slower velocity inside the microimpression. In order to understand the reason for this delay, it has to be compared with the peak cavity temperature at the same test conditions.

Table 5 - Flow front delays FFD_1 and FFD_2

Experiment Nº	FFD_1			FFD_2		
	PP	ABS	POM	PP	ABS	POM
DOE1	2,60	2,80	2,80	1,07	1,16	1,17
DOE2	1,80	1,90	2,20	1,02	1,13	1,18
DOE3	2,90	3,20	2,78	1,11	1,16	1,18
DOE4	1,90	2,00	2,58	1,03	1,11	1,15
DOE5	2,50	2,70	2,69	1,13	1,17	1,16
DOE6	1,60	2,90	2,09	1,02	1,13	1,18
DOE7	2,90	3,30	3,35	1,19	1,15	1,17
DOE8	1,80	2,10	2,13	1,03	1,14	1,19

A decrease of the microimpression’s thickness affects the flow dynamics of ABS and POM very distinctly and quite differently for each polymer (Table 5). FFD_2 of the PP shows a very clear dependence on the injection velocity which tends to be smaller at high injection velocity, when comparing to that at slow injection. FFD_2 of the ABS features only a slight decrease with faster injection, whilst neither the mould nor the melt temperatures appear to exert any influence. In the case of the POM, FFD_2 does not seem to vary with the change of the processing conditions in any definite fashion. The only conclusion which can be drawn with some degree of certainty is that, similarly to ABS and POM, the reduction of the moulding thickness favours the cooling of the melt and hence reduction of melt velocity.

5.2 Estimation of the µIM process variability

For each set of the injection moulding conditions, 35 microparts were obtained and respectively 35 sets of pressure and temperature data were recorded. Variability of the µIM process of ABS, PP and POM polymers was calculated with Equation 31 through the eight combinations of the controlled parameters presented in Table 2. The results of the calculations are summarized in Table 6, where the higher percentage means less process variability. PP was found out to be less susceptible to variability at the tested processing conditions with the acceptance ratio between 94% and 100%, while µ-parts moulded from ABS showed lower rate of acceptance (71%-94%). Even more difficulties were encountered during micromoulding of POM where the ratio of acceptable parts varies between 66% and 91%. Although it is not easy to discern any definite trend in µIM variability, the latter seems to decrease at high injection velocity.

Bering in mind that the mould temperature for all tested polymers was varied in the range well below the transition temperature of the polymer, such low percentage of acceptance for ABS and POM may suggest that for the given microimpression's geometry the mould temperature is too low and should be maintained above the transition temperature of the polymer to prevent premature solidification. It appears, however, that PP may be successfully moulded with the mould temperature at the upper level of the conventional range, high injection velocity and/or high melt temperature (DOE6, 7 and 8).

Table 6 - Acceptance ratio of ABS, PP and POM microparts

Experiment Nº	Number of cycles				Acceptance ratio (%)		
	Recorded (ABS, PP, POM)	Filtered (ABS)	Filtered (PP)	Filtered (POM)	ABS	PP	POM
DOE1	35	31	33	29	89	94	81
DOE2		33	34	33	94	97	92
DOE3		26	34	25	74	97	70
DOE4		29	34	32	83	97	91
DOE5		31	33	24	89	94	68
DOE6		29	35	32	83	100	91
DOE7		28	35	23	80	100	66
DOE8		32	35	28	91	100	80

5.3 Assessment of the cavity temperature

5.3.1 Peak cavity temperature

Figure 53, Figure 54 and Figure 55 show the ABS, PP and POM peak cavity temperatures from DOE1 through DOE8. In order to minimize the measurement error, for PP and ABS the averaged values of the peak cavity temperatures over 25 injection moulding cycles were used for analysis, while for POM only the data of 23 cycles were considered due to higher rejection rate.

As expected, the peak cavity temperature reflect the low (DOE1-DOE4) and high (DOE5-DOE8) mould temperature set-up. For ABS and PP, the peak cavity temperature at the thicker section is higher than at the thinner one in all eight injection moulding runs, reflecting the faster melt solidification as the cavity thickness decreases.

During the injection of ABS (Figure 53), there is a slight increase in the peak cavity temperature as the injection velocity rises, probably caused by the shear heating effect (DOE2, 4, 8). This effect seems to be more prominent in DOE2, when the melt and mould temperatures were at the lowest levels. With higher mould temperature, low melt temperature and high injection speed (DOE6) the peak cavity temperature at the thicker section (300µm) was slightly lower than for DOE5 with the same melt and mould temperature but slower injection velocity. This observation corroborates the time intervals data in Figure 50 and in Table 5, where the longer time interval of DOE6 are likely to be connected to the lower peak cavity temperature and, therefore, higher polymer viscosity. Altogether, it may be an indication of external disturbances in the µIM process.

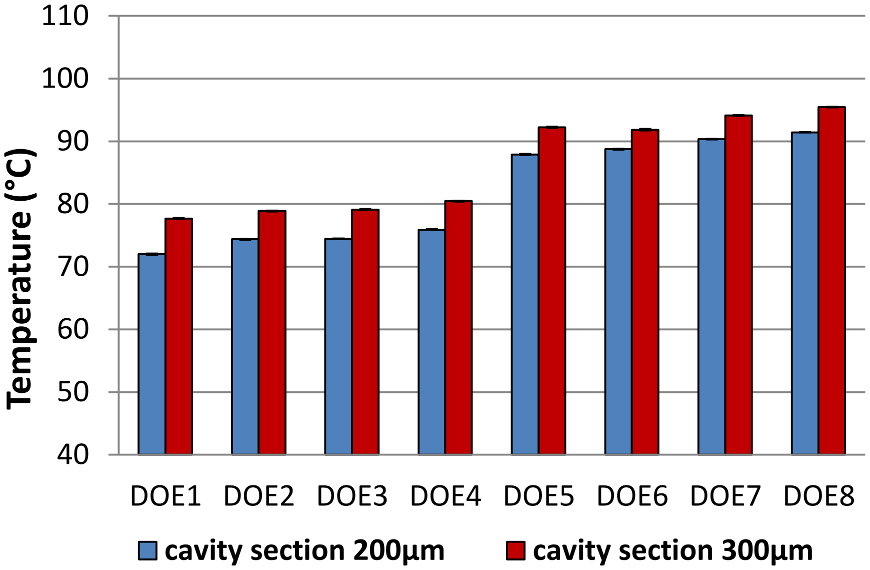

Figure 53 - Peak cavity temperatures at the micropart sections of 200µm and 300µm (ABS)

An increase of the peak cavity temperature associated with a higher injection velocity was also observed in the DOE2 injection run of PP (Figure 54). However, for the other combinations of the processing conditions, the injection velocity does not seem to affect the peak cavity temperature of PP in any definite manner. In addition, the influence of the melt temperature was not confirmed for any combination of the processing conditions.

Similarly to ABS and PP, the peak cavity temperature at the thinner section of POM was found out to be lower than at the thicker one from DOE1 through DOE6 (Figure 55). However, when the melt temperature and mould temperature are at the upper level regardless to the injection velocity, the difference in the peak cavity temperature becomes almost imperceptible (DOE7 and 8). This observation in conjunction with the data presented in tables Table 5 and Table 6 suggest that at these processing conditions, the µIM process becomes less stable. Neither the melt temperature nor the injection velocity appear to affect the pattern of the peak cavity temperatures of POM.

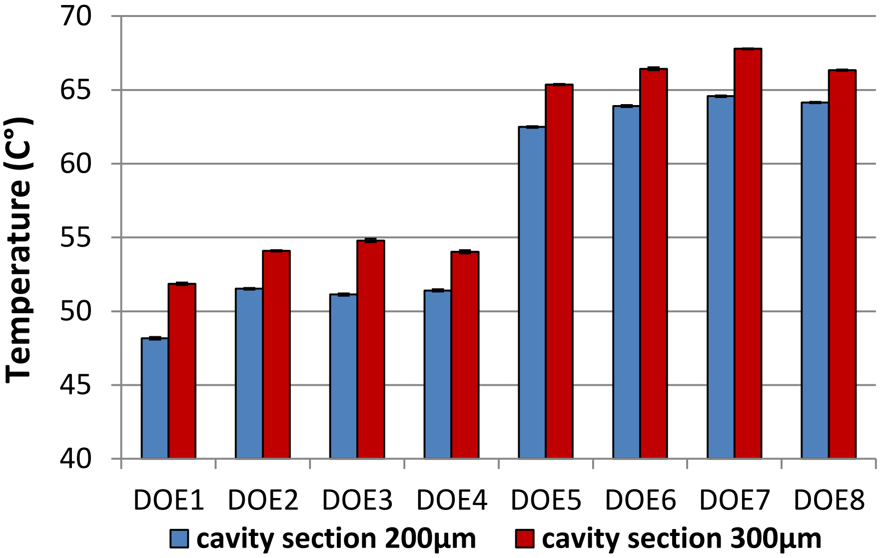

Figure 54 - Peak cavity temperatures at the micropart sections of 200µm and 300µm (PP)

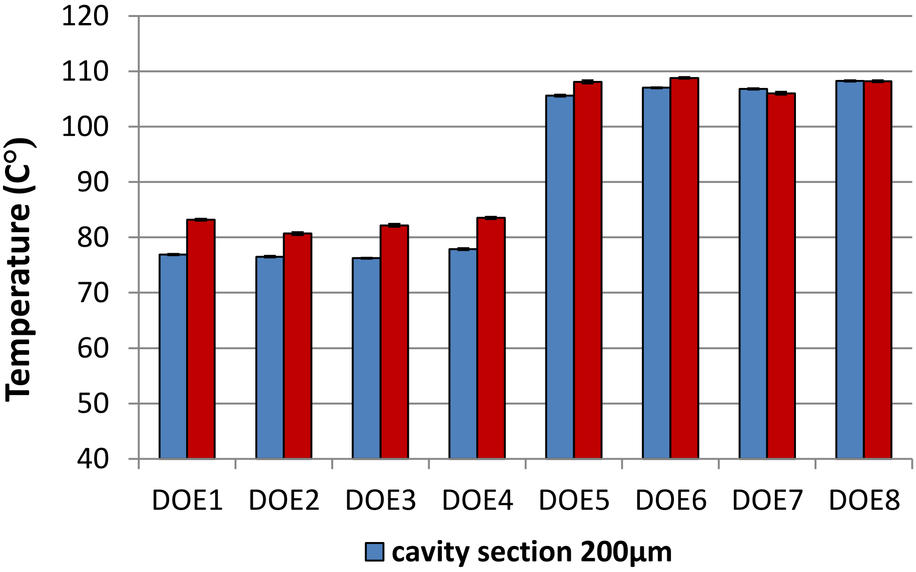

Figure 55 - Peak cavity temperatures at the micropart sections of 200µm and 300µm (POM)

5.3.2 Signal-to-Noise (SN) Ratios

Higher values of the SN ratio mean that the influence of the input signal (controlled processing parameter) is higher than the disturbances of the experiments. The results of the SN ratio calculations are summarized in Figure 56Figure 58 for the ABS, PP and POM polymers, respectively. The highest value of the SN_{lb} response for each factor indicates the best combination of parameters for the maximum cavity temperature. As it has already been referred above, the peak temperatures were found out to be higher at the 300µm section, which also corresponds to the higher SN values and higher polymer fluidity at those locations. Moreover, regardless of the section's thickness, for all the polymers tested the highest peak cavity temperature is achieved with the controlled factors at the upper levels.

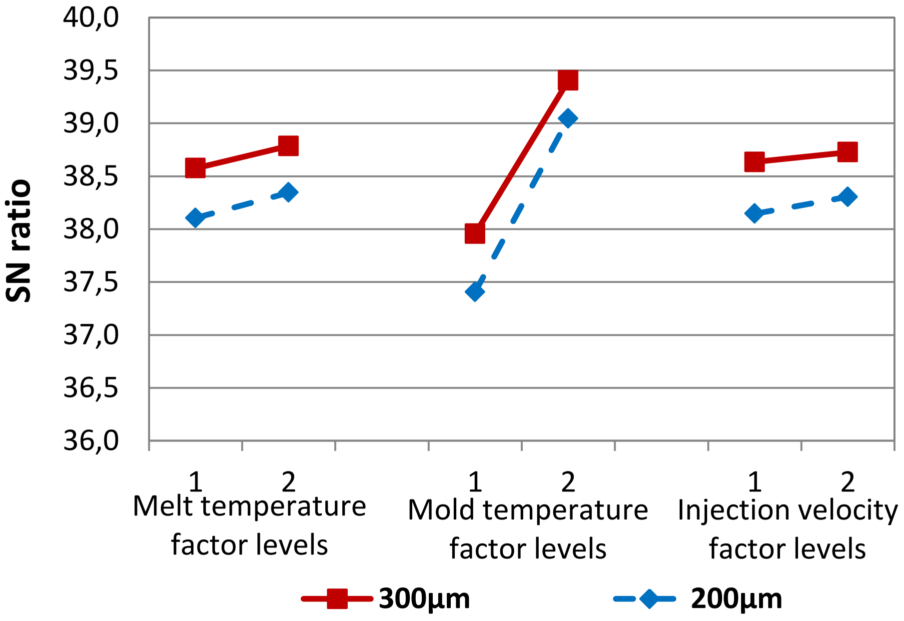

Figure 56 - SN response for the ABS peak cavity temperature.

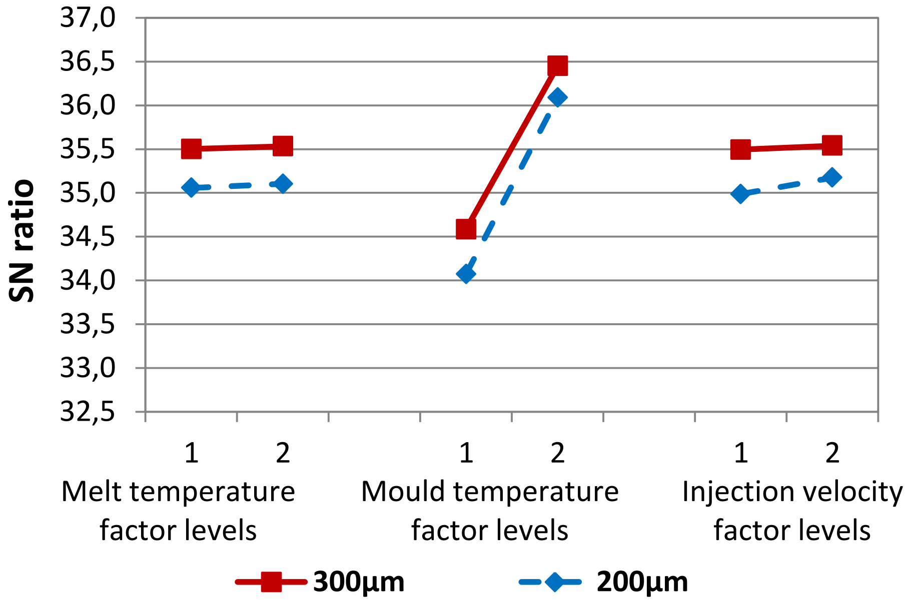

Figure 57 - SN response for the PP peak cavity temperature.

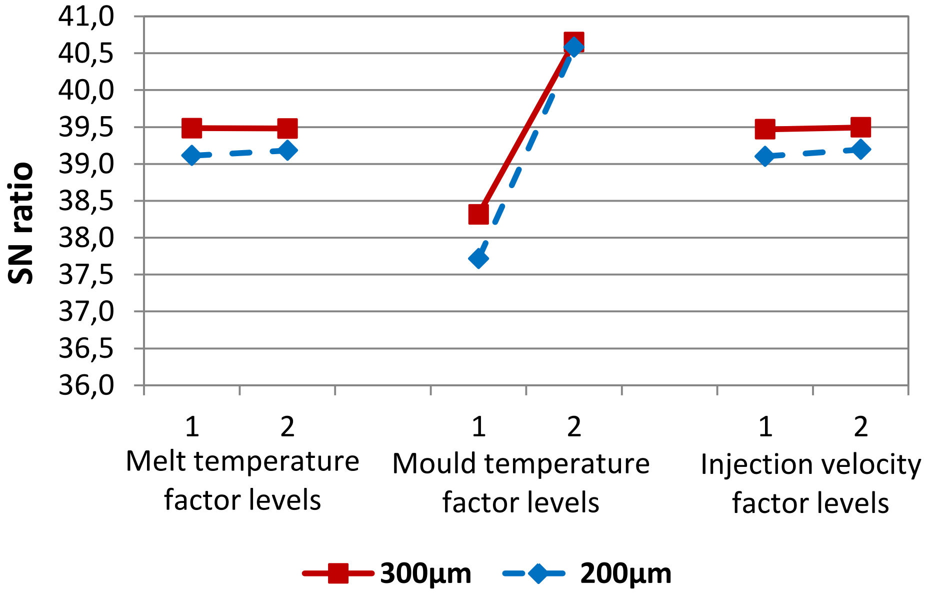

Figure 58 - SN response for the POM peak cavity temperature.

Differences between the SN ratio maximum and minimum levels (Figure 59, Figure 60 and Figure 61) convey more detailed assessment of each factor influence on the peak cavity temperatures of ABS, PP and POM, at both 200µm and 300µm sections. As presented in Figure 59, Figure 60 and Figure 61, the difference in levels highlights the mould temperature as the most influencing factor for the peak cavity temperature of all the polymers tested, being however more significant at the thinner section (200µm). The melt temperature appears to have a very similar, but lower effect on the peak cavity temperature of ABS. The injection velocity seems to exert less influence in comparison to the other control factors. However, its significance is almost doubled at the thinner section. Contrary to the observed for ABS, the second significant factor for PP (Figure 60) at the thinner section was not the melt temperature but the injection velocity, while for the thicker section its effect was barely visible. When comparing to the other control factors, the melt temperature does not appear to affect the peak cavity temperatures of PP (Figure 60) and POM (Figure 61).

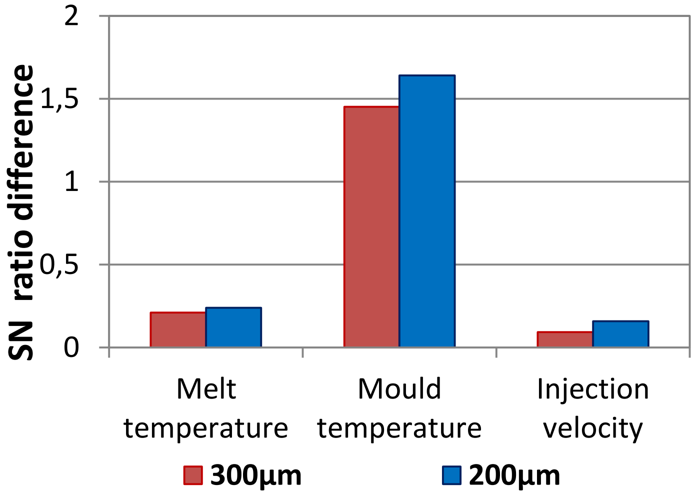

Figure 59 - SN difference for the peak cavity temperature at 300µm and 200µm sections (ABS).

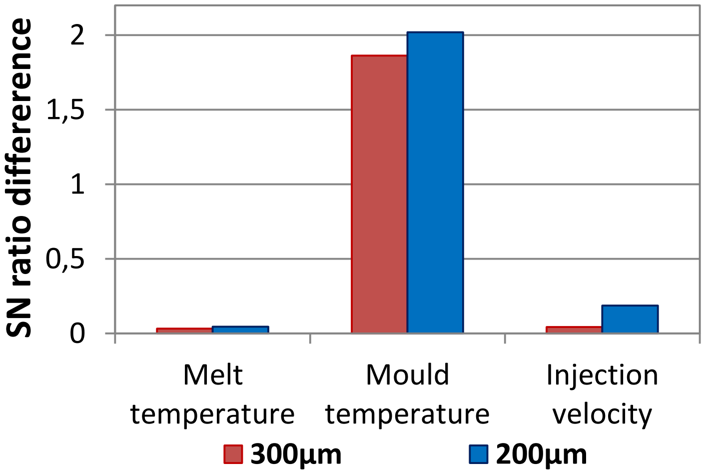

Figure 60 - SN difference for the peak cavity temperature at 300µm and 200µm sections (PP).

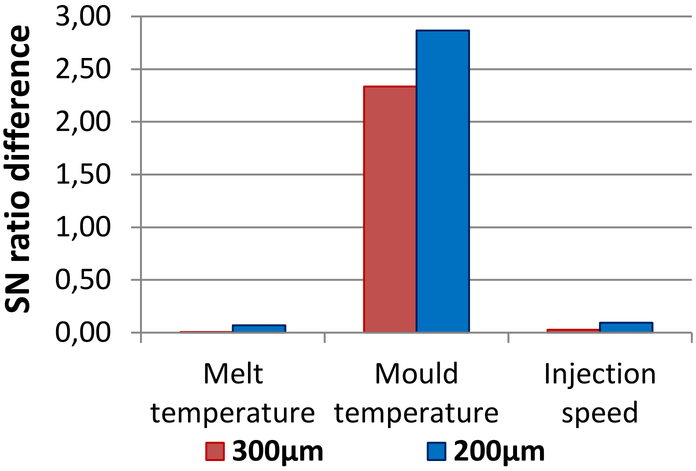

Figure 61 - SN difference for the peak cavity temperature at 300µm and 200µm sections (POM).

5.4 Assessment of weld line position and width

5.4.1 ABS

Figure 62 shows a micrograph of the weld line fragment in the ABS micropart moulded with the DOE5 processing conditions (Table 2), where its shape and position is clearly visible under a magnification of 5.

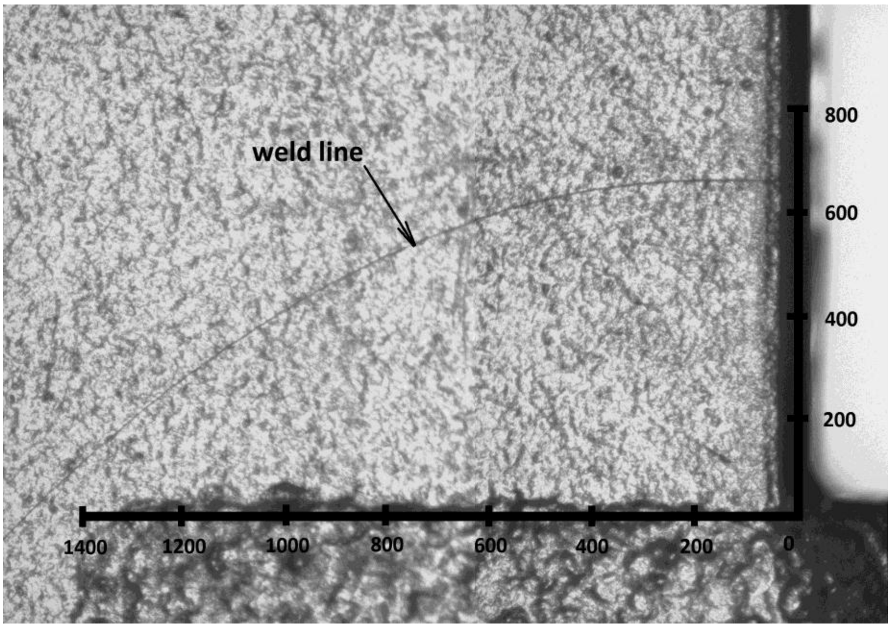

Figure 62 - The micrograph of the weld line fragment of ABS observed by optical microscopy (DOE5)

The weld line position was visualized and assessed according to the methodology previously described in section 3.7. As shown in Figure 63, the fragments of the weld lines seem to cluster in 2 groups and clearly show the influence of the injection velocity on the weld line position. The first group encompasses the weld lines obtained at low injection velocity (processing conditions DOE1, 5, 3 and 7) and one weld line fragment obtained, at high injection velocity (DOE6). They are unevenly spaced and located nearer the interior corner of the micropart i.e. the origin of measurement. The second cluster includes all the remaining weld line fragments, i.e. of the microparts moulded at high injection velocity (DOE2, 4 and 8), located further from the zero point and spaced more closely. This observation supports the data collected on the ABS dynamics in section 5.1 (Table 5 and Figure 50) where at high injection velocity reduction of the polymer viscosity was attributed to the shear heating effect counteracting this way the flow front delays due to the thickness variation resulting in more advanced weld line position. It also has to be noted that weld line at DOE6 setup (solid line) overlaps that of the DOE7 (black dashed line). This occurrence is likely to be attributed to the external disturbances in the µIM process and explained earlier in the sections 5.1 and 5.3.1.

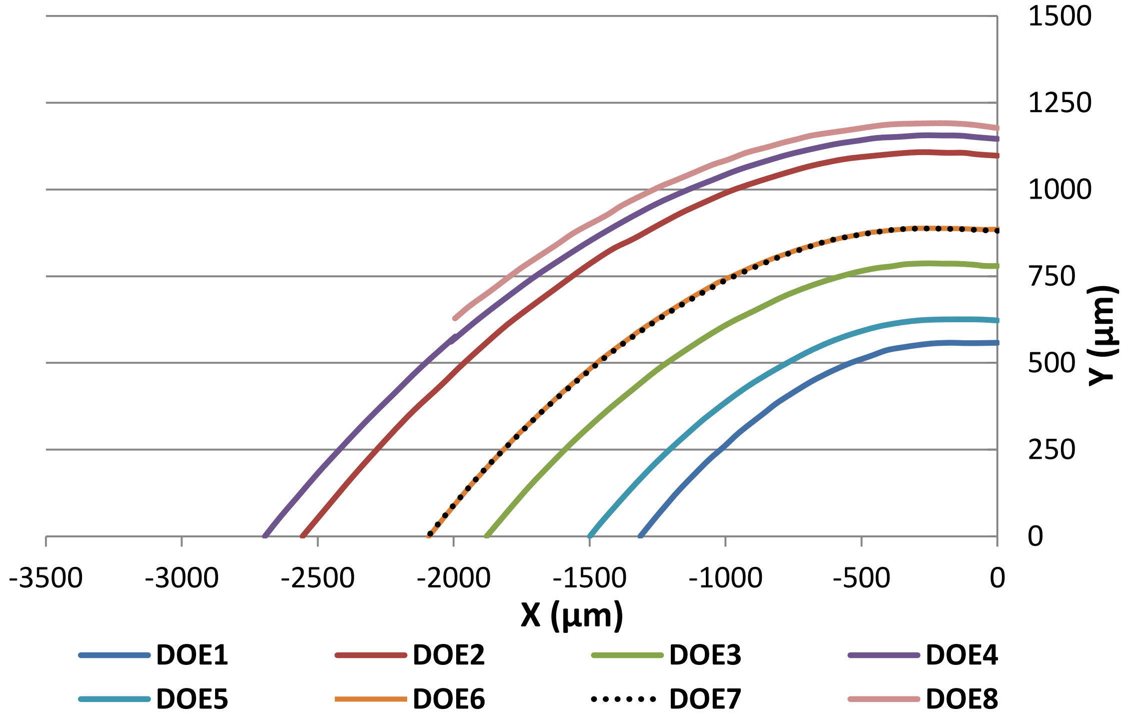

Figure 63 - Fragment of the averaged weld line location of ABS from DOE1 up to DOE8 experimental setups

In addition, melt temperature appears to exert greater influence on the polymer viscosity than the tested range of the mould temperatures. This was observed equally for the weld lines obtained at both low and high injection velocities, as the weld line positions with the lower melt temperature setups were always preceded those of the microparts moulded at high melt temperature. This difference becomes more even more evident for the microparts moulded at low injection velocity. For example, the weld line at DOE3 setup (high T_{melt} and low T_m) is more advanced than DOE5 (high T_m and low T_{melt}) on 380μm in X direction and 158μm in Y direction (Figure 63). It also has to be noted that the weld lines of the microparts moulded with the controlled parameters at high levels (DOE8) become less distinguishable and impossible to trace entirely through the area under the observation and therefore only a visible segment was shown in Figure 63. After consulting the temperature data at these conditions (Figure 53), it was evident that the highest values of the peak temperatures were correlated with the low values of the FFD_1 and FFD_2 from Table 5, altogether indicating better polymer fluidity at the end of filling. Therefore the above mentioned difficulties in visualization may be attributed to the better interfusion of the flow fronts and eventually superior weld line quality.

The overall influence of the injection moulding processing conditions on the weld line position was summarized by applying the SN ratio (larger-the-better) criterion Equation 32, previously used for the analysis of the peak cavity temperature. Considering the implicit asymmetry of the weld line position (Figure 49), the more advanced weld line position from the zero point clearly suggests a decrease in polymer viscosity. The latter being the reason why, the more distantly located weld line coordinate in Y direction (Figure 63) was chosen as a quality signature. SN ratio difference between the maximum and minimum levels of the experimental output was considered as a measure of influence of each controlled factor on the weld line position. As shown in Figure 64a and 64b, the weld line position is affected by the injection moulding processing conditions in the following order of importance: V_i, T_{melt} and $T_{m.}$ These results appear to be in good agreement with the data of polymer dynamics, presented in section 5.1 (Figure 50 and Table 5). It is also worth noting that influence of the tested range mould temperature on the weld line position is almost non-existent.

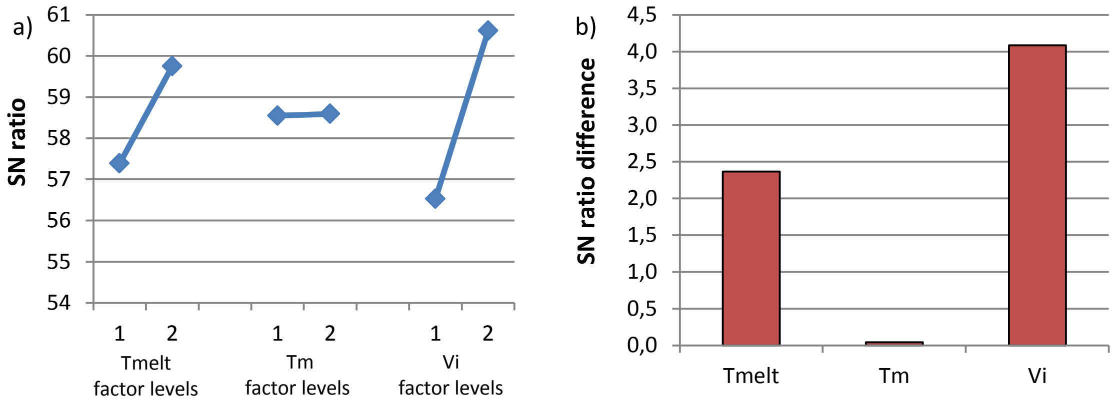

Figure 64 - ABS: a) SN response for the maximum weld line position, b) SN ratio difference of the maximum weld line position

The averaged weld line width in ABS microparts, presented in Figure 65, vary from 2.8 to 5.6µm. The thickest weld line was observed in two setups: first, with all controlled parameters at the low levels (DOE1) and second, with low T_m, V_i and high T_{melt} (DOE3). It suggests that flow front temperature during the weld line formation is quite low and hence the weld line strength is weaker. As expected, high levels of the V_i, T_{melt}, and T_m result in thinner weld line (DOE8). The similar correlations were reported by Wu *et al.* [37] for the weld line width in PP and HDPE micro tensile specimens.

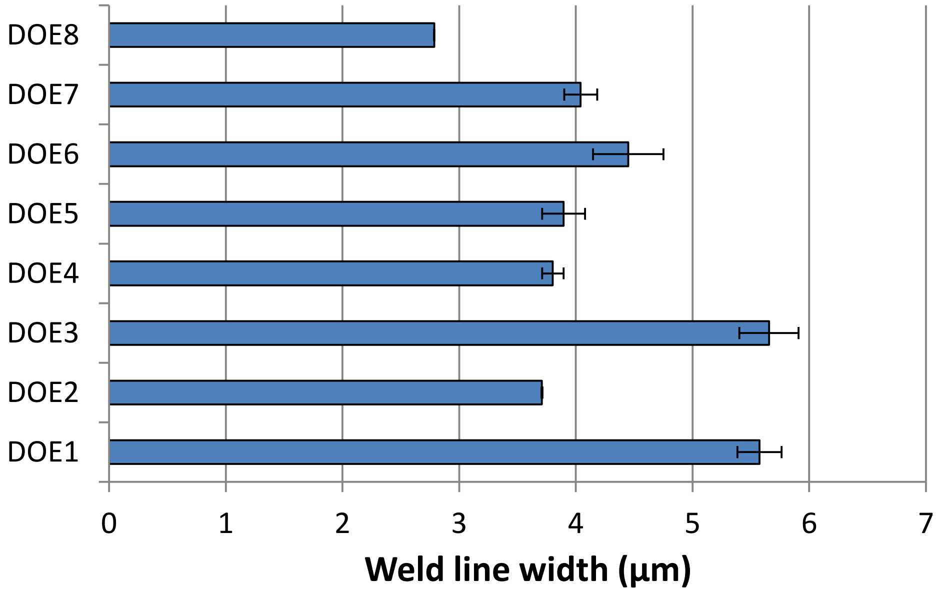

Figure 65 - Weld line width in ABS microparts

Apart from these extreme cases, it did not seem possible to trace any definite trend about the influence of the injection moulding processing conditions on the weld line width by mere observation

To cope with this problem, SN_{sb} (smaller-the-better) ratio was used to correlate the deviation of the quality characteristic (minimum weld line width) from the desired value. SN ratios were calculated according the Equation 33 and their respective values were shown in Figure 66a and Figure 66b. SN ratio response (Figure 66a) confirmed the data depicted in Figure 65 indicating that the weld line thickness tends to decrease with an increase of the controlled parameters. In addition, the difference between high and low SN ratios (Figure 66b) supplies additional information about how much each controlled factor is likely to influence the weld line thickness . The main factor affecting the weld line width of ABS microparts was the injection velocity while the mould temperature effect was less significant. Melt temperature appears to have only a slight effect.

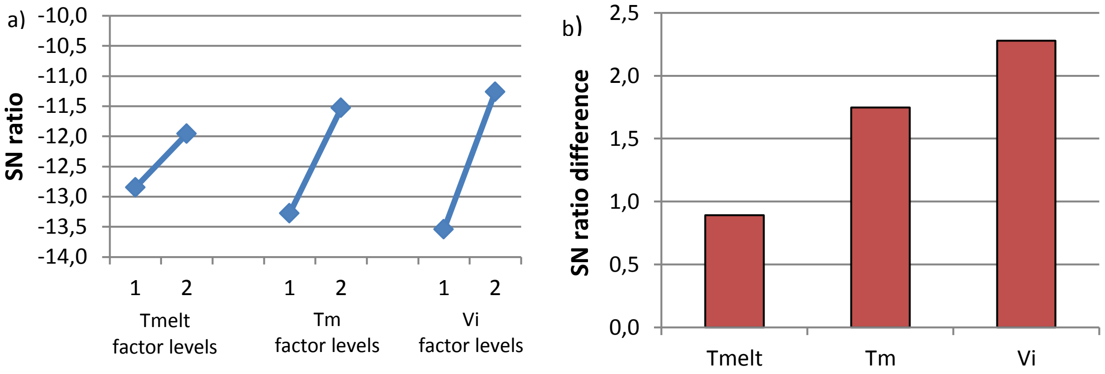

Figure 66 - ABS: a) SN response for the weld line width, b) SN ratio difference of the weld line width

5.4.2 POM

Similarly to ABS, the same fragment in POM microparts was used for assessment of the weld line position (Figure 67). The averaged weld line positions from DOE1 through DOE8 can be depicted from Figure 68. Weld lines position seems to depend primarily on the injection velocity. The weld lines, most closely located to the zero point, were obtained at low injection velocity, low mould temperature, either low (DOE1) or high melt temperature (DOE3). At the same time, the weld lines generated at high injection velocity, high mould temperature, or either low (DOE6) or high (DOE8) melt temperature, were the most distantly located from the origin of measurements.

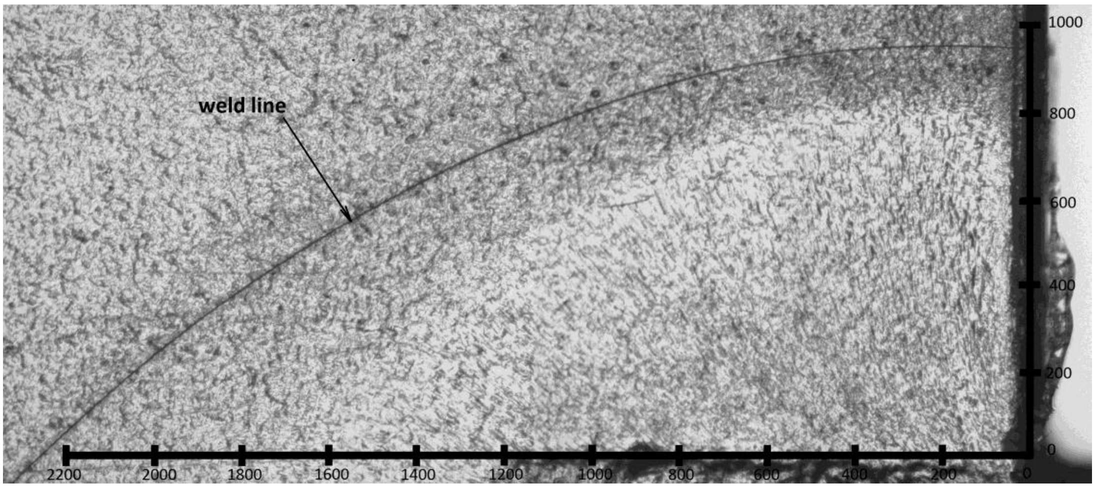

Figure 67 - The micrograph of the weld line fragment of POM observed by optical microscopy (DOE1)

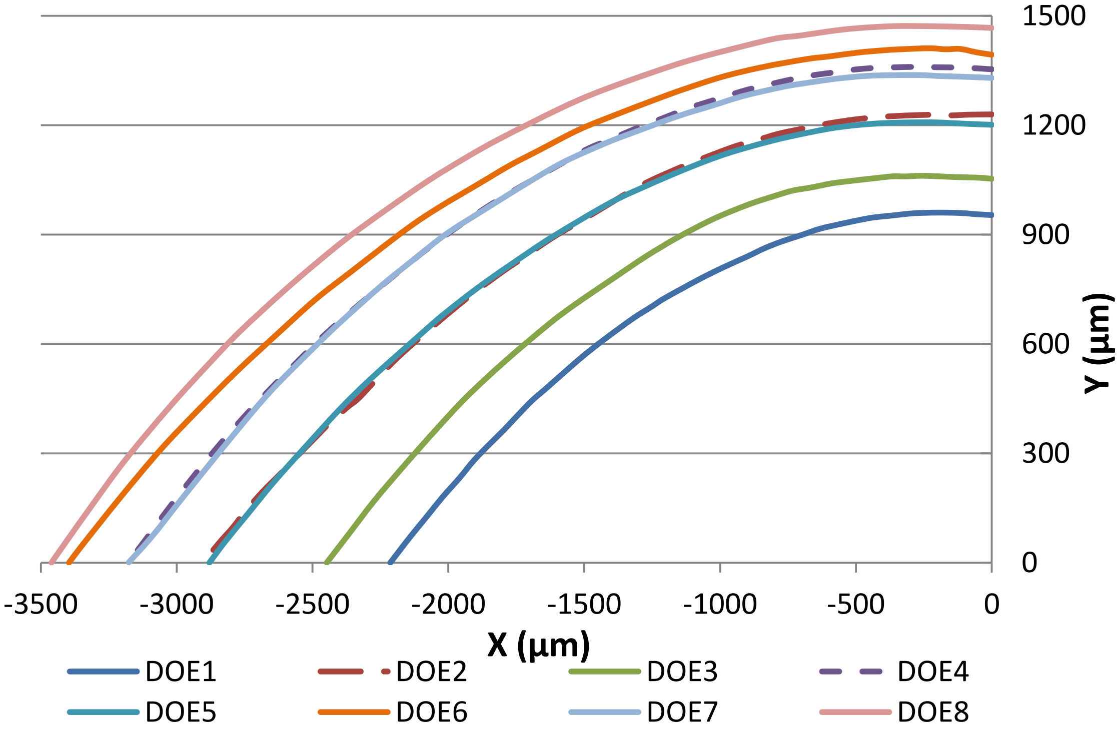

Figure 68 - Fragment of the averaged weld line location of POM for the range of experimental setups

It is clearly visible from Figure 68 that the two pairs of the weld lines overlap each other. First, the weld line (solid line) in DOE5 microparts moulded with low T_{melt}, V_i and high T_m was almost overlapped by the one (dashed line) in DOE2 microparts (low

T_{melt}, T_m and high V_i). Another pair of weld lines, located progressively further, in DOE7 (high T_{melt}, T_m and low V_i) and DOE4 (high T_{melt}, V_i and low T_m) microparts were quite superimposed too. Comparison of these processing conditions shows certain resemblances between these two cases suggesting that the effect of the mould temperature on the polymer fluidity at the end of filling may be roughly the same as that of the injection velocity leading to the weld lines superposition. Moreover, this observation seems to be equally valid for either low (DOE5, DOE2) or high (DOE7, DOE4) melt temperatures. SN ratios of POM show a similar tendency to ABS in what concerns an apparent dependence of the weld line position on the experiment controlled factors (Figure 69a). A more advanced weld line position corresponds to higher values of T_{melt}, V_i and T_m suggesting an improvement of the polymer fluidity at the thinner section of the micropart. Figure 69b shows the order of importance of each controlled factor on the weld line position. Similarly to the data observed for ABS, the injection velocity continues to be the most critical factor likely to affect the weld line position. The second factor, contrary to that observed for ABS microparts, was the mould temperature, whilst the melt temperature was found out to be the less significant.

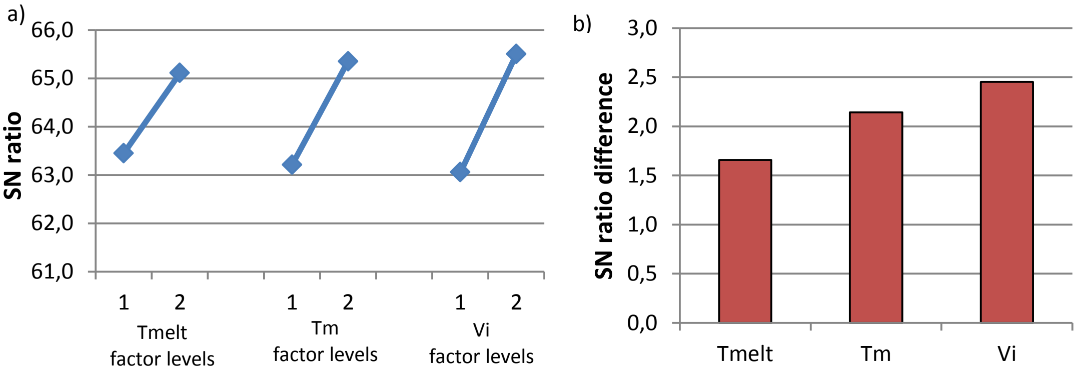

Figure 69 - POM: a) SN response for the maximum weld line position, b) SN ratio difference of the maximum weld line position

The weld line widths in POM microparts were found out to be quite similar to those in ABS varying between 2.9 up to 5.2µm (Figure 70). The SN ratio analysis was applied for correlation of the weld line severity with variation of the injection moulding processing conditions. The results, depicted in Figure 71a, indicated that the weld line width decreases with an increase of the controlled factors. SN ratio differences (Figure

71b) highlighted the prime influence of the mould temperature on the reduction of the weld line width in POM microparts. The injection velocity seemed to affect the weld line width slightly less and the melt temperature influence did not appear significant.

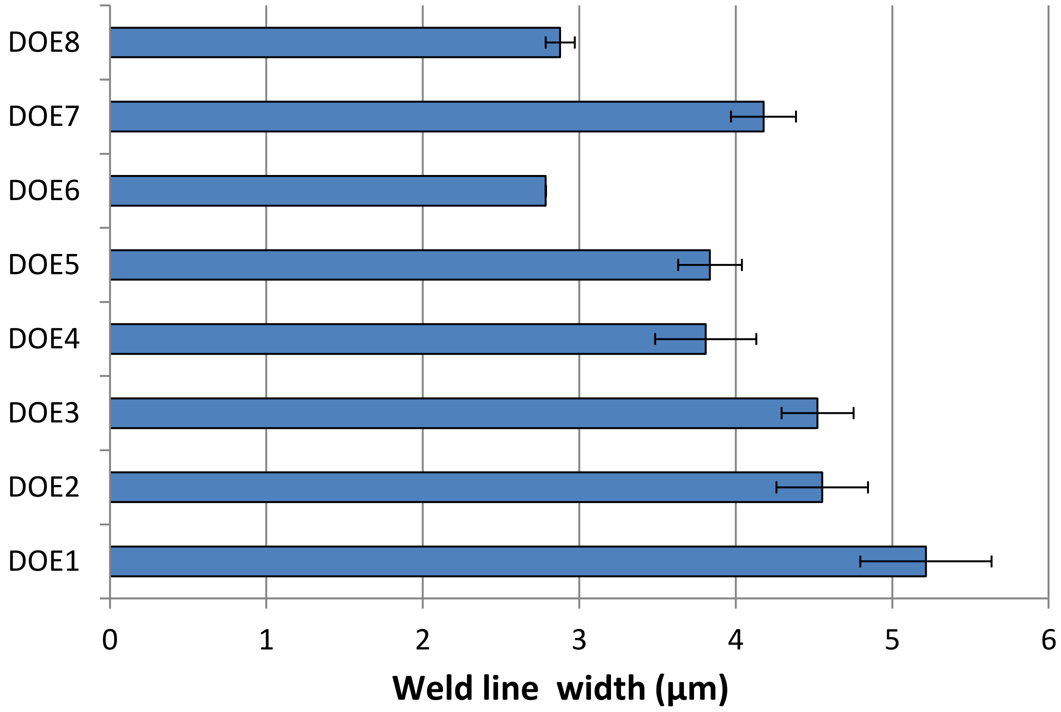

Figure 70 - Weld line width in POM microparts

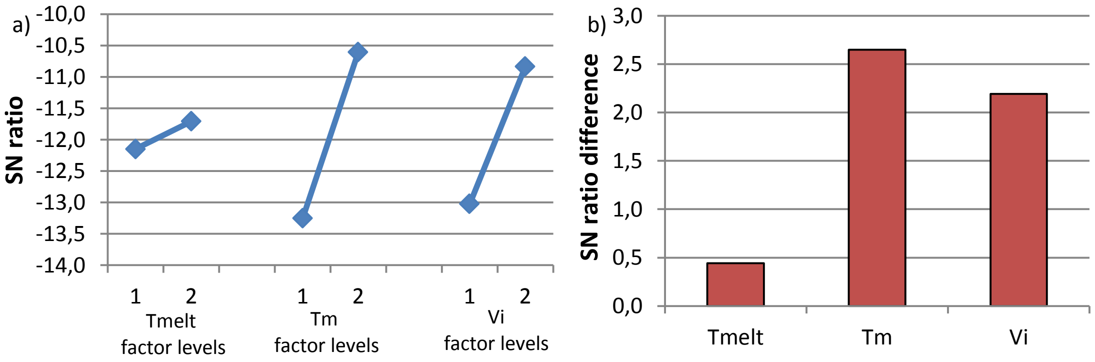

Figure 71 - POM: a) SN response for the weld line width, b) SN ratio difference of the weld line width

5.4.3 PP

The weld line positions in PP microparts were obtained by PLM (Figure 72). Unlike the micrographs, acquired by OM, the PLM weld line image is somewhat blurry, yet quite distinguishable. Variation of the weld line positions in Figure 73 bear some resemblance with the pattern observed for ABS in Figure 63. It suggested that the injection velocity plays a predominant role in the weld line positioning. It also indicated that at low injection velocity, the melt temperature seems to surpass the mould temperature influence as the weld line of DOE5 (high T_m and low T_{melt}, V_i) precedes the weld line in DOE3 micropart (high T_{melt} and low T_m, V_i). However, the latter conclusion has to be considered in connection with the fact that the mould temperature was varied in a range below the transition temperature. At faster injection, predominance of the melt temperature over the mould temperature was not detected which, as demonstrated in Figure 73, led to the overlapping of the weld lines of DOE4 (high V_i, T_{melt} and low T_m) and DOE6 (high T_m, V_i and low T_{melt}).

Influence of the other controlled factors can be better perceived from the Figure 74. SN differences suggest that the more advanced weld line position were achieved when the V_i, T_{melt} and T_m were at high levels which may indicate slower cooling rate and hence better polymer fluidity at this combination of the processing conditions. Injection velocity was by far the most influential factor followed by the melt temperature and the mould temperature. The influence of the latter was found out to be quite small in the tested range.

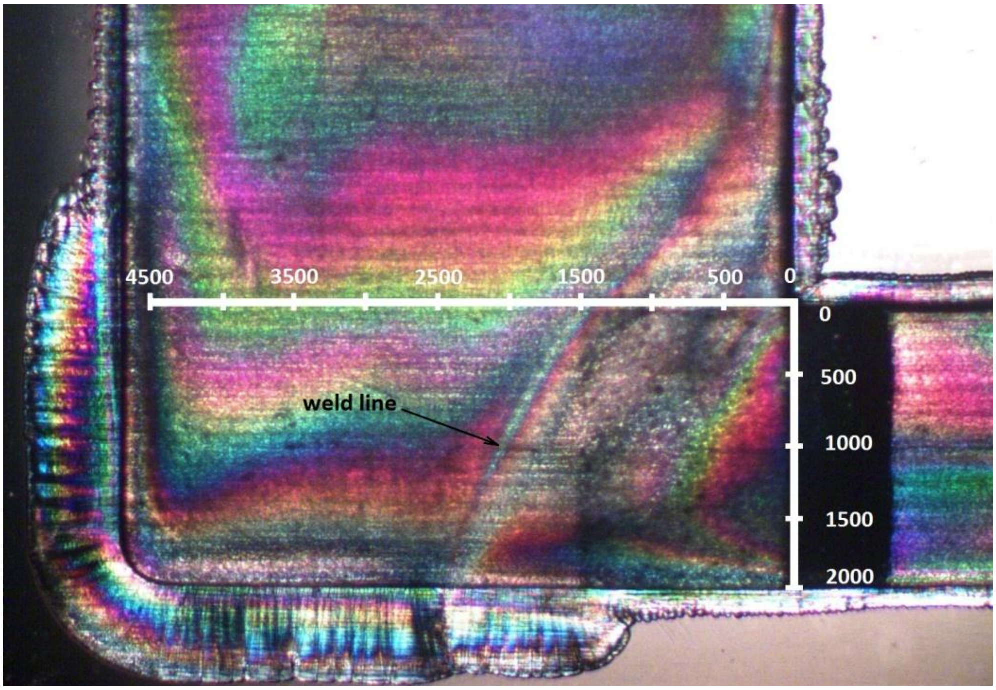

Figure 72 - The micrograph of the weld line of PP observed by polarized light microscopy (DOE1)

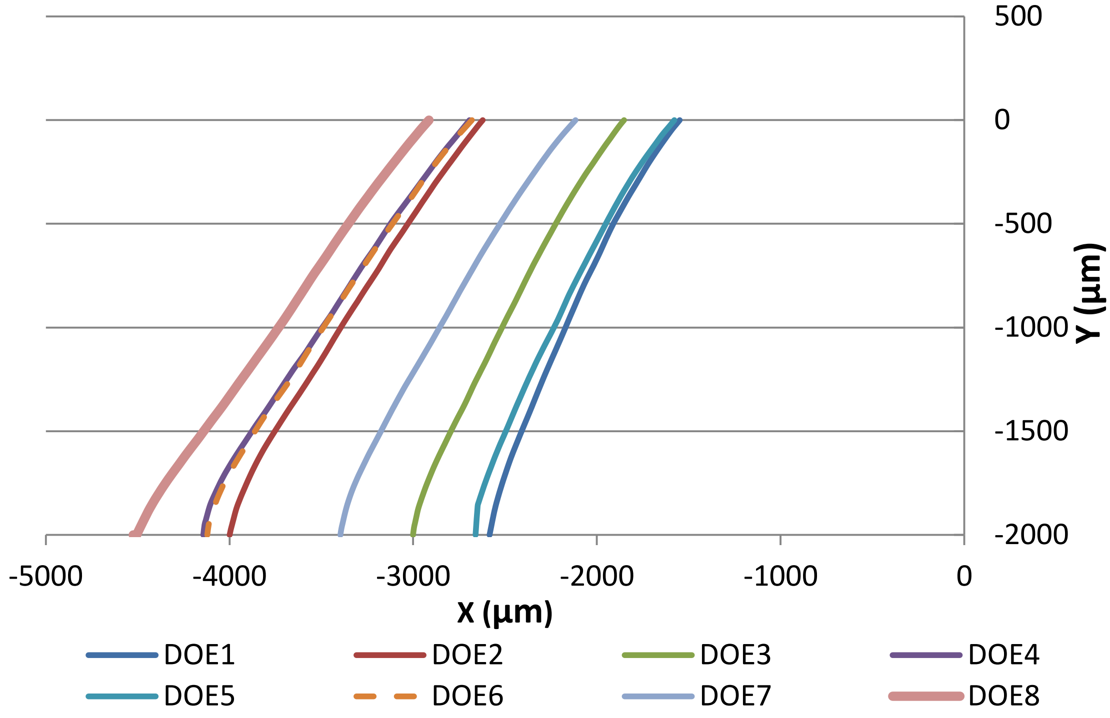

Figure 73 - Fragment of the averaged weld line location of PP for the range of experimental setups

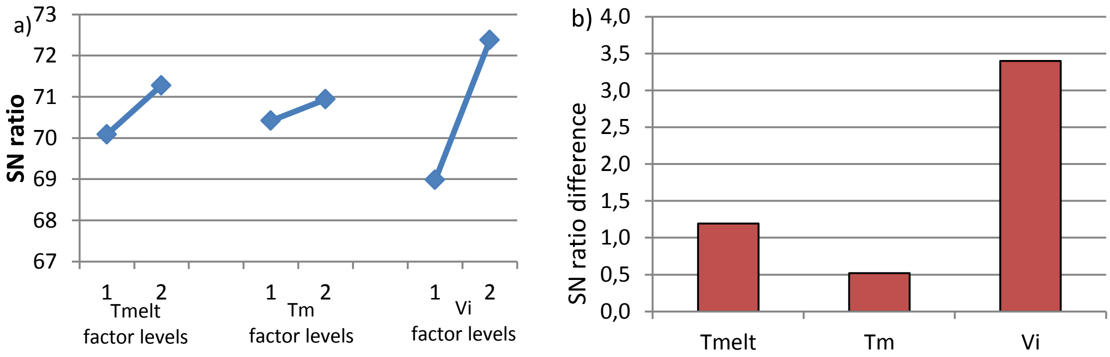

Figure 74 - PP: a) SN response for the maximum weld line position, b) SN ratio difference of the maximum weld line position

5.5 Autodesk Moldflow Insight® (AMI) numerical simulations

5.5.1 Finite element mesh and prediction accuracy

Three types of mesh, previously described in subsection 4.1, have been tested in order to ascertain the influence of the finite element mesh discretization on the polymer flow pattern in the microimpression. Filling and packing simulations have been carried out for PP duplicating the DOE4 setup. Weld line shape and position were adopted as a quality signature of the tested finite element meshes. Weld line shape and position of a randomly chosen (DOE4) micropart has been inspected and compared with those predicted by the AMI® (Figure 75).

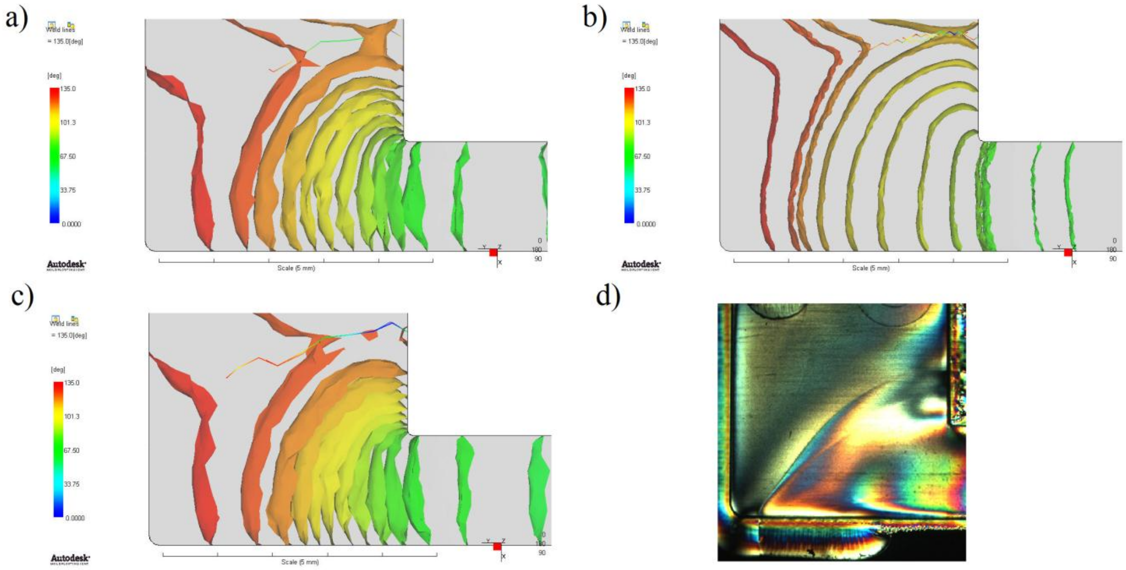

Figure 75 - Numerical prediction of weld line location: a) MDL/AMI mesh prediction (6 layers through the thickness), b) Hypermesh/Mouldflow mesh (6 layers through the thickness), c) MDL/AMI prediction (8 layers through the thickness), d) weld line PLM micrograph

The weld line micrograph (Figure 75d) shows where the two flow fronts met. The AMI® algorithm used to visualize the weld formation is based on the meeting angle criteria of converging flow fronts. If the meeting angle is less than 135°, a weld line will form and hence will be reproduced graphically. In order to show the flow pattern in the microimpression (Figure 75a, Figure 75b and Figure 75c), the weld line image was overlaid with the fill time result, where each contour represents the time frame. Meanwhile, as it can be seen, the weld line shape and position were predicted only partially. However, the start of the weld line at the inner side of the part was predicted with reasonable accuracy in all three cases. The most dissimilar results were obtained for the two meshes generated by AMDL (Autodesk Moldflow Design Link) where the weld line follows a direction (Figure 75a and Figure 75c) that diverges from that observed experimentally. In the case of the more uniform fine mesh, pre-processed by the Hypermesh module, the start of the weld line shape follows more closely the real case scenario with the flow front convergence almost identical to the experimental

(Figure 75b). It confirms the general trends discussed in section 5.4. An optimized mesh presented a reasonable agreement in weld line shape and also confirms the flow front delay originated by the restriction in the microimpression’s thickness and therefore was adopted for further simulations. Nevertheless, the predicted weld line position seems to overestimate progress of the polymer flow at the thinner section of the microimpression (Figure 75d). The discrepancies between the experimental and predicted data will be addressed in the next section dedicated to the parametrical AMI® simulations, carried out with the optimized finite element representation of the micropart and feeding system.

5.5.2 Comparison of the experimental and predicted polymer dynamics

Eight numerical simulations of filling, packing and warpage were conducted for PP, POM and ABS using the experimental ram speed (mm/s) vs. ram position (mm) (Table 2, page70), which gives a total of 24. To compare experimentally predicted polymer’s dynamics with the simulated one, the predicted time intervals were calculated from the Fill Time Path Plot (Figure 76), from which the exact times of polymer flow passing each sensor may be exported as a text file. The dots on the micropart (Figure 76) are the mesh nodes equivalent to the centre points of the pressure and temperature sensors: P1 - N 29484, P2 - N 28214, T1 - N 14610, T2 - N 15632. Their locations on the 3D mesh are shown in Figure 77a for temperature sensors and in Figure 77b for pressure sensors. Predicted time intervals were further compared with the experimental time intervals P1-T1, P1-T2 and T1-P2.

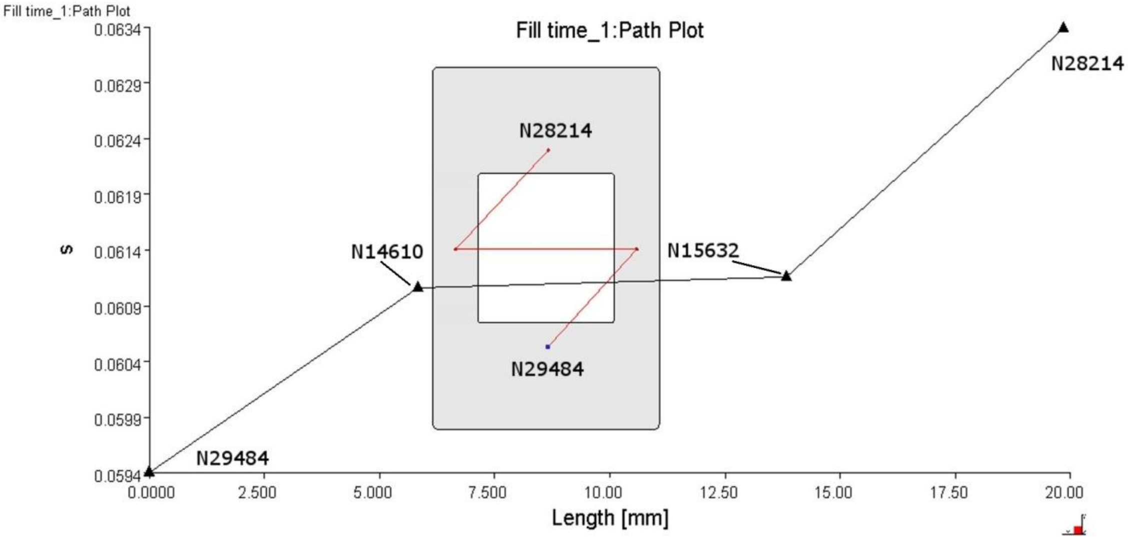

Figure 76 - PP DOE2- Fill Time Path Plot

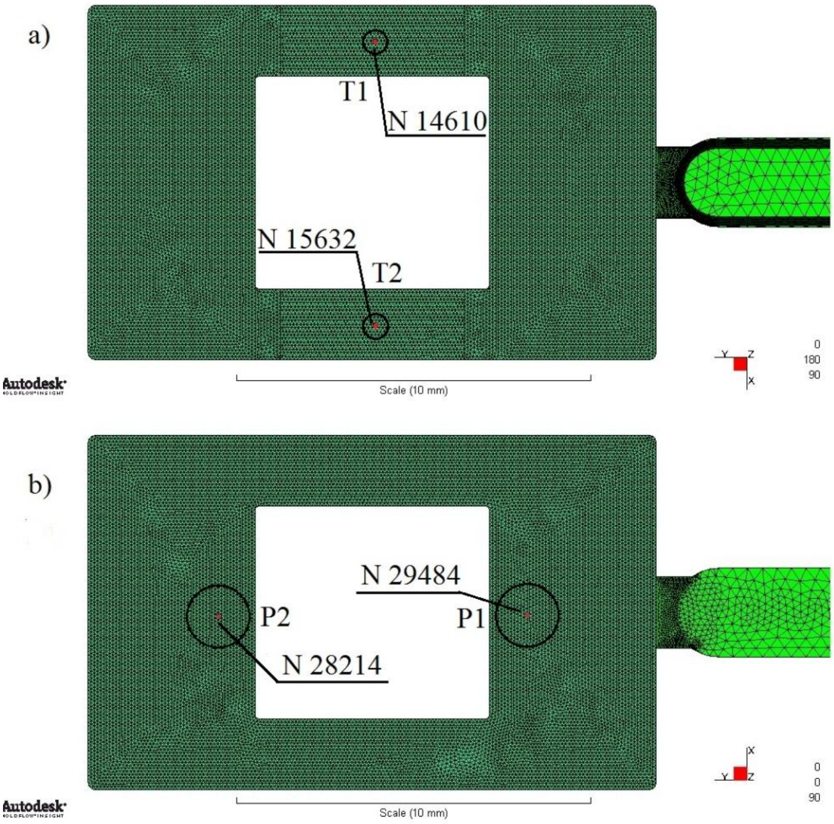

Figure 77 - Mesh nodes equivalent to the sensors locations: a) ejection side - temperature sensors T1, T2; b) injection side – pressure sensors P1, P2

A ratio between the experiment time intervals P1-T1, P1-T2 and T1-P2 and those predicted numerically was adopted as a criterion for prediction accuracy and was accomplished by a division of the experimentally obtained time intervals by their predicted values. Three accuracy criteria (AC) AC_{P1-T1}, AC_{P1-T2} and AC_{T1-P2} have been established. When this ratio is equal to one, the maximum accuracy is achieved meaning that the predicted time interval matches completely the experimental one. A greater value than one indicates filling faster than the experimental one and the inverse scenario implies slower filling than experimentally obtained one.

As it can be seen from Table 7, the time intervals predicted by AMI® for PP were overestimated and AC_{P1-T1}, AC_{P1-T2} and AC_{T1-P2} values vary between 1.63 and 3.99, which indicates that in reality microimpression's filling is slower. The predicted time intervals of POM and ABS polymers and hence injection times were also significantly shorter than the experimental ones as it can be seen from Table 8 and Table 9 respectively.

Table 7 - Comparison of the predicted (Ram speed) and experiment time intervals PP

Experiment Nº	t(s) AMI Ram Speed PP			t(s) Experiment PP			AC_{P1-T1}	AC_{P1-T2}	AC_{T1-P2}
	P1-T1	P1-T2	T1-P2	P1-T1	P1-T2	T1-P2			
1	0,0030	0,0032	0,0054	0,0065	0,0070	0,0165	2,13	2,19	3,03
2	0,0017	0,0018	0,0022	0,0041	0,0042	0,0073	2,48	2,39	3,30
3	0,0026	0,0027	0,0056	0,0053	0,0059	0,0149	2,02	2,17	2,65
4	0,0017	0,0017	0,0023	0,0036	0,0037	0,0066	2,11	2,14	2,92
5	0,0029	0,0030	0,0041	0,0063	0,0072	0,0157	2,17	2,40	3,81
6	0,0016	0,0016	0,0029	0,0045	0,0046	0,0069	2,88	2,79	2,41
7	0,0030	0,0032	0,0036	0,0049	0,0059	0,0142	1,63	1,83	3,99
8	0,0017	0,0018	0,0026	0,0036	0,0037	0,0063	2,08	2,07	2,41

Table 8 - Comparison of the predicted (Ram speed) and experiment time intervals POM

Experiment Nº	t(s) AMI Ram Speed POM			t(s) Experiment POM			AC_{P1-T1}	AC_{P1-T2}	AC_{T1-P2}
	P1-T1	P1-T2	T1-P2	P1-T1	P1-T2	T1-P2			
1	0,0030	0,0033	0,0051	0,0079	0,0093	0,0222	2,63	2,82	4,36
2	0,0013	0,0014	0,0028	0,0048	0,0056	0,0105	3,55	3,90	3,74
3	0,0034	0,0037	0,0047	0,0083	0,0098	0,0232	2,46	2,68	4,93
4	0,0019	0,0020	0,0029	0,0043	0,0049	0,0110	2,26	2,48	3,84
5	0,0033	0,0035	0,0051	0,0081	0,0093	0,0217	2,44	2,63	4,30
6	0,0016	0,0017	0,0030	0,0045	0,0053	0,0094	2,83	3,21	3,16
7	0,0036	0,0038	0,0051	0,0068	0,0079	0,0227	1,88	2,07	4,50
8	0,0019	0,0020	0,0025	0,0041	0,0049	0,0107	2,16	2,39	4,21

Table 9 - Comparison of the predicted (Ram speed) and experiment time intervals ABS

Experiment Nº	t(s) AMI Ram Speed ABS			t(s) Experiment ABS			AC_{P1-T1}	AC_{P1-T2}	AC_{T1-P2}
	P1-T1	P1-T2	T1-P2	P1-T1	P1-T2	T1-P2			
1	0,0030	0,0031	0,0054	0,0062	0,0072	0,0167	2,09	2,28	3,12
2	0,0014	0,0014	0,0030	0,0034	0,0039	0,0065	2,48	2,71	2,19
3	0,0029	0,0030	0,0058	0,0057	0,0066	0,0146	1,98	2,19	2,53
4	0,0018	0,0018	0,0031	0,0036	0,0040	0,0064	2,02	2,16	2,04
5	0,0037	0,0038	0,0043	0,0062	0,0073	0,0160	1,67	1,92	3,70
6	0,0019	0,0019	0,0020	0,0038	0,0043	0,0098	1,98	2,22	4,88
7	0,0031	0,0032	0,0056	0,0056	0,0064	0,0160	1,82	2,01	2,85
8	0,0018	0,0018	0,0029	0,0034	0,0039	0,0070	1,96	2,17	2,42

There are many factors that are likely to be responsible for this divergence between the predicted time intervals and the experimental ones. For µIM numerical simulation some general assumptions valid at the macro scale may not hold, including constant melt/wall interface heat transfer coefficient during injection stage, “non-slip” boundary condition at the mould wall and incompressibility of the polymer melt during injection stage [214]. Recent research of Nguyen *et al.* [217] emphasized that the effect of melt compressibility in μ-injection moulding during the filling phase should not be underestimated as it becomes more pronounced with a decrease in part thickness. Moreover, high flow resistance in the microimpression may significantly reduce the volume rate due to the melt compression in the injection barrel. Similar phenomena was reported in a previous study by the same authors when numerical modelling of a micro spiral was conducted with the previous version of AMI® (MPI 6.1) [106].

Flow of molten polymer is generally in shear deformation where layers of material are sliding over each other (Figure 78a). However, when polymer undergoes abrupt change in cavity thickness (gate region) polymer particles are elongated as it can be depicted from Figure 78b. This type of deformation is called extensional flow [137]. It is likely to occur when molten polymer is passed from the runners of conventional size to the micrometric gate, as it is the case of the micropart under investigation (Figure 27, page 62).

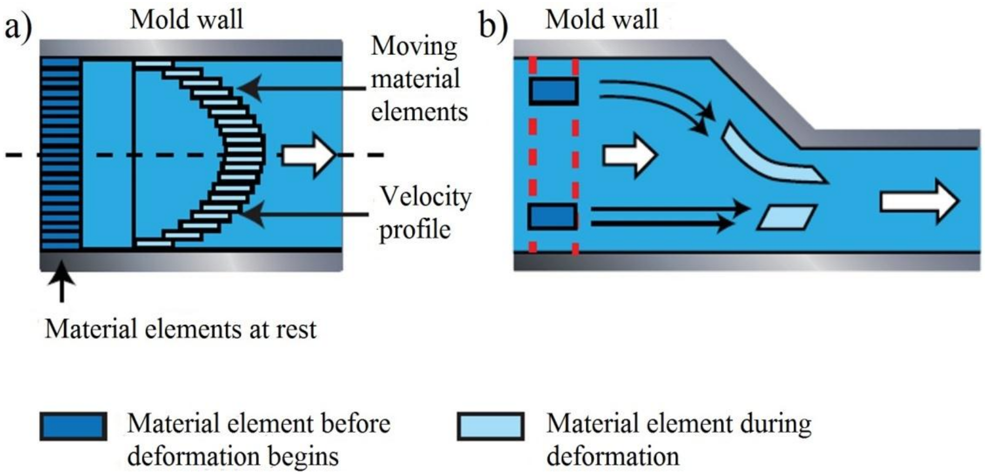

Figure 78 - a) A shear flow in cavity filling; b) Extensional flow in cavity filling [137]

Shear rate is an important flow parameter. It affects polymer viscosity and the amount of shear heating may aid microimpression's filling even without increasing mould and melt temperature. Shearing of polymer melt, however, should not be excessive, at too fast injection velocity the polymer chains may break and the material degrade [218]. For steady simple shear flow (Figure 79), shear rate is given by [214]:

$$\dot{\gamma} = \frac{dv_x}{dz}$$ Equation 50

Over predicted velocity in the microimpression also suggests that shear stress resulting from high shear rate and elongation deformation may be over predicted as well. Therefore, accurate prediction of the filling dynamics in microimpression becomes essential considering a connection between shear rate and residual stress [137, 219]. As a matter of fact, the current version of AMI® program does not allow for the introduction of the compressibility effect and wall slip phenomenon in the filling stage of simulation.

To approximate filling times to more realistic values and hence improve prediction accuracy under such conditions, a compromised decision has been adopted. Another set of the numerical simulations was conducted using the filling times as the filling control instead of the experimental ram speed (mm/s). The filling times used in the simulations were introduced as equal to the times recorded during the acquisition of the pressure and temperature data. Elongation deformation of polymer flow was also accounted in the numerical simulations. The Bagley correction constants C1 and C2, also known as the juncture loss coefficients, were used in rheological properties of polymers.

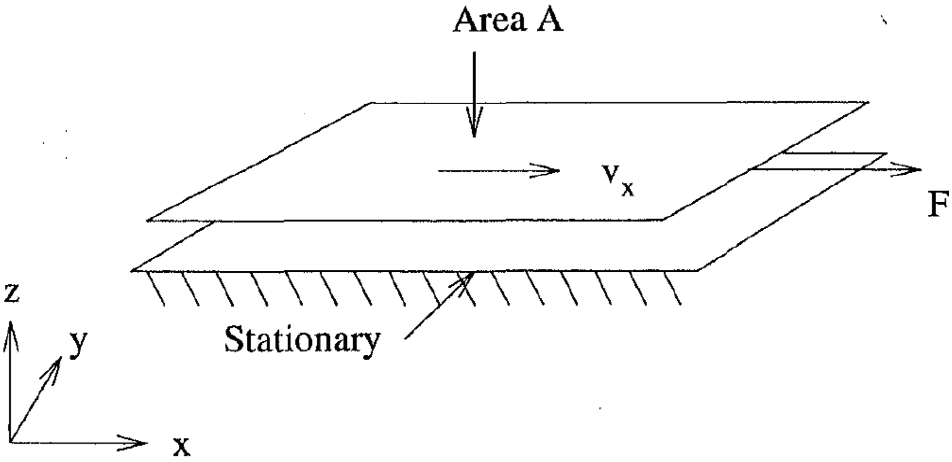

Figure 79 - Steady simple shear flow [214]

The juncture loss model can be used to improve the predictions of pressure and flow balance in the feed system in presence of high extension rate. It allows to incorporate the effect of extensional viscosity in the simulation results [189]. In order to understand how the injection velocity affects the shear rates of PP, POM and ABS, shear rate maximum results for DOE2 processing conditions were compared for two methods of filling control: a) ram speed (mm/s) vs. ram position (mm); b) recorded filling time. The shear rate maximum result is generated at a given node and represents its maximum value during the injection molding cycle.

For DOE2 experiment, maximum shear rate of PP with filling controlled by ram speed (mm/s) varies from 40.99 to 1049000(1/s), as it can be depicted from Figure 80. The shear rate limit for this particular grade of PP is established in AMI® database as 100000(1/s). It is evident that the shear rate predicted by the simulation exceeds several times the established material's limit in four distinct areas of the microimpression. The rise in shear rates can be attributed to an increase in polymer velocity in microimpression, which occurs when its cross-section tends to decrease. The highest shear rate -713900(1/s), as expected, was encountered at the gate region. After passing the gate, the polymer flow becomes fully established in the 400µm section. It flows slower and the shear rate drops below the material's limit.

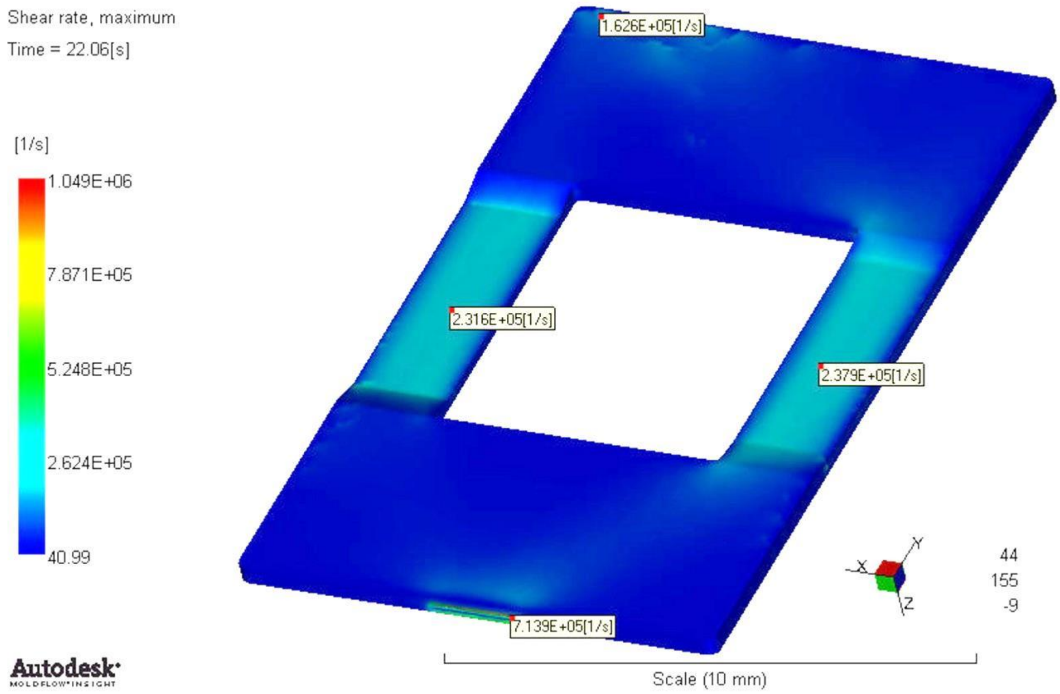

Figure 80 - Shear rate, maximum - PP (DOE2); injection controlled with ram speed (mm) vs. ram position (mm)

Next increase in the shear rate was observed when molten polymer enters restricted left side 200µm - 231600(1/s) and right side 300µm - 237900(1/s) sections of the microimpression. After entering wider 400µm section, where flow fronts from the 200µm and 300µm sections will meet, shear rate values decrease again. The last zone with elevated shear rate - 162600(1/s) is situated on the extremity of the micropart, at the end of filling.

When injection is controlled by the experimental time (Figure 81), the predicted shear rate drops significantly varying from 22.79 up to 364000(1/s). Shear rates above the material's limit were concentrated in two zones: at the gate and at the end of filling. Their values, however, are much lower than the ones predicted for injection controlled with ram speed (mm/s) versus ram position (mm). Restrictions imposed by the 200µm and 300µm sections show some increase in shear rate comparing with 400µm sections but below the material's limit.

Magnitude and distribution of the shear rate for DOE1 (Figure A.1) and DOE8 (Figure A.2) processing conditions may be consulted in Appendix A. These two sets of the processing conditions were particularly chosen as representative of the bottom and top levels of the control parameters (DOE1 and DOE8, respectively).

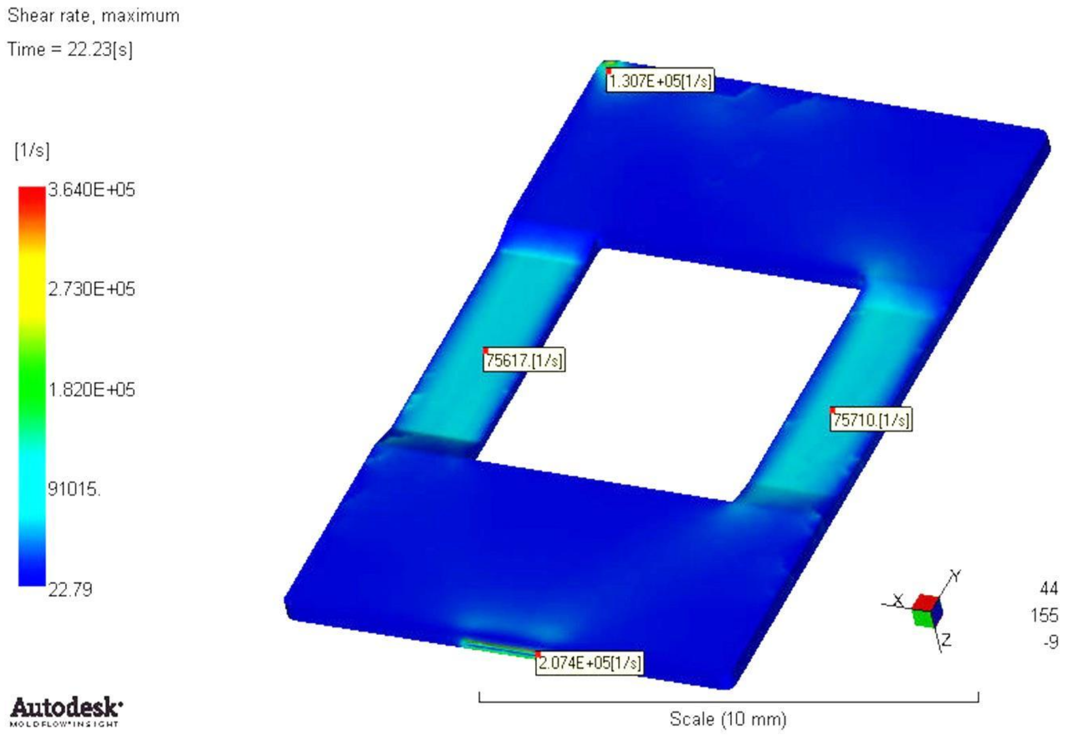

Figure 81 - Shear rate, maximum - PP (DOE2); injection controlled with the recorded filling time

Shear rate distribution through the PP micropart's thickness can be visualized as an XY probe plot (Figure 82). Probe values, chosen for the comparison, correspond to the center points of the pressure and temperature sensors presented earlier in Figure 77: P1 - N 29484, P2 - N 28214, T1 - N 14610, T2 - N 15632. In order to distinguish the shear rates for different modes of the filling control, each node has a subscript either "*rs*" or "*ft*", which stands for ram speed and filling time respectively. Shear rate profile through the thickness has a parabolic shape where the maximum shear rate occurs at the mould/part interface then drops toward the centre of the microimpression.

When injection was controlled by ram speed (mm/s) vs. ram position (mm), some portions of the cross-section closest to the mould cavity in both 200µm (N15632rs) and 300µm (N14610rs) sections are above the shear rate material's limit, which can be depicted on the plot as a red dashed line. It was possible to determine the exact thickness of the zone subjected to excessive shearing, which was about 120µm in case of 200µm section and 136µm for 300µm section. Regions above the limit are prone to material degradation, embrittlement and poor surface finish [220]. At slower injection, the shear rate profiles of all probes are below the material limit, independently on the section thickness.

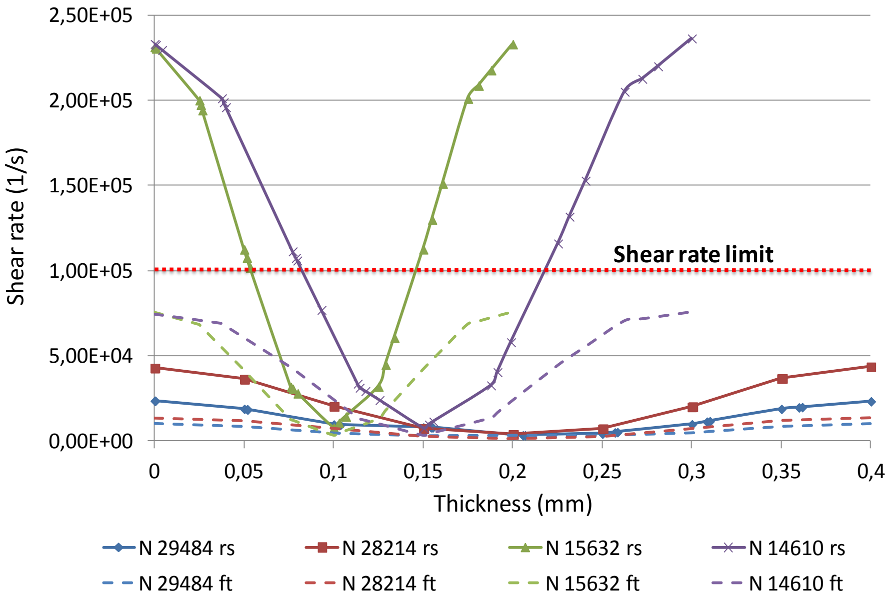

Figure 82 - Shear rate, maximum -Probe XY Plot: PP (DOE2) for injection controlled with Ram speed (mm/s) vs. ram position (mm) and Fill Time

Considering significant divergence between the shear rates predicted for injection controlled by ram speed (mm/s) vs. ram position (mm) and ones obtained when injection is controlled by the recorded filling time, it seems reasonable to assume that the numerical results in the former case may be misleading and enforce the choice of the recorded injection time as a filling control method.

Shear limit for POM C 9021 is established at 40000(1/s), which is lower than shear limit of PP. Estimated maximum shear rate reaches 1323000(1/s) (Figure 83), suggesting that the surface area of the micropart exposed to the excessive shearing may be even larger than that of the PP when injected with the identical velocity (ram speed filling control). Micropart’s areas under excessive shear rate have the similar mapping observed for PP. Slower injection velocity obtained with the recorded fill time control (Figure 84) led to a significant decrease in the shear rate from 1323000(1/s) to 422700(1/s). However, even with the slower injection velocity, the shear rates for both 200μm and 300μm sections were above the material’s limit. More data about the magnitude and distribution of the shear rate in POM μ-parts are provided in Appendix A (Figure A.3 and Figure A.4).

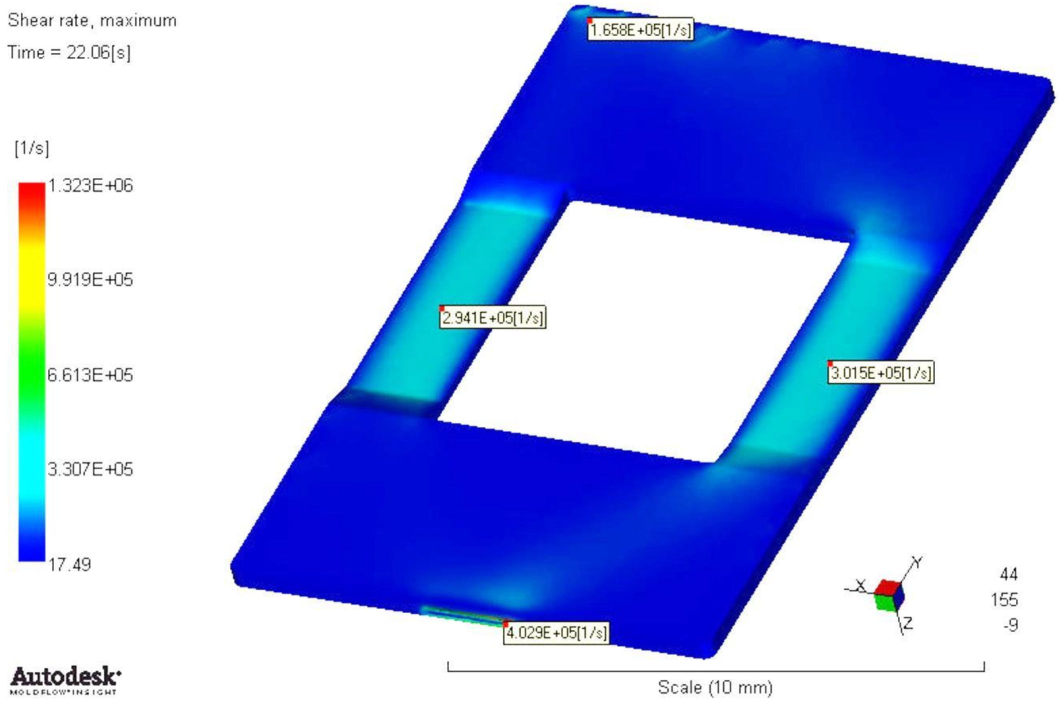

Figure 83 - Shear rate, maximum - POM (DOE2); injection controlled with Ram Speed (mm/s)

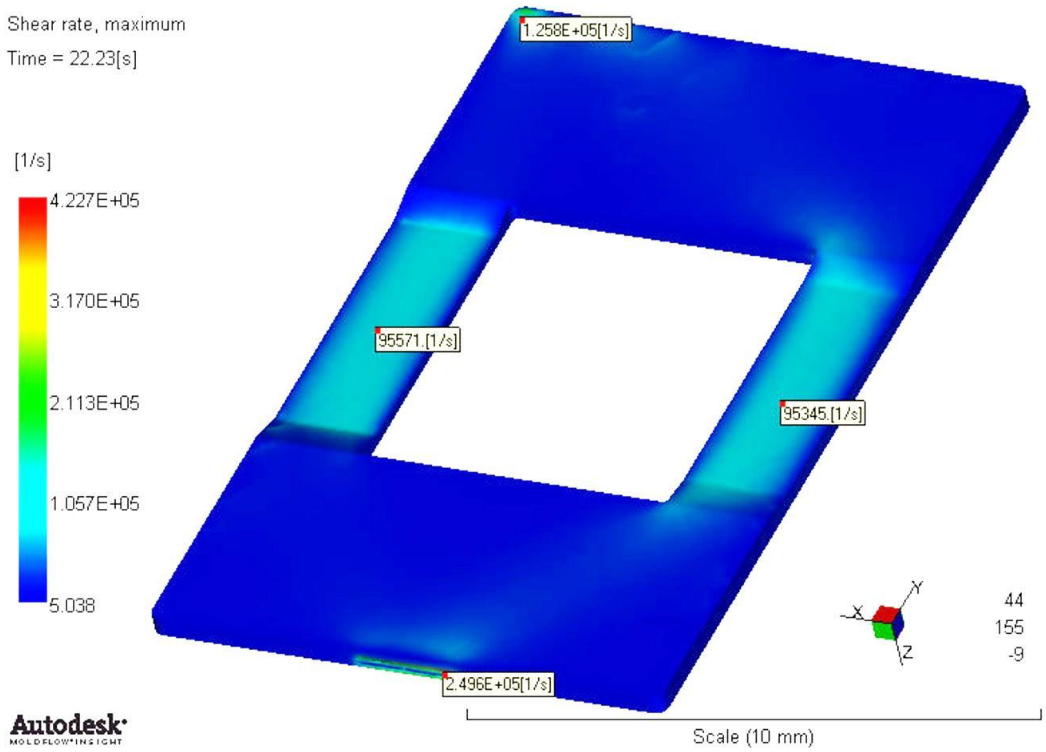

Figure 84 - Shear rate, maximum - POM (DOE2); injection controlled with the recorded Fill Time

Figure 85 provided more detailed information about the shear rate distribution through the POM micropart's thickness. A significant portion of the cross-sections in both 200µm (N 15632rs) and 300µm (N 14610rs) sections are prone to excessive shearing when the ram speed filling control is used in the simulation. Moreover, the shear rate through the 400µm section at the P2 (N 28214rs) sensor location indicated that a small portion of its cross-section is also under excessive shearing. Slower injection velocity results in less shearing through the thickness of 200µm (N 15632ft) and 300µm (N 14610rs) micropart's sections.

Towards a better comprehension of the filling control influence on the shear rate distribution through the thickness, in Table 10, micropart's thickness with the shear rate above and below the limit were compared. It became clear that for 200µm and 300µm thickness sections, thickness of the layer with shear rate below the material's limit increased with slower injection velocity.

The shear rate gradient through the thickness is likely to generate structural and morphological heterogeneity in the micromoulded part and lead to a pronounced variation in molecular orientation. To understand more clearly the influence of the excessive shear rates on the heat transfer phenomena in the microimpression morphology, future research might be addressed for assessment of the morphological structure of polypropylene and polyoxymethylene microparts.

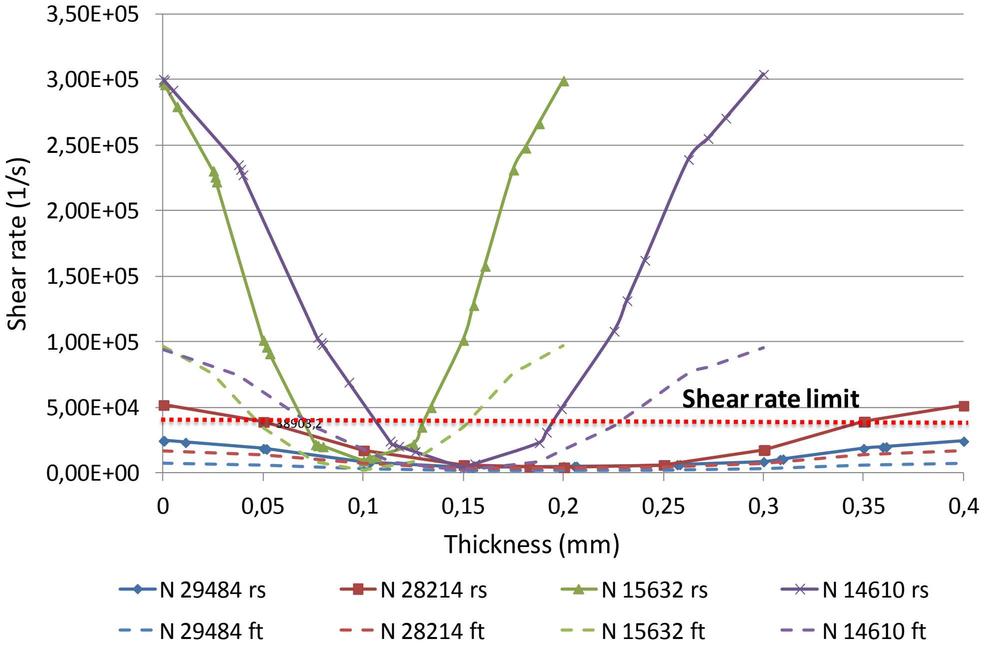

Figure 85 - Shear rate, maximum -Probe XY Plot: POM (DOE2) for injection controlled with Ram Speed (mm/s) and Fill Time

Table 10 - Influence of the filling control on the POM (DOE2) shear rate distribution through the thickness

Method of filling control	Probe locations	Section thickness (µm)	Micropart's thickness with shear rate below the limit (µm)	Micropart's thickness with shear rate above the limit (µm)
Ram speed (mm/s)	P2-(N 28214rs)	400	310	90
	T2-(N 15632rs)	300	61	139
	T1-(N 14610rs)	200	89	211
Fill time (s)	T2-(N 15632ft)	200	106	94
	T1 (N 14610ft)	300	158	142

Shear rates of ABS simulated with ram speed (mm/s) control are shown in Figure 86. The shear rate values are of the same order and similar pattern as that of POM and, to a great extent, surpasses 50000(1/s) shear rate limit of the CYCOLAC GPM5500S.

However, there was one peculiarity not verified for POM and PP polymers. Maximum shear rate at 300µm section is higher than that of the thinner one, while for the other two polymers they were approximately equal.

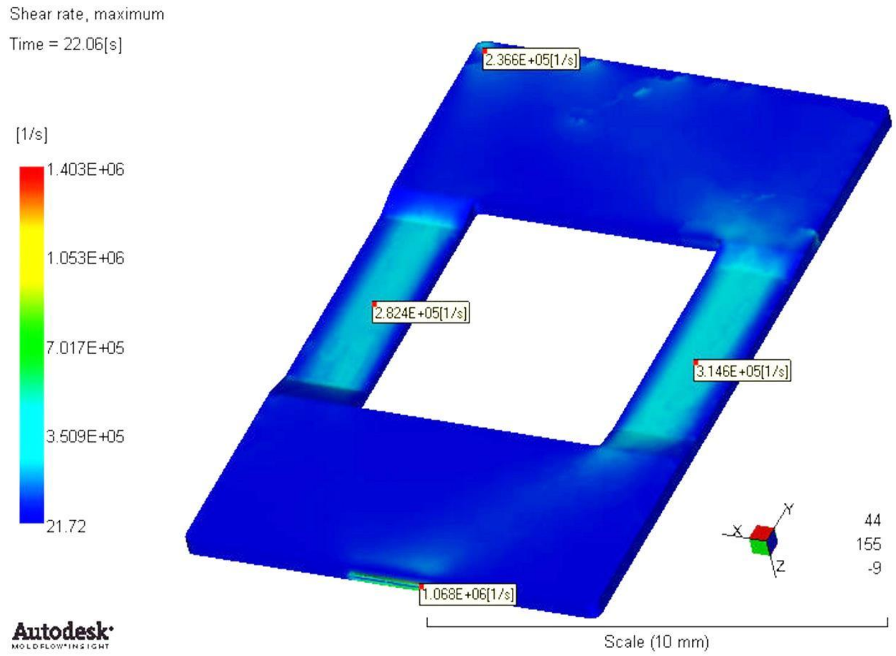

Figure 86 - Shear rate, maximum - ABS (DOE2); injection controlled with ram speed (mm/s)

With a decrease in the injection velocity (Figure 87), shear rate tends to decrease. In the 300µm section, however, the shear rate became almost twice of that in 200µm section. Moreover, this difference is tripled, when ABS is injected with low injection velocity, low mould and melt temperatures (Figure A.5). However, with the control parameters at high level (DOE8), the previously mentioned divergence becomes less pronounced as it can be depicted from Figure A.6.

In Figure 88, this difference was shown with more clarity. It appears that ABS is more prone to excessive shearing than PP and POM. It may be also confirmed by comparison (Table 11) of the thickness of layers with the shear rate above and below the shear rate limit of ABS. Comparing the thickness of the ABS micropart with the shear rate above the limit for T1 (N 14610ft) and T2 (N 15632ft) sensors locations with the homologue values of POM (Table 10), it was found out that for thinner section of ABS a size of layer under excessive shearing was 100µm against 94µm predicted for POM. For the thicker section, 192µm of 300µm of the total thickness were subjected to the shear rate above the material's limit.

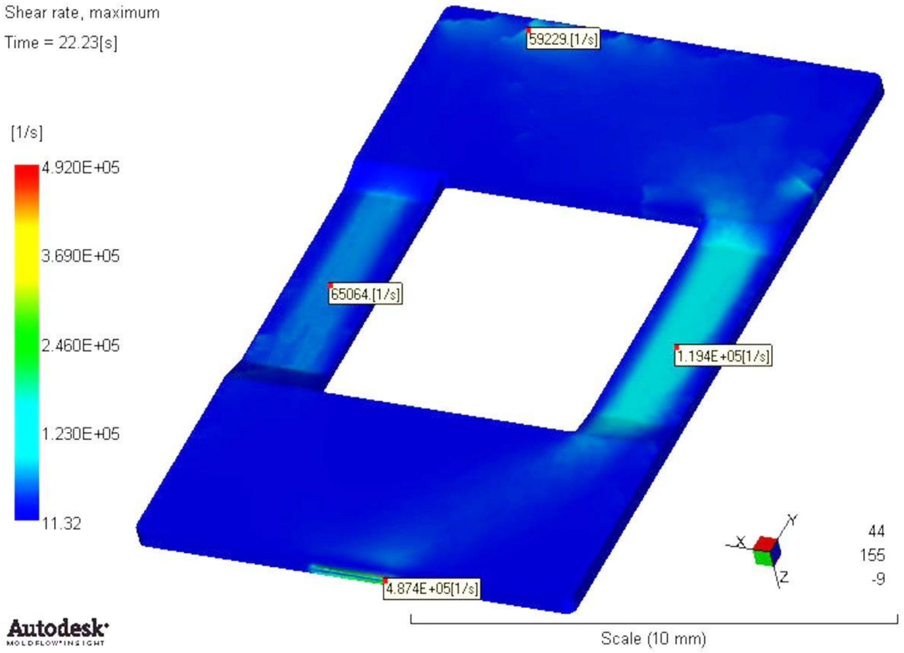

Figure 87 - Shear rate, maximum - ABS (DOE2); injection controlled with the recorded filling time

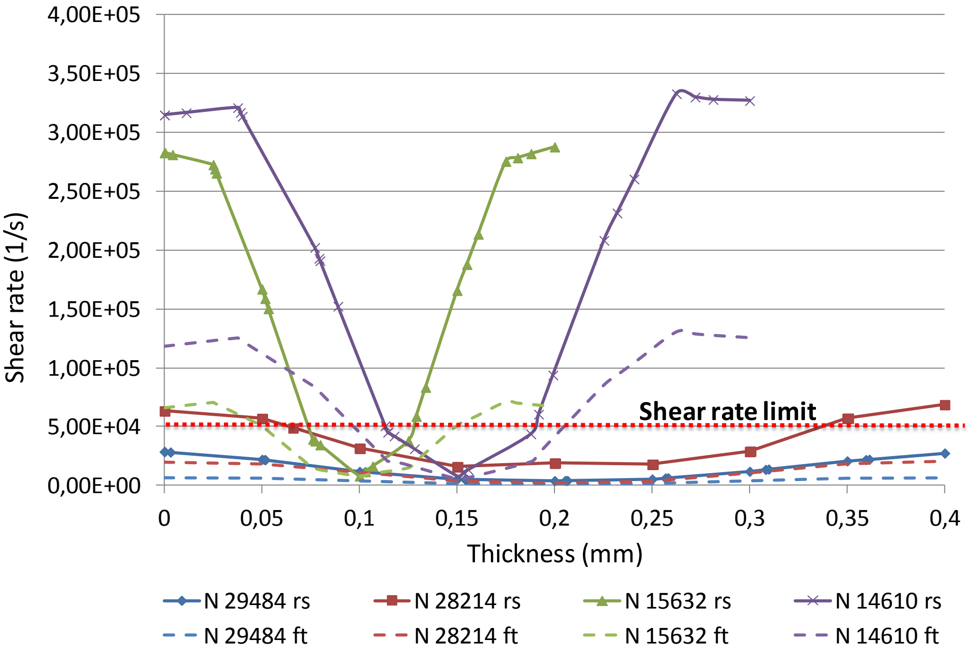

Figure 88 - Shear rate, maximum -Probe XY Plot: ABS (DOE2) for injection controlled with Ram speed (mm/s) vs. ram position (mm) and Fill Time

Table 11 - Influence of the filling control on the ABS (DOE2) shear rate distribution through the thickness

Method of filling control	Probe locations	Section thickness (µm)	Micropart's thickness with shear rate below the limit (µm)	Micropart's thickness with shear rate above the limit (µm)
Ram speed (mm/s)	P2-(N 28214rs)	400	274	126
	T2-(N 15632rs)	200	54	146
	T1-(N 14610rs)	300	78	222
Fill time (s)	T2-(N 15632ft)	200	100	100
	T1 (N 14610ft)	300	108	192

It is generally known that excessive shear rates will lead to polymer degradation. This degradation may be explained by tearing of the polymers molecules when the relative velocity reaches a critical value. Guidelines for the shear rate limits, widely used as a criterion for prediction polymer failure and degradation, were established by the Moldflow laboratories. The shear stress and shear rates limits, available in the material database, provide for a conservative safe design. Unfortunately, besides the data available from AMI®, there is no information available in the literature about the maximum allowable shear rate for a given plastic material. However, research conducted by Beaumont [221] indicated that the guidelines for non-thermally sensitive polymers can be exceeded. Moreover, the visual observation of the PP, POM and ABS microparts, supposedly injected under the excessive shear rate, did not reveal any visible signs of degradation.

A new set of the numerical simulations, using time as a filling control, was carried out. The predicted time intervals P1-T1, P1-T2 and T1-P2 were compared with the experimental data in Table 12, Table 13 and Table 14 for PP, POM and ABS polymers respectively. There were several common patterns encountered between the predicted and experimental data for all three polymers:

- Predicted P1-T2 time intervals were longer than P1-T1 ones which imply slower flow front velocity in thinner 200µm section.
- P1-T1 and P1-T2 time intervals reflect the change of the injection velocity, increasing and decreasing according to filling time.

- As the melt flows further from the gate, it keeps cooling and progressively flows more slowly. For all experiments, time intervals T1-P2 were longer than those P1-T1. It may suggest higher cooling rate through conduction to the mould wall and respectively slower flow front advancement as the melt flows further from the gate.

As it was established earlier, the accuracy criteria suggest that for polypropylene, the predicted time intervals with filling time control match more closely the experimentally recorded data (Table 12). Precision of the numerical simulations tends to increase when the accuracy criteria approach one, while deviation larger than one means faster than experimental filling and vice versa. $AC_{P1\text{-}T1}$ varies from 0.66 to 0.94 meaning somewhat slower than experimentally recorded filling. However, it approaches more closely the experimental data than injection controlled with ram speed (Table 7). $AC_{P1\text{-}T2}$ follows a similar pattern clustering in the range from 0.76 to 0.95. $AC_{T1\text{-}P2}$ variation from 1.07 to 1.76 indicated faster than experimental filling at the most remote from the gate portion of the microimpression. This divergence with the experimental data was especially evident for experiments 1, 3, 5 and 7 with slow injection velocity (Table 12). The only exception was verified for the experiment number 8 where polymer flows slightly slower than in the real conditions with $AC_{T1\text{-}P2}$ equal to 0.91.

Table 12 - Comparison of the predicted (Fill Time control) and experiment time intervals PP

Experiment Nº	t(s) AMI Fill Time PP			t(s) Experiment PP			$AC_{P1\text{-}T1}$	$AC_{P1\text{-}T2}$	$AC_{T1\text{-}P2}$
	P1-T1	P1-T2	T1-P2	P1-T1	P1-T2	T1-P2			
1	0,0071	0,0073	0,0100	0,0065	0,0070	0,0165	0,92	0,95	1,65
2	0,0045	0,0046	0,0058	0,0041	0,0042	0,0073	0,92	0,90	1,26
3	0,0070	0,0072	0,0099	0,0053	0,0059	0,0149	0,76	0,81	1,51
4	0,0042	0,0045	0,0061	0,0036	0,0037	0,0066	0,86	0,83	1,07
5	0,0076	0,0080	0,0102	0,0063	0,0072	0,0157	0,84	0,90	1,54
6	0,0048	0,0049	0,0060	0,0045	0,0046	0,0069	0,94	0,92	1,15
7	0,0074	0,0077	0,0080	0,0049	0,0059	0,0142	0,66	0,76	1,76
8	0,0042	0,0043	0,0069	0,0036	0,0037	0,0063	0,87	0,86	0,91

Precision of the polymer dynamics prediction for polyoxymethylene can be assessed from Table 13. The numerical simulations time intervals (P1-T1) results indicate slightly slower injection for the experiment number 8 ($AC_{P1\text{-}T1}$=0.96) while for the other combinations of the processing conditions faster than experimental flow front velocity was predicted through the variation of the $AC_{P1\text{-}T1}$ (1.01-1.27). $AC_{P1\text{-}T2}$ and $AC_{T1\text{-}P2}$ indicated that polymer flows faster than in reality at the 200μm section (P1-T2) and at the portion of the microimpression most distantly located from the gate (T1-P2). Accuracy prediction of the latter time interval decreases for the simulations carried out with longer fill times or speaking otherwise slow injection velocity. $AC_{T1\text{-}P2}$ for the experiments 1, 3, 5 and 7 vary in the range from 2.02 to 2.12 while for the simulations carried out with high injection velocity (experiments 2, 4, 6 and 8) prediction becomes more precise. A similar trend has been verified for the (T1-P2) time interval of PP although not so emphasized.

Table 13 - Comparison of the predicted (Fill Time) and experiment time intervals POM

Experiment Nº	t(s) AMI Fill Time POM			t(s) Experiment POM			$AC_{P1\text{-}T1}$	$AC_{P1\text{-}T2}$	$AC_{T1\text{-}P2}$
	P1-T1	P1-T2	T1-P2	P1-T1	P1-T2	T1-P2			
1	0,0063	0,0066	0,0109	0,0079	0,0093	0,0222	1,26	1,41	2,05
2	0,0044	0,0047	0,0071	0,0048	0,0056	0,0105	1,07	1,21	1,48
3	0,0066	0,0068	0,0115	0,0083	0,0098	0,0232	1,27	1,44	2,02
4	0,0043	0,0045	0,0079	0,0043	0,0049	0,0110	1,01	1,11	1,41
5	0,0068	0,0070	0,0103	0,0081	0,0093	0,0217	1,19	1,33	2,12
6	0,0042	0,0044	0,0072	0,0045	0,0053	0,0094	1,08	1,21	1,31
7	0,0064	0,0067	0,0111	0,0068	0,0079	0,0227	1,06	1,17	2,04
8	0,0043	0,0047	0,0075	0,0041	0,0049	0,0107	0,96	1,04	1,42

In Table 14, $AC_{P1\text{-}T1,}$ $AC_{P1\text{-}T2}$ and $AC_{T1\text{-}P2}$ ratios between the experiment time intervals P1-T1, P1-T2 and T1-P2 of ABS and their predicted values mean slightly slower than experimental polymer velocity in the microimpression with an exception for the time interval T1-P2 when slow fill times were used. A possible explanation for this inconsistency, which may be applied for all three polymers, may lie in the fact that the recorded fill times indicate the amount of time required to fill not only the microimpression but also the runner system. Volume of the microimpression is about 3.5% of the total volume of the cavity (Table 4, page87) and therefore the time required to fill the former is by an order of magnitude shorter than for the complete moulding. As a consequence, it was not possible to establish when exactly the microimpression's filling starts and how much time it took to fill it. To clarify how this divergences may influence the flow pattern prediction, the experimental weld line results will be compared with the weld line results from AMI® simulations.

In addition, the discrepancies encountered between the predicted and experimentally observed polymer flow velocities may be attributed to some assumptions used in the AMI® simulation code, which may have bearing on the precision of the numerical simulation at µ-scale.

Table 14 - Comparison of the predicted (Fill Time) and experimental time intervals ABS

Experiment Nº	t(s) AMI Fill Time ABS			t(s) Experiment ABS			AC_{P1-T1}	AC_{P1-T2}	AC_{T1-P2}
	P1-T1	P1-T2	T1-P2	P1-T1	P1-T2	T1-P2			
1	0,0085	0,0089	0,0133	0,0062	0,0072	0,0167	0,73	0,81	1,25
2	0,0056	0,0057	0,0086	0,0034	0,0039	0,0065	0,61	0,68	0,75
3	0,0073	0,0076	0,0098	0,0057	0,0066	0,0146	0,78	0,87	1,49
4	0,0045	0,0048	0,0090	0,0036	0,0040	0,0064	0,80	0,82	0,71
5	0,0085	0,0090	0,0133	0,0062	0,0073	0,0160	0,73	0,81	1,20
6	0,0047	0,0048	0,0095	0,0038	0,0043	0,0098	0,81	0,89	1,03
7	0,0071	0,0073	0,0117	0,0056	0,0064	0,0160	0,79	0,88	1,37
8	0,0047	0,0048	0,0085	0,0034	0,0039	0,0070	0,74	0,81	0,82

A premise about the incompressibility of the polymer melt in microimpression during the injection stage have already been questioned in the recent research of Nguyen *et al.* [217]. They found out that melt compressibility has important effects on cavity pressure and density distribution in the micropart.

An assumption of the constant polymer conductivity during injection [214] may be valid for the conventional injection molding process, where cooling rates are relatively slow.

However in µIM, reduced cavity dimensions promote almost instantaneous cooling of polymer and therefore a significant fraction of the microcavity thickness may be solidified during injection if no specific technology is used to keep the polymer temperature above the transition point. Cooling of the polymer melt can be, to a certain degree, counteracted by the heat generated by viscous dissipation (shear heating), however, the experimental data does not seem to prove a significant influence of the shear heating on the advancement of the polymer in the microimpression. It appears that for the given set of the processing conditions and microimpression's geometry the principal mechanism affecting the µIM filling is the conduction of the polymer melt through the mould wall. Bearing in mind high cooling rates inherent to the µIM process, it may be advisable to reconsider an application of constant thermal conductivity for modelling the polymer state during the microimpression's filling.

Another premise likely to influence the polymer dynamics in the microimpression is the value of the heat transfer coefficient (HTC) at the interface between the melt and the mould wall. For thin-wall moulding, the influence of the coefficient is more significant. The part can shrink from the mould, leaving an isolating gap, the bigger the gap, the lower the heat transfer coefficient. In the present numerical simulations, a default value of HTC =5000 W/m^2°C was used during the filling stage.

Reverse engineering based on the relationship between the cavity pressure and the filling degree was adopted by Nguyen-Chung *et al.* [106]. Their conclusions may be summarized as follows: heat transfer coefficient increases by decreasing cavity thickness or injection speed; and the pressure level in the cavity was mostly responsible for the thermal contact between the polymer and the mould wall. They also questioned the use of pressure-dependent model for the heat transfer coefficient instead of the constant value currently used in AMI® simulations.

Despite some divergences between the experimental and predicted polymer dynamics, it was possible to achieve a certain degree of accuracy, using the recorded fill times. Therefore it seems reasonable to assume that predicted pattern of the residual stresses in the micropart may reflect, to a certain degree, a complex thermo-rheological history of the moulded component generated during processing.

In µIM, process-induced residual stresses along with the mechanical solicitations define performance of the moulded part. Calculation of residual stress is mandatory for prediction warpage and shrinkage and requires knowledge of the thermal and mechanical properties of the material. The finality of the complete (filling + packing + warpage) AMI® simulations was the prediction of the residual stresses distribution and its magnitude. Thermo-rheological history of the moulded component has to be taken into account towards a better prediction of the structural performance of the micromoulded parts. It was accomplished by translation the finite element model information, material properties and residual stresses from the AMI® into a partial ABAQUS input file for further structural analysis.

5.5.3 Comparison of the experimental and predicted weld line location and shape

The weld line location can be easily predicted by the flow pattern in the microimpression. Any obstacle, occurring in the flow path, forces the flow fronts to divide and thereafter join which results in the weld line. It can be easily seen from Figure 89, where the weld line was overlaid with the fill time result. For the sake of clarity, the fill time is presented as a bunch of contours where every contour is a representative of a lapse of time during injection. As expected, the fill time and the weld line results reflect the flow pattern observed earlier experimentally in section 5.1, i.e. asymmetry of the weld line due to the differential thickness at the narrow sections of the microimpression. The weld line result has a scale associated with its severity, based on the angle in which the two flow fronts meet.

By default, the weld line visibility is limited in the range from 0º to 135º of the maximum angle of collision. These two ends of the spectrum are shown in Figure 90, with 135º being a slight meeting angle and 0º being a direct collision. The latter occurs where the flow fronts are heading in the opposite directions and indicates more severe weld line while as that angle increases, the severity decreases. In order to guaranty the weld line quality, the temperature of the flow front must be high enough to assure good interfusion of polymer. Higher temperature means less severe weld lines which favours visual appearance and decreases probability of mechanical failures. The overall significance of the weld line have to be evaluated considering two criteria: angle of the flow fronts collision and the temperature of molten polymer at the weld line area.

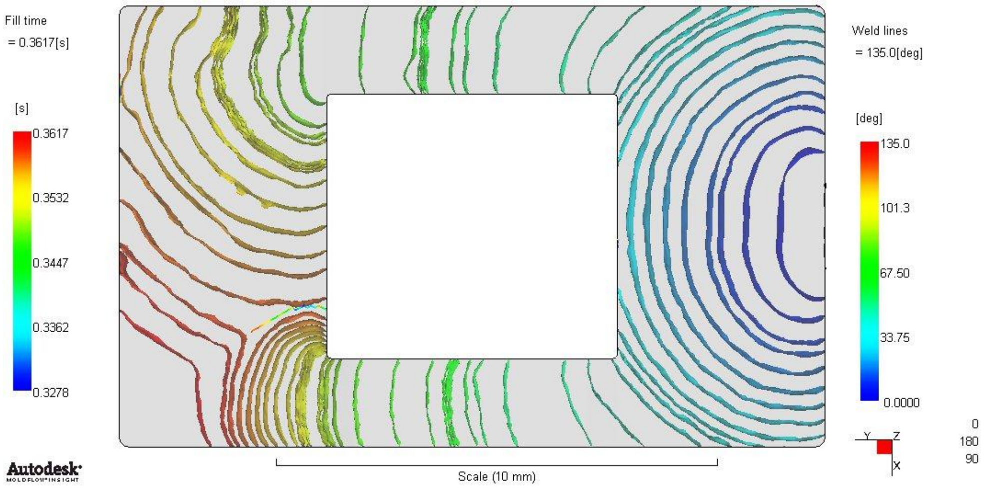

Figure 89 - Overlaid fill time and weld line results for ABS (DOE1)

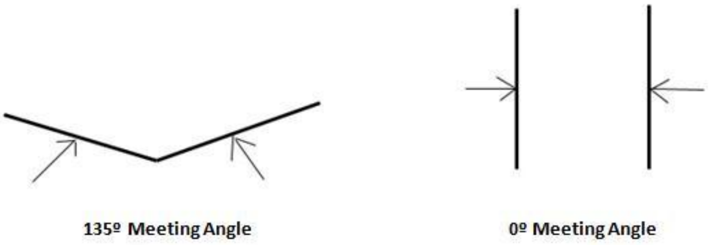

Figure 90 - Flow front' meeting angle (adapted from [222])

The angle of the flow fronts collision is depicted in Figure 91, where the variation of the weld line colour reflects its severity, the scale may be consulted from Figure 89.

Temperature of the molten polymer during the weld line formation in the ABS micropart (DOE1) is shown in Figure 92a and Figure 92b. Here, (Figure 92a) the weld line result was overlaid with the temperature result at the time span close to the end of injection. An amplified fragment of the micropart (Figure 92b), from which the weld line position and the temperature of the meeting flow fronts can be assessed more clearly, indicates that the ABS polymer exits from the thinner section at about 218°C which is colder than the opposite flow front (223°C). This observation confirms the tendency encountered previously in the analysis of the polymer dynamics, cavity temperature and experimental weld line position. However, the injection temperature for this particular simulation was set at 210°C and therefore did indicate heating of the polymer due to high shear rate.

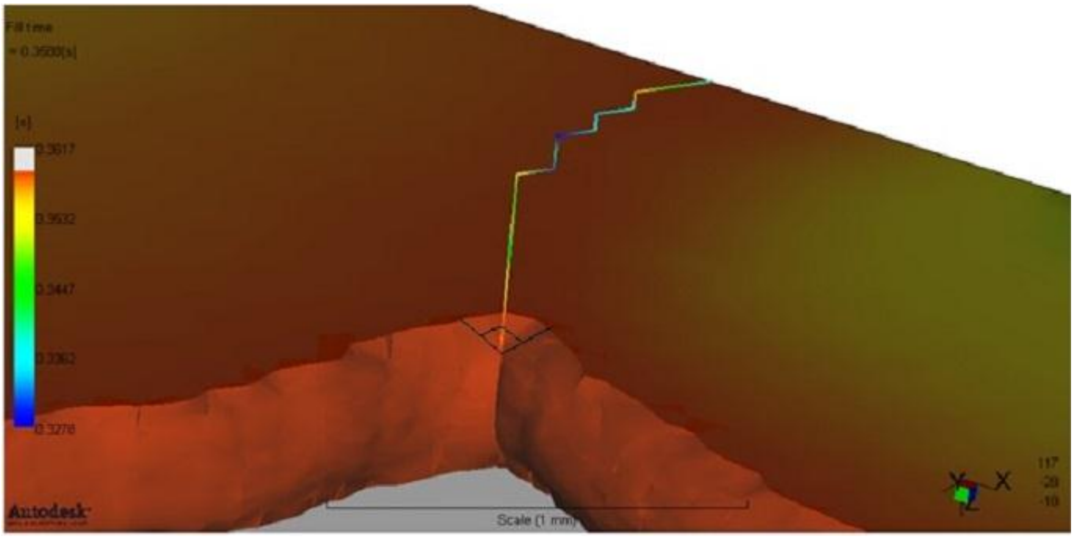

Figure 91 - Meeting angle of the two flow fronts for ABS, DOE1

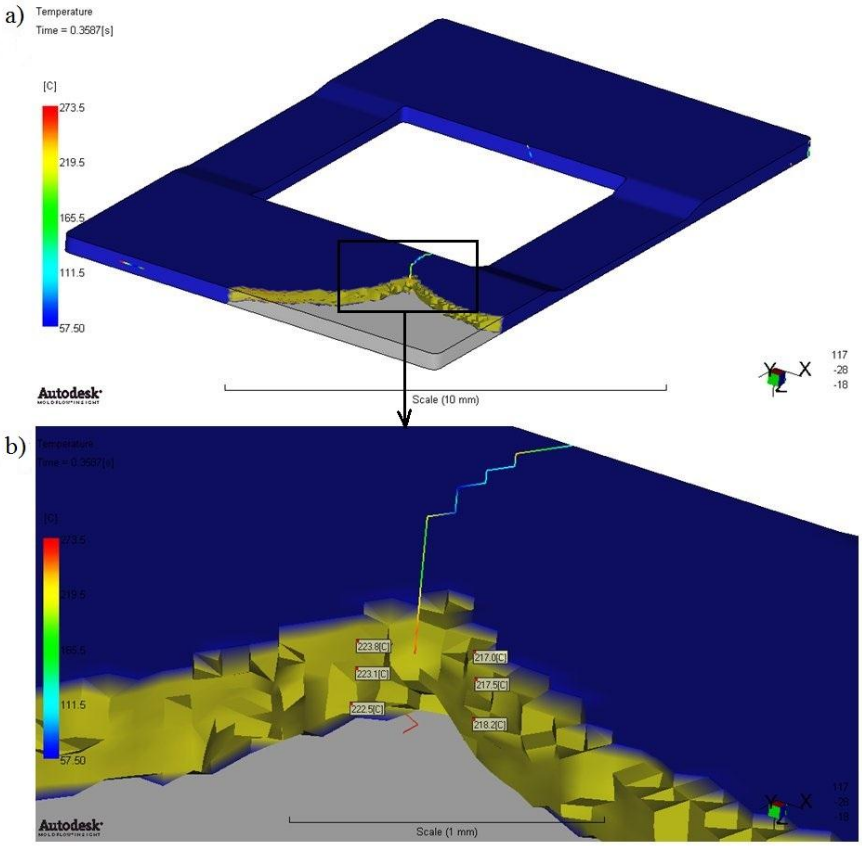

Figure 92 - Overlaid temperature and weld line results for ABS (DOE1)

Weld line position can be seen as an indicator of the polymer fluidity at such critical area of the microimpression as the end of filling. As no sensor was installed at the immediate proximity of the weld line, the position of the latter may supply important information about the influence of the µIM processing conditions on the polymer dynamics, unlikely to be retrieved otherwise.

Previously, several discrepancies have been proven to exist between the experimental and numerically predicted polymer dynamics. Comparison of the predicted and experimental weld line position aims to verify the accuracy of the flow pattern prediction at the end of filling. Assessment of the predicted weld line positions were performed in the same fashion as the experimental ones, previously described in section 3.7. According to the simulation default, when angle of collision surpasses 135° a weld line becomes a meld line, where the flow fronts move in parallel direction leaving a less visible mark on the part surface and therefore not available for visualization. However, the meld line position and direction may be assessed from the fill time result, observing convergence of the flow fronts, as demonstrated in Figure 89.

In reality, the two-dimensional (in-plane) assessment of the weld line position does not allow for clear distinction of the weld and meld lines, showing the continuous mark of the flow fronts encounter over the scanned area. Nevertheless, a direction and position of the initial portions of the predicted weld lines may be compared with homologue experimental values. A wavy appearance of the predicted weld lines was due to the fact that the flow fronts follow the edges of the mesh elements.

As it can be seen from Figure 93, the predicted weld lines (wavy dotted lines) in ABS microparts were at a more advanced position from the zero point than the experimental ones for all combination of the processing conditions.

Nevertheless, there were some traces similar to the experimental results. For example, the predicted weld line curvature matches quite closely the experimentally observed one. Partial similarity was detected in the order of the weld line positions, where the DOE1 is followed by the DOE5. The last and more distanced weld line of the DOE8 also indicated that the controlled parameters at high levels led to the more advanced predicted weld line. Other weld lines were positioned between the DOE5 and DOE8 and did not seem to follow the experimental pattern.

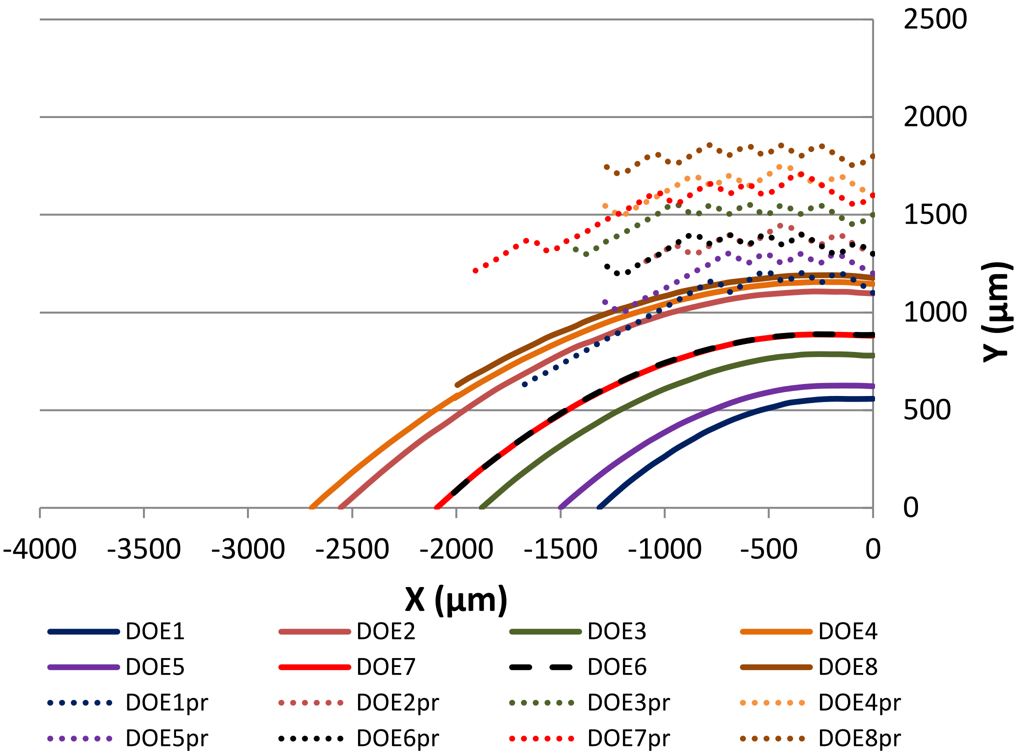

Figure 93 - Comparison of predicted and experimental weld lines of ABS

Being a reflection of the polymer dynamics in the microimpression, the weld line position was analysed in conjunction with the accuracy criteria $AC_{T1\text{-}P2}$ of the ABS predicted polymer dynamics (Table 14, page137). The time interval (T1-P2) represents dynamics of the polymer flowing from the thicker 300µm section towards the flow fronts encounter and therefore accuracy of its prediction is related to the precision of the weld line estimation.

$AC_{T1\text{-}P2}$ values evidenced that the ABS polymer flows slightly faster than predicted between the sensor T1 and P2 when injected with high injection speed (experiments 2, 4, 8) and somewhat slower when the injection velocity was set at low level (experiments 1, 3, 5, 7). The only exception was the experiment 6, where the $AC_{T1\text{-}P2}$ must be left without consideration, recollecting the signs of external disturbances in the µIM process described in the sections 5.1 and 5.3.

Faster than experimental averaged velocity of the polymer from T1 to P2 sensors, however, did not lead to the weld line shift behind the experimental location. It may suggest that the above mentioned discrepancies are related to higher than predicted cooling rates of the polymer flowing through the 200μm section, which leads to an increase in viscosity and reduction of the polymer velocity at the end of filling.

In the same fashion, predicted and experimental weld lines in POM microparts were compared in Figure 94. The predicted weld lines are closely spaced, almost overlapping each other and only a slight offset from 100 to 200μm may be distinguished for DOE1 and DOE8 weld lines.

AC_{T1-P2} of the polyoxymethilene vary from 1.31 to 2.12 (Table 13) indicating that in reality polymer flows slower between the sensor T1 and P2 than predicted by the numerical analysis for all combinations of the processing conditions and eventually cools faster. Bearing this in mind and comparing the simulated weld lines with the experimental ones, which were more evenly distributed and shifted towards the 200μm section of micropart, it is reasonable to assume that the polymer also cools faster than it was predicted in the thinner section.

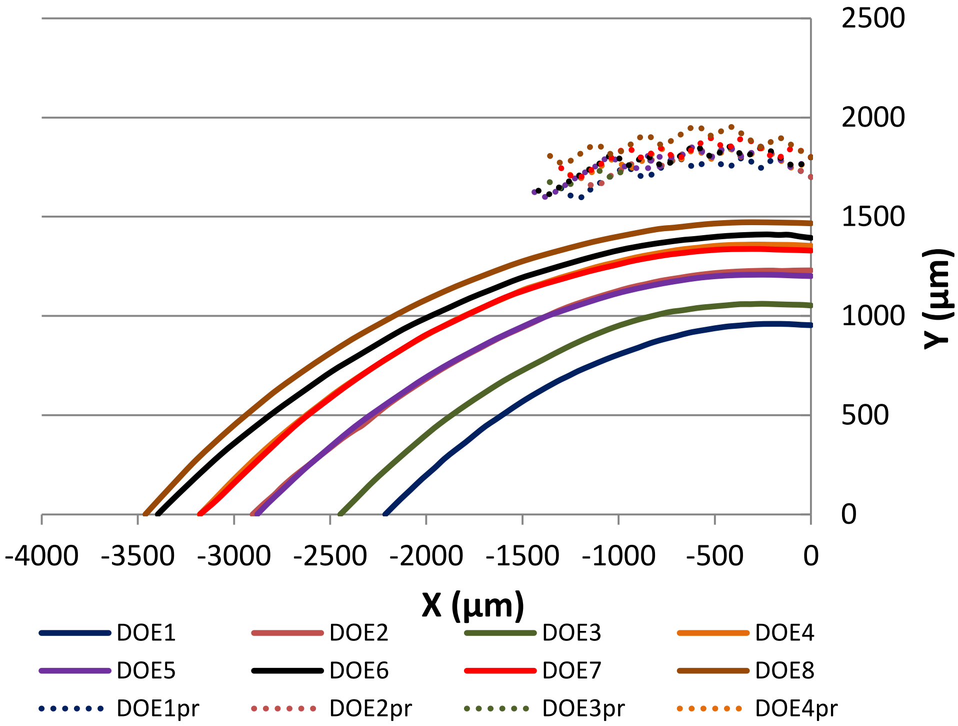

Figure 94 - Comparison of predicted and experimental weld lines of POM

A direct comparison of the experimental and estimated weld lines in PP microparts was not possible, as different zones of the surface were used for mapping the weld lines position (Figure 95). Nevertheless, by following the experimental weld line curvature, an educated guess about tracing the weld line toward the inner edge of the micropart can be made. It seems highly unlikely that experimental weld lines would match the estimated ones. The predicted weld lines, contrarily to the assessed experimentally, overlaid each other making impossible to discern any influence of the injection moulding conditions on their position. It appears that the only relevant factor, affecting the predicted weld line position was the differential thickness of the microimpression.

A hypothesis about drastic cooling of the polymer at the end of filling was also confirmed for polypropylene, where AC_{T1-P2} ratio (Table 12) for the majority of the experiments have indicated that the estimated velocity was faster than recorded.

Considering all discussed above, the failure to predict the exact weld line position in the three investigated polymers may be attributed to the assumption, in AMI®, of a constant heat transfer coefficient (HTC) used during the simulation of filling stage, which does not seem to fully represent the polymer dynamics at micro scale. The experimental weld lines position and the AC_{T1-P2} indicator of the numerical simulation accuracy suggest that for all polymers cooling rates in the microimpression were above the estimated values and also varied with the thickness and surface to volume ratio of the micropart.

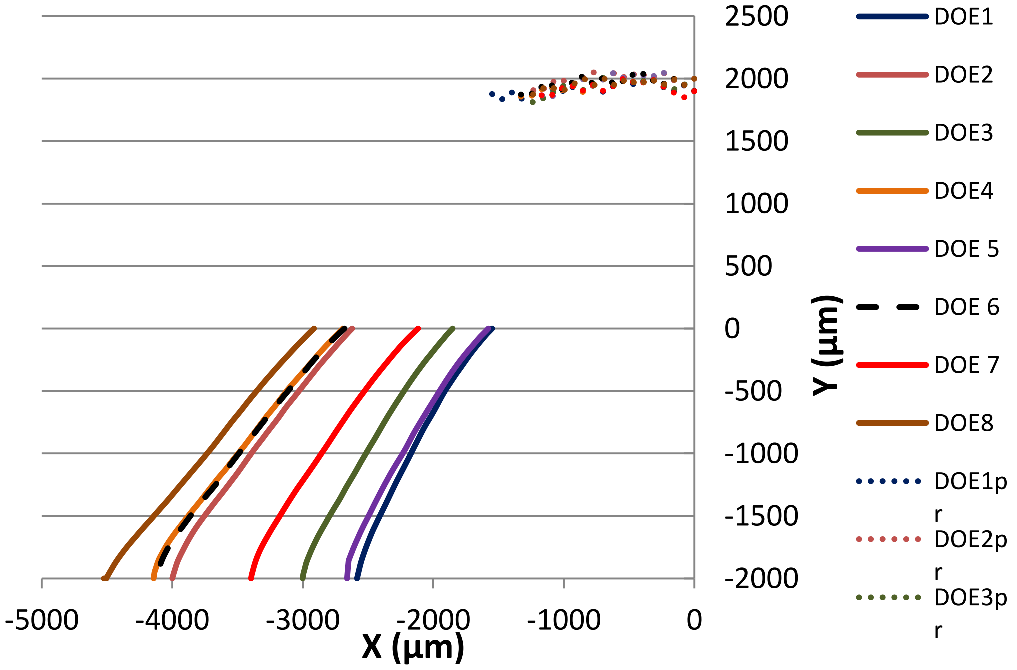

Figure 95 - Comparison of predicted and experimental weld lines of PP

5.6 Parametrical analysis of the predicted process induced residual stresses

As it has already been mentioned, the state of residual stresses in µ-parts is not directly available in a quantified form from AMI® results. To retrieve this information, the partial input file obtained from AMI® was submitted for analysis according to the routine previously described in section 4.6.1. At this stage, the partial input file contains one step "general static step", which means that only linear elastic properties of the polymer were used for assessment of the internal residual stresses after ejection of the micropart from the mould. Quantification of the residual stresses gives valuable information about whether or not their values exceed the critical yield limit for a given polymer and allows for prediction of material's failure. There are several failure theories established for prediction of failure in metals such as Lame-Navier, Tresca and von Mises. Polymers, due to their time dependent nature, may not always be well described by the theories developed for metals. Nevertheless, being ductile materials, they tend to be better represented by von Mises (maximum octahedral shear stress theory) than by the other failure theories [167, 171].

Von Mises theory states that failure occurs when the maximum distortion energy (or maximum octahedral shear stress) at an arbitrary point in a stressed body reaches the value equivalent to the maximum distortion at failure (yield) in simple tension and may be expressed in terms of the principal components of stress as follows [171]:

$$\sigma_1^2 + \sigma_2^2 + \sigma_3^2 - (\sigma_1\sigma_2 + \sigma_2\sigma_3 + \sigma_3\sigma_1) = 2\sigma_f^2 \qquad \text{Equation 51}$$

where σ_1, σ_2, σ_3 are principal stresses and σ_f is von Mises equivalent stress.

It is worth mentioning that the von Mises stress is always positive because it is a square-root of a sum of stress values squared. Hence it is impossible to know from this alone, if the model is undergoing tension or compression. It, however, may be determined with the principal stress values. In the subsequent analysis, the residuals stresses in µ-parts were represented with both von Mises and maximum principal stresses. The former was used for assessment of the residuals stresses through the thickness while with the latter the µ-parts' failure probability was evaluated. Distribution of the maximum principal stresses through the µ-part's thickness was visualized as a probe through the thickness.

Moreover, similarly to analysis of the shear rate distribution through the thickness (section 5.5.2), the same four node paths were chosen to assess the variation in the residual stress pattern, through the change in the processing conditions. For each node path, one of the surface nodes corresponded to the centre points of the pressure and temperature sensors depicted earlier in Figure 77: P1 - N 29484 (400µm), P2 - N 28214 (400µm), T1 - N 14610 (300µm), T2 - N 15632 (200µm). For the sake of brevity, these paths through the µ-part's thickness will be further designated as: P1, P2, T1 and T2.

5.6.1 ABS

The state of the residual stresses in a µ-part (moulded with DOE2 processing conditions) constrained by the mould walls can be seen in Figure 96a. Right after ejection (Figure 96b), the constrained force from the mould is released and the µ-part shrinks to release the tensile process-generated residual stress reaching eventually its equilibrium state. The residual stresses in the µ-moulded part were analysed by applying elastic properties of the solid polymer. It can be easily seen that the stresses dropped by an order of magnitude after ejection. Moreover, uniform distribution of colours indicated no significant residual stress variation along the µ-part's length, which has to be expected due to typically low shrinkage rate of amorphous polymers.

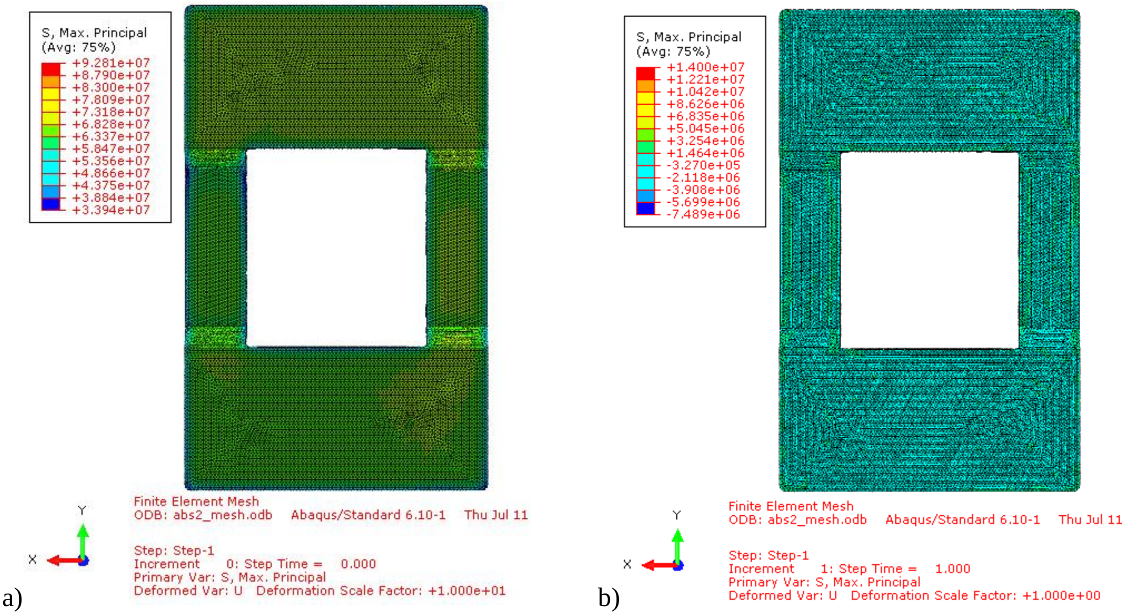

a) b)

Figure 96 - Maximum principal stress ABS (DOE2): a) inside the mould, b) after ejection

The finite element's state of the residual stresses, generated during AMI® simulations, is presented in a tensor form, where the normal stresses are equal in all direction and the shear stresses are null. Therefore, contrary to the observed for the maximum principal stress, the von Mises equivalent stresses are zero in magnitude while the µ-part still resides in the mould. After ejection from the mould and subsequent shrinkage, the distribution of the von Mises equivalent stresses is depicted in Figure 97. Here, the gradient in the stress distribution along the length became quite noticeable. Moreover, it suggests the stress magnitude may be related to the thickness of the µ-part as the thinner 200 and 300µm sections appear to be under lower residual stress than the thicker 400µm sections (Figure 97a). To understand how this non uniformity in residual stress distribution may affect the dimensional stability of the µ-part, a deformation scale factor was amplified ten times. However, non-visible deformation was detected as shown in Figure 97b.

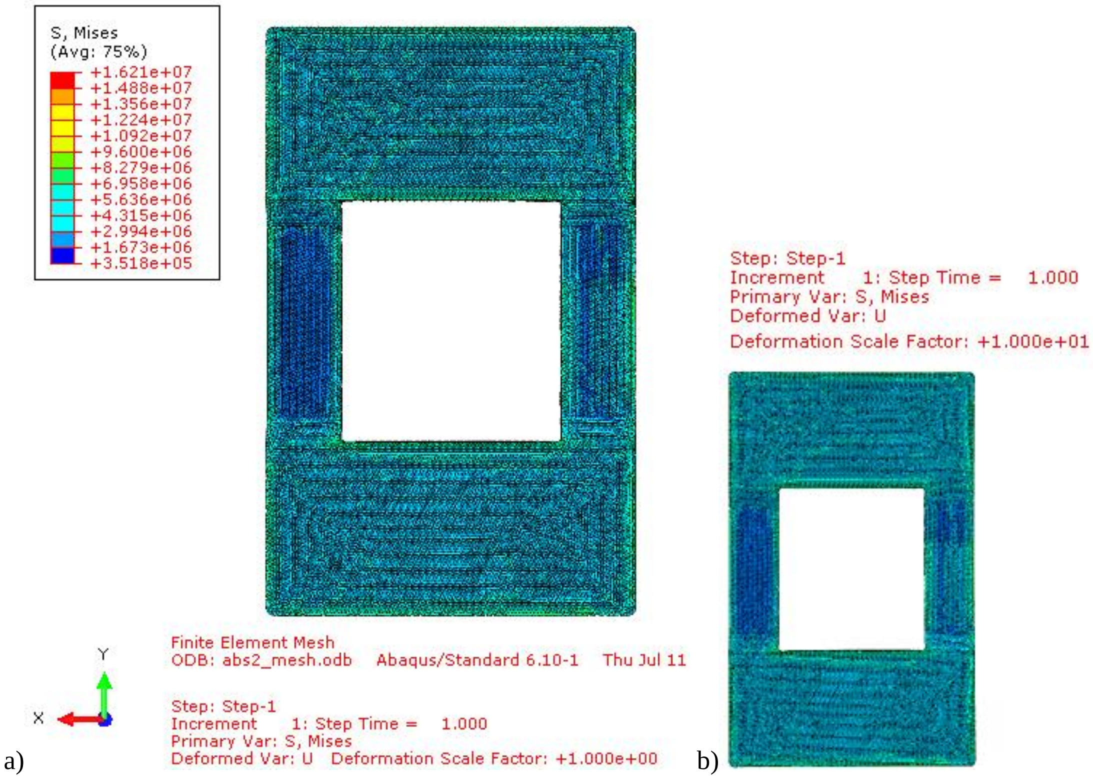

Figure 97 - Distribution of the equivalent von Mises stresses in ABS µ-part (DOE2): a) scale 1, b) scale 10

Distribution of the maximum principal stresses through the normalized thickness in four locations, designated earlier as P1, P2, T1 and T2, is depicted in Figure 98. The predicted residual stress is parabolic in shape for all probed locations, where the thicker interior portion of the µ-part is under tension and thinner surface layers are under compression. The simulation also indicates that in absolute values, the middle of the µ-part experiences higher residual stresses of 3.5MPa than the section closer to the surface (-1,2MPa). It was also evident that after ejection, the residual stresses are far below, 45MPa the yield stress limit established for CYCOLAC GPM5500S.

The overall level of the maximum principal stresses was assessed in terms of difference between the maximum tensile and compressive stresses which alternatively maybe expressed as the flatter the curve, the lower the stress. The lowest tensile and compressive stresses were both observed for the thinnest T2 (200µm) section of the µ-part, depicted as a green line, rising as it follows: T1, P1 and P2. Slightly higher residual stress was observed for the 400µm section, furthest from the injection point, which may occur due to faster cooling rates of this µ-part's section which may prevent enough pressure to build up and assure proper packing.

To perceive the differences in the residual stress distribution and magnitude in ABS µ-parts may change with alteration of the IM processing conditions, DOE1 (low T_m, T_{melt} and V_i) and DOE8 (high T_m, T_{melt} and V_i) residual stress results may be consulted in Appendix B (Figure B.1 and Figure B.2)

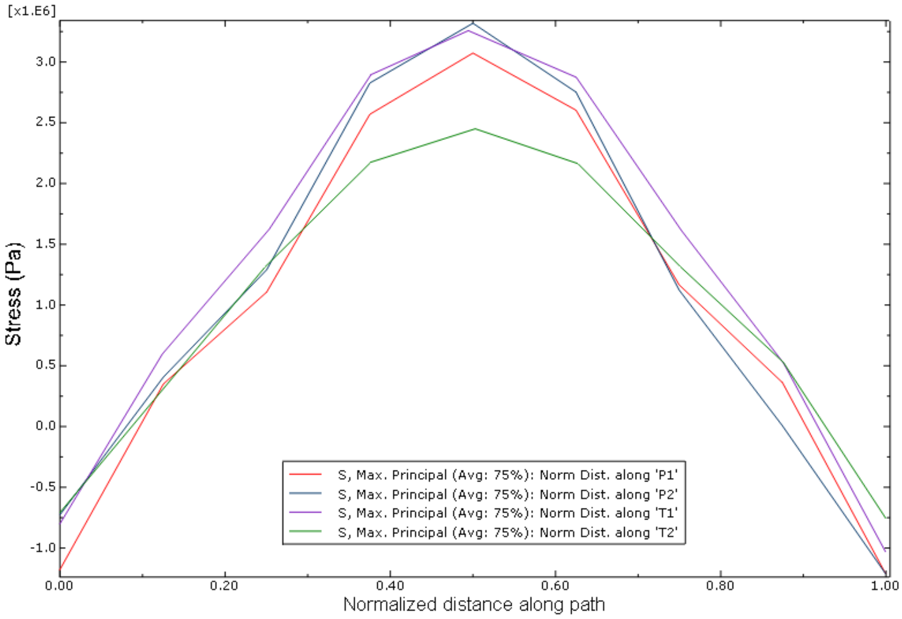

Figure 98 - Post ejection distribution of the maximum principal stresses through the thickness of ABS µ-part (DOE2)

The referred above pattern of the residual stresses maybe explained by the differential shrinkage through the thickness of the AMI® result, as can be verified from Figure 99. The shrinkage gradient through the thickness as well as the maximum values may be directly related to the residual stress magnitude and distribution. Shrinkage magnitude and gradient through the thickness of the μ-parts moulded under DOE1 and DOE8 processing condition are shown in Figure B.3 and Figure B.4, respectively.

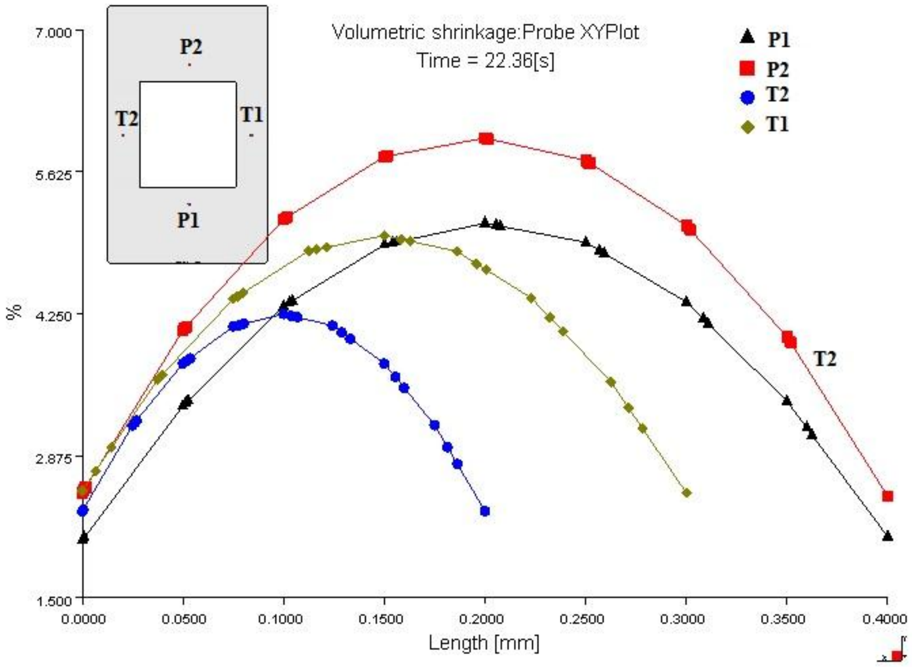

Figure 99 - Volumetric shrinkage through the thickness of ABS μ-part (DOE2)

As it has already been mentioned, the von Mises equivalent stress provides more adequate failure criteria for safe design of polymeric parts. As shown in Figure 100, when the residual stresses are assessed in terms of the maximum distortion energy (Equation 51), the maximum stresses moves from the centre of the μ-part (Figure 98) to its surface for all probed locations following the same increase trend as for the maximum principal stresses (Figure 100). Moreover, the influence of the thickness on the magnitude of the residual stresses becomes even more perceptible showing a strong positive correlation.

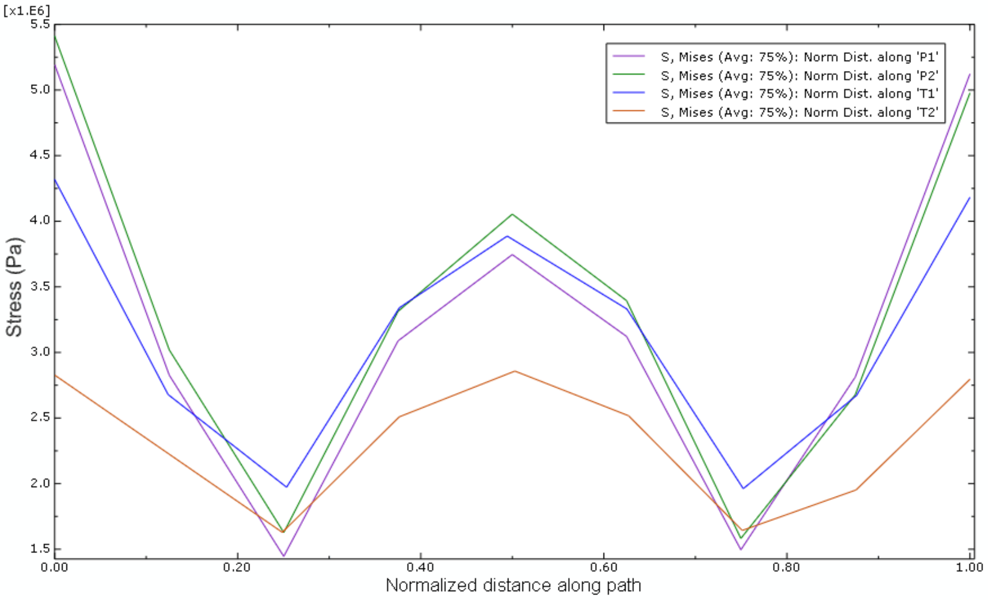

Figure 100 - Distribution of the von Mises stresses through the thickness of ABS µ-part (DOE2)

To emphasize the general trends in how the µIM processing conditions variation (Table 2) may influence the residual stresses in ABS µ-parts, the maximum values of von Mises stresses for P1, P2, T1 and T2 were compared in Table 15 and in Figure 101.

The choice for the optimized µIM processing conditions is unavoidably biased towards the required quality criteria which in the presented cases are the minimum built-in residual stresses. The latter is of utmost importance for long-term mechanical performance of the µ-parts. First of all, at higher mould temperature residual stresses tend to decrease (DOE5-DOE8) for all probed locations. Injection velocity appears to exert less influence. Its effect, however, becomes more evident when moulded with the low mould temperatures: DOE1 - low V_i vs. DOE2 - high V_i. Melt temperature may be considered as the less important factor for diminishing the residual stresses in ABS µ-moulded parts. Although, a decision about what set of the IM processing conditions results in the lowest residual stresses in the µ-moulded part may be not easy, mainly due to the fact that different combinations of the processing condition may not affect in the same manner the residual stress patterns at the sections with different thicknesses. However, comparing the data presented in Figure 101 and Table 15, it seems reasonable to conclude that DOE5 and DOE6 processing conditions lead to moulding of the µ-parts with the minimum levels of residual stresses.

The optimized µIM processing conditions can be therefore enumerated by an order of importance as follows: high T_m, low T_{melt} and either low or high V_i. Crossing this data with the assessment of the experimental variability of the µIM process for the ABS DOE5 and DOE6 processing conditions (Table 6), we get 89% of the µ-parts acceptance for the latter and 83% for the former. Thus, it is reasonable to conclude that DOE5 (high T_m, low T_{melt} and low V_i) constitutes the set of optimum processing conditions for successive moulding of the µ-parts of this particular geometry.

Table 15 - Maximum von Mises stress through the thickness of ABS µ-part

Experiment Nº	von Mises stress (Pa)			
	P1	P2	T1	T2
DOE1	4.46E+06	4,73E+06	3,14E+06	2,84E+06
DOE2	3.91E+06	4,14E+06	3,28E+06	2,10E+06
DOE3	3.73E+06	4,44E+06	2,83E+06	2,32E+06
DOE4	3.73E+06	4,64E+06	2,82E+06	2,20E+06
DOE5	**2.64E+06**	**3,47E+06**	**2,23E+06**	**1,47E+06**
DOE6	**2.87E+06**	**3,25E+06**	**2,41E+06**	**1,50E+06**
DOE7	3.17E+06	4,00E+06	2,46E+06	2,11E+06
DOE8	2,62E+06	4,19E+06	2,54E+06	2,11E+06

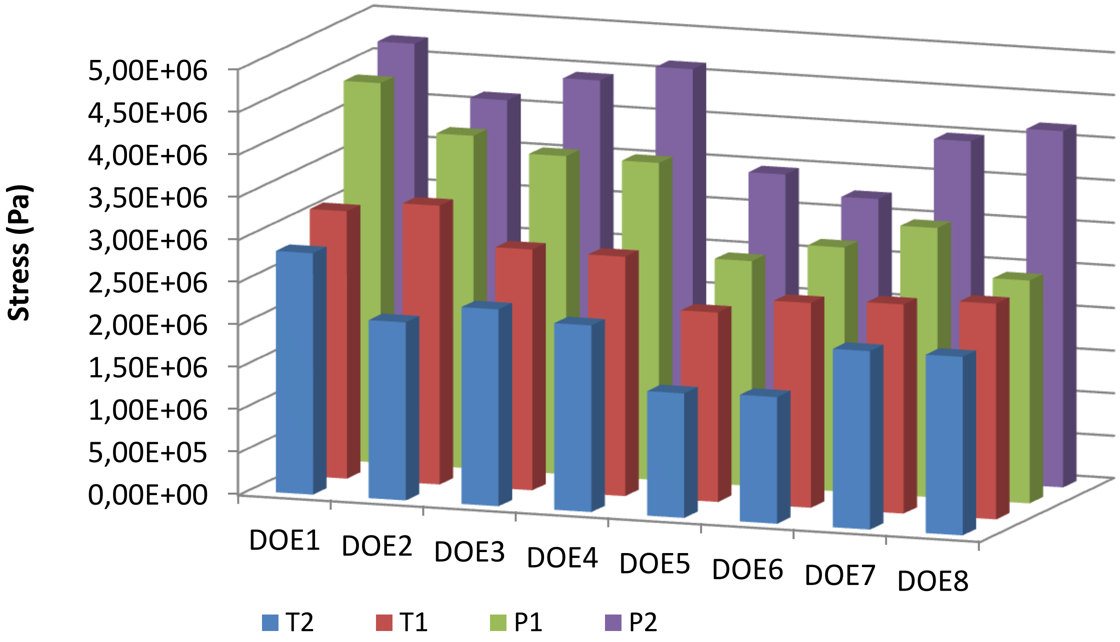

Figure 101 - Maximum von Mises stress from DOE1 to DOE8 processing conditions (ABS)

5.6.2 POM

For DOE2 processing conditions of POM, a highly non uniform distribution of the maximum principal stresses is visualized before ejection from the mould with a clear prevalence at the end of filling (Figure 102a). The majority of these stresses, however, were relieved after ejection from the mould (Figure 102b). To obtain a clearer picture of the residual stresses state, the latter were presented as von Mises equivalent stresses in Figure 103. The pattern of the residual stresses along the µ-part's length is quite peculiar. Beside the variation with the µ-part's thickness, also detected for ABS, it suggests highly uneven distribution of the residual stresses at the 400µm section at the end of filling. This can be attributed to excessive shear rate occurring during injection of POM (Table 10 and Figure 84). These observations suggest that the POM µ-part has much more tendency for warpage than the ABS one. It was confirmed by applying the same deformation factor as for ABS µ-part. As a result the POM µ-part appears severely distorted (Figure 103b).

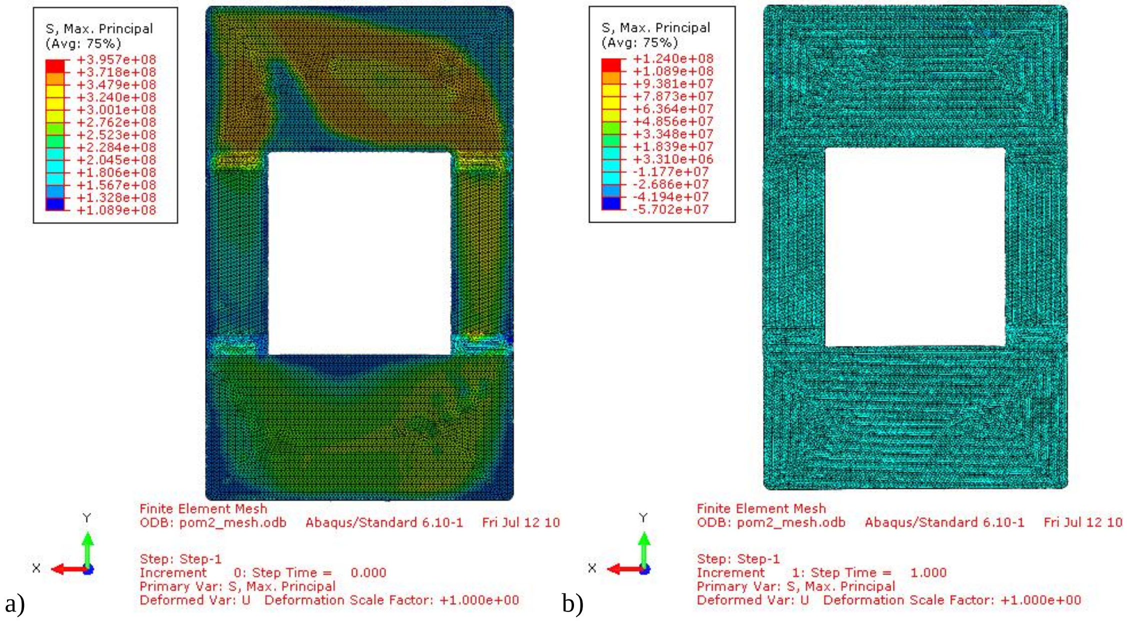

Figure 102 - Maximum principal stress POM (DOE2): a) inside the mould, b) after ejection

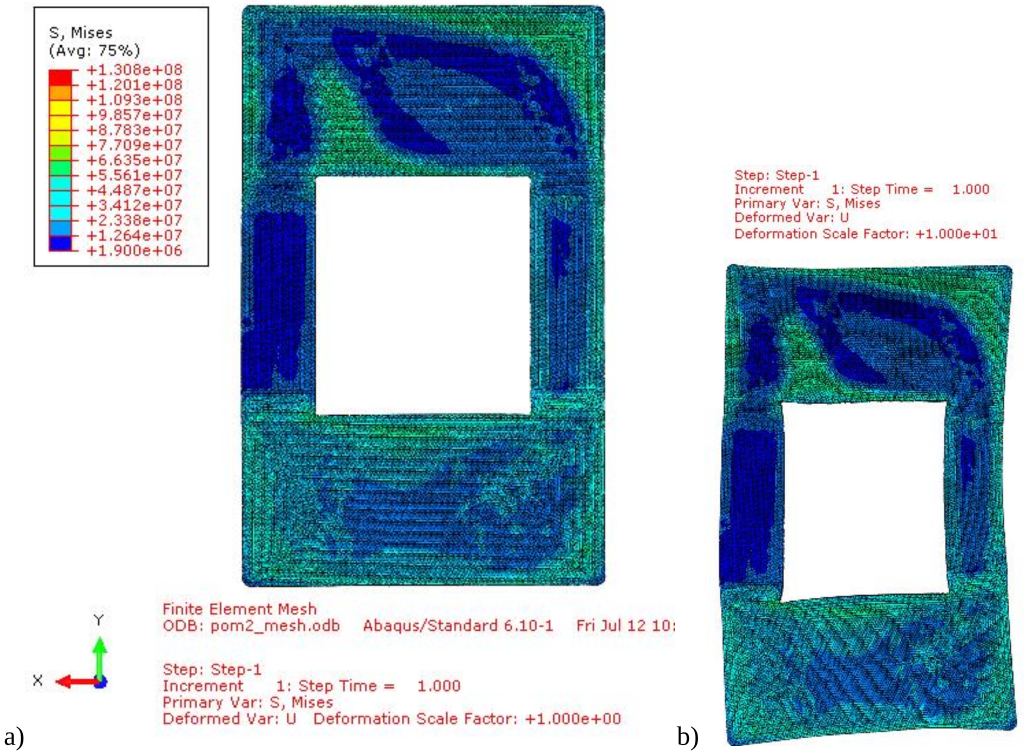

Figure 103 - Distribution of the equivalent von Mises stresses in POM μ-part (DOE2): a) scale, b) scale of 10

The profiles of the maximum principal stresses through the normalized thickness (P1, P2, T1 and T2) are similar in shape to the ones observed for ABS for all probed locations, where the thicker interior portion of the μ-part is under tension and thinner surface layers are under compression. However, the maximum stress values in both tension and compression deformation modes are almost by one order of magnitude higher than that of ABS, as shown in Figure 104, which suggests very high differential shrinkage in these locations. Despite the elevated residual stresses, the yield stress limit (64MPa) established for HOSTAFORM C 9021 was not surpassed. This statement is also valid for other combinations of the IM processing conditions as it can be confirmed from Figure B.5 and Figure B.6.

Using the same flatness-curve residual stress criterion, applied earlier for ABS, the lowest von Mises equivalent stresses were observed from Figure 105 for the thinnest T2 (200μm) section. The residual stresses in the other probed locations increased in the following order: P2, T1 and P1. This distribution of the residual stresses along the μ-parts length and especially highest residual stress close to the injection point may be explained by assessment of the shrinkage gradients in the probed location as depicted in Figure 106.

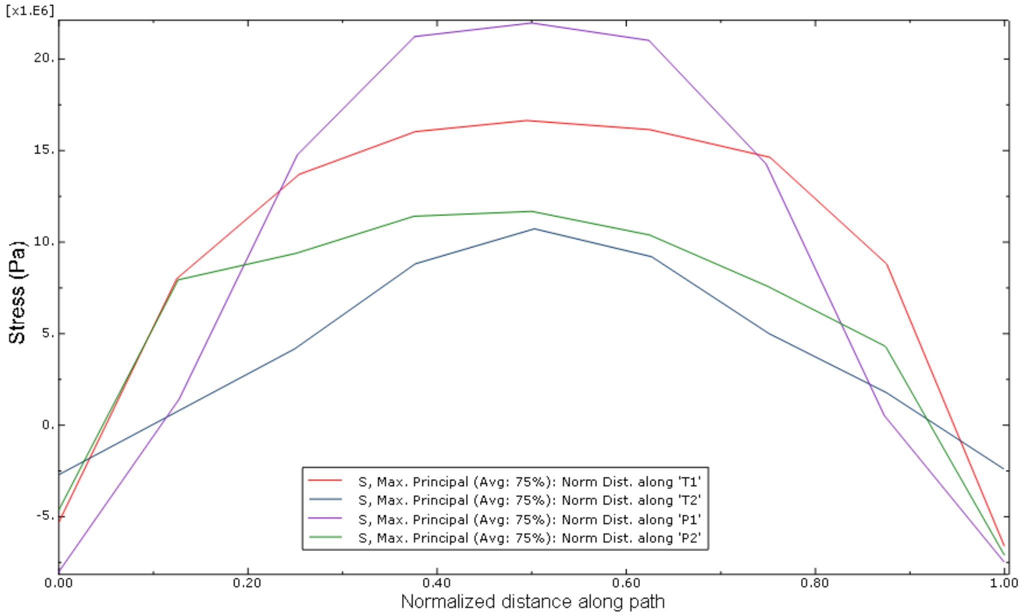

Figure 104 - Post ejection distribution of the maximum principal stresses through the thickness of POM μ-part (DOE2)

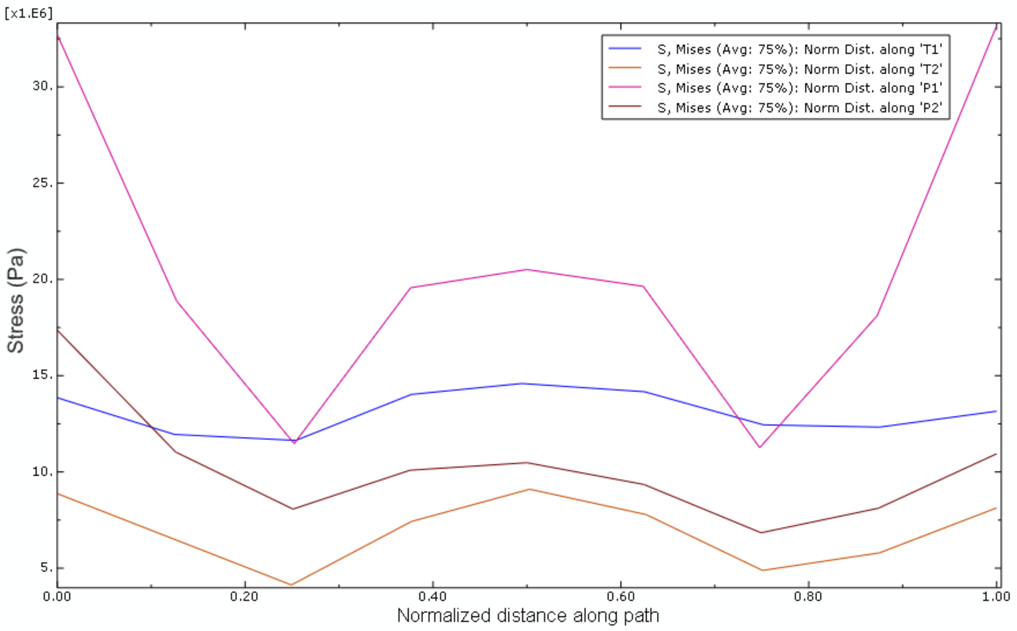

Figure 105 - Distribution of the von Mises stresses through the thickness of POM μ-part (DOE2)

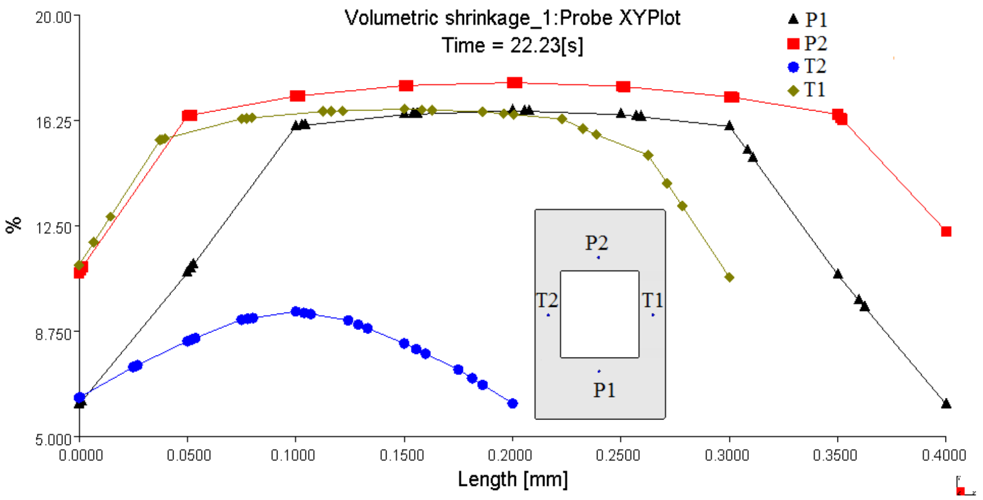

Figure 106 - Volumetric shrinkage through the thickness of POM μ-part (DOE2)

High shrinkage gradient through the P1 section (from 6.2% at the surface to 16.8% in the middle of the μ-part) generated elevated residual stresses, while at P2 section shrinkage variation does not exceed 5.3%, increasing from the 12.8% at surface to 17.8% in the centre. Altogether, it may represent serious problems, which as it has been shown in Figure 103b may compromise the structural integrity of the POM μ-part especially in case of some additional deformation. Some examples of the shrinkage gradient generated with different from DOE2 processing conditions are presented in Figure B.7 and Figure B.8.

Influence of the µIM processing conditions on the residual stresses in POM µ-parts is presented in Figure 107 and Table 16. Considering significant hesitation of the polymer flow in the microimpression, it becomes quite difficult to establish any pattern in the residual stress variation. Nevertheless, the mould temperature seems to exert positive effects on the reduction of the built-in residual stresses observed almost in all probe locations for DOE5-DOE8. In addition, the DOE2 processing conditions also result in residual stress reduction, when comparing to the other µ-parts moulded at lower temperature (DOE1, DOE3 and DOE4). The positive effect of the injection velocity on the residual stress reduction when moulded at low mould temperature was also detected for ABS polymer.

Table 16 - Maximum von Mises stress through the thickness of POM µ-part

Experiment Nº	von Mises stress (Pa)			
	P1	P2	T1	T2
DOE1	3,47E+07	3,67E+07	3,63E+07	2,83E+07
DOE2	**3,32E+07**	**1,74E+07**	**1,46E+07**	**9,10E+06**
DOE3	2,16E+07	4,38E+07	4,45E+07	1,79E+07
DOE4	2,38E+07	4,13E+07	4,30E+07	1,79E+07
DOE5	1,59E+07	4,15E+07	1,54E+07	1,97E+07
DOE6	1,46E+07	1,93E+07	1,45E+07	2,29E+07
DOE7	1,36E+07	3,44E+07	2,34E+07	7,40E+06
DOE8	1,48E+07	4,16E+07	1,29E+07	5,92E+06

After consulting the data in Table 16, it was found out that when moulded with the DOE2 and DOE6 processing conditions the residual stresses are lowest in the majority of locations. However, after verification of the experimental µIM process variability for the POM at DOE6 processing conditions (Table 6), it was found out the acceptance rate for this particular injection set was only 68%, indicating one of the highest rejection rates for this polymer. Meanwhile, the acceptance rate of the µ-parts moulded with DOE2 processing conditions was significantly higher (91%). Therefore, by conjugating these two quality criteria, the DOE2 (low T_m, low T_{melt} and high V_i) experiment run represented the best combination of the processing conditions towards the reduction of the residual stresses.

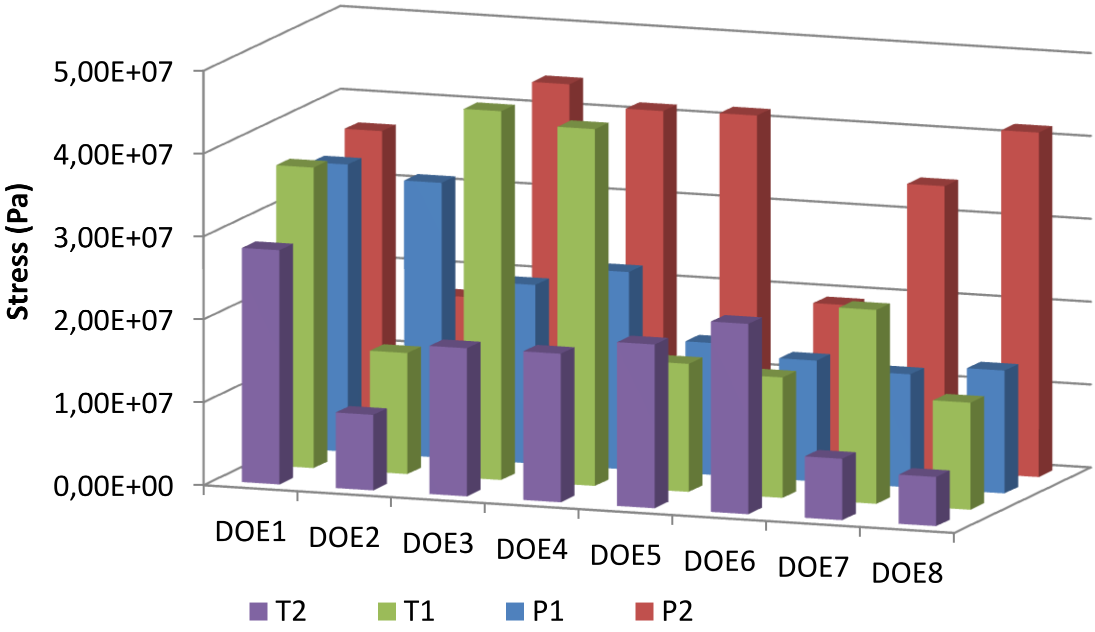

Figure 107 - Maximum von Mises stress from DOE1 to DOE8 processing conditions (POM)

5.6.3 PP

Residual stress distribution in the PP µ-part constrained inside the mould shows the higher values at the 400µm section more distantly located from the injection point (Figure 108a). After removing the mould constraints and allowing the part to shrink, the major portion of these built-in stresses was relieved (Figure 108b). More precise estimation of the remained residual stresses was obtained from the von Mises stress plot (Figure 109a). The previously mentioned 400µm section is definitely under significantly higher residual stresses than the rest of the µ-part, which was also confirmed after amplifying ten times the deformation scale (Figure 109b).

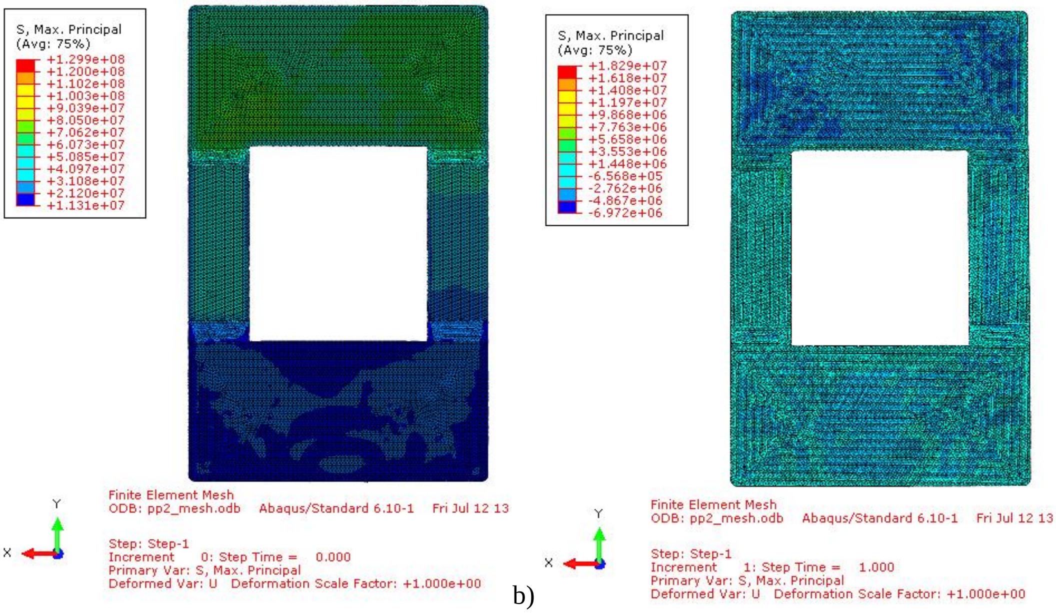

a) b)

Figure 108 - Maximum principal stress in PP (DOE2): a) inside the mould, b) after ejection

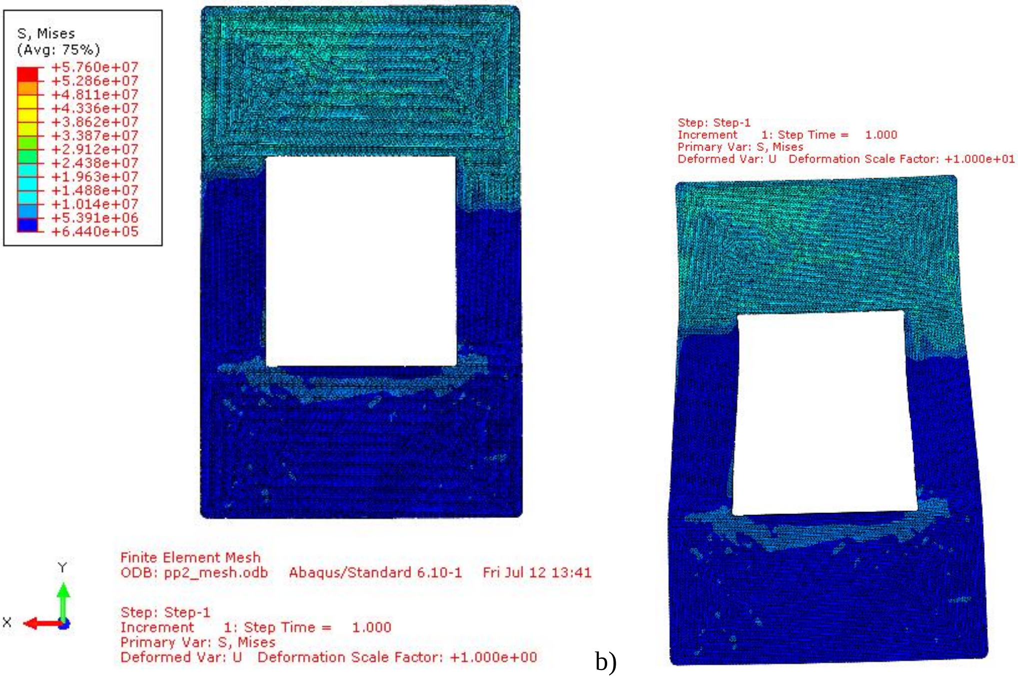

a) b)

Figure 109 - Distribution of the equivalent von Mises stresses in PP μ-part (DOE2): a) scale, b) scale 10

Typical parabolic shapes of the maximum principal stresses through the normalized thickness (P1, P2, T1 and T2) may be seen in Figure 110. The stresses are quite low, being the same order of magnitude as in ABS µ-parts, with an exception for the stress distribution for P2 (400µm) location, which maximum (11MPa) is several times higher than that of the other three stress profiles. However, this high stress is still several times lower than the yield stress limit (35MPa) for Moplen HP500N. To illustrate how the residual stresses change in µ-moulded PP parts under different µIM processing conditions, their patterns for DOE1 and DOE8 runs are presented in Figure B.9 and Figure B.10.

The similar to ABS dependence of the residual stress magnitude on thickness was also verified for PP, where the residual stress steadily rises with an increase in thickness. The post-ejection part shrinkage and warpage are driven by the in-cavity residual stress (Figure 108a). High differential shrinkage in P2 (400µm) path from 4.7% at the surface to 16% in the µ-part's centre (Figure 111) is connected to high residual stress depicted in Figure 110. Similar conclusions may be applied for DOE1 and DOE8 experiments as it can be observed from Figure B.11 and Figure B.12.

As the thinner 200µm and 300µm sections solidify much faster than the 400µm one, the P2 400µm section was cut from the polymer supply whilst at the region closer to the gate (P1) the packing pressure was acted longer, which resulted in lower shrinkage.

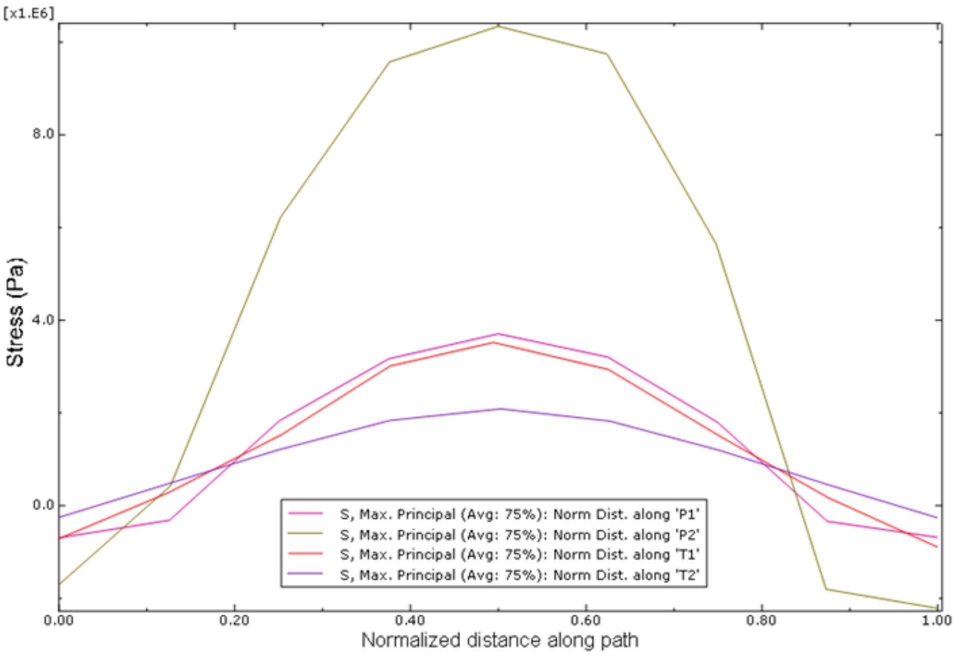

Figure 110 - Distribution of the maximum principal stresses in PP µ-part (DOE2)

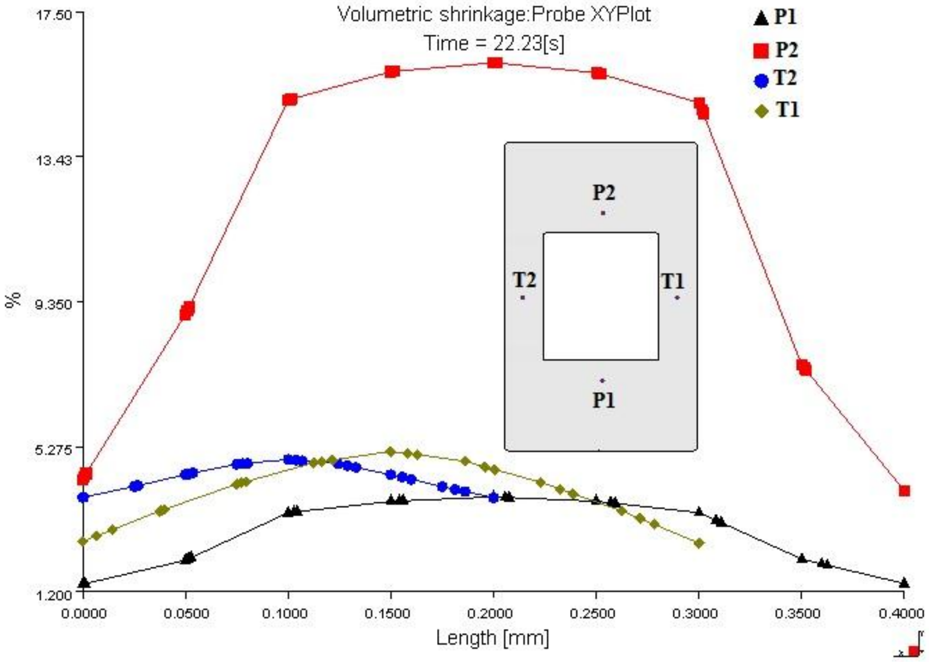

Figure 111 - Volumetric shrinkage through the thickness of PP µ-part (DOE2)

The µIM processing conditions (Table 2) had definite influence on the residual stresses in PP µ-parts. From Figure 112 and Table 17, the prevalence of the high mould temperature on the decrease in residual stresses is notable especially for the thicker (P1, P2) 400µm sections. After analyzing the values presented in Table 17, it was found out that the DOE6 experiment conditions (high T_m, low T_{melt} and high V_i) result in lower residual stresses, which is more notable for P2 location. The µIM process variability with this processing condition is zero, meaning a 100% acceptance rate (Table 6). Therefore this set of the processing conditions was considered to be an optimum for moulding of the PP µ-parts of this particular geometry.

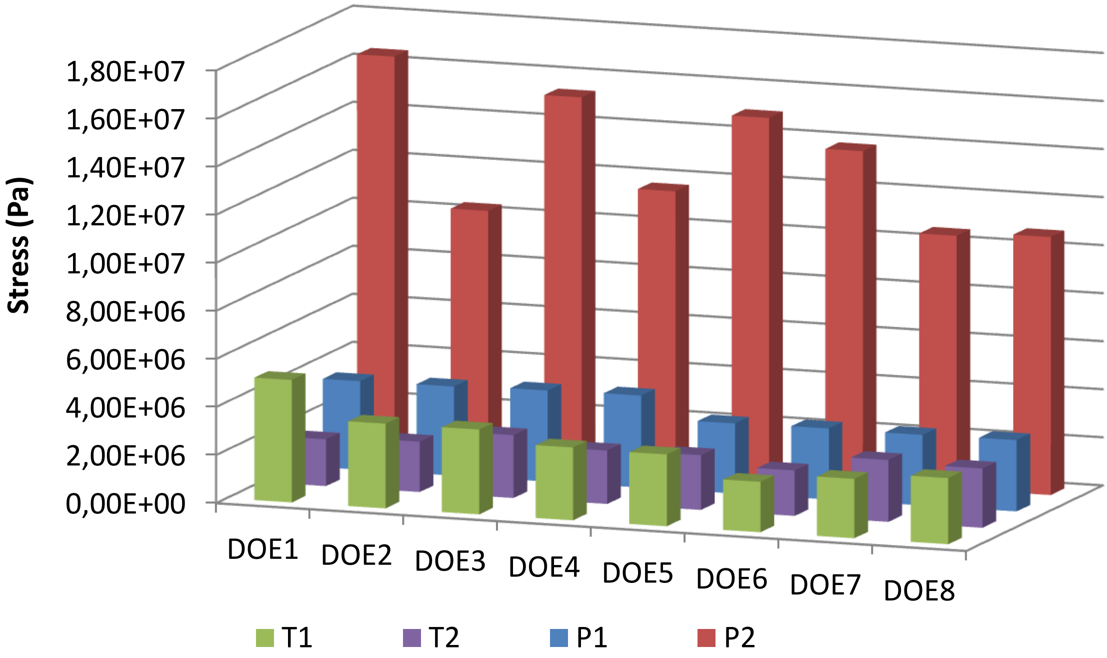

Figure 112 - Maximum von Mises stress from DOE1 to DOE8 processing conditions (PP)

Table 17 - Maximum von Mises stress through the thickness of PP μ-part

Experiment Nº	von Mises stress (Pa)			
	P1	P2	T1	T2
DOE1	4,59E+06	1,58E+07	4,11E+06	2,16E+06
DOE2	5,43E+06	1,44E+07	3,83E+06	1,81E+06
DOE3	4,51E+06	1,45E+07	4,57E+06	3,12E+06
DOE4	4,48E+06	1,48E+07	2,94E+06	1,97E+06
DOE5	3,15E+06	1,43E+07	3,54E+06	2,76E+06
DOE6	**3,71E+06**	**1,31E+07**	**3,23E+06**	**1,91E+06**
DOE7	3,76E+06	1,42E+07	2,52E+06	2,80E+06
DOE8	3,87E+06	1,43E+07	3,37E+06	2,77E+06

5.7 Assessing mechanical properties of ABS

5.7.1 200 and 300µm microparts

In order to determine the applicability of the TTSP for mechanical testing of µ-moulded parts, thermorheological simplicity of the material might be ascertained. To do so, the DMTA experimental data is transferred into the developed MATLAB® application for construction of the van Gurp-Palmen plot, which relates the phase angle tan(δ) to the absolute value of the complex modulus G*. In addition, this method may indicate the necessity of vertical shifting [173, 223]. Two van Gurp-Palmen plots were constructed as depicted in Figure 113 and Figure 114 for 300µm and 200µm parts respectively. This way of plotting eliminates the effect of shifting along the frequency axis and yields temperature independent curves when TTSP is applicable. From the van Gurp Palmen plots, it became clear that a unique single curve was not obtained for both µ-parts, indicating failure of the TTSP. However, some kind of superposition tends to form for the temperature range from 30 to 55ºC, being especially notable in 300µm part.

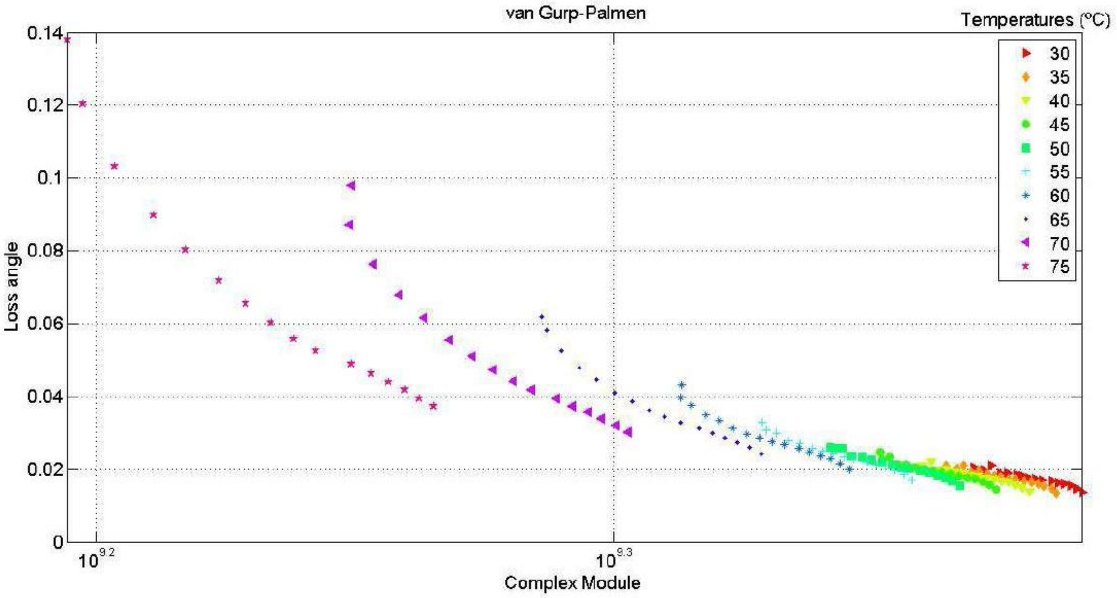

Figure 113 - van Gurp-Palmen plot for 300µm micropart

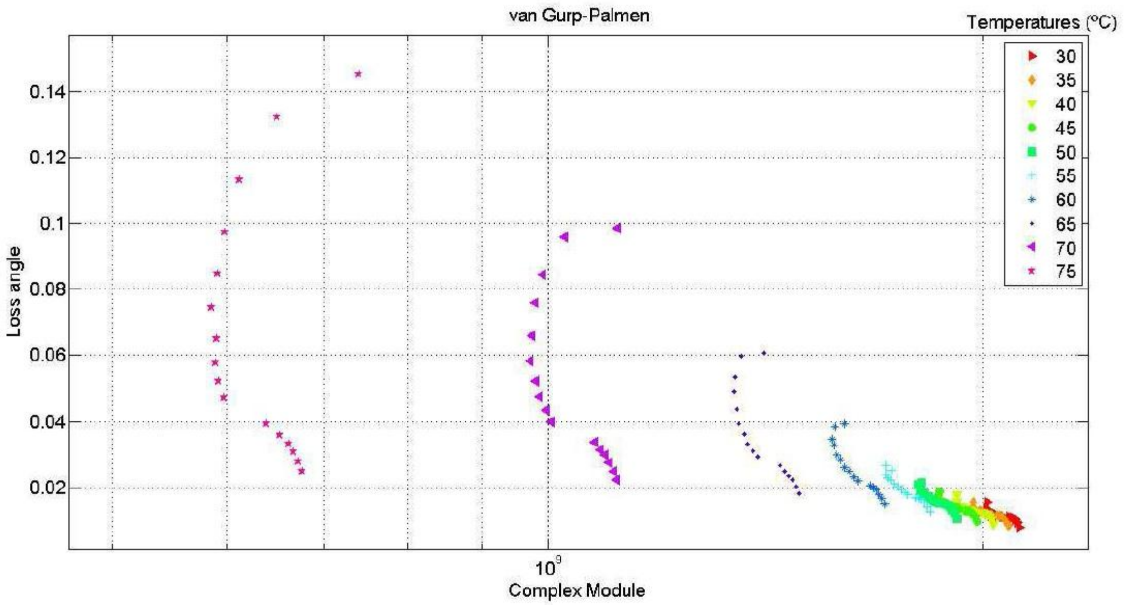

Figure 114 - van Gurp-Palmen plot for 200µm micropart

In order to improve the superposition, the vertical shift was added. The latter, however, did not seem to improve the accuracy of the superposition for both µ-parts. As it can be seen in Figure 115 and Figure 116 for the 300µm part and in Figure 117 and Figure 118 for the 200µm part, neither loss nor storage moduli were possible to superpose into a single master curve.

Only partial superposition was detected for the loss modulus indicating that the isotherms are likely to merge up to 60ºC. A degree of superposition was lower for the storage modulus starting to diverge at 55ºC. The obtained results suggested that TTSP was not holding for both µ-parts. A possible explanation may lay in the non-uniform thickness of the specimen. The latter was mounted in the DMTA in way that the clamps hold the µ-part at the thicker 400µm section while sinusoidal deformation was applied at the thinner one and therefore alteration in thickness may be responsible for the uneven distribution of the applied stress. This may bring a certain level of uncertainty to the obtained results. That is the reason why no definite conclusion about the validity of the TTSP may be drawn by testing the samples of these particular geometries.

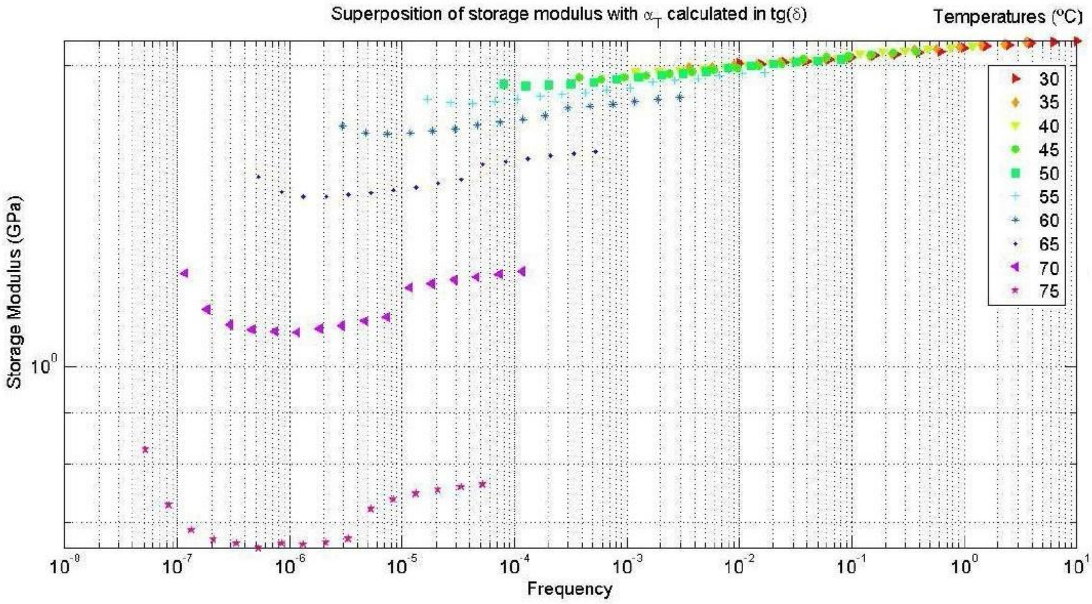

Figure 115 - Superposition of the storage modulus with vertical shifting (300µm part)

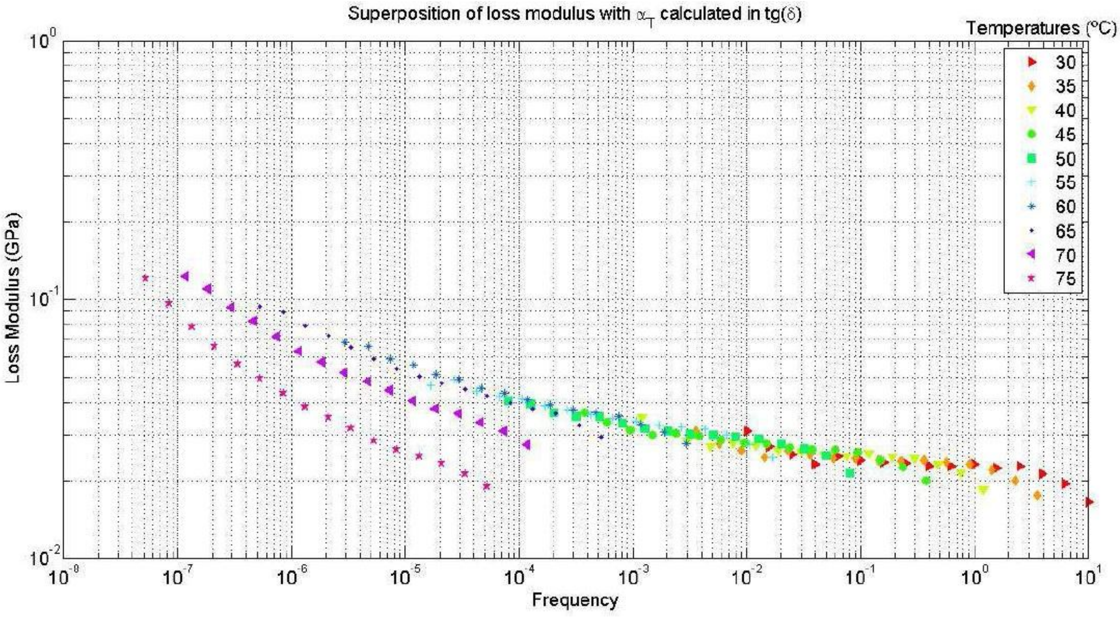

Figure 116 - Superposition of the loss modulus with vertical shifting (300µm part)

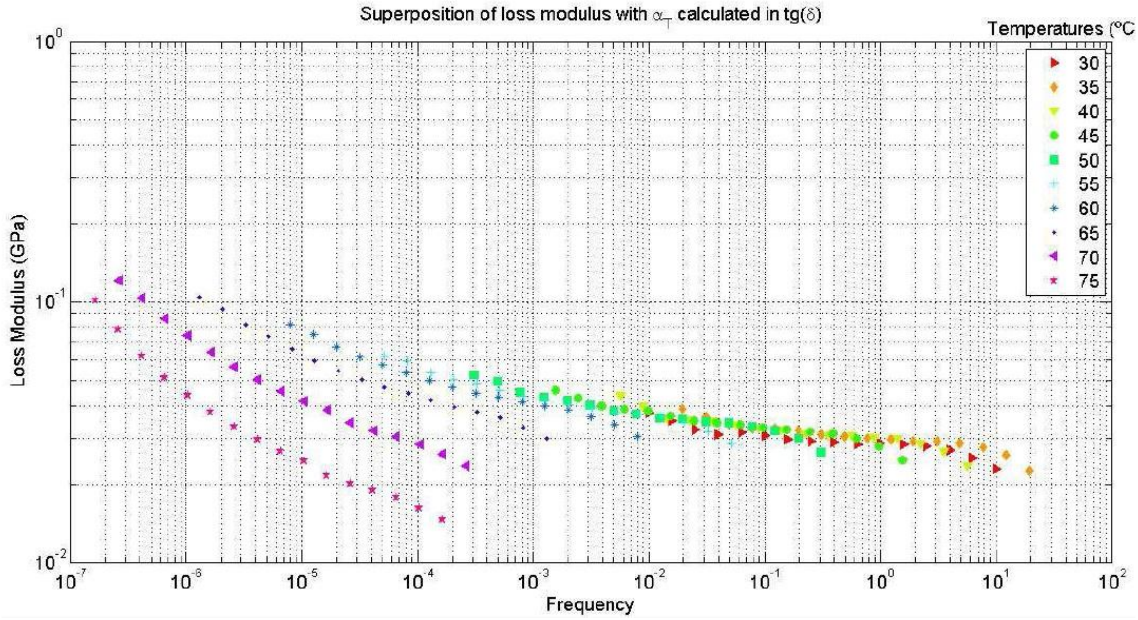

Figure 117 - Superposition of the loss modulus with vertical shifting (200µm part)

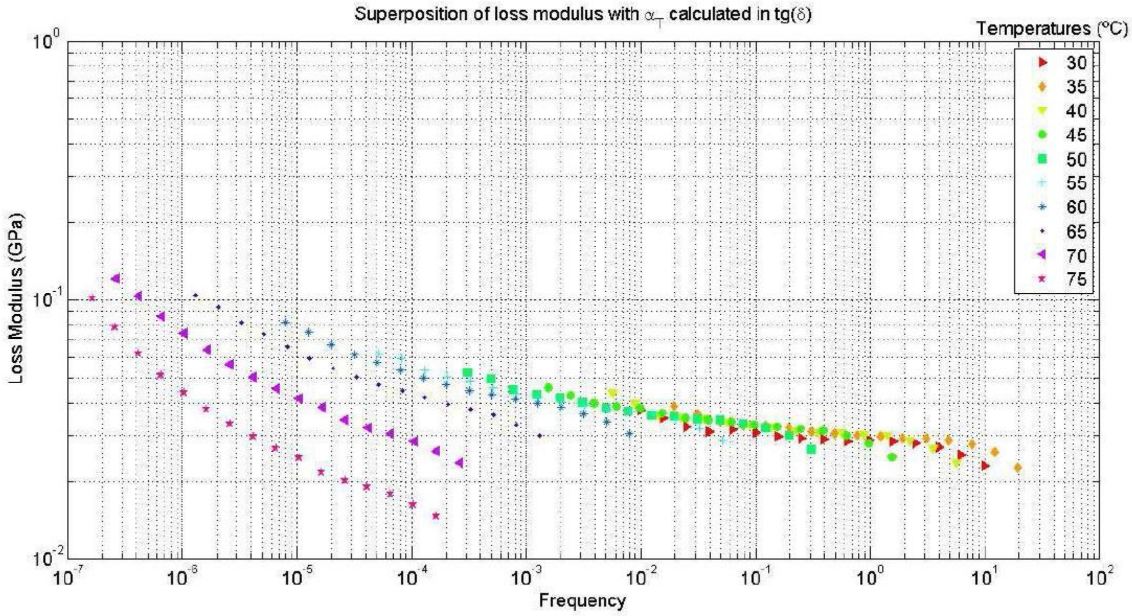

Figure 118 - Superposition of the storage modulus with vertical shifting (200µm part)

5.7.2 600μm microparts

The same analysis routine, as described in the previous section, was used for applying the TTSP towards the assessment of the mechanical properties of the ABS 600μm parts. Van Gurp-Palmen plot (Figure 119) indicated much better superposition in comparison with the μ-parts of variable thickness. Although some deviations in the matching curves were observed at higher temperatures, the majority of data were superimposed successfully, indicating that the influence of the vertical shift b_T was insignificant. The latter ascertains the thermorheological simplicity of the material and hence the TTSP validity for ABS. Then, the storage and loss moduli were superimposed into the respective master curves at a reference temperature of 30ºC, as presented in Figure 120 and Figure 121.

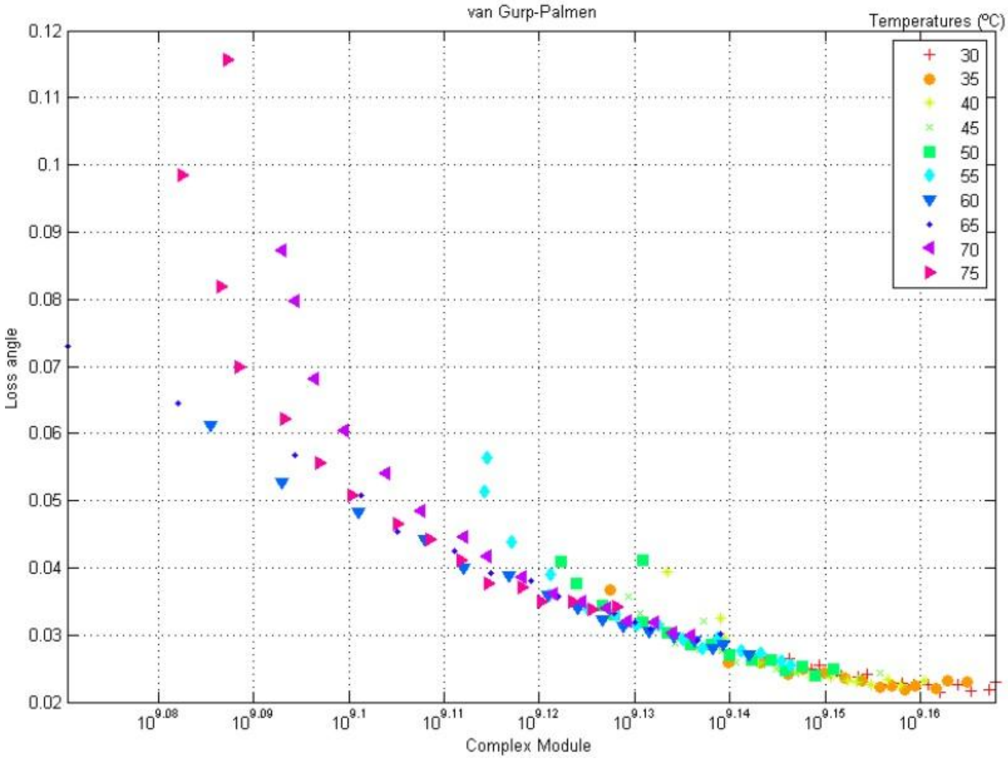

Figure 119 - van Gurp Palmen plot for 600μm part

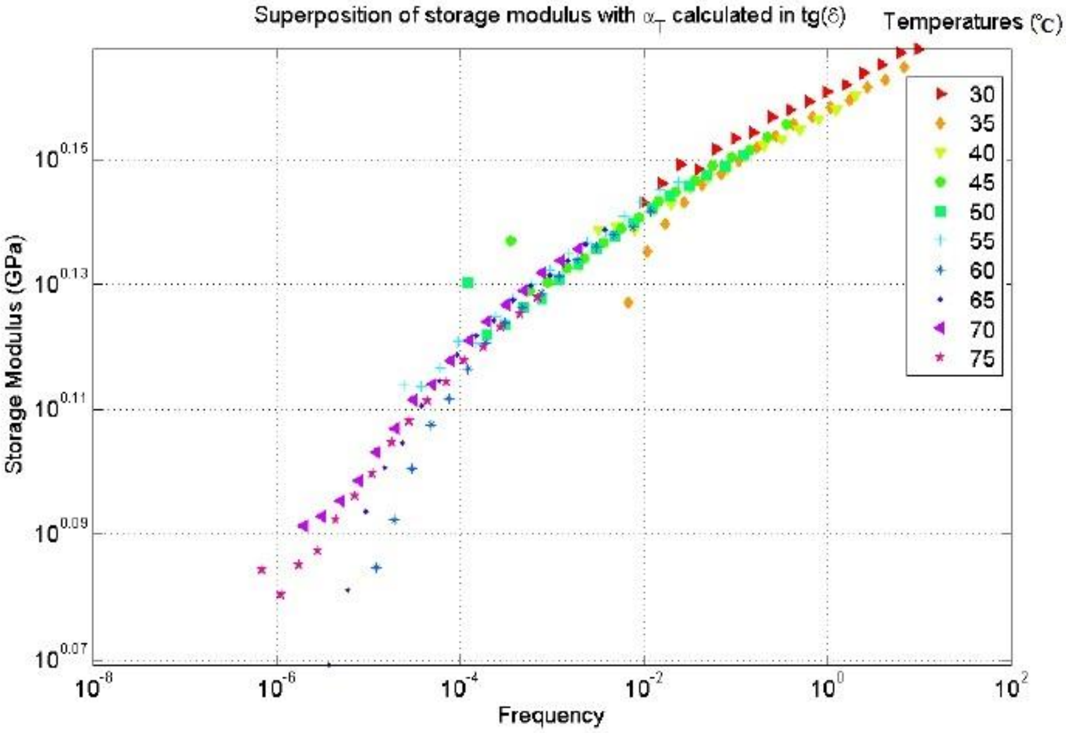

Figure 120 - Master curve for storage modulus for 600µm parts

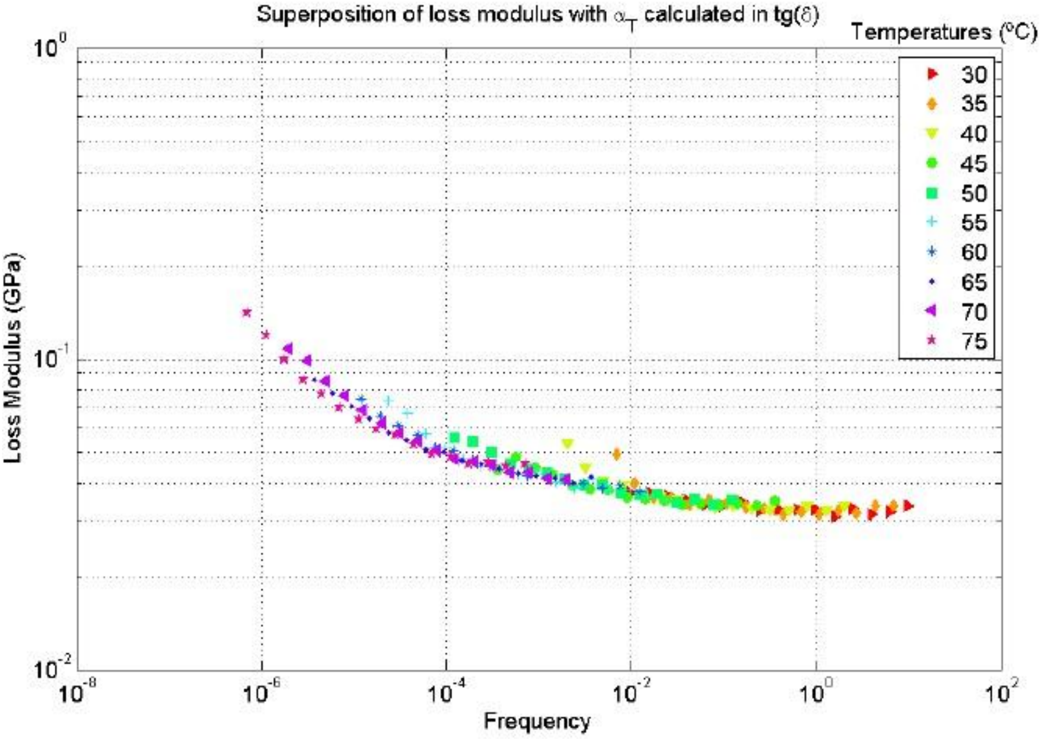

Figure 121 - Master curve for loss modulus for 600µm parts

The condition for applicability of the TTSP appears to be satisfied as the same values of α_T were adequate for superposing both storage and loss moduli. Nevertheless, a slight dispersion of some experimental points must be mentioned. There are several possible explanations for this occurrence. At higher temperatures, it may be attributed to an increase in movement on the molecular segments. While at lower temperature, both systematic and random errors may exert influence, for example, slight misalignment of the test specimen between the dynamical mechanical analyser clamps. The shift factors obtained during the superposition were used for calculation of the activation energy E_a in the Arrhenius equation (Equation 28). The activation energy then was obtained as a function of the slope of Log α_T (T) versus (1/T) − (1/T_0) in Figure 122, amounting to 198.4kJ/mol.

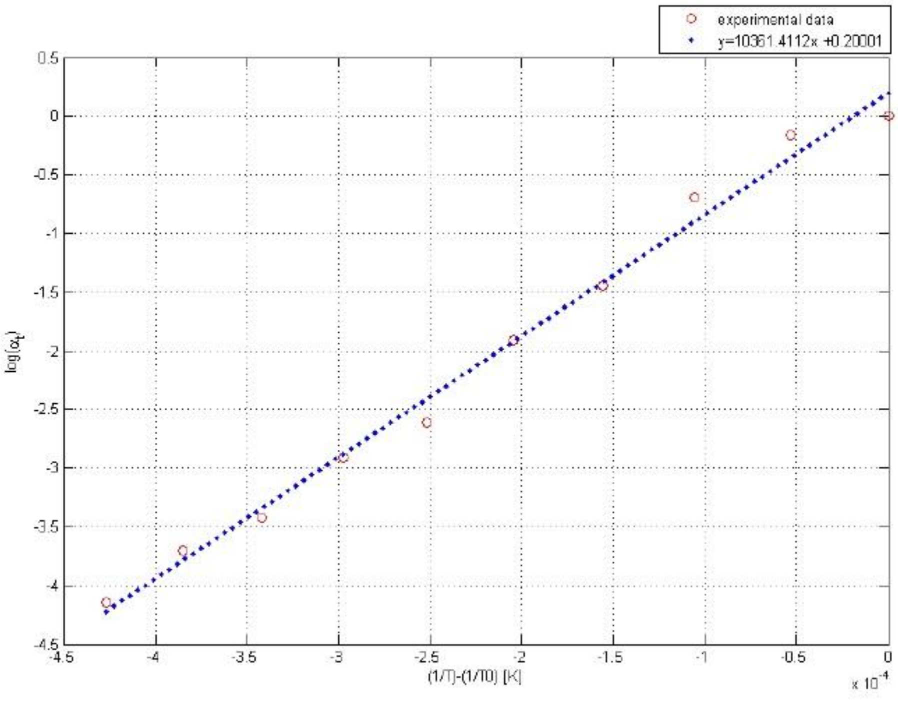

Figure 122 - Linear regression for activation energy

5.8 Structural analysis of ABS µ-part

The frequency dependent test data required for calibration of the viscoelastic model was automatically calculated with the MATLAB® application. The values were extracted from the master curves for loss and storage moduli and presented in Table 18.

Table 18 - Data for calibration of the linear viscoelastic material model

$\omega(g^*)$real	$\omega(g^*)$imaginary	Frequency ω
0.119521	-0.05694	3.39E-006
0.10016	-0.252621	1.26E-005
0.0703479	-0.262141	4.23E-005
0.0584746	-0.287159	0.000101767
0.0464621	-0.346769	0.00101763
0.0428491	-0.372563	0.00214426
0.0385594	-0.399576	0.0142132
0.0350469	-0.41453	0.0364421
0.0338099	-0.42357	0.245169
0.0341313	-0.47817	10

The submitted test data was calibrated with a nonlinear least-square fit (Equation 45) to determine the Prony series parameters from the storage and loss moduli cyclic test data.

The calibration results for storage and loss modulus are shown respectively in Figure 123 and Figure 124. It becomes clear that the best fit was obtained for the loss modulus. The storage component, however, represents some deviation from the test data although the maximum average root-mean-square error was quite small (1.3%).

The experiment was conducted as follows. After applying the first “general static” step, which simulates the ejection of the µ-part from the mould, a second “static” step was incorporated into the input file. At this step, an instantaneous strain of 20µm was imposed at the one 400µm side if the µ-part, whilst the opposite side was fixed in all directions. The relaxation process was simulated by applying the third - ”Visco” step and fixing the experiment time at 360000 seconds.

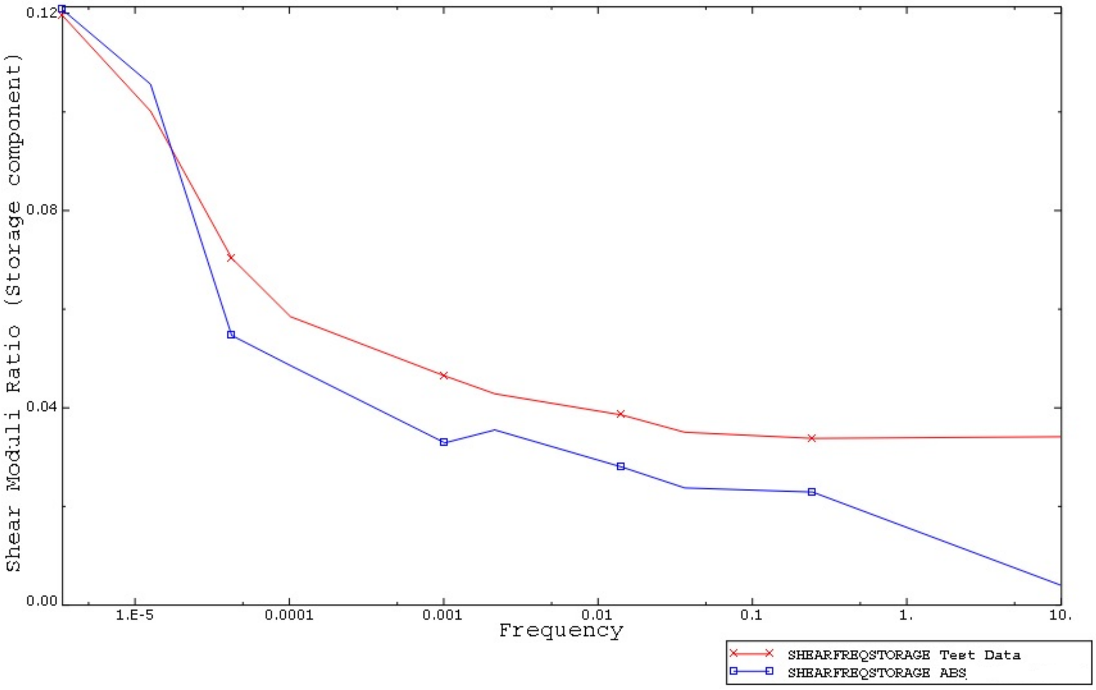

Figure 123 - Shear moduli ratio (storage component)

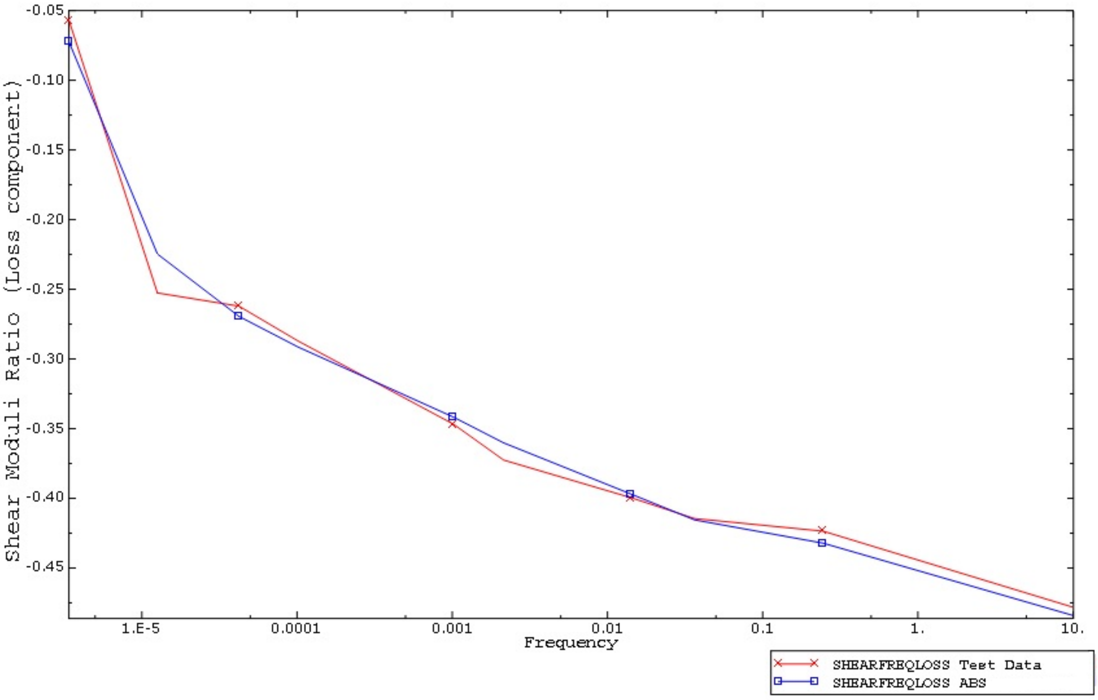

Figure 124 - Shear moduli ratio (loss component)

Analysing the stress distribution in the µ-parts after applying the fixed deformation with DOE2 generated residual stresses (Figure 125a) and for the µ-part without residual stress (WRS) (Figure 125b), the former was found out to be under significantly lower stress. After maintaining the µ-part in that condition for 100 hours, the results observed in Figure 126 indicate that the stresses decay over time which is in accordance with the viscoelastic nature of polymers.

To see more closely how the stress relaxation progresses, its decay over time was monitored for elements 729585, 782248 and 824373 in the 300µm section and for elements 514288, 536083 and 585076 in 200µm sections (Figure 126). These sets of elements are evenly spaced through the length of the section and therefore it turns possible to figure out which area is under higher stress.

The results depicted in Figure 127 show gradual reduction of the stress levels which can be explained with the rearrangements of molecular chains in order to accommodate the stress. Moreover, the maximum stress generated during deformation appears to concentrate right in the middle of both thicker and thinner sections, where their respective elements 782248 and 536083 are represented by the brown and green lines. As it can be seen from Figure C.1 and Figure C.2, this gradual reduction of the stress levels was also typical for other experiments.

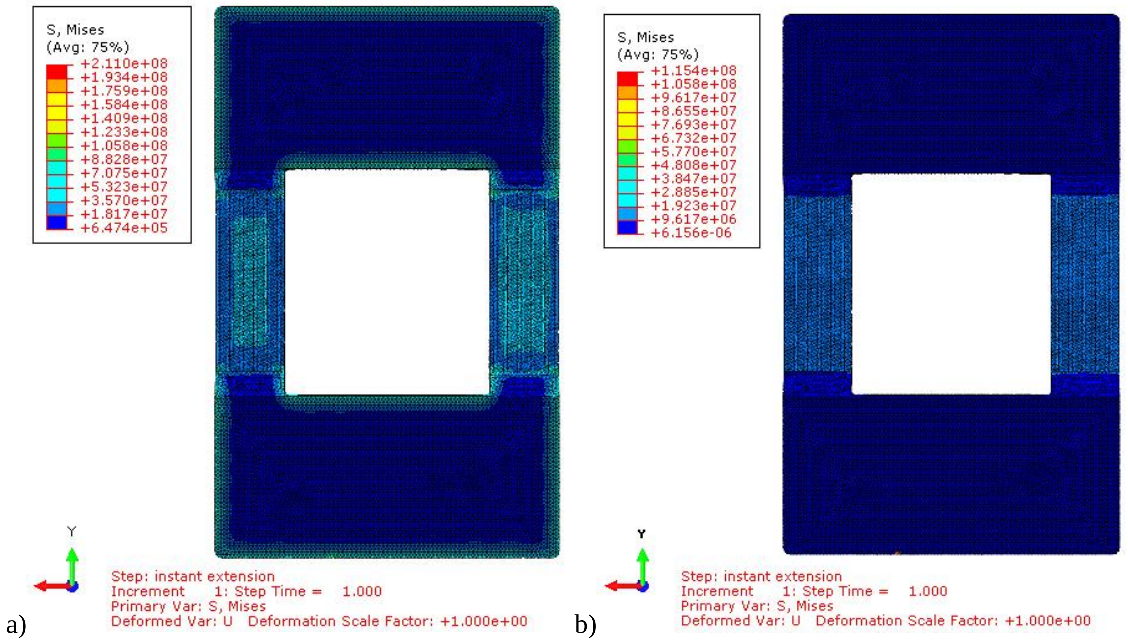

Figure 125 - von Mises stresses after initial extension: a) DOE2, b) WRS

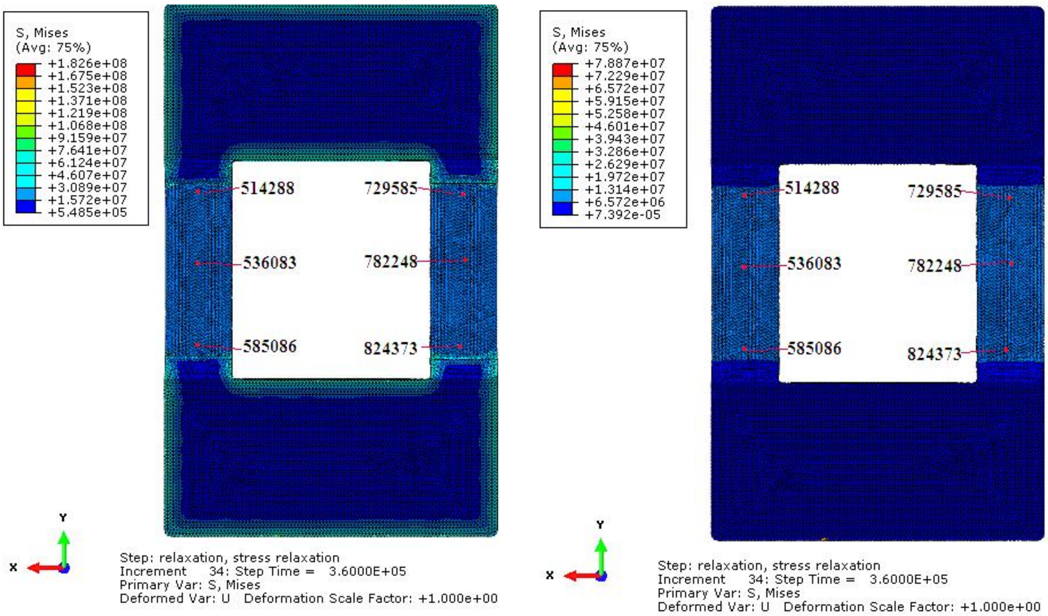

Figure 126 - von Mises stresses after 100 hours of relaxation: a) DOE2, b) without residual stresses

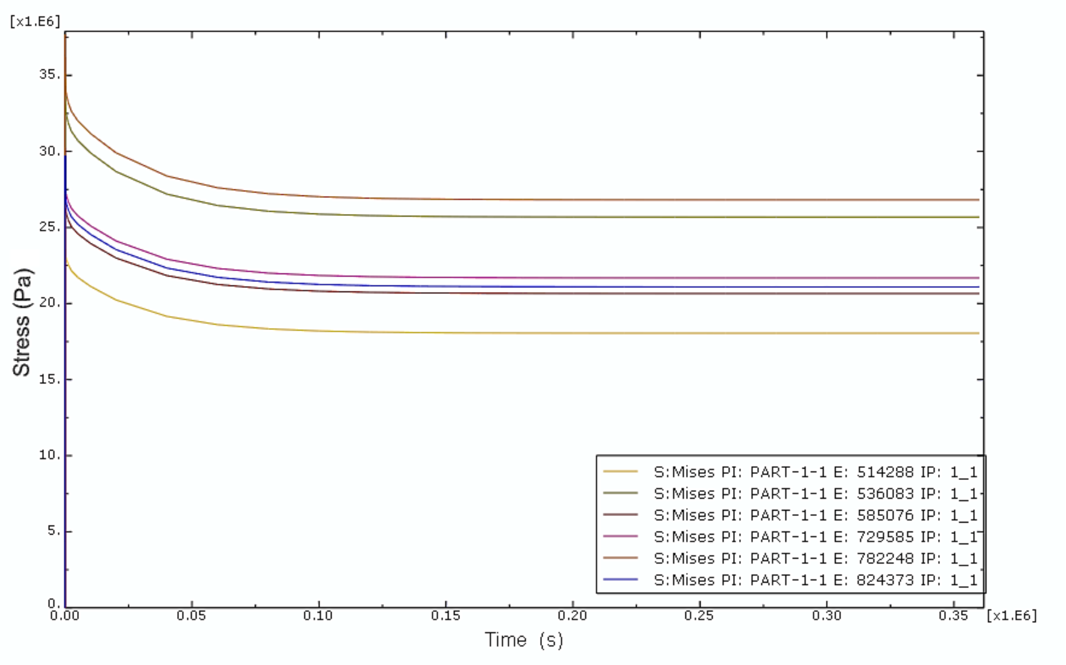

Figure 127 - Relaxation of the stresses in 200 and 300µm sections of µ-part (DOE2)

Stress relaxation in the µ-part without residual stresses is shown in Figure 128. The stress generated during the deformation step was about 12MPa which is several times lower comparing with the µ-part which thermo mechanical history was taken into account.

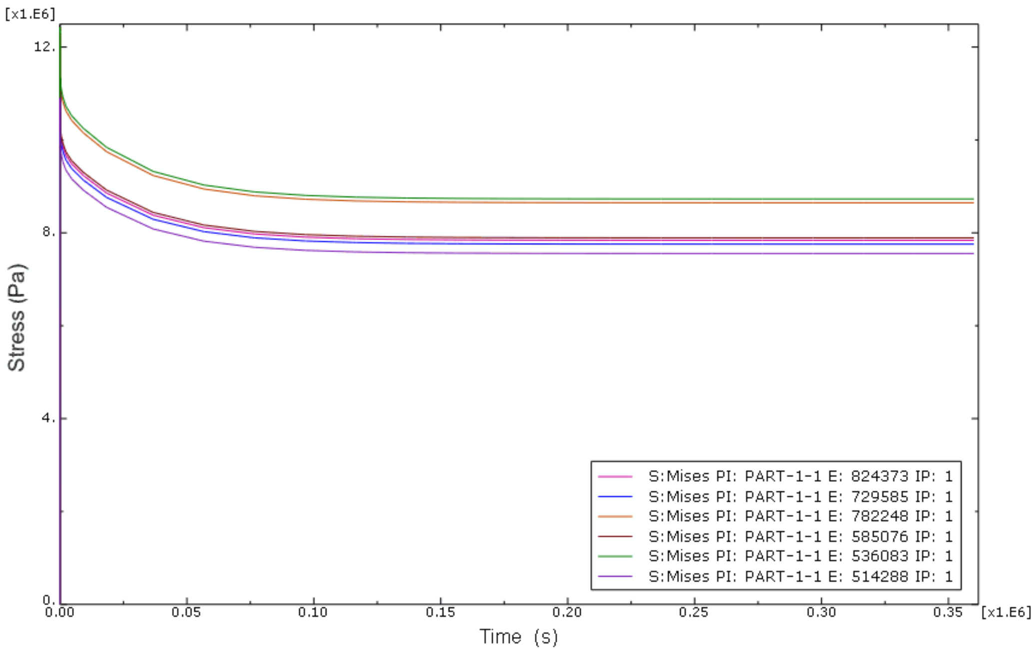

Figure 128 - Relaxation of the stresses in 200 and 300µm sections of WRS µ-part

Comparing the stresses for elements in the middle of each 200µm and 300µm sections for the initial stage of the stress relaxation, it is evident that during the first two steps, both deformation and residual stress increment are linear (Figure 129). After initiation of the “visco” step, stresses start to decay over time.

It has already been discussed in section 5.6 that distribution of the residual stresses is not uniform through the thickness of the µ-part. In order to understand the effect of the non-homogeneity on the stress relaxation, stress distribution through the 200µm and 300µm sections for DOE2 and WRS microparts is shown in Figure 130. After 100 hours of stress relaxation in DOE2 µ-part, typical parabolic distribution of the residual stress was maintained in both thicker and thinner section which reflects heterogeneity generated during moulding. This general trend was also confirmed through the variation of the processing conditions for other experiments (Figure C.3 and Figure C.4).

The WRS µ-part as expected does not show any difference in distribution of stress through the thickness. The cumulative stresses imposed by processing and deformation are quite high in DOE2 µ-part approximating before relaxation very closely to the yield limit of ABS (45MPa). After 100 hours of relaxation, the maximum stresses encounters in the middle of the µ-part decays from 41.7 to 29.8MPa for 300µm section and from 38.7 to 27.6MPa for 200µm section. The stress relaxation in WRS µ-part show almost no difference between thicker and thinner sections relaxing uniformly through the thickness for the former from 12.2 to 8.6 MPa and for the latter from 12.4 to 8.7MPa

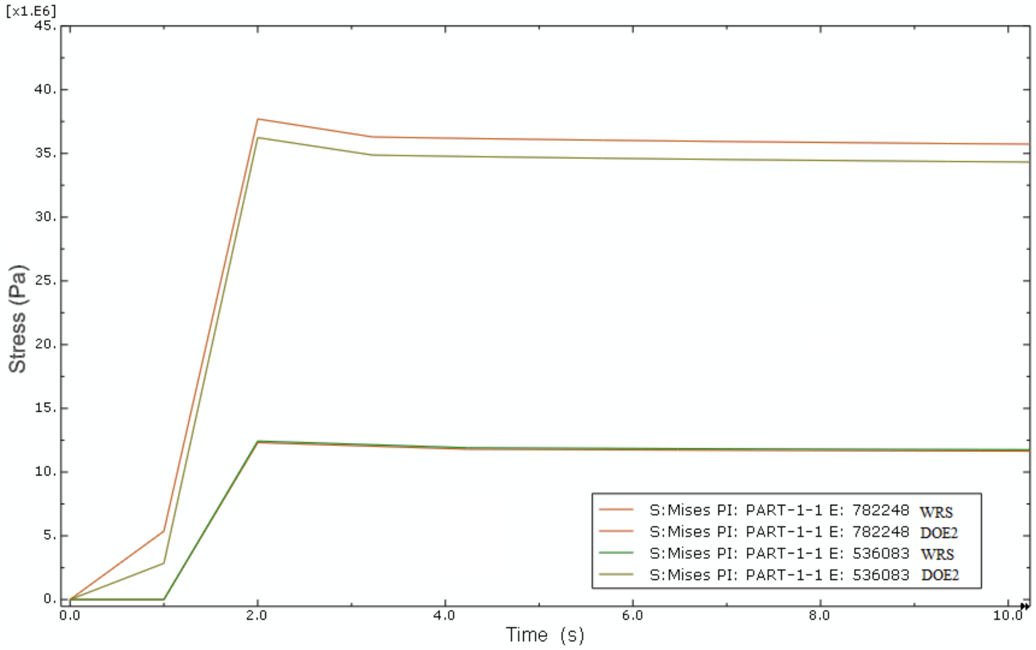

Figure 129 - Initial stage of stresses relaxation in 200 and 300μm sections of DOE2 and WRS μ-parts

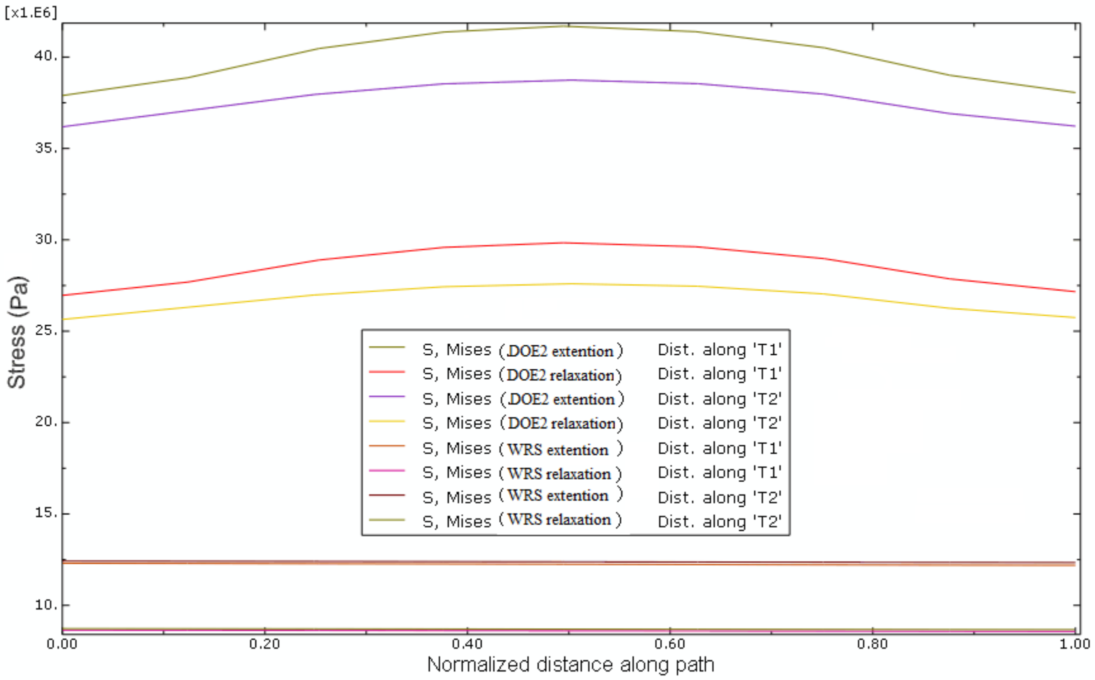

Figure 130 - Residual stress distribution through 200μm and 300μm sections for DOE2 and WRS μ-parts

To understand the stress relaxation over time through the variation of the processing conditions (Table 2), the maximum along the thickness values of the stress were presented in Table 19, where T1, T2 are the section designation, b.r. and a.r. stand for before and after relaxation. It can be concluded that in 100 hours, the cumulative built-in and deformation stresses relax 28.4% for 300µm section, while for the thinner section stress decays 0.4% more which appears to be a rather tiny difference. Nevertheless, it must be accounted, that as for longer relaxation times the difference in the rate of the stress decay may eventually increase, being a reflection of µ-part's stress history. The stress decay for the WRS µ-part was slightly higher and equal in both sections.

Although the process generated residual stresses for ABS were quite low, presented in detail in section 5.6.1, the 20µm deformation increased very considerably the stress magnitude. The latter can be verified from Table 19 for the sections T1 and T2 before relaxation or alternatively after the deformation was applied. The max stress values were approximating the limit of plastic deformation while the same value for the µ-part without residual stresses was 3.5 times lower and therefore well below the safety limit. This observation highlights the importance of considering the stress generated during µIM process in the structural simulations of the µ-moulded parts.

Table 19 - Maximum values of stress before and after 100h relaxation

Experiment №	T1 b.r.(Pa)	T1 a.r. (Pa)	Stress decrease %	T2 b.r. (Pa)	T2 a.r. (Pa)	Stress decrease %
DOE1	4.25E+07	3.04E+07	28.4	3.93E+07	2.80E+07	28.8
DOE2	4.17E+07	2.98E+07	28.4	3.87E+07	2.76E+07	28.8
DOE3	4.28E+07	3.06E+07	28.4	4.12E+07	2.94E+07	28.8
DOE4	4.30E+07	3.08E+07	28.4	4.17E+07	2.97E+07	28.7
DOE5	4.09E+07	2.93E+07	28.4	3.74E+07	2.66E+07	28.8
DOE6	4.21E+07	3.01E+07	28.4	3.89E+07	2.77E+07	28.8
DOE7	4.26E+07	3.05E+07	28.4	4.10E+07	2.92E+07	28.8
DOE8	4.28E+07	3.07E+07	28.4	4.13E+07	2.94E+07	28.8
WRS	1.23E+07	8.64E+06	29.8	1.24E+07	8.72E+06	29.8

Chapter 6 Conclusions and future work

6.1 Conclusions

1. Full factorial design of experiment has been carried out to explore the effect of injection moulding processing conditions and micromoulding thickness on the melt dynamics. Experimental data were gathered in an instrumented mould with pressure and temperature sensors, which also were used for tracking polymer progress in the microimpression. Apparently, neither the mould nor the melt temperatures seem to have any definite effect on the velocity of ABS, PP and POM, as it flows from the middle sections to the end of the micropart. Polymer cools drastically as the flow front progress becomes approximately three times slower at low injection velocity and about twice slower at high injection velocity. Polypropylene (PP) flows slightly faster than ABS and POM. No significant influence of the shear heating on the advancement of the polymer in the microimpression was verified. For the given set of the processing conditions and microimpression's geometry the principal mechanism affecting the µIM filling was the conduction of the polymer melt through the mould wall. For all processing conditions, the polymer flows slowly at the thinner 200µm section due to the higher cooling rates and the increase in viscosity.

2. The variability of microinjection moulding was assessed in terms of the completeness of the micropart. PP was found out to be less susceptible to variability at the tested processing conditions with the acceptance ratio between 94% and 100%. Microparts moulded from ABS show lower rate of acceptance (71%-94%). Even more difficulties were encountered during micromoulding of POM where the ratio of acceptable parts varies between 66% and 91%. Although, it was not easy to discern any definite trend in µIM variability, the latter seems to decrease at high injection velocity. It should be stressed that the mould temperature for PP, ABS and POM was varied in the conventional range, i.e. well below the transition temperature of polymer. Such low percentage of acceptance for ABS and POM may suggest that for the given microimpression's geometry the mould temperature is too low and should be maintained above the transition temperature of the polymer to prevent premature

solidification. PP, however, may be successfully moulded with the mould temperature at the upper level of the conventional range, high injection velocity and rather high or low melt temperature.

3. High mould temperature, as expected, was the most influencing factor for the peak cavity temperature of all the polymers tested, being however more significant at the thinner 200μm section. The melt temperature appears to have a very similar but lower effect for the peak cavity temperature of ABS. The injection velocity seems to exert less influence in comparison to the other controlled factors. However, its significance is almost doubled at the thinner section. Contrary to ABS polymer results, the second significant factor for PP at the 200μm section of micropart was not the melt temperature but the injection velocity, while for the thicker 300μm section its effect was barely visible. When comparing to the other controlled factors, the melt temperature seems quite irrelevant to the peak cavity temperatures of PP and POM.

4. Statistical analysis of the weld line position was carried out in order to find out the degree of influence of each controlled parameter. Weld line position can be seen as an indicator of the polymer fluidity at such critical area of the microimpression as the end of filling. Independently of polymer type, the more advanced weld line position was observed when the V_i, T_{melt} and T_m were at high levels which may indicate slower cooling rate and hence better polymer fluidity at the pre-set combination of the processing conditions. The weld line position in microparts moulded from ABS, POM and PP was primarily affected by the injection velocity. For ABS and PP polymers, the next by order of importance were the melt and mould temperatures whilst influence of those processing conditions was inverted for weld line position in polyoxymethylene microparts. The results appear to be in a good agreement with the data of polymer dynamics

5. Statistical assessment of the weld lines quality was undertaken for POM and ABS microparts. The initial evaluation of the weld line thickness was performed by optical microscopy. Then, SN (smaller-the-better) ratio was used to correlate the sensitivity of the weld line width to the noise factors present in the μIM process. Narrower weld line width was attributed to better interfusion of the polymer fronts and consequently less probability to fail when subjected to mechanical solicitations. In all microparts, the minimum weld line width was observed with high levels of the injection velocity,

mould and melt temperatures. The main factor affecting the weld line width of ABS microparts was the injection velocity while the mould temperature effect was less significant. Melt temperature appears to have only slight effect. The mould temperature had prime influence on reduction of the weld line width in POM microparts. The injection velocity seemed to affect the weld line width slightly less and the melt temperature influence did not appear significant.

6. Autodesk Moldflow Insight software was used to simulate µIM process. Three different scenarios for discretization of the micropart and the runner system domains were considered. Two meshes were created in AMI® through the Autodesk Moldflow Design Link 2013. Generation of the third type (adaptive) mesh was carried out with Hypermesh and AMI® computer programs. An adaptive discretization of both micropart and runner system led to precise and gradual mesh adjustment to the geometry. All three types of mesh were adequate to predict the unbalanced filling but with different levels of accuracy. The flow pattern was better predicted with the Hypermesh/AMI adaptive discretization of the model. This highlights the importance of mesh type and refinement in µ-injection moulding simulation, especially for the prediction of the flow field. By minimizing the element size and increasing their density better correlation with experimental data was possible.

7. In order to approximate the predicted with AMI® polymer dynamics to that recorded experimentally, several numerical simulations were conducted. After comparison of the final results with the experimentally obtained data, it was concluded that the degree of prediction accuracy vary from polymer to polymer. Considering the time scale of the injection, the predicted values did not diverge much from the experimental data. The discrepancies encountered between the predicted and experimentally observed polymer flow velocities may be attributed to some assumptions used in the AMI® simulation code, which may have bearing on the precision of the numerical simulation at µ-scale.

8. The built-in residual stresses in µ-moulded ABS, POM and PP parts, are generated in AMI® but not directly assessable from there. Quantification of the residual stresses was carried out with ABAQUS® code through the embedded interface. Residual stress patterns were very different for all three polymers subjected to the analysis, reflecting their processing conditions and molecular structure. POM µ-parts were at highest residual stresses comparing with PP and ABS. However, no residual stresses above the

yield limit were detected. Optimized set of the processing conditions was established by conjugating the minimum residual stress criterion and the minimum experimentally assessed µIM variability. It was concluded that the processing conditions closely approximating both these criteria were: DOE5 for ABS, DOE2 for POM and DOE6 for PP.

9. Dynamical mechanical testing of the ABS µ-parts was performed. After several trial and errors more adequate for the testing specimen geometry was chosen. With the multiplexing temperature frequency scan, the necessary data was collected and then used for extending the experiment time. The latter was achieved with the TTS principle which allowed for prediction the mechanical behaviour of ABS µ-parts. TTSP was applied in automated fashion through a MATLAB® code. The resultant data was thereafter used for the calibration of the linear viscoelastic model in ABAQUS®

10. Parametrical study of the stress relaxation in ABS µ-parts was carried out in ABAQUS®. Numerical simulations with and without the process induced residual stresses were carried out. After conducting the stress relaxation experiment for 100 hours, it was found out that with the elastic initial deformation step, the max stress values were approximating the limit of plastic deformation while the same value for the µ-part without residual stresses was 3.5 times lower and therefore well below the safety limit. After relaxing during 100 hours, the residual stresses decrease about 28%. Moreover, the residual stresses decays at slightly faster rate for the 200µm section. These results reinforce the importance of considering the stress generated during µIM process in the structural simulations towards more accurate failure and service-life prediction of polymer µ-parts

6.2 Future work proposals

Towards better comprehension of the µIM process and performance of the µ-moulded components, the following issues may be considered in the future:

- For better assessment of the weld line width, depth and v-notch shape three dimensional approach might be adopted;
- In order to understand more clearly the influence of the excessive shear rates on the heat transfer phenomena in the microimpression morphology, morphological

structure of polypropylene and polyoxymethilene polymers has to be investigated;

- Mechanical testing should be conducted under the various deformation to establish the limits of linear viscoelastic region of µ-moulded parts;
- Several assumptions used in the AMI® simulation code may have bearing on the precision of the numerical simulation at µ-scale and therefore have to be questioned. Excessive cooling rates may invalid an assumption of the constant polymer conductivity during injection. For the same reason, transient heat transfer coefficient at melt/mould interface, instead of constant value currently used in AMI® simulation, may be considered.

References

1. Consultek. *MICRO INJECTION MOLDING*. 2013 [cited 2013 13 February]; Available from: http://www.consultekusa.com/pdf/Consulting/Process/MICRO%20INJECTION%20MOLDING.pdf.
2. Giboz, J., Copponnex, T. and Mélé, P., *Microinjection molding of thermoplastic polymers: a review.* Journal of Micromechanics and Microengineering, 2007. **17**(6): p. 96-109.
3. Piotter, V., Bauer, W., Hanemann, T., Heckele, M., and Müller, C., *Replication technologies for HARM devices: status and perspectives.* Microsystem Technologies, 2008. **14**(9): p. 1599-1605.
4. Whiteside, B.R., et al., *Micromoulding: process characteristics and product properties.* Plastics, rubber and composites, 2003. **32**(6): p. 9.
5. Mohren, P., M. Walter, and G. Menges, eds. *How to Make Injection Molds*. 3 ed. Library of Congress Cataloging-in-Publication Data. 2001, Hanser Gardner Publications, Inc.: Cincinnati. p.643.
6. Xie, L., Shen, L., and Jiang, B, *Modelling and Simulation for Micro Injection Molding Process*, in *Computational Fluid Dynamics Technologies and Application*2011, InTech. p. 396
7. Ram, A., *Fundamentals of Polymer Engineering*. 1997, New York: Congress Cataloging-in-Publication Data.
8. Gava, A., Tosello, G. Hansen, H., Salvador, M., Lucchetta, G., *A New Approach For The Validation Of Filling Simulations In Micro Injection Moulding.* AIP Conference Proceedings, 2007. **908**(1): p. 307-312.
9. Yao, D., Kim, B. , *Simulation of the filling process in micro channels for polymeric materials.* Journal of Micromechanics and Microengineering, 2002. **12**(5): p. 604-610.
10. Tofteberg, T., *Injection molding of microfeatured polymer components.* Doctoral Dissertation, 2010.
11. Sha, B., Dimov, S., Griffiths, C. and Packianather, M. , *Investigation of micro-injection moulding: Factors affecting the replication quality.* Journal of Materials Processing Technology, 2007. **183**(2-3): p. 284-296.
12. Lee, B., Kim, D., and Kwon, T., *Replication of microlens arrays by injection molding.* Microsystem Technologies, 2004. **10**(6): p. 531-535.
13. Kalima, V., Pietarinen, J., Siitonen, S., Immonen, J., Suvanto, M., Kuittinen, M., Mönkkönen, K. and Pakkanen, T., *Transparent thermoplastics: Replication of diffractive optical elements using micro-injection molding.* Optical Materials, 2007. **30**(2): p. 285-291.
14. Zhao, J., Mayes, R., Chen, G., Xie, H. and Chan, P., *Effects of process parameters on the micro molding process.* Polymer Engineering & Science, 2003. **43**(9): p. 1542-1554.
15. Attia, U. and Alcock, J., *An evaluation of process-parameter and part-geometry effects on the quality of filling in micro-injection moulding.* Microsystem Technologies, 2009. **15**(12): p. 1861-1872.
16. Zhang, H., Ong, N. and Lam, Y., *Mold surface roughness effects on cavity filling of polymer melt in micro injection molding.* The International Journal of Advanced Manufacturing Technology, 2008. **37**(11): p. 1105-1112.
17. Liou, A. and Chen, R., *Injection molding of polymer micro- and sub-micron structures with high-aspect ratios.* The International Journal of Advanced Manufacturing Technology, 2006. **28**(11): p. 1097-1103.
18. Theilade, U., Hansen, H., *Surface microstructure replication in injection molding.* The International Journal of Advanced Manufacturing Technology, 2007. **33**(1): p. 157-166.
19. Xie, L. and Ziegmann, G., *Influence of processing parameters on micro injection molded weld line mechanical properties of polypropylene (PP).* Microsystem Technologies, 2009. **15**(9): p. 1427-1435.
20. Xie, L., Ziegmann, G., Hlavac, M. and Wittmer, R., *Effect of micro tensile sample's cross section shape on the strength of weld line in micro injection molding process.* Microsystem Technologies, 2009. **15**(7): p. 1031-1037.

21. Attia, U., S. Marson, and J. Alcock, *Micro-injection moulding of polymer microfluidic devices.* Microfluidics and Nanofluidics, 2009. **7**(1): p. 1-28.
22. Co, D.B.G. *BOY 12 A/M*. 2013 [cited 2013 22 February]; Available from: http://www.boy.ltd.uk/filestore/Product.pdf.
23. Michaeli, W., A. Spennemann, and R. Gärtner, *New plastification concepts for micro injection moulding.* Microsystem Technologies, 2002. **8**(1): p. 55-57.
24. Chang, P., Hwang, S., Lee, H. and Huang, D., *Development of an external-type microinjection molding module for thermoplastic polymer.* Journal of Materials Processing Technology, 2007. **184**(1-3): p. 163-172.
25. TEC, D. *Formica PLAST®* 2011; Available from: http://www.desma-tec.de/en/machines/micro_injection/pdf/FormicaPlast_1K_E.pdf.
26. 50, m.-m. *Männer/solutions for plastics* 2011; Available from: http://www.maenner-group.com/text/191/en/jump,191/hot-runner/about-maenner/the-maenner-company.html.
27. Giboz, J. Copponnex, T. and Mélé P., *Microinjection molding of thermoplastic polymers: morphological comparison with conventional injection molding.* Journal of Micromechanics and Microengineering, 2009. **19**(2): p. 025023.
28. Nguyen-Chung, T. Löser, C., Jüttner, G., Pham, T., Obadal, M. and Gehde, M., *Simulation of the micro-injection moulding process: effect of the thermo-rheological status on the morphology.* Proceedings of the Institution of Mechanical Engineers, Part E: Journal of Process Mechanical Engineering, 2011.
29. Pouzada, A.S., Ferreira, E.C. and A.J. Pontes, *Friction properties of moulding thermoplastics.* Polymer Testing, 2006. **25**(8): p. 1017-1023.
30. Fu, G., Loh, N., Tor, S., Tay, B., Murakoshi, Y. and Maeda, R., *Analysis of demolding in micro metal injection molding.* Microsystem Technologies, 2006. **12**(6): p. 554-564.
31. Griffiths, C.A., Dimov, S.S. and Pham,D.T. *Micro injection moulding: the effects of tool surface finish on melt flow behaviour*. in *Proceedings of International Conference 4M2006*. 2006. Elsevier (Oxford).
32. Neto, V. F., Vaz, R., Oliveira, M. S. A. And Grácio, J., *CVD diamond-coated steel inserts for thermoplastic mould tools—Characterization and preliminary performance evaluation.* Journal of Materials Processing Technology, 2009. **209**(2): p. 1085-1091.
33. Griffiths, C.A., Dimov, S. S., Brousseau, E.B., Chouquet, C., Gavillet, J., Bigot, S. , *Micro-Injection moulding: surface treatment effects on part demoulding*, in *4M2008 Conference on Multi-Material Micro Manufacture* W. Publishing, Editor 2008: UK, Cardiff.
34. Navabpour, P.,Teer, D. G.,Hitt, D. J. and Gilbert, M., *Evaluation of non-stick properties of magnetron-sputtered coatings for moulds used for the processing of polymers.* Surface and Coatings Technology, 2006. **201**(6): p. 3802-3809.
35. De Grave A., Eriksson T.and Hansen H.N., *Demouldability of Microstructures in Polymer Moulding*. in *3rd International Conference on Multi-Material Micro Manufacture, 4M2007* 2007. Borovets Bulgaria.
36. Yu, L., Koh C., Lee, L., Koelling K. and Madou, M., *Experimental investigation and numerical simulation of injection molding with micro-features.* Polymer Engineering & Science, 2002. **42**(5): p. 871-888.
37. Wu, C. H. and Liang, W. J., *Effects of geometry and injection-molding parameters on weld-line strength.* Polymer Engineering & Science, 2005. **45**(7): p. 1021-1030.
38. Michaeli, W., Rogalla, A. and Ziegmann, C., *Processing technologies for the injection moulding of hybrid microstructures.* Macromolecular Materials and Engineering, 2000. **279**(1): p. 42-45.
39. Rötting, O.,Röpke, W., Becker, H. and Gärtner, C., *Polymer microfabrication technologies.* Microsystem Technologies, 2002. **8**(1): p. 32-36.
40. Fleischer, J.H., G.Haupt, S. , *Process parameter analysis in ablating micro-mold manufacturing.* Microsystem Technologies, 2008. **14**(9): p. 1367-1372.
41. Hormes, J., Gottert, J., Lian, K., Desta, Y. and Jian, L., *Materials for LiGA and LiGA-based microsystems.* Nuclear Instruments and Methods in Physics Research Section B: Beam Interactions with Materials and Atoms, 2003. **199**: p. 332-341.
42. Despa, M.S., Kelly, K.W. and Collier, J.R., *Injection molding of polymeric LIGA HARMs.* Microsystem Technologies, 1999. **6**(2): p. 60-66.
43. Munnik, F., Benninger, F., Mikhailov, S., Bertsch, A., Renaud, P., Lorenz, H. and Gmür, M., *High aspect ratio, 3D structuring of photoresist materials by ion beam LIGA.* Microelectronic Engineering, 2003. **67-68**: p. 96-103.

44. Meyer, P., Schulz, J., Hahn, L. and Saile, V., *Why you will use the deep X-ray LIG(A) technology to produce MEMS?* Microsystem Technologies, 2008. **14**(9): p. 1491-1497.
45. Hirata, Y., *LIGA process - micromachining technique using synchrotron radiation lithography - and some industrial applications.* Nuclear Instruments and Methods in Physics Research Section B: Beam Interactions with Materials and Atoms, 2003. **208**: p. 21-26.
46. Kim, D., Lee, H., Lee, B., Yang, S., Kwon, T. and Lee, S., *Replications and analysis of microlens array fabricated by a modified LIGA process.* Polymer Engineering & Science, 2006. **46**(4): p. 416-425.
47. Watt, F., *Focused high energy proton beam micromachining: A perspective view.* Nuclear Instruments and Methods in Physics Research Section B: Beam Interactions with Materials and Atoms, 1999. **158**(1-4): p. 165-172.
48. Wenmin, Q., Wenzel, C. Jahn, A. and Zeidler, D., *UV-LIGA: a promising and low-cost variant for microsystem technology*. in *Optoelectronic and Microelectronic Materials Devices, 1998. Proceedings. 1998 Conference on*. 1998.
49. Yang, R., Jiang, J., Meng, W. J. and Wang, W., *Numerical simulation and fabrication of microscale, multilevel, tapered mold inserts using UV-Lithographie, Galvanoformung, Abformung (LIGA) technology.* Microsystem Technologies, 2006. **12**(6): p. 545-553.
50. Zhang, J., Tan, K. L., Hong, G. D., Yang L. J., and Gong,H. Q. , *Polymerization optimization of SU-8 photoresist and its applications in microfluidic systems and MEMS.* Journal of Micromechanics and Microengineering, 2001. **11**(1): p. 20.
51. Heckele, M. and W.K. Schomburg, *Review on micro molding of thermoplastic polymers.* Journal of Micromechanics and Microengineering, 2004. **14**(3): p. R1.
52. Chien, R., W. Jong, and S. Chen, *Study on rheological behavior of polymer melt flowing through micro-channels considering the wall-slip effect.* Journal of Micromechanics and Microengineering, 2005. **15**(8): p. 1389.
53. Li, Y., S. Minoru, and H. Kazuhiro, *Micro-optical components based on silicon mold technology.* Optics and Lasers in Engineering, 2004. **41**(3): p. 545-552.
54. Franssila, S., *Introduction to Microfabrication*. 2004, John Wiley & Sons Ltd,: Chichester,. 401.
55. Masuzawa, T., *State of the Art of Micromachining.* CIRP Annals - Manufacturing Technology, 2000. **49**(2): p. 473-488.
56. Uhlmann, E., S. Piltz, and U. Doll, *Machining of micro/miniature dies and moulds by electrical discharge machining--Recent development.* Journal of Materials Processing Technology, 2005. **167**(2-3): p. 488-493.
57. Davim, J.P. and Jackson., M., *Nano and Micromachining*. 2009, Wiley-Iste. 212.
58. Gower, M.C., *Industrial applications of laser micromachining.* Opt. Express, 2000. **7**(2): p. 56-67.
59. Heyl, P., Olschewski, T. and Wijnaendts, R.W., *Manufacturing of 3D structures for micro-tools using laser ablation.* Microelectronic Engineering, 2001. **57-58**: p. 775-780.
60. Su, Y. C., Shah, J. and Lin, L., *Implementation and analysis of polymeric microstructure replication by micro injection molding.* Journal of Micromechanics and Microengineering, 2004. **14**(3): p. 415-422.
61. Piotter, V., Hanemann, T., Ruprecht, R. and Haußelt, J., *Injection molding and related techniques for fabrication of microstructures.* Microsystem Technologies, 1997. **3**(3): p. 129-133.
62. Gornik, C., *Injection Moulding of Parts with Microstructured Surfaces for Medical Applications.* Macromolecular Symposia, 2004. **217**(1): p. 365-374.
63. Chang, P. C. and Hwang, S. J., *Experimental investigation of infrared rapid surface heating for injection molding.* Journal of Applied Polymer Science, 2006. **102**(4): p. 3704-3713.
64. Yoo, Y., Kim, T., Choi, D., Hyun, S., Lee, H., Lee, K., Kim, S., Kim, B., Seo, Y., Lee, H. and Lee, J., *Injection molding of a nanostructured plate and measurement of its surface properties.* Current Applied Physics, 2009. **9**(2, Supplement 1): p. e12-e18.
65. Shia-Chung Chen, W. R.J., Yaw-Jen Chang, Jen-An Chang, and Jin-Chuan Cin, *Rapid mold temperature variation for assisting the micro injection of high aspect ratio micro-feature parts using induction heating technology.* Journal of Micromechanics and Microengineering, 2006. **16**(9): p. 1783.
66. Xie, L. and Ziegmann, G., *A visual mold with variotherm system for weld line study in micro injection molding.* Microsystem Technologies, 2008. **14**(6): p. 809-814.

67. McFarland, A.W. and Colton, J.S., *Chemical sensing with micromolded plastic microcantilevers.* Microelectromechanical Systems, Journal of, 2005. **14**(6): p. 1375-1385.
68. Whiteside, B., Martyn M., Coates, P., Allan, P., Hornsby, P.and Greenway, G., *Micromoulding: process measurements, product morphology and properties.* Plastics Rubber and Composites, 2004. **33**(1): p. 11-17.
69. Tseng, S., Chen, Y., Kuo, C. and Shew, B., *A study of integration of LIGA and M-EDM technology on the microinjection molding of ink-jet printers' nozzle plates.* Microsystem Technologies, 2005. **12**(1): p. 116-119.
70. Abreu, B., Lamas, B., Fonseca, A., Martins, N. and Oliveira, M. S. A., *Experimental characterization of convective heat transfer with MWCNT based nanofluids under laminar flow conditions.* Heat and Mass Transfer, 2013: p. 1-10.
71. Kim, Y., Choi, Y. and S. Kang, *Replication of high density optical disc using injection mold with MEMS heater.* Microsystem Technologies, 2005. **11**(7): p. 464-469.
72. Yao, D., Kimerling, T.E. and Kim, B., *High-frequency proximity heating for injection molding applications.* Polymer Engineering & Science, 2006. **46**(7): p. 938-945.
73. Chang, P. C. and Hwang, S. J., *Injection Molding of Microprobe Array Parts.* Journal of Polymer Research, 2006. **13**(1): p. 25-32.
74. Saito, T., Satoh, I. and Kurosaki, Y.,*A new concept of active temperature control for an injection molding process using infrared radiation heating.* Polymer Engineering & Science, 2002. **42**(12): p. 2418-2429.
75. Yu, M.C., Young, W.B. and Hsu, P.M., *Micro-injection molding with the infrared assisted mold heating system.* Materials Science and Engineering: A, 2007. **460-461**: p. 288-295.
76. Sha, B. Dimov, S.S. Pham, D.T. and Griffiths, C. A.. *Study of Factors Affecting Aspect Ratios Achievable in Micro-injection Moulding*. in *4M2005: First International Conference on Multi-Material Micro Manufacture* 2005. Elsevier
77. Zhao, J.L., X. H.; Chen, G.; Liu, S. L.; Juay, Y. K.; Yong, M. S., *Micromold filling behavior studies of polymer materials.* Materials Research Innovations, 2006. **10**: p. 394-397.
78. Yan, C., Nakao, M., Go, T., Matsumoto, K. and Hatamura, Y., *Injection molding for microstructures controlling mold-core extrusion and cavity heat-flux.* Microsystem Technologies, 2003. **9**(3): p. 188-191.
79. Huang, J. T. and Cheng, S.C., *Study of injection molding pressure sensor with low cost and small probe.* Sensors and Actuators A: Physical, 2002. **101**(3): p. 269-274.
80. Luo, R.C. and Pan, Y.L., *Rapid Manufacturing of Intelligent Mold With Embedded Microsensors.* Mechatronics, IEEE/ASME Transactions on, 2007. **12**(2): p. 190-197.
81. Ono, Y., Whiteside, B.R., Brown, E.C., Kobayashi, M., Cheng, C.C., Jen, C.K. and Coates, P.D., *Real-time process monitoring of micromoulding using integrated ultrasonic sensors.* Transactions of the Institute of Measurement and Control, 2007. **29**(5): p. 383-401.
82. Kistler. *p-T-Sensor for mold cavity pressure and temperature with front ø1 mm, cable length 0,4 m*. 2010 [cited 2013; Available from: http://www.kistler.com/pt/en/product/pressure/6188AA0,4.
83. PRIAMUS®. *Cavity temperature sensors*. 2010; Available from: http://www.priamus.com/.
84. Michaeli, W., Opfermann, D. and Kamps, T., *Advances in micro assembly injection moulding for use in medical systems.* The International Journal of Advanced Manufacturing Technology, 2007. **33**(1): p. 206-211.
85. Srirojpinyo, C., Yoon, S.H., Lee, J., Sung, C., Mead, J. L. and Barry, C.M.F., *Processing Parameters Affecting Nanoinjection Molding*. in *NSTI Nanotechnology Conference*. 2004
86. Tofteberg, T. and Andreassen, E., *Injection moulding of microfeatured parts*. in *Polymer Processing Society 24th Annual Meeting ~ PPS-24 ~* 2008. June 15-19, 2008 Salerno (Italy).
87. Mönkkönen, K., Pakkanen, T., Hietala, J., Pääkkönen, E., Pääkkönen, P., Jääskeläinen, T. and Kaikuranta, T., *Replication of sub-micron features using amorphous thermoplastics.* Polymer Engineering & Science, 2002. **42**(7): p. 1600-1608.
88. Malkin, A.Y. and Isayev, A., *Rheology: Concepts, Methods, and Applications*. Rheology: Concepts, Methods, and Applications. Vol. 1. 2005, ChemTec Publishing. 1-474.
89. Oluranti Sadiku-Agboola, E.R.S., Adesola Taoreed Adegbola, Olusesan Frank Biotidara, *Rheological Properties of Polymers: Structure and Morphology of molten Polymer Blends.* Materials Sciences and Applications, 2011. **2**(1): p. 30-41.
90. Chen, C., Chen, S., Liaw, W. and Chien, R., *Rheological behavior of POM polymer melt flowing through micro-channels.* European Polymer Journal, 2008. **44**(6): p. 1891-1898.

91. Chen, S. C., Tsai, R. I., Chien, R. D. and Lin, T. K., *Preliminary study of polymer melt rheological behavior flowing through micro-channels.* International Communications in Heat and Mass Transfer, 2005. **32**(3-4): p. 501-510.
92. Piotter, V., Mueller, K., Plewa, K., Ruprecht, R. and Hausselt, J., *Performance and simulation of thermoplastic micro injection molding.* Microsystem Technologies, 2002. **8**(6): p. 387-390.
93. Xu, G., Yu, L., Lee, L. J. and Koelling, K. W., *Experimental and numerical studies of injection molding with microfeatures.* Polymer Engineering & Science, 2005. **45**(6): p. 866-875.
94. Lee, J. G., Lee, B. K., Kang, T. G. and Kwon, T. H., *Experimental and numerical investigation of injection molding with microrib patterns.* Polymer Engineering & Science, 2010. **50**(6): p. 1186-1198.
95. Mnekbi, C., M. Vincent, and Agassant, J., *Polymer rheology at high shear rate for microinjection moulding.* International Journal of Material Forming, 2010. **3**(0): p. 539-542.
96. Rosenbaum, E.E. and Hatzikiriakos, S.G., *Wall slip in the capillary flow of molten polymers subject to viscous heating.* AIChE Journal, 1997. **43**(3): p. 598-608.
97. Vasco, J. C., Maia, J.M., and Pouzada, A. S., *Thermo-rheological behaviour of polymer melts in microinjection moulding.* Journal of Micromechanics and Microengineering, 2009. **19**(10): p. 105012.
98. Cardozo, D., *Three Models of the 3D Filling Simulation for Injection Molding: A Brief Review.* Journal of Reinforced Plastics and Composites, 2008. **27**(18): p. 1963-1974.
99. Weng, C., Lee, W. B., To, S. and Jiang, B.,, *Numerical simulation of residual stress and birefringence in the precision injection molding of plastic microlens arrays.* International Communications in Heat and Mass Transfer, 2009. **36**(3): p. 213-219.
100. Zhiltsova, T.,Oliveira, M., Vasco, J., Pouzada, A. and Pontes, A., *Influence of mesh discretization on the prediction of polymer flow behaviour in microcavities*. in *VI International Materials Symposium MATERIAIS 2011 | XV meeting of SPM*. 2011. Guimarães, Portugal.
101. Yang, C., Huang, H., Castro, J.and Yi, Allen Y., *Replication characterization in injection molding of microfeatures with high aspect ratio: Influence of layout and shape factor.* Polymer Engineering & Science, 2011. **51**(5): p. 959-968.
102. Dong Sung Kim, Kwang-Cheol Lee, Tai Hun Kwon, Seung S. Lee, *Micro-channel filling flow considering surface tension effect.* Journal of Micromechanics and Microengineering, 2002. **12**(3): p. 236.
103. Fan Shi, X.Z., Qian Li, Changyu Shen, *Mould wall friction effects on micro injection moulding based on simulation of MIS.* IOP Conference Series: Materials Science and Engineering, 2010. **10**(1): p. 012141.
104. Yu, L., L.J. Lee, and Koelling, K.W., *Flow and heat transfer simulation of injection molding with microstructures.* Polymer Engineering & Science, 2004. **44**(10): p. 1866-1876.
105. Young, W.B., *Simulation of the filling process in molding components with micro channels.* Microsystem Technologies, 2005. **11**(6): p. 410-415.
106. Nguyen-Chung, T., Jüttner, G., Löser, C., Pham, T. and Gehde, M., *Determination of the heat transfer coefficient from short-shots studies and precise simulation of microinjection molding.* Polymer Engineering & Science, 2010. **50**(1): p. 165-173.
107. Keller, A., *Morphology of polymers.* Pure & Appl. Chem., 1992 **Vol. 64**(No. 2): p. 193-204.
108. Favaro, M. M., Marinelli, A. L., Farah, M. and Bretas, R. E., *Optical monitoring of polypropylene crystallization during injection molding.* Polymer Engineering & Science, 2008. **48**(2): p. 257-266.
109. Cao, J.W., Ke Cao, Wen Zhang, Qin Du, RongNi Fu and Qiang, *Combined effect of shear and nucleating agent on the multilayered structure of injection-molded bar of isotactic polypropylene.* Journal of Applied Polymer Science, 2009. **112**(3): p. 1104-1113.
110. Fellahi, S., Favis, B.D.and Fisa, B., *Morphological stability in injection-moulded high-density polyethylene/polyamide-6 blends.* Polymer, 1996. **37**(13): p. 2615-2626.
111. Zhang, K. and Lu, Z., *Analysis of morphology and performance of PP microstructures manufactured by micro injection molding.* Microsystem Technologies, 2008. **14**(2): p. 209-214.
112. Lu, Z. and Zhang, K., *Morphology and mechanical properties of polypropylene micro-arrays by micro-injection molding.* The International Journal of Advanced Manufacturing Technology, 2009. **40**(5): p. 490-496.
113. Osswald, T. A. and Hernández-Ortiz J. P. *Polymer processing: modeling and simulation*. 2006 Hanser Verlag: Cincinnati. 606.

114. Chanda, M. and Roy, S. K., *Plastics Fundamentals, Properties and Testing*. ed. T.F. Grou. 2009: Boca Raton.
115. Crawford, R.J., ed. *PLASTICS ENGINEERING*. 1998: Oxford.
116. Hemker, K.J. and Sharpe, W.N., *Microscale Characterization of Mechanical Properties.* Annual Review of Materials Research, 2007. **37**(1): p. 93-126.
117. W.C. Oliver and Pharra, G.M., *Measurement of hardness and elastic modulus by instrumented indentation: Advances in understanding and refinements to methodology.* . Journal of Materials Research, 2004. **19**(1).
118. Nguyen-Chung, T., Mennig, G., Boyanova, M., Fakirov, S. and Baltá Calleja, F. J., *Effect of an obstacle during processing on the weld line of injection-molded glassy polystyrene: Microhardness study.* Journal of Applied Polymer Science, 2004. **92**(5): p. 3362-3367.
119. Beake, B., *Modelling indentation creep of polymers: a phenomenological approach.* Journal of Physics D: Applied Physics, 2006. **39**(20): p. 4478.
120. Huang, G., B. Wang, and Lu, H., *Measurements of Viscoelastic Functions of Polymers in the Frequency-Domain Using Nanoindentation.* Mechanics of Time-Dependent Materials, 2004. **8**(4): p. 345-364.
121. Huang, G. and Lu, H., *Measurements of Two Independent Viscoelastic Functions by Nanoindentation.* Experimental Mechanics, 2007. **47**(1): p. 87-98.
122. Lu, H., Wang, B., Ma, J., Huang, G. and Viswanathan, H., *Measurement of Creep Compliance of Solid Polymers by Nanoindentation.* Mechanics of Time-Dependent Materials, 2003. **7**(3): p. 189-207.
123. VanLandingham, M.R., Villarrubia J. S. and Meyers, G. F., *NANOINDENTATION OF POLYMERS: OVERVIEW.* Polymer Preprints 2000. **41**(2): p. 1412-1413.
124. Fang, T.H., Chang, W.J. and Tsai, S.L., *Nanomechanical characterization of polymer using atomic force microscopy and nanoindentation.* Microelectronics Journal, 2005. **36**(1): p. 55-59.
125. Poilane, C.,Delobelle, P., Lexcellent, C., Hayashi, S. and Tobushi, H., *Analysis of the mechanical behavior of shape memory polymer membranes by nanoindentation, bulging and point membrane deflection tests.* Thin Solid Films, 2000. **379**(1-2): p. 156-165.
126. Tweedie, C.A. and Van Vliet, K. J., *Contact creep compliance of viscoelastic materials via nanoindentation.* J. Mater. Res., 2006. **Vol. 21**(No. 6): p. 1576-1589.
127. Odegard, G., Gates, T. and H. Herring, *Characterization of viscoelastic properties of polymeric materials through nanoindentation.* Experimental Mechanics, 2005. **45**(2): p. 130-136.
128. Fischer-Cripps, A.C., *Nanoindentation*. 3 ed. 2011, Springer New York. 279.
129. Oyen, M.L., *Sensitivity of polymer nanoindentation creep measurements to experimental variables.* Acta Materialia, 2007. **55**(11): p. 3633-3639.
130. Liu, X. and Piotter, V., *Mapping micro-mechanical properties of carbon-filled polymer composites by TPM.* Precision Engineering, 2007. **31**(2): p. 162-168.
131. Ah-Young Jee and Minyung Lee, *Comparative analysis on the nanoindentation of polymers using atomic force microscopy.* Polymer Testing, 2010. **29**(1): p. 95-99.
132. Tranchida, D., Piccarolo, S., Loos, J. and Alexeev, A., *Mechanical Characterization of Polymers on a Nanometer Scale through Nanoindentation. A Study on Pile-up and Viscoelasticity.* Macromolecules, 2007. **40**(4): p. 1259-1267.
133. Hinz, M., Kleiner, A., Hild, S., Marti, O., Dürig, U., Gotsmann, B., Drechsler, U., Albrecht, T. R. and Vettiger, P., *Temperature dependent nano indentation of thin polymer films with the scanning force microscope.* European Polymer Journal, 2004. **40**(5): p. 957-964.
134. Nigel, M., *Plastics Microstructure and Applications*. Third Edition. 2005, Oxford: Elsevier. 517.
135. Rosato, D.V., Rosato, D. V., Rosato, M. G. , *Injection Molding Handbook*. 3 ed. 2000.
136. Kamal, M. R., Lai-Fook, R. A. and Hernandez-Aguilar, J. R., *Residual thermal stresses in injection moldings of thermoplastics: A theoretical and experimental study.* Polymer Engineering & Science, 2002. **42**(5): p. 1098-1114.
137. Shoemaker, J., *Moldflow Design Guide A Resource for Plastics Engineers*. 1 ed. 2006: Hanser Gardner Publications. 326.
138. Daly, B., Nguyen, H., Sanschagrin, K. T. and Cole, B., *The build-up and measurement of molecular orientation, crystalline morphology, and residual stresses in injection molded parts : A review*. Vol. 2. 1998, Brookfield, CT, ETATS-UNIS: Society of Plastics Engineers.
139. Douven, L.F.A., *Towards the computation of properties of injection moulded products : flow- and thermally induced stresses in amorphous thermoplastics*, in *Department of Mechanical*

Engineering 1991, Technische Universiteit Eindhoven: Eindhoven : Technische Universiteit Eindhoven, 1991. p. VI, 169

140. Zoetelief, W.F., Douven, L. F., Housz, A.and Ingen, A. J., *Residual thermal stresses in injection molded products.* Polymer Engineering & Science, 1996. **36**(14): p. 1886-1896.
141. Shen, C.Y. and Li, Hai-Mei, *Numerical Simulation for Effects of Injection Mold Cooling on Warpage and Residual Stresses.* Polymer-Plastics Technology and Engineering, 2003. **42**(5): p. 971-982.
142. Baaijens, F.P.T., *Calculation of residual stresses in injection molded products.* Rheologica Acta, 1991. **30**(3): p. 284-299.
143. Withers, P.J. and Bhadeshia, H.K.D.H., *Residual stress. Part 1 – Measurement techniques.* Materials Science and Technology, 2001. **17**(4): p. 355-365.
144. Malloy, R.A., *Plastic Part Design for Injection Molding: An Introduction*. 1994 Hanser Verlag, - Technology & Engineering. 460
145. Shah, V., *Handbook of Plastics Testing and Failure Analysis*. 2008: John Wiley & Sons, technology & Engineering.
146. Scheirs, J., *Compositional and Failure Analysis of Polymers: A Practical Approach*, in *2000* John Wiley & Sons Science p. 766
147. Treuting, R. and Read, W., *A mechanical determination of biaxial residual stress in sheet materials.* Journal of Applied Physics, 1951. **22**(2): p. 130-134.
148. Kabanemi, K.K., Vaillancourt, H., Wang and H.Salloum, G., *Residual stresses, shrinkage, and warpage of complex injection molded products: Numerical simulation and experimental validation.* Polymer Engineering & Science, 1998. **38**(1): p. 21-37.
149. Siegmann, A., A. Buchman, and Kenig, S.,*Residual stresses in polymers III: The influence of injection-molding process conditions.* Polymer Engineering & Science, 1982. **22**(9): p. 560-568.
150. Hastenberg, C. H. V., Wildervanck, P. C., Leenen, A. J. H. and Schennink, G. G. J., *The measurement of thermal stress distributions along the flow path in injection-molded flat plates.* Polymer Engineering & Science, 1992. **32**(7): p. 506-515.
151. Pham, H.T., C.P. Bosnyak, and Sehanobish, K., *Residual stresses in injection molded polycarbonate rectangular bars.* Polymer Engineering & Science, 1993. **33**(24): p. 1634-1643.
152. Wimberger-Friedl, R., *Molecular orientation induced by cooling stresses. Birefringence in polycarbonate: III. Constrained quench and injection molding.* Journal of Polymer Science Part B: Polymer Physics, 1994. **32**(4): p. 595-605.
153. Kim, C.H. and Youn, J.R., *Determination of residual stresses in injection-moulded flat plate: Simulation and experiments.* Polymer Testing, 2007. **26**(7): p. 862-868.
154. Chen, T., *Digital Photoelasticity*, in *Photomechanics*, P. Rastogi, Editor. 2000, Springer Berlin / Heidelberg. p. 197-232.
155. Alger, M.S.M., *Polymer Science Dictionary*. 1997, London: Chapman & Hall.
156. Sawyer, L. C., Grubb, D. T. and Meyers, G.F., *Polymer Microscopy*. 3 ed. 2008: Springer.
157. Kamal, M.R. and Tan, V., *Orientation in injection molded polystyrene.* Polymer Engineering & Science, 1979. **19**(8): p. 558-563.
158. Hemsley, D.A. and Robinson, A.M., *A simple method for the assessment of molecular orientation in transparent plastics mouldings.* Polymer Testing, 1992. **11**(5): p. 373-385.
159. Yu, J.S., Wagner, A.H. and D.M. Kalyon, *Simulation of microstructure development in injection molding of engineering plastics.* Journal of Applied Polymer Science, 1992. **44**(3): p. 477-489.
160. Neves, N. M., Pouzada, A. S., Voerman, J. H. D. and Powell, P. C., *The use of birefringence for predicting the stiffness of injection molded polycarbonate discs.* Polymer Engineering & Science, 1998. **38**(10): p. 1770-1777.
161. Lee, K. and Mackley, M.R., *The significance of slip in matching polyethylene processing data with numerical simulation.* Journal of Non-Newtonian Fluid Mechanics, 2000. **94**(2-3): p. 159-177.
162. Chen, M., D. Yao, and Kim, B., *Eliminating flow induced birefringence and minimizing thermally induced residual stresses in injection molded parts.* Polymer-Plastics Technology and Engineering, 2001. **40**(4): p. 491-503.
163. Weng, C., Lee, W.B.and To, S., *Birefringence techniques for the characterization of residual stresses in injection-moulded micro-lens arrays.* Polymer Testing, 2009. **28**(7): p. 709-714.
164. Riande, E., *Polymer viscoelasticity : stress and strain in practice*. 2000, Marcel Dekker: New York.

165. Shaw, M.T. and MacKnight, W. J., *Introduction to Polymer Viscoelasticity*. 2005, JOHN WILEY & SONS, INC: Hoboken.
166. Ferry, J.D., *VISCOELASTIC PROPERTIES OF POLYMERS*. 3 ed. 1980, United States of America: JOHN WILEY & SONS.
167. ASM, I., *Characterization and Failure Analysis of Plastics*. 2003: ASM International. 482.
168. Marques, S., Creus, G., *Computational Viscoelasticity*. 2012: Springer. 124.
169. Ward, I.M. Sweeney J., *An Introduction to the Mechanical Properties of Solid Polymers, 2nd Edition* 2004: Wiley-Blackwel.
170. Brydson, J.A., *Plastics materials*. 7 ed. 1999, Butterworth-Heinemann: Linacre House, Jordan Hill, Oxford.
171. Brinson, H.F. and Brinson, L. C., *Polymer Engineering Science and Viscoelasticity: An Introduction*. 2007 Springer.
172. Brostow, W., *Performance of Plastics*. 2000 Hanser Verlag. 682
173. van Gurp, M. and Palmen, J., *Time-temperature superposition for polymeric blends.* Rheol Bull, 1998. **67**(1): p. 5-8.
174. Wiley, *Properties and Behavior of Polymers*. 2012 John Wiley & Sons. 1605
175. Dealy, J. and Plazek, D., *Time-temperature superposition—a users guide.* Rheol. Bull, 2009. **78**(2): p. 16-31.
176. Menczel, J.D. and Prime, R. B., *Thermal Analysis of Polymers, Fundamentals and Applications*. 2009 John Wiley & Sons. 420
177. Akinay, A.E. and Brostow, W., *Long-term service performance of polymeric materials from short-term tests: prediction of the stress shift factor from a minimum of data.* Polymer, 2001. **42**(10): p. 4527-4532.
178. Mark, J., *Physical Properties of Polymers*. 2004 Cambridge University Press.
179. Struik, L.C.E., *Physical aging in plastics and other glassy materials.* Polymer Engineering & Science, 1977. **17**(3): p. 165-173.
180. Urzhumtsev, Y.S., *Time — Temperature superposition for thermorheologically complex materials.* Polymer Mechanics, 1974. **10**(2): p. 180-185.
181. O'Connell, P.A. and McKenna, G.B., *Large deformation response of polycarbonate: Time-temperature, time-aging time, and time-strain superposition.* Polymer Engineering & Science, 1997. **37**(9): p. 1485-1495.
182. Heymans, N., *Constitutive equations for polymer viscoelasticity derived from hierarchical models in cases of failure of time-temperature superposition.* Signal Processing, 2003. **83**(11): p. 2345-2357.
183. Macaúbas, P. H. P.; Demarquette, N. R., *Time-temperature superposition principle applicability for blends formed of immiscible polymers.* Polymer Engineering & Science, 2002. **42**(7): p. 1509-1519
184. Alcock, B., Cabrera, N. O., Barkoula, N. M., Reynolds, C. T., Govaert, L. E. and Peijs, T., *The effect of temperature and strain rate on the mechanical properties of highly oriented polypropylene tapes and all-polypropylene composites.* Composites Science and Technology, 2007. **67**(10): p. 2061-2070.
185. Mano, J. F., Sousa, R. A., Reis, R. L., Cunha, A. M. and Bevis, M. J., *Viscoelastic behaviour and time–temperature correspondence of HDPE with varying levels of process-induced orientation.* Polymer, 2001. **42**(14): p. 6187-6198.
186. Mano, J. F., Sencadas, V.,Costa, A. and Lanceros-Méndez, S., *Dynamic mechanical analysis and creep behaviour of [beta]-PVDF films.* Materials Science and Engineering A, 2004. **370**(1-2): p. 336-340.
187. Guedes, R.M., *A viscoelastic model for a biomedical ultra-high molecular weight polyethylene using the time-temperature superposition principle.* Polymer Testing, 2011. **30**(3): p. 294-302.
188. Colby, R.H., *Breakdown of time-temperature superposition in miscible polymer blends.* Polymer, 1989. **30**(7): p. 1275-1278.
189. Moldflow®, A. *Autodesk® Moldflow®*. 2011; Available from: http://usa.autodesk.com/moldflow/.
190. ABAQUS. *ABAQUS interface for Moldflow User´s Manual*. 2004.
191. Yoo, K., Lee, S., Youn, J., Yoon, D., Cho, Y., Yu, J. and Park, H, *Injection molding of vertebral fixed cage implant.* Fibers and Polymers, 2003. **4**(2): p. 89-96.

192. Grujicic, M., Sellappan, V., Arakere, G., Seyr, N. and Erdmann, M., *Computational feasibility analysis of direct-adhesion polymer-to-metal hybrid technology for load-bearing body-in-white structural components.* Journal of Materials Processing Technology, 2008. **195**(1-3): p. 282-298.
193. Seong Yun Kim, Hwa Jin Oh, Sung Ho Kim, Chae Hwan Kim, Seung Hwan Lee and Jae Ryoun Youn, *Prediction of residual stress and viscoelastic deformation of film insert molded parts.* Polymer Engineering & Science, 2008. **48**(9): p. 1840-1847.
194. Kröner, C., Altenbach, H. and Naumenko, K., *Coupling of a structural analysis and flow simulation for short-fiber-reinforced polymers: property prediction and transfer of results.* Mechanics of Composite Materials, 2009. **45**(3): p. 249-256.
195. Sha, B., Dimov, S., Griffiths, C. and Packianather, M., *Micro-injection moulding: Factors affecting the achievable aspect ratios.* The International Journal of Advanced Manufacturing Technology, 2007. **33**((10)): p. 147-156.
196. Harper, C. and Petrie, E., *Plastics Materials and Processes: A Concise Encyclopedia*. 2003, John Wiley & Sons: Hoboken. 1008
197. Peacock, A. and Calhoun, A., *Polymer Chemistry: Properties and Applications*, 2007, Hanser Verlag: Munchen. p. 397.
198. McKeen, L.W., *Effect of Temperature and other Factors on Plastics and Elastomers*. 2008 New York: William Andrew. 824
199. Song, M. C., Liu, Z., Wang, M. J., Yu, T. M. and Zhao, D. Y., *Research on effects of injection process parameters on the molding process for ultra-thin wall plastic parts.* Journal of Materials Processing Technology, 2007. **187-188**: p. 668-671.
200. SolidWorks®. 2011; Available from: http://www.solidworks.com/sw/products/10141_ENU_HTML.htm.
201. Ruprecht, R.,Gietzelt, T.,Müller, K.,Piotter, V. and Haußelt, J., *Injection molding of microstructured components from plastics, metals and ceramics.* Microsystem Technologies, 2002. **8**(4-5): p. 351-358.
202. Vasco, J., *A study on the performance of microinjection moulds obtained using additive manufacturing*, 2010.
203. Zhil'tsova, T.V., Neto, V.F., Ferreira, J.A. and Oliveira, M.S.A. . *On the suitability of the conventional injection moulding process for microfeatured parts replication - a doe approach.* in *ICIT & MPT 2009*. 2009. International Conference, Ljubljana, Slovenia, 4-7 October 2009
204. Osswald, T.A., Turng L. and Gramann, P., *Injection Molding Handbook*. 2008, Carl Hanser Verlag: Munich. 764.
205. Roy, R.K., *A Primer on the Taguchi Method*. 2010, Society of Manufacturing Engineers: Dearborn, Michigan.
206. Tosello, G.,Gava, A.,Hansen, H. N.,Lucchetta, G. and Marinello, F., *Characterization and analysis of weld lines on micro-injection moulded parts using atomic force microscopy (AFM).* Wear, 2009. **266**(5-6): p. 534-538.
207. Xie, L. and Ziegmann, G., *Effect of gate dimension on micro injection molded weld line strength with polypropylene (PP) and high-density polyethylene (HDPE).* The International Journal of Advanced Manufacturing Technology, 2010. **48**(1-4): p. 71-81.
208. Fava, R.A., *Polymers Physical Properties*. 1980, London: Academic press.
209. Gedde, U.W., *Polymer Physics*. 1 ed. 1995 Chapman & Hall.
210. Tang, S. H.,Tan, Y. J.,Sapuan, S. M.,Sulaiman, S.,Ismail, N. and Samin, R., *The use of Taguchi method in the design of plastic injection mould for reducing warpage.* Journal of Materials Processing Technology, 2007. **182**(1–3): p. 418-426.
211. Malpass, V.E., *Prediction of long-term ABS relaxation behavior.* Journal of Applied Polymer Science, 1968. **12**(4): p. 771-788.
212. Donggang, Y. and Byung, K., *Simulation of the filling process in micro channels for polymeric materials.* Journal of Micromechanics and Microengineering, 2002. **12**(5): p. 604-610.
213. HyperWorks, A. 2011 [cited 2013 7 March]; Available from: http://www.altair.com/.
214. Kennedy, P., *Flow analysis of injection molds*. 1995, Carl Hanser Verlag: Munich. 237.
215. Autodesk, *Autodesk Simulation Moldflow Insight help*, 2012.
216. Abaqus, *Abaqus Analysis User's Manual, Version 6.10*.
217. Nguyen,Q. M. P., Chen, X., Lam, Y. C. and Yue, C. Y., *Effects of polymer melt compressibility on mold filling in micro-injection molding.* Journal of Micromechanics and Microengineering, 2011. **21**(9): p. 095019.

218. Boronat, T., Segui, V. J., Peydro, M. A. and Reig, M. J., *Influence of temperature and shear rate on the rheology and processability of reprocessed ABS in injection molding process*. Vol. 209. 2009, Amsterdam, PAYS-BAS: Elsevier. 11.
219. Goodship, V., *Arburg Practical Guide To Injection Moulding*. 2004: iSmithers Rapra Publishing - Technology & Engineering
220. Zhou, H., *Computer Modeling for Injection Molding: Simulation, Optimization, and Control*. 2013: John Wiley & Sons, Inc. 1-24.
221. Beaumont, J.P., *Runner and Gating Design Handbook: Tools for Successful Injection Molding*. 2007: Hanser Verlag,Technology & Engineering
222. Support, A.S.M.S. *Utilizing and Understanding Weld Line Results*. 2013 [cited 2013 28.06.13]; Available from: http://usa.autodesk.com/adsk/servlet/ps/dl/item?siteID=123112&id=15482985&linkID=13030537.
223. Menard, K.P., *DYNAMIC MECHANICAL ANALYSIS A Practical Introduction*, Boca Raton: London New York Washington,.

Appendix A

Magnitude and distribution of the maximum shear rate for DOE1 (high T_m, T_{melt} and V_i) and DOE8 (low T_m, T_{melt} and V_i) can be depicted from Figures A.1 – A6, for PP, POM and ABS polymer respectively.

A.1. Magnitude and distribution of shear rate in PP μ-parts

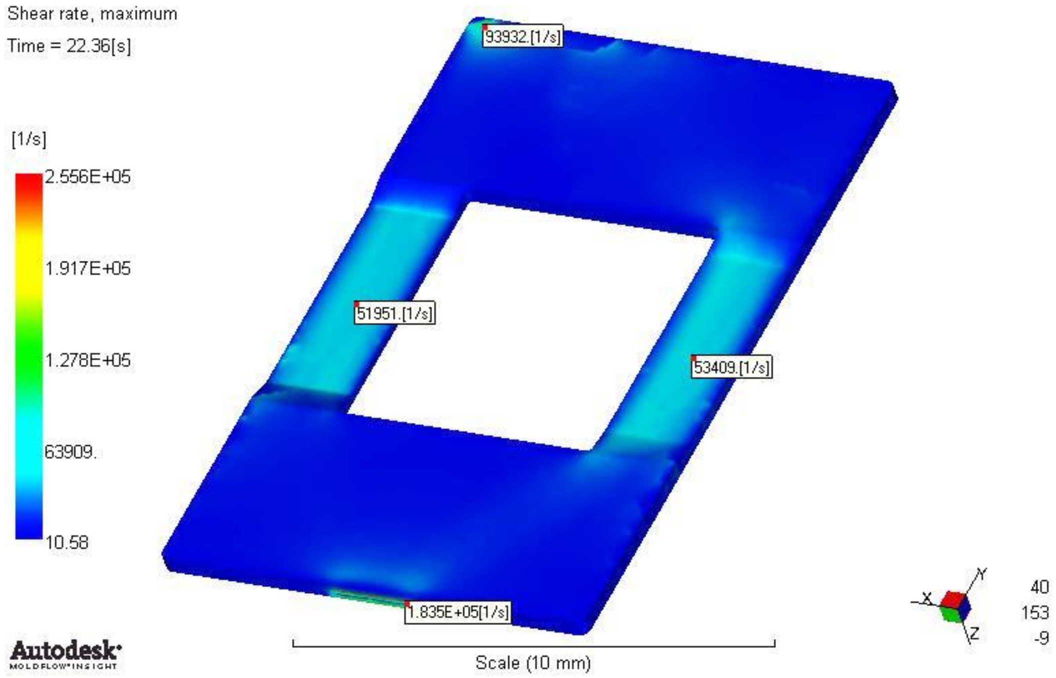

Figure A.1- Shear rate, maximum - PP (DOE1); injection controlled with the recorded Fill Time

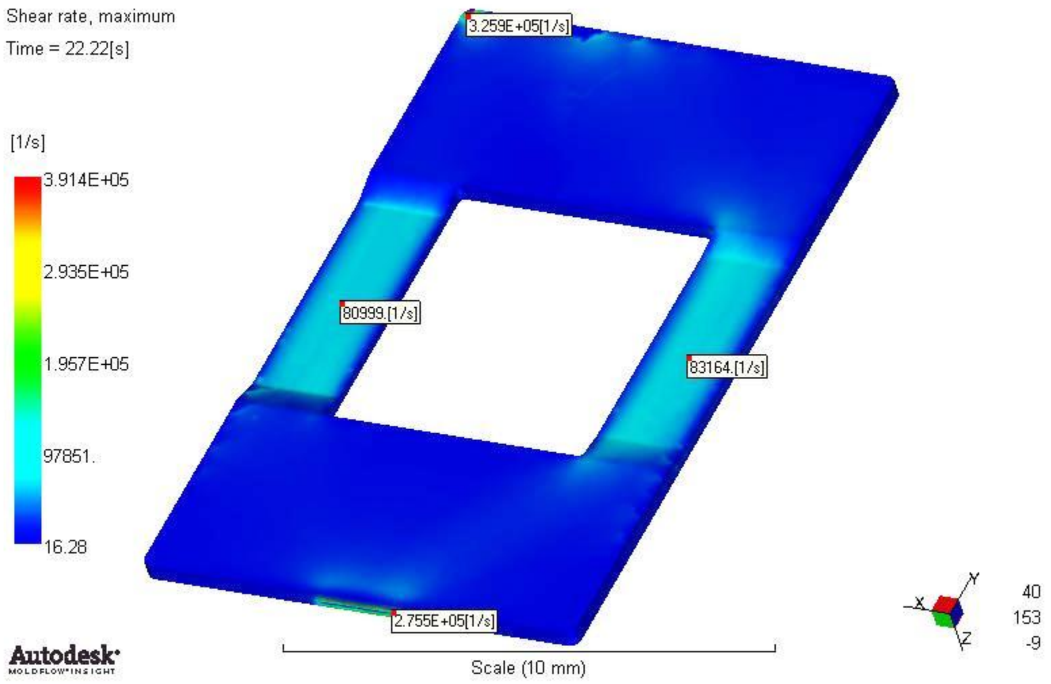

Figure A.2 - Shear rate, maximum – PP (DOE8); injection controlled with the recorded Fill Time

A.2. Magnitude and distribution of shear rate in POM μ-parts

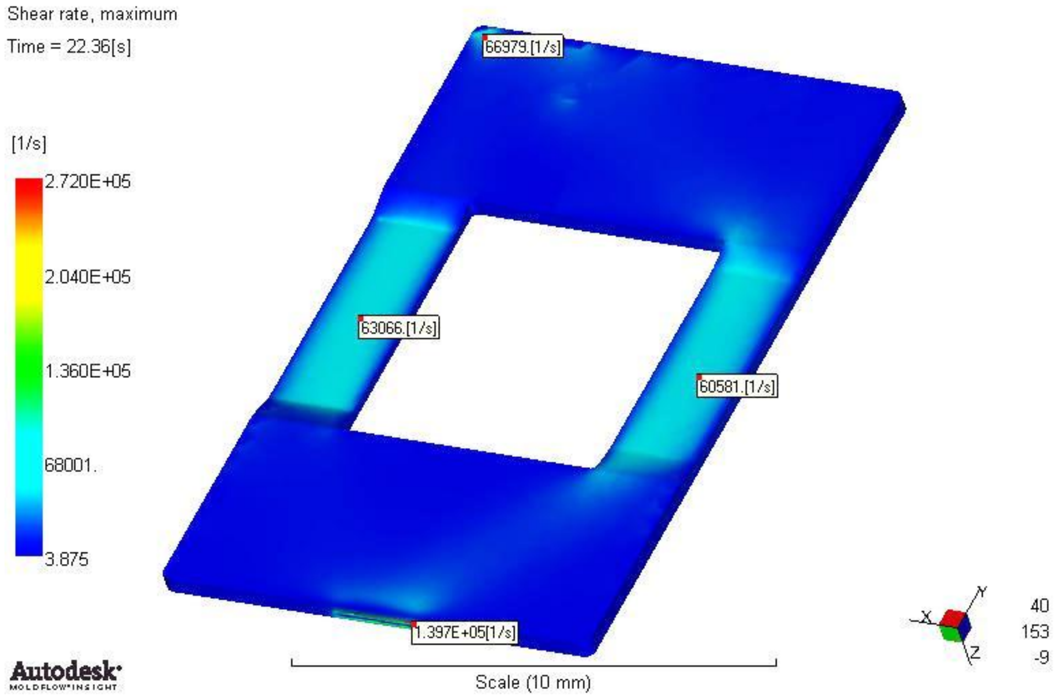

Figure A.3 - Shear rate, maximum - POM (DOE1); injection controlled with the recorded Fill Time

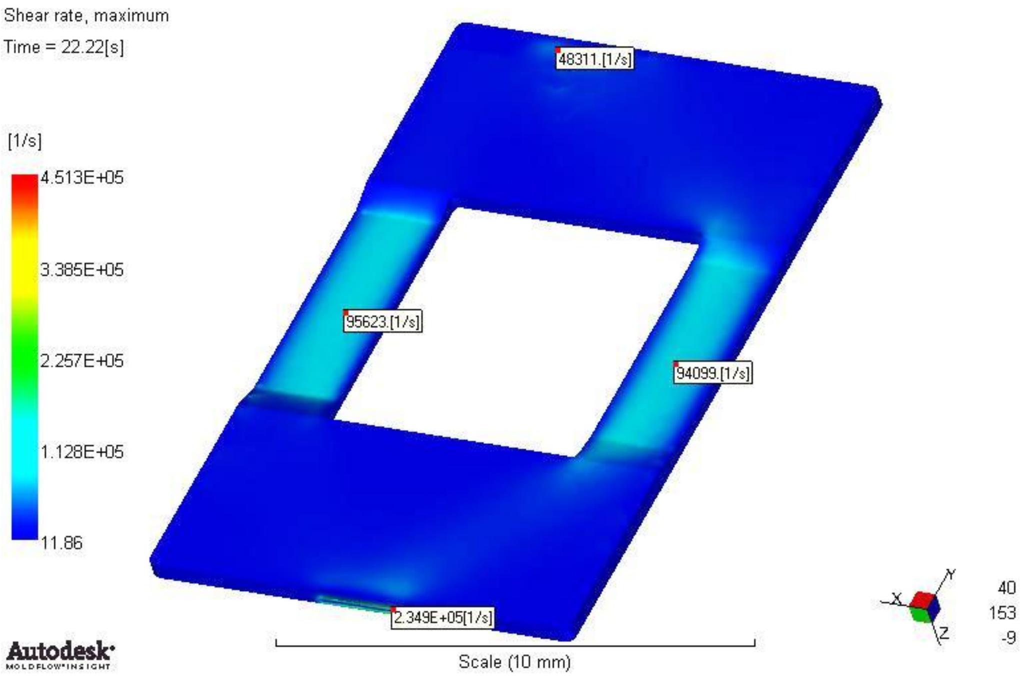

Figure A.4 - Shear rate, maximum - POM (DOE8); injection controlled with the recorded Fill Time

A.3. Magnitude and distribution of shear rate in ABS μ-parts

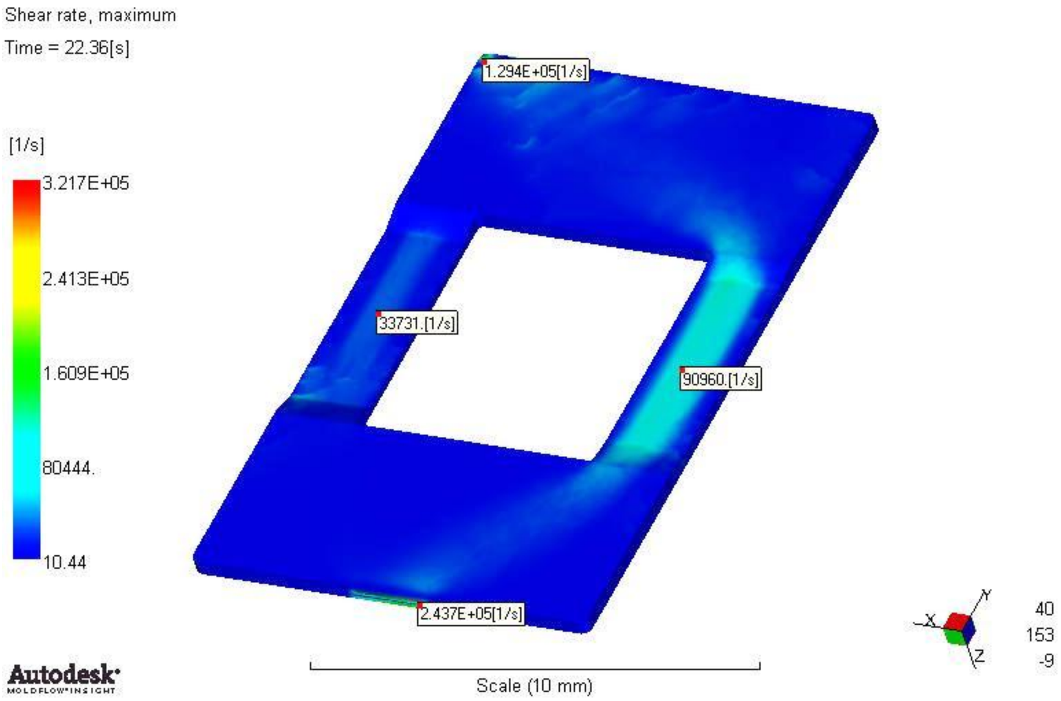

Figure A.5 - Shear rate, maximum - ABS (DOE1); injection controlled with the recorded Fill Time

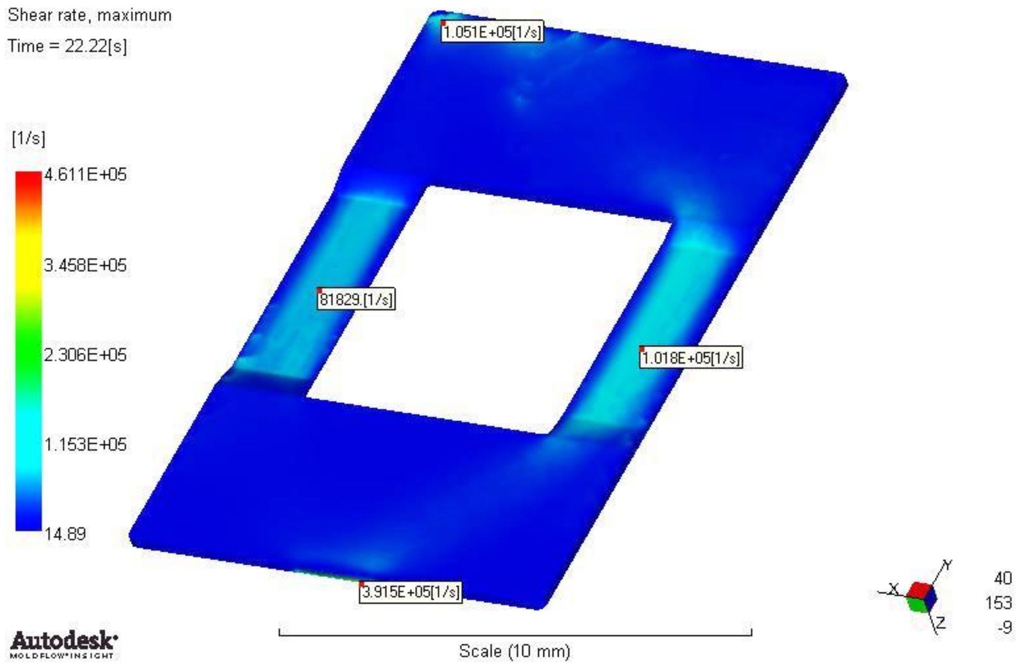

Figure A.6 - Shear rate, maximum - ABS (DOE8); injection controlled with the recorded Fill Time

Appendix B

Distribution of the maximum principal stresses through the normalized thickness of ABS, POM and PP µ-parts, for DOE1 (high Tm, Tmelt and Vi) and DOE8 (low Tm, Tmelt and Vi) processing conditions are shown in Appendixes B.1., B.3., and B.5., respectively. Shrinkage gradient through the thickness for the same experiments are presented in Appendixes B.2., B.4., and B.6.

B.1. Predicted process induced residual stresses in ABS µ-parts

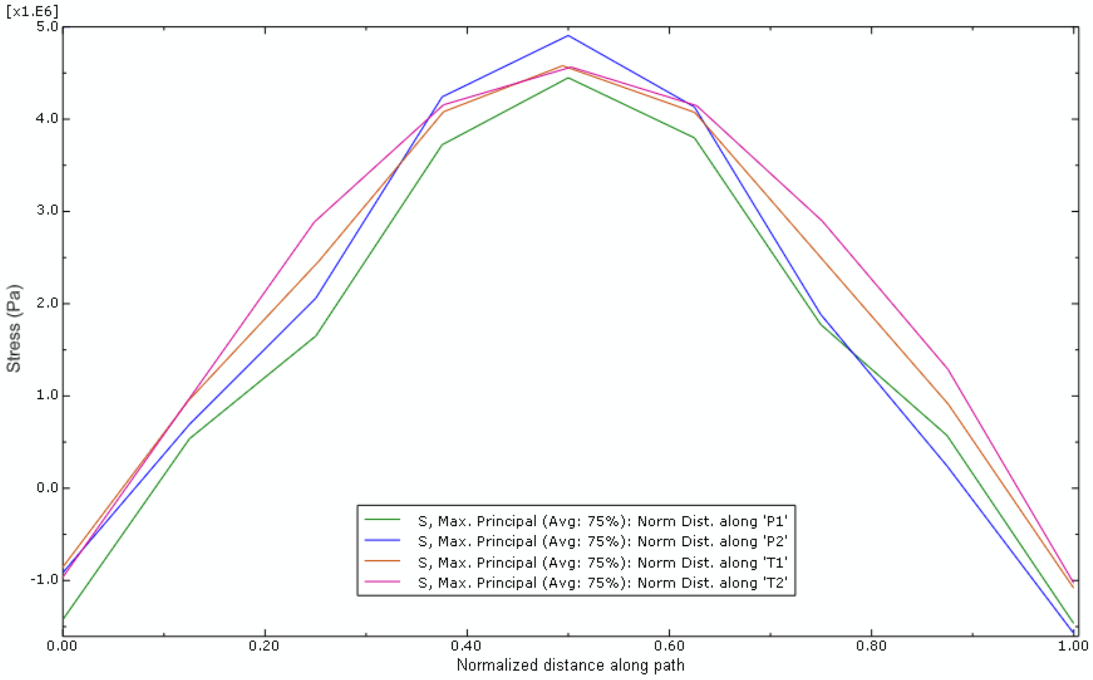

Figure B.1 - Post ejection distribution of the maximum principal stresses through the thickness of ABS µ-part (DOE1)

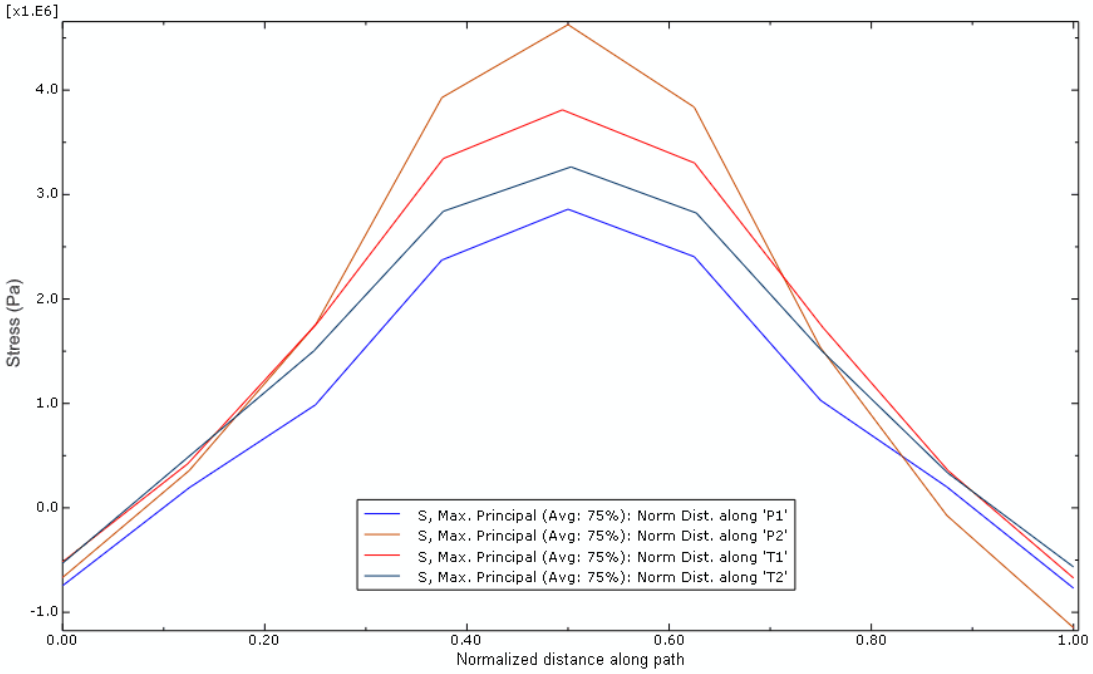

Figure B.2 - Post ejection distribution of the maximum principal stresses through the thickness of ABS µ-part (DOE8)

B.2. Volumetric shrinkage through the thickness of ABS µ-parts

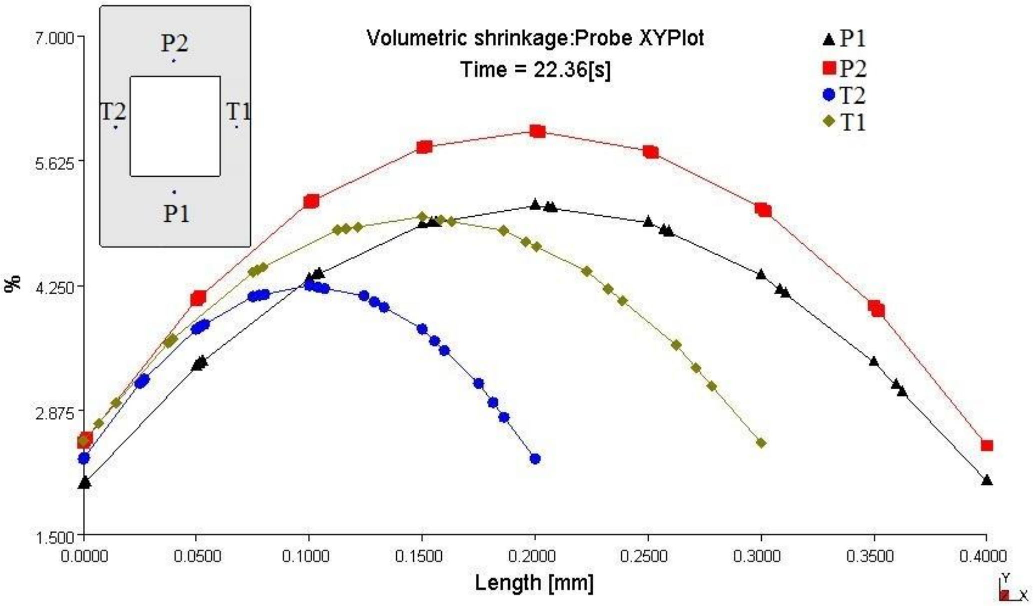

Figure B.3 - Volumetric shrinkage through the thickness of ABS µ-part (DOE1)

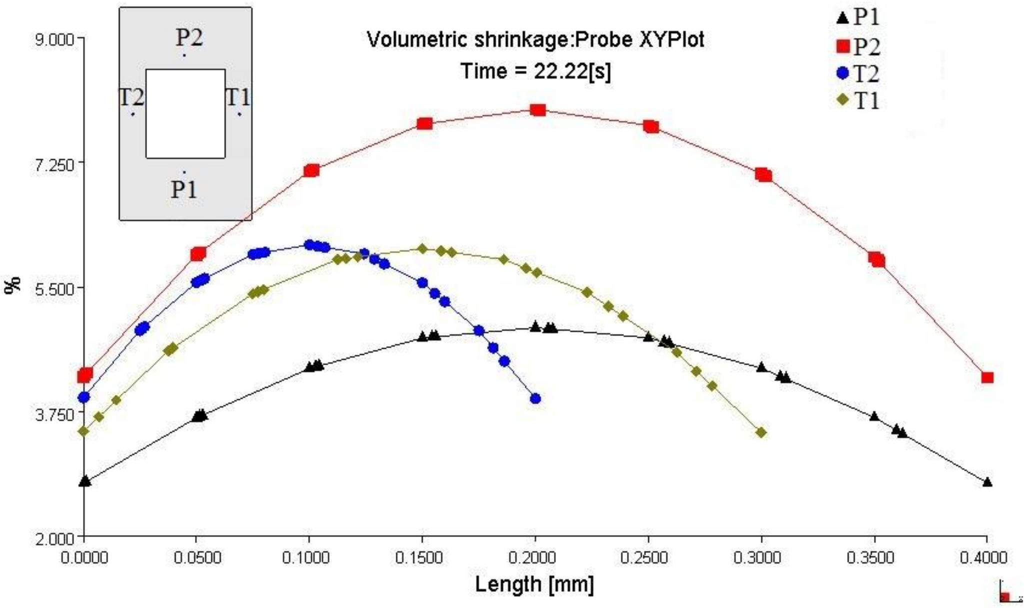

Figure B.4 - Volumetric shrinkage through the thickness of ABS µ-part (DOE8)

B.3. Predicted process induced residual stresses in POM µ-parts

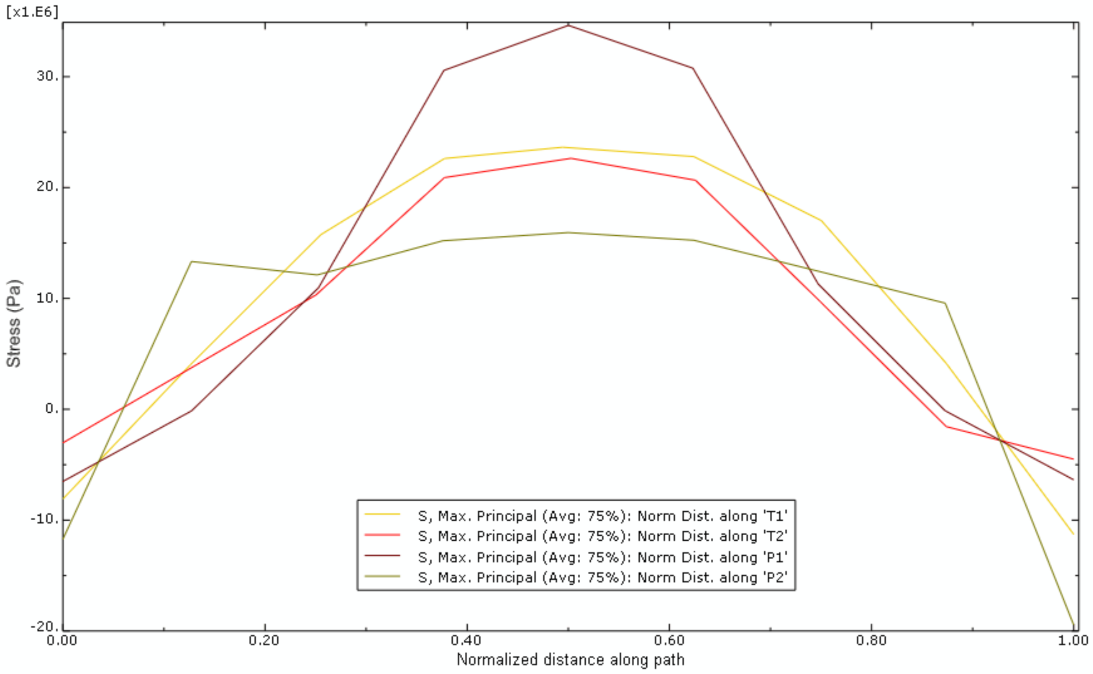

Figure B.5 - Post ejection distribution of the maximum principal stresses through the thickness of POM µ-part (DOE1)

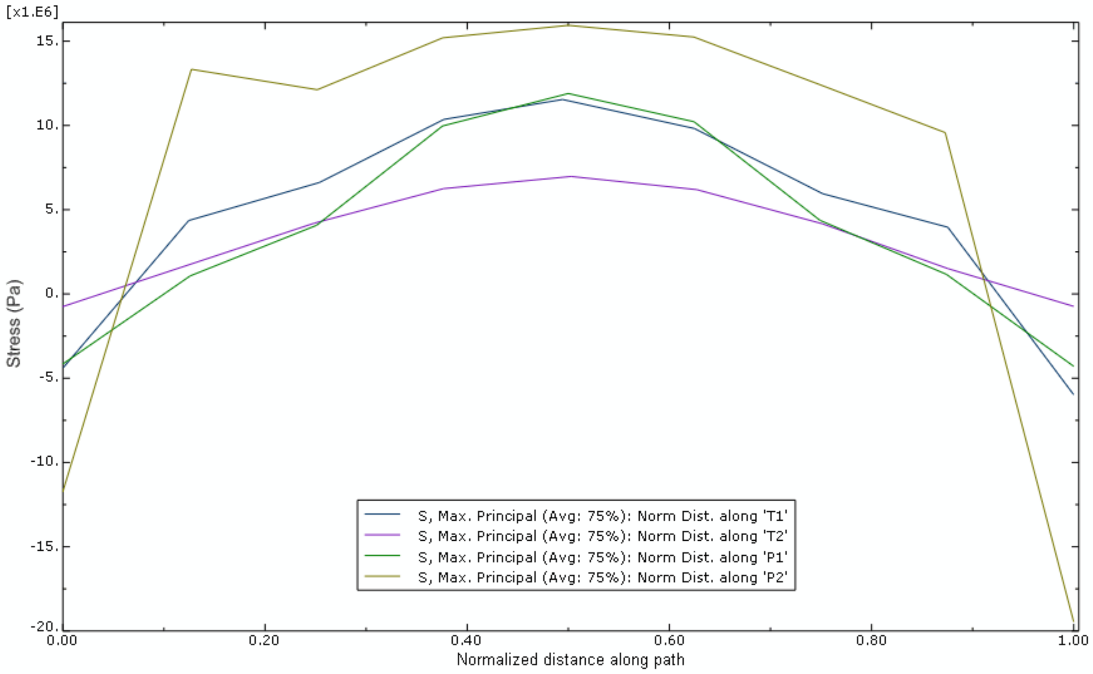

Figure B.6 - Post ejection distribution of the maximum principal stresses through the thickness of POM μ-part (DOE8)

B.4. Volumetric shrinkage through the thickness of POM μ-parts

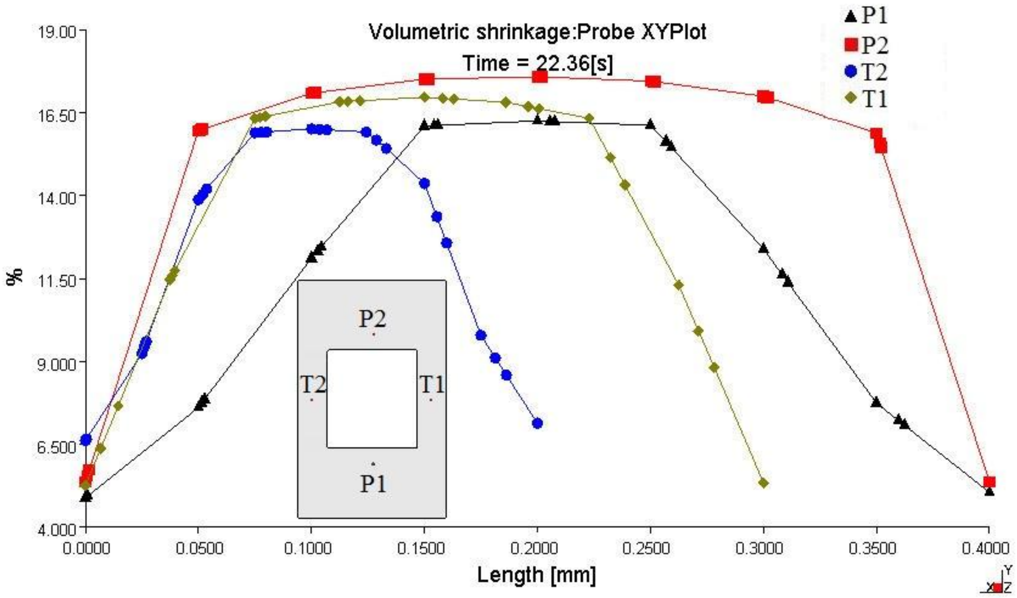

Figure B.7 - Volumetric shrinkage through the thickness of POM μ-part (DOE1)

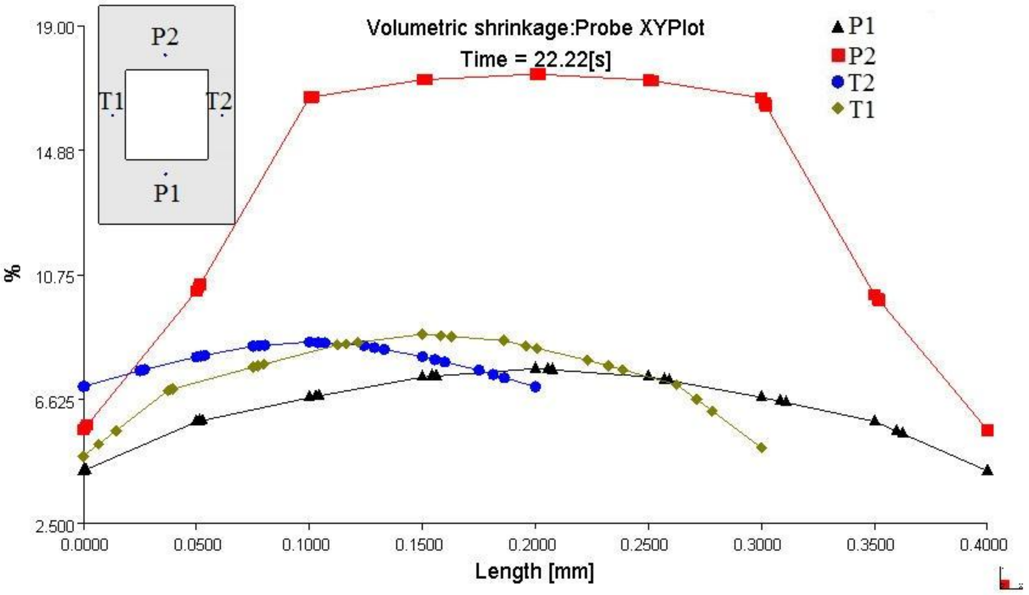

Figure B.8 - Volumetric shrinkage through the thickness of POM μ-part (DOE8)

B.5. Predicted process induced residual stresses in PP μ-parts

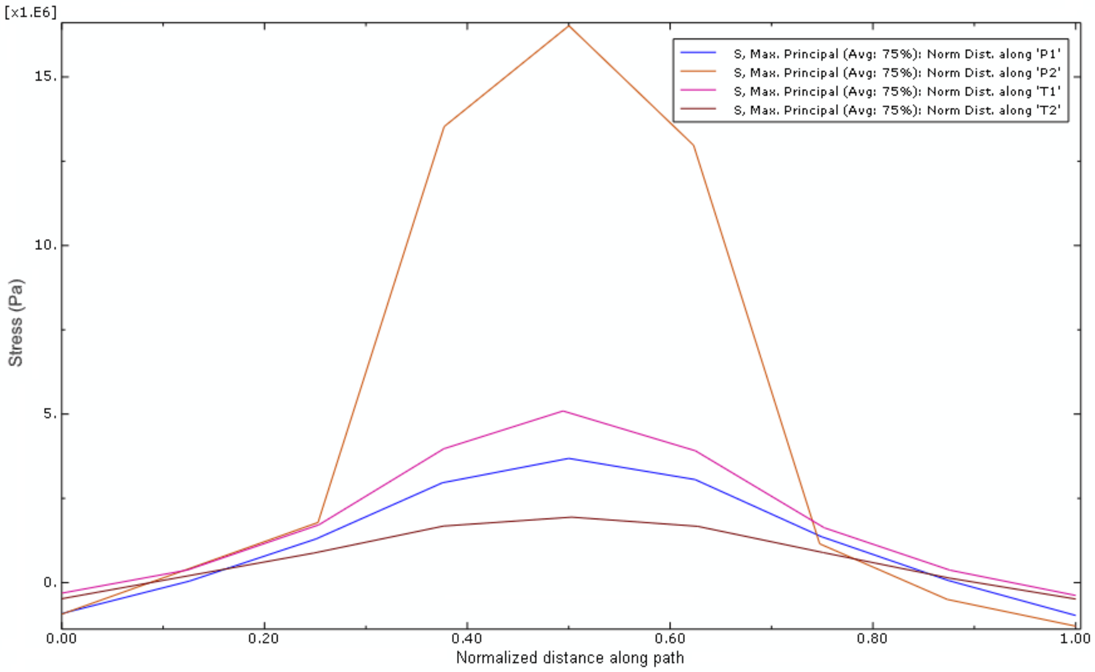

Figure B.9 - Post ejection distribution of the maximum principal stresses through the thickness of PP μ-part (DOE1)

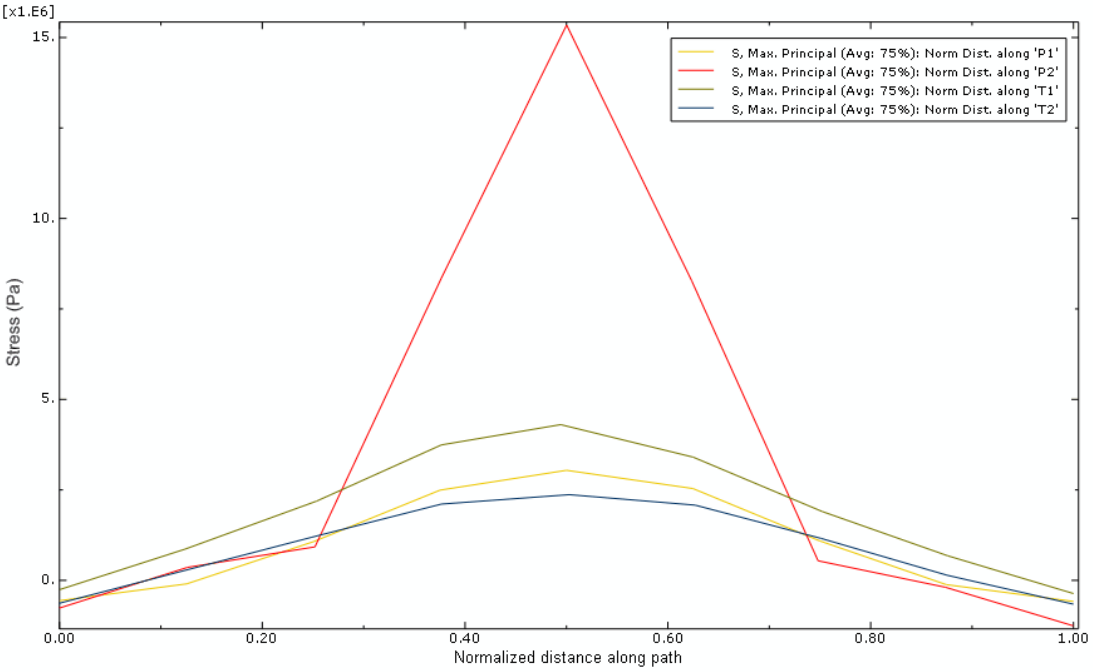

Figure B.10 - Post ejection distribution of the maximum principal stresses through the thickness of PP µ-part (DOE8)

B.6. Volumetric shrinkage through the thickness of PPµ-parts

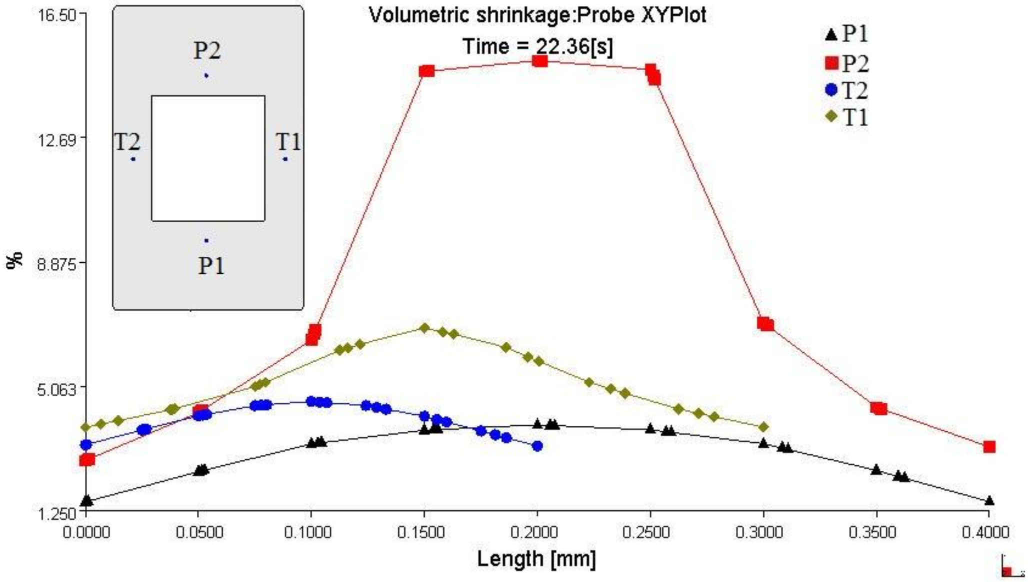

Figure B.11 - Volumetric shrinkage through the thickness of PP µ-part (DOE1)

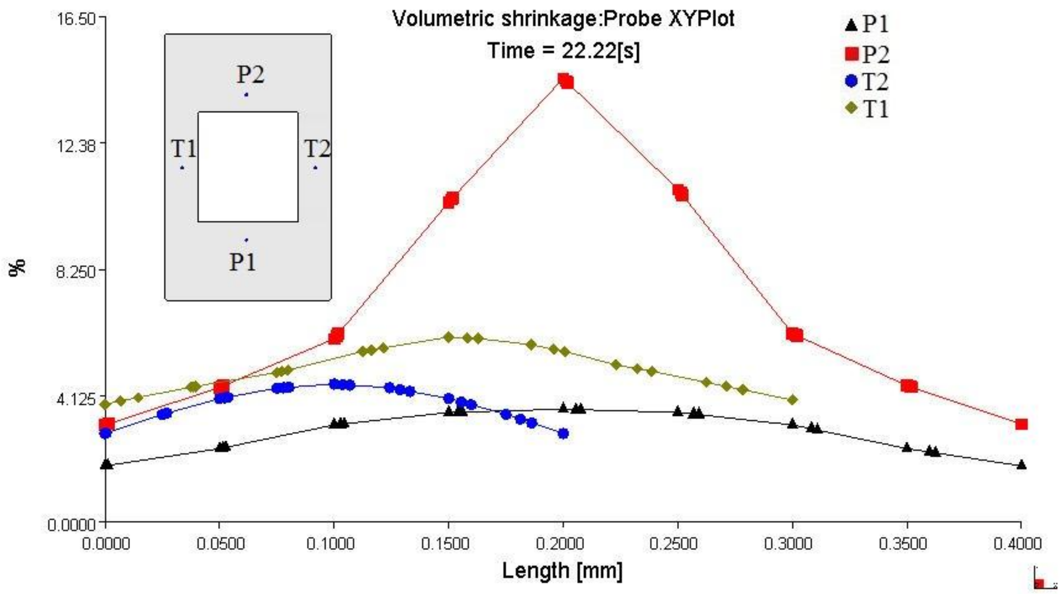

Figure B.12 - Volumetric shrinkage through the thickness of PP μ-part (DOE8)

Appendix C

C.1. Relaxation of the stresses in 200 and 300μm sections of ABS μ-part

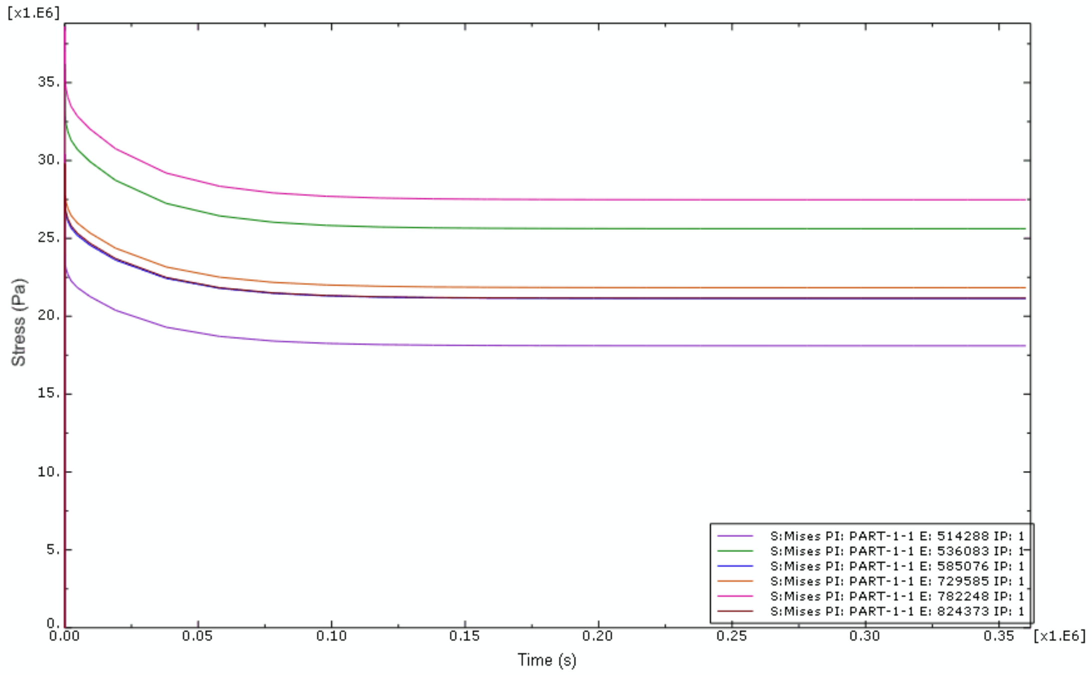

Figure C.1 - Relaxation of the stresses in 200 and 300μm sections of ABS μ-part (DOE1)

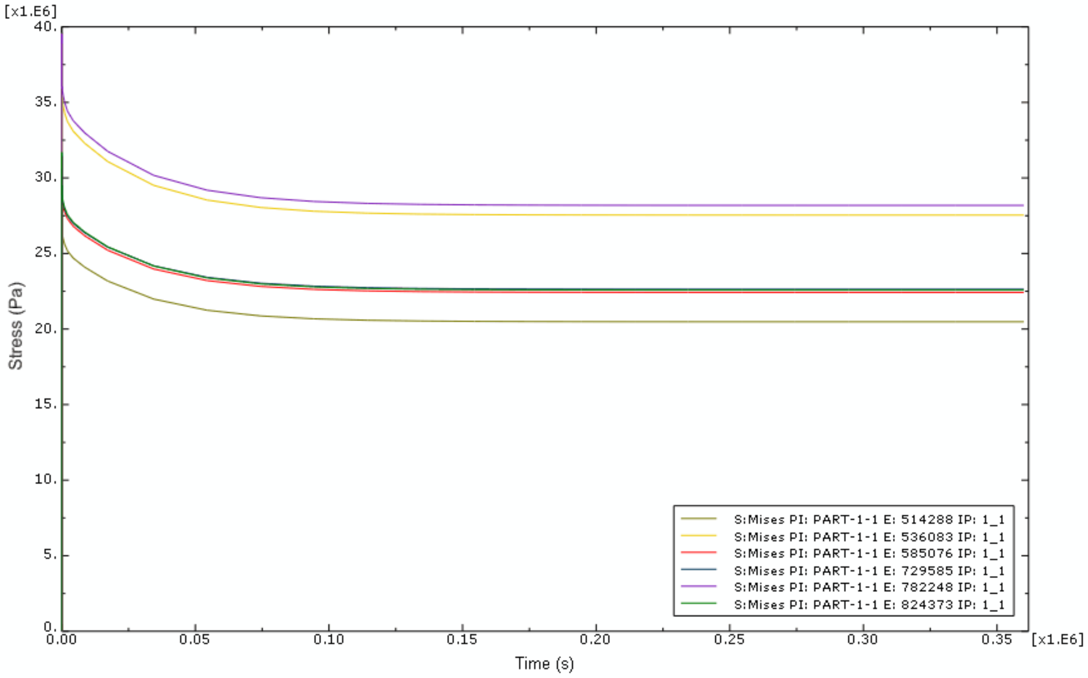

Figure C.2 - Relaxation of the stresses in 200 and 300µm sections of ABS µ-part (DOE8)

C.2. Residual stress distribution through 200µm and 300µm sections of ABS µ-part

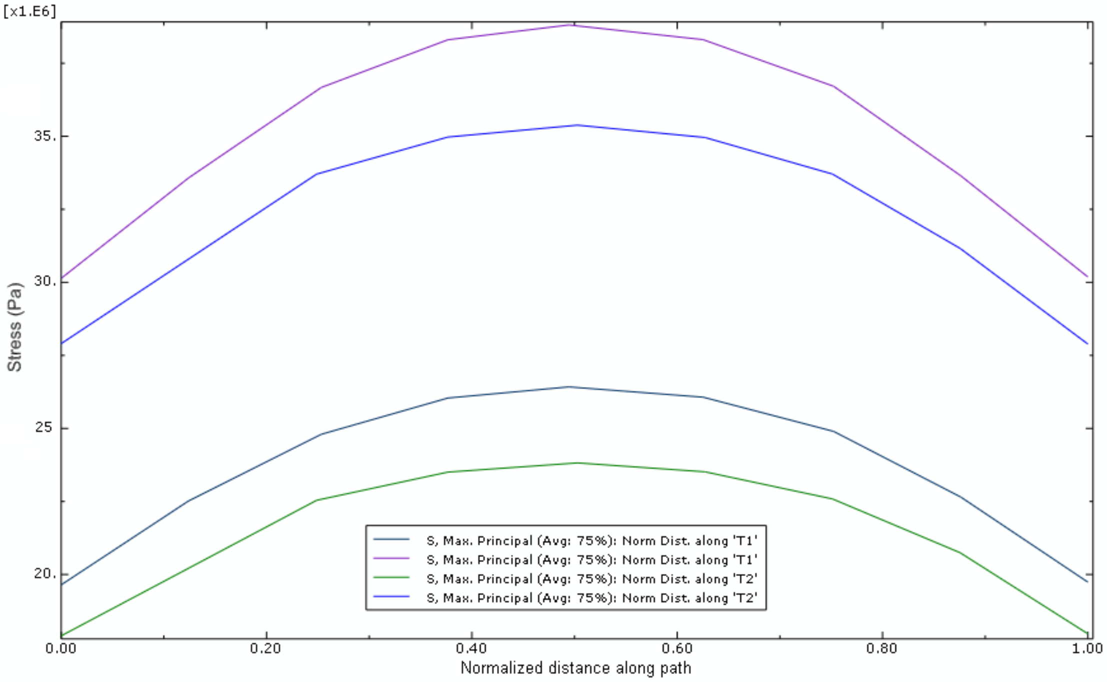

Figure C.3 - Residual stress distribution through 200µm and 300µm sections for DOE1 µ-part

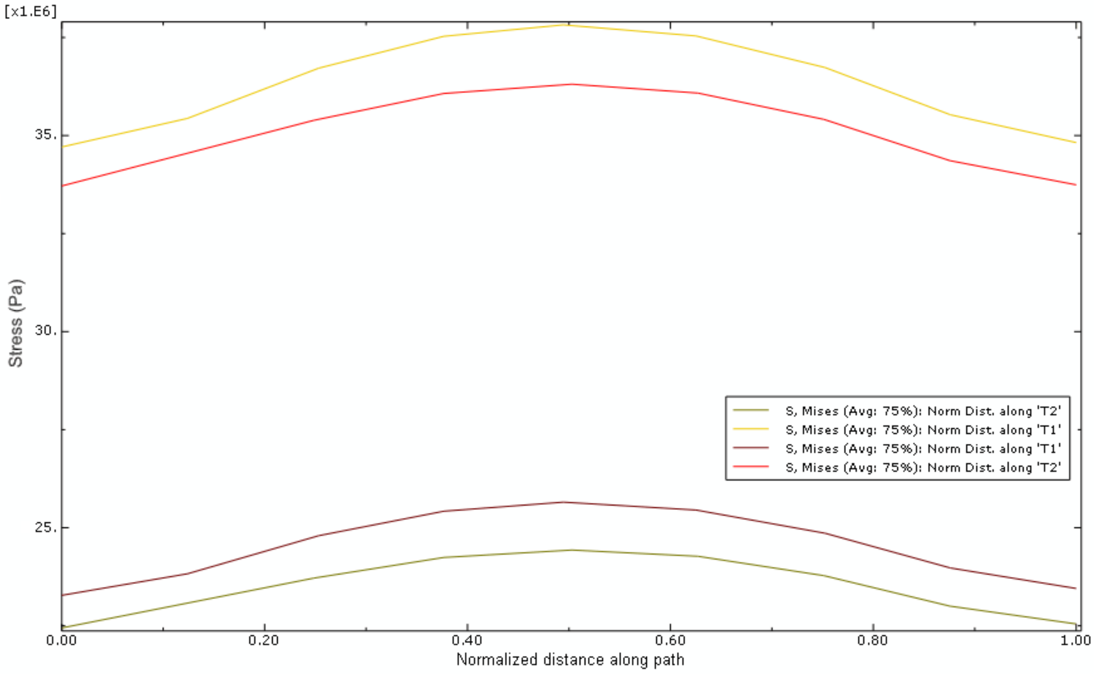

Figure C.4 - Residual stress distribution through 200µm and 300µm sections for DOE8 µ-part